

M. SANTANDREA

DESIGN OF NONLINEAR INTEGRATED
DEVICES FOR QUANTUM OPTICS
APPLICATIONS

Design of nonlinear integrated devices for quantum optics applications

Der Naturwissenschaftlichen Fakultät
der Universität Paderborn
zur Erlangung des Doktorgrades
Dr. rer. nat.
vorgelegt von

MATTEO SANTANDREA

2019

Erklärung der Selbstständigkeit

Hiermit versichere ich, die vorliegende Arbeit selbstständig verfasst und keine anderen als die angegebenen Quellen und Hilfsmittel benutzt sowie die Zitate deutlich kenntlich gemacht zu haben.

Paderborn, den November 21, 2019

Matteo Santandrea

Erstgutachter:	Prof. Dr. Christine Silberhorn
Zweitgutachter:	Prof. Dr. Torsten Meier
Vertreter des Mittelbaus:	Dr. Uwe Gerstmann
Vorsitzender der Prüfungskommission:	Prof. Dr. Dirk Reuter
Tag der Abgabe:	28. 11.2019

Contents

Erklärung der Selbstständigkeit	E
Summary	v
Zusammenfassung	vii
Preface	ix
Introduction	xiii
List of abbreviations and nomenclature	xv
I Background	1
1 Integrated waveguides	3
1.1 Ray optics description	3
1.2 Rigorous mathematical description	5
1.3 Asymmetric slab waveguide	8
1.4 Numerical methods	11
2 Nonlinear optics in waveguiding structures	13
2.1 Nonlinear material response	13
2.1.1 Second-order nonlinear polarisation density	17
2.2 Nonlinear coupled-mode theory in waveguides	19
2.2.1 Three wave mixing in waveguides	20
2.2.2 SFG at perfect phase matching	22
2.2.3 Phase matching spectrum of SHG processes under NPDA	23

Contents

2.2.4	Final remarks	25
2.3	Understanding and tailoring three wave mixing	27
2.3.1	Birefringent phase matching	27
2.3.2	Quasi-phase matching	31
2.4	Elements of ultrafast quantum optics	34
2.4.1	PDC and broadband modes	35
2.4.2	FC and broadband modes	36
2.4.3	Decorrelated JSA	38
3	Nonlinear materials and waveguide fabrication	41
3.1	Lithium niobate	41
3.1.1	Optical properties	42
3.1.2	Diffused waveguide in LN	45
3.1.3	Thin film LNOI	47
3.2	KTP	48
3.2.1	Optical properties	50
3.2.2	Rb exchanged waveguides in KTP	51
3.3	Linear characterisation	54
3.3.1	Propagation losses	54
3.3.2	Waveguide-fibre coupling efficiency	56
3.4	Periodic poling	57
II	Design of nonlinear processes	59
4	Design of nonlinear processes in KTP	61
4.1	Frequency conversion IR→UV	61
4.1.1	Sample fabrication	62
4.1.2	Linear characterisation	65
4.1.3	Frequency conversion measurement	67
4.2	Decorrelated PDC source at 1300nm	76
5	Effect of inhomogeneities in nonlinear systems	83
5.1	Qualitative model	84

5.1.1	Numerical analysis of $ \partial_w \Delta\beta $ for Ti:LN waveguides	86
5.2	Phase matching in inhomogeneous waveguides.	90
5.2.1	Mathematical modelling of waveguide inhomogeneities	90
5.2.2	Analysis of different types of noises	92
5.2.3	Impact of fabrication errors in squeezing generation.	96
5.2.4	Impact of fabrication errors on quantum information encoding.	99
5.2.5	Impact of fabrication errors on the performance of a bandwidth compressor.	100
5.3	Reconstruction of sample inhomogeneity	105
5.3.1	Experiment	105
5.4	Correction of fabrication imperfection	111
5.4.1	Simulation of the inhomogeneous system and its correction	112
5.5	General theory of waveguide inhomogeneities	115
5.5.1	Mathematical formulation	116
5.5.2	Simulation of inhomogeneous systems	117
5.5.3	General design rule for nonlinear systems	118
5.5.4	Comparison with simulations of different physical systems	120
6	Second harmonic losses	123
6.1	Measurement Strategy and Theory	124
6.2	Fitting procedure	127
6.3	Results	128
7	Design of nonlinear processes in LNOI	135
7.1	Dispersion relations of LNOI waveguides	135
7.1.1	Modelling of LNOI waveguides	135
7.1.2	Numerical derivation of the dispersion relations	137
7.1.3	Dependence of the dispersion relation on the waveguide geometry: a qualitative analysis	138
7.2	Process engineering in LNOI waveguides	143
7.2.1	$\Delta\beta$ contour lines: a novel method of analysis	143
7.2.2	Engineering of PDC processes in LNOI waveguides	144
7.3	Pure degenerate PDC states in LNOI	151

Contents

7.3.1	Identification of the design parameters	151
7.3.2	Sensitivity of the PDC process to fabrication errors	153
7.3.3	Conversion efficiency of type II PDC	155
7.4	Analysis of facet reflectivity	161
8	Conclusions	169
III	Appendix	171
A	Coefficients for LNOI waveguides	173
	Acknowledgement	179
	Bibliography	181

Summary

In this work, we theoretically and experimentally investigate the design and the performance of integrated nonlinear optical devices for quantum optics applications.

We discuss the in-house fabrication of two KTP systems implementing two processes of interest for the quantum optical community. The first sample performs a frequency conversion bridging the gap between the ultraviolet and the infrared range and the second is an infrared source of decorrelated photon pairs. We show that the performance of the samples is affected by fabrication imperfections and expand the discussion to the case of nonlinear processes in lithium niobate waveguides. We develop a model that provides design rules to optimise the spectral quality of nonlinear devices and discover that such a theory can be extended to nonlinear processes realised in a wide variety of nonlinear systems.

To improve the characterisation of our samples, we develop a technique to estimate the losses of the second harmonic field in a nonlinear waveguide system. The work is completed by an in-depth analysis of the effect of the waveguide geometry in determining the dispersion and nonlinear properties of lithium niobate on insulator (LNOI) waveguides. We conclude with a discussion on the impact of fabrication errors on the performance of these systems.

Zusammenfassung

Diese Arbeit behandelt die theoretische und experimentelle Untersuchung integrierter nichtlinearer optischer Bauelemente für quantenoptische Anwendungen.

Wir betrachten zwei KTP-Systeme aus eigener Herstellung, welche für die quantenoptische Gemeinschaft interessante Prozesse realisieren. Die erste Probe führt eine Frequenzkonversion durch, um die Lücke zwischen dem Ultraviolett- und dem Infrarotbereich zu überbrücken. Die zweite Probe ist eine Infrarotquelle für dekorrelierte Photonenpaare. Wir zeigen, dass die nichtlinearen Eigenschaften der Proben durch Imperfektionen im Herstellungsprozess beeinflusst werden und erweitern die Untersuchungen um Lithiumniobat Systeme. Wir entwickeln ein Modell, das Entwurfsregeln zur Optimierung der spektralen Qualität nichtlinearer Bauelemente enthält. Wir zeigen, dass diese Theorie auf eine Vielzahl nichtlinearer Systeme ausgeweitet werden kann.

Um die Charakterisierung unserer Proben zu verbessern, entwickeln wir eine Methode zur Verlustabschätzung des zweiten harmonischen Feldes in nichtlinearen Wellenleitern. Die Arbeit wird durch eine eingehende Analyse des Einflusses der Wellenleitergeometrie auf die Bestimmung der Dispersion und der nichtlinearen Eigenschaften von Lithiumniobat auf Isolator (LNOI) Wellenleitern vervollständigt. Wir schließen mit einer Diskussion der Auswirkungen von Fabrikationsfehlern auf die Eigenschaften dieser Systeme.

Preface

The work of this doctoral thesis has been performed during the years 2015-2019 in the IQO (Integrated Quantum Optics) group of Prof. Dr. Christine Silberhorn. We started our doctoral studies with the task of optimising the fabrication of periodically poled waveguides written in potassium titanyl phosphate (KTP). During the first one and a half year, we learnt the pre-existing techniques for the in-house fabrication of periodically poled KTP waveguide and helped optimising them, both by improving the processing steps and by characterising the properties of the fabricated samples. The direct involvement in the fabrication of KTP samples led to a deep understanding of waveguide processing and its limitations. This helped addressing the challenges presented by the fabrication process of nonlinear systems. Beside improving the waveguide processing, we developed new techniques for the characterisation of the KTP waveguides. In particular, we optimised the technique to measure the propagation losses of these system, providing useful feedback for the improvement of the fabrication process. Alongside the production of KTP samples, we were also actively involved in the modelling of these systems and we helped designing the first periodically poled, rubidium-exchanged ridge KTP waveguide, in collaboration with the group of Prof. Kip (Helmut Schmidt University, Hamburg) - see publications VI and VII here below.

Our work in the cleanroom was focused on the production of two different types of KTP samples. The first type implemented a sum frequency generation process to convert light from the IR to the UV. The target application was the realisation of a quantum frequency converter as an interface between ion qubits and single photons. The second type implemented a parametric down conversion process for the generation of heralded pure single photons in the telecom O-band - see publication IV below.

Interestingly, the phase matching properties of the second sample were very different from the theoretical expectation. Therefore, we investigated the reasons behind such behaviour and discovered that the effect of fabrication imperfections in our systems was much higher than formerly believed. For this reason, we spent the following years developing a model to properly describe the impact of fabrication imperfections onto the nonlinear performance of the nonlinear systems produced in our cleanroom. This model provided also design rules useful to minimise the effect of fabrication errors on the phase matching performance of the samples - see publication I. In this context, the knowledge about the fabrication techniques gained during the first two years proved invaluable in developing such model. We applied this theory to reconstruct the imperfections present in our fabrication process - see publication II, thus providing extremely useful information to improve the fabrication and the design of new devices.

The presentation of our model in different conferences stimulated interesting discussions with other groups working on different nonlinear systems. Thanks to these

exchanges, we were able to generalise the first model and develop a widely encompassing framework for the analysis of fabrication imperfections in a wide class of nonlinear systems - see publication III.

The last years of our doctorate included investigations of waveguides realised in a new technological platform, lithium niobate on insulator (LNOI). This platform offers at the same time high nonlinearities and the possibility of engineer novel nonlinear processes. Intrigued by these characteristics, we theoretically studied some of the processes available exclusively in LNOI waveguides and, at the same time, applied the theory previously developed to understand the technological challenges presented by the fabrication of these systems.

First author publications

Publication I

MS, M. Stefszky, V. Ansari, C. Silberhorn, *Fabrication limits of waveguides in nonlinear crystals and their impact on quantum optics applications*, New Journal of Physics 21 (3), 033038 (2019)

Publication II

MS, M. Stefszky, G. Roeland, C. Silberhorn, *Characterisation of Inhomogeneities in Ti:LiNbO₃ waveguides*, arXiv:1906.10018

Publication III

MS, M. Stefszky, C. Silberhorn, *General framework for the analysis of imperfections in nonlinear systems*, Opt. Lett. 44 (22), 5398-5401 (2019)

Publication IV

MS, M. Stefszky, G. Roeland, C. Silberhorn, *An interferometric method for determining the losses of spatially multi-mode nonlinear waveguides based on second harmonic generation*, In preparation.

Author contributions

Publication V

V. Ansari, E. Roccia, MS, M. Doostdar, C. Eigner, L. Padberg, I. Gianani, M. Sbroscia, J. M. Donohue, L. Mancino, M. Barbieri, C. Silberhorn, *Heralded generation of high-purity ultrashort single photons in programmable temporal shapes*, Optics express 26 (3), 2764-2774 (2018)

Publication VI

M. F. Volk, C. E. Rüter, MS, C. Eigner, L. Padberg, H. Herrmann, C. Silberhorn, D. Kip, *Fabrication of low-loss Rb-exchanged ridge waveguides in z-cut KTiOPO₄*, *Optical Materials Express* 8 (1), 82-87 (2018)

Publication VII

C. Eigner, MS, L. Padberg, M. F. Volk, C. E. Rüter, H. Herrmann, D. Kip, C. Silberhorn, *Periodically poled ridge waveguides in KTP for second harmonic generation in the UV regime* *Optics express* 26 (22), 28827-28833, (2018)

Patents

Patent I

Herstellung von Wellenleitern aus Materialien der KTP-Familie/Fabrication of waveguides from materials of the KTP family. Filed on 11/04/2018 Patent number DE 10 2018 108 636.9

Software

PyNumericalPhasematching, a Python API developed to calculate the phase matching spectrum of nonlinear processes in homogeneous and inhomogeneous systems. It is publicly available at <https://github.com/mattsantand/pynumericalphasematching>.

Introduction

It is a shared belief that one of the next technological leaps will be the successful implementation of quantum protocols and devices in our everyday life. The advent of secure quantum communications and the development of quantum computers and simulators are going to impact a great number of different sectors of our society, from developing new drugs to securing bank transactions, from understanding and harnessing efficient energy generation and storage to the development of new optical devices. In analogy with the electronic revolution, which gained enormous momentum with the development of the first transistors and integrated devices, the quantum revolution will most likely take off with the realisation of efficient integrated devices implementing state of the art quantum protocols. Among the different technologies racing to demonstrate their effectiveness in performing such tasks, integrated optical devices play an important role, since photons are perhaps the most promising medium for the transmission of quantum states, due to their weak interaction with the environment. In particular, the integration of guiding structures into nonlinear crystals is key to achieve small footprint devices that would allow efficient manipulations of diverse optical states and thus the realisation of the quantum protocols of interest. Motivated by these observations, this work theoretically and experimentally investigates the design and performance of integrated nonlinear quantum optical devices. In particular, it concentrates on waveguides fabricated in lithium niobate and potassium titanyl phosphate substrates, two of the most common nonlinear crystals used for the realisation of integrated nonlinear waveguides.

This thesis is divided into two parts. The first part covers the theoretical background relevant in the context of this work and presents the fundamentals of integrated nonlinear optics in $\chi^{(2)}$ materials. The aim is to present a unified and accurate discussion of such theory, often scattered among many different sources. In chapter 1, the theory of dielectric optical waveguides is presented. Strong emphasis is placed on the derivation of the equations describing the behaviour of light into guiding structures. In particular, the various approximations, their interpretation and their limitations are discussed as they are introduced along the derivation. Chapter 2 reports the theory of second order nonlinear optics in integrated waveguides. Here, the system of coupled mode equations describing the classical evolution of the fields involved in the nonlinear process is derived taking into account the presence of a guiding structure in the nonlinear material. Moreover, the concepts of birefringent and quasi phase matching are introduced. A small section outlining the description of phase matched processes in the context of ultrafast quantum optics concludes the chapter. Chapter 3 is devoted to the description of the two substrates investigated in this thesis, namely lithium niobate and potassium titanyl phosphate. In particular, their crystallographic, linear and nonlinear optical properties are reported. Moreover, the fabrication of waveguides in these platforms,

their numerical modelling and the techniques to characterise them are discussed here.

The second part of the thesis reports the original material developed throughout the doctoral studies. In chapter 4, the in-house fabrication of two different KTP waveguide systems is reported and their application as quantum frequency converter and heralded photon pair source is presented. Chapter 5 contains a detailed analysis of the performance of nonlinear waveguides in presence of imperfections. Two approaches towards this analysis are presented and several case studies are analysed both theoretically and experimentally. The theory outlined in this chapter is verified with the reconstruction of the phase matching spectra of a few waveguides produced in our facility. At the same time, this reconstruction provided the very first characterisation of our fabrication processes, a key step for the improvement of the performance of our systems. At the end of this chapter, a general theory describing the degradation of performance in any nonlinear material is discussed. Chapter 6 reports a novel approach for the estimation of losses in a multimode nonlinear waveguide. In chapter 7, the properties of waveguides realised in a novel technological platform, lithium niobate on insulator, are investigated in detail for the first time. In particular, with the help of numerical modelling, a wide variety of waveguide structures are studied as potential candidates for the realisation of innovative quantum optical devices.

Finally, appendix A reports the coefficients of the modified dispersion relations used in chapter 7 for the analysis of LNOI waveguides.

List of abbreviations and nomenclature

Abbreviations

- DFG - difference frequency generation
- FC - frequency conversion
- FDTD - finite difference, time domain
- FDM - finite difference method
- FEM - finite element method
- FWM - four-wave mixing
- FWHM - full width at half maximum
- (a/s/f)GVM - (asymmetric/symmetric/full) group velocity matching
- HIC - high-index contrast
- JSA/JSI - joint spectral amplitude/intensity
- KTP - potassium titanyl phosphate
- LN, LiNbO_3 - Lithium niobate
- QPM - quasi phasematching
- PDC - parametric down conversion
- SFG -sum frequency generation
- SH - second harmonic
- SHG - second harmonic generation
- TE/TM mode - Transverse electric/magnetic mode
- TWM - three-wave mixing

Nomenclature

- $\underline{\underline{\epsilon}}$ - rank-2 tensor
- E - 1D field
- \mathbf{E} - 3D, time-dependent field: $\mathbf{E} = [E_x(\vec{r}, t), E_y(\vec{r}, t), E_z(\vec{r}, t)]^T$
- \mathbf{E} - 3D, frequency-dependent field: $\mathbf{E} = [E_x(\vec{r}, \omega), E_y(\vec{r}, \omega), E_z(\vec{r}, \omega)]^T$
- \mathcal{E} - 3D, frequency-dependent waveguide eigenmode
- $\tilde{\mathcal{E}}$ - 3D, frequency-dependent waveguide eigenmode, normalised to carry unit power: $\iint dx dy |\tilde{\mathcal{E}}|^2 = 1$
- \perp - components of a vector (or of a field) perpendicular to the optical axis of the system
- \parallel - components of a vector (or of a field) parallel to the optical axis of the system
- β - propagation constant of a waveguide mode
- $\Delta\beta$ - phase mismatch between the fields in a nonlinear process
- η - conversion efficiency, normalised to the pump power, usually in [% W^{-1}]
- η_{norm} - normalised conversion efficiency, normalised to the pump power and the squared sample length, usually in [% $W^{-1}cm^{-2}$]

Part I.

Background

Integrated waveguides

Contents

1.1	Ray optics description	3
1.2	Rigorous mathematical description	5
1.3	Asymmetric slab waveguide	8
1.4	Numerical methods	11

In this work, we study the design of waveguiding structures in nonlinear dielectric materials. For this reason, in this chapter we introduce the concept of dielectric waveguides and discuss their mathematical modelling. We describe in detail the analytical treatment of 1D guiding structures and discuss their properties, with particular emphasis on the different

classes of guided modes and on the connection between the waveguide geometry and the number of modes guided by the system. Since the modes of the 2D structures studied in this work cannot be calculated analytically, a section describing the most common numerical methods for the solution of the guided mode equations is presented.

1.1. Ray optics description

A waveguide is a structure that confines light in a small region of space and allows its propagation without suffering from diffraction. The simplest type of guiding structure is the one dimensional *symmetric slab dielectric waveguide*. It consists of an inner region (*core*) with a refractive index n_{core} and two outer regions (usually referred to as *cladding*, *substrate* or *jacket*) with refractive indices $n_{clad} < n_{core}$. The guiding properties of such systems can be naïvely understood in terms of total internal reflection of the optical rays of the light launched in the structure, as depicted in Figure 1.1.

Due to the higher refractive index of the core region, rays propagating with an angle $\theta_m < \theta_c$, where $\theta_c = \pi - \arcsin\left(\frac{n_{clad}}{n_{core}}\right)$, experience total reflection at the core-cladding boundary. Therefore, the light remains confined inside the core and can propagate along the structure. However, since light is “bouncing” between the two interfaces, a self-consistent condition imposing a constructive interference between each reflection is required. In particular, from the sketch shown in Figure 1.1, the difference in phase between points A and C must be equal to the difference in phase between A and B, up

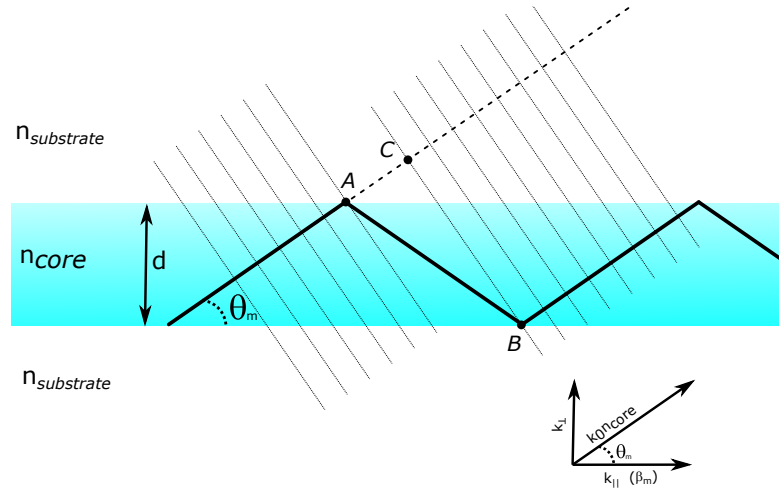


Figure 1.1. – Ray optical description of a 1D symmetric slab dielectric waveguide. The sketch illustrates the phase condition that leads to the eigenvalue equation. All rays that travel in the same direction belong to the same plane wave. Therefore, the optical path difference between \overline{AC} and \overline{AB} must differ by a multiple of 2π . In the corner, the decomposition of the \vec{k} vector into a longitudinal ($k_{\parallel} = \beta$) and transversal k_{\perp} component is shown.

to a multiple of 2π . Therefore, the self-consistent condition reads

$$\begin{aligned} k_0 n_{core} \overline{AB} + 2\phi_r &= k_0 n_{core} \overline{AC} + 2m\pi \Rightarrow^1 \\ 2k_0 n_{core} d \sin \theta + 2\phi_r &= 2m\pi, \end{aligned} \quad (1.1)$$

where ϕ_r is the phaseshift acquired by the light field upon reflection at the interface between the core and the cladding of the waveguide. It is evident that not all angles $\theta < \theta_c$ will satisfy this self-consistent condition and therefore only a discrete set of guided solutions θ_m , also called waveguide *modes*, can be found. As shown in Figure 1.1, a waveguide mode propagating at an angle θ_m is characterised by a longitudinal propagation vector $\beta_m = k_{\parallel} = k_0 n_{core} \cos \theta_m$, describing the propagation speed of the mode inside the waveguide, and a transversal wavevector $k_{m,\perp} = k_0 n_{core} \sin \theta_m$, defining the transversal distribution of the mode profile. In analogy with the definition of refractive index of a bulk material $n = k/k_0$, one can define an effective refractive index describing the propagation of a light mode into a waveguide as

$$n_{eff} = \frac{\beta_m}{k_0}$$

¹Since $\overline{AB} = d/\sin \theta$ and $\overline{AC} = \overline{AB} \cos 2\theta$.

1.2. Rigorous mathematical description

and, in the case of the symmetric 1D slab waveguide here analysed, $n_{eff} = n_{core} \cos(\theta_m)$.

The number of modes depends on the thickness of the slab: for narrow slabs, only one mode is guided at a very small angle θ_m ; as the thickness increases, more solutions of Eq. (1.1) corresponding to bigger angles θ_m become available. These solutions corresponds to the higher order modes of the structure, characterised by smaller β_m with respect to the fundamental mode.

This ray optics picture conveys the main peculiarities of guided optics but is very limited in its applications. In particular, it is not easy to extend to more complex geometries, like two dimensional waveguide structures. Therefore, it is important to introduce a more mathematically rigorous description of waveguides. As this subject has been extensively studied over the past 60 years, we will outline here the salient points of the mathematical treatment, while redirecting the reader to [1, 2] for a more complete and detailed analysis.

1.2. Rigorous mathematical description

Let's start considering an ideal waveguide aligned along the z axis. In such a system, Maxwell's equations for a monochromatic wave at frequency ω read

$$\nabla \times \mathbf{H}(\vec{r}, \omega) = i\omega \mathbf{D}(\vec{r}, \omega) \quad (1.2a)$$

$$\nabla \times \mathbf{E}(\vec{r}, \omega) = -i\omega \mathbf{B}(\vec{r}, \omega) \quad (1.2b)$$

$$\nabla \cdot \mathbf{H}(\vec{r}, \omega) = 0 \quad (1.2c)$$

$$\nabla \cdot \mathbf{D}(\vec{r}, \omega) = 0 \quad (1.2d)$$

and the constitutive relations read

$$\mathbf{D}(\vec{r}, \omega) = \varepsilon_0 \underline{\underline{\varepsilon_r}}(\vec{r}, \omega) \mathbf{E}(\vec{r}) = \underline{\underline{\varepsilon}}(\vec{r}) \mathbf{E}(\vec{r}, \omega) \quad (1.3a)$$

$$\mathbf{B}(\vec{r}, \omega) = \mu_0 \mathbf{H}(\vec{r}, \omega), \quad (1.3b)$$

where the fields \mathbf{E} , \mathbf{D} , \mathbf{H} , \mathbf{B} are 3×1 vectors whose components describe different *polarisation* components of the fields. For example, $\mathbf{E} = [E_x, E_y, E_z]^T$ and $E_{x/y/z}(\vec{r}, \omega)$ describes the electric field component oscillating parallel to the $x/y/z$ -axis. Therefore, a x -polarised electric field will have the form $\mathbf{E}(\vec{r}, \omega) = [E_x(\vec{r}, \omega), 0, 0]^T$.

For generality, we start our analysis considering an *anisotropic* dielectric medium, and thus its relative permittivity is described by $\underline{\underline{\varepsilon_r}}$, a 3×3 matrix. The matrix describing the refractive index distribution n is thus given by $\underline{\underline{n}}(x, y)^2 = \underline{\underline{\varepsilon_r}}(x, y)$. The refractive index distribution does not depend on the z coordinate since the existence of an ideal waveguide along z implies translational invariance of the system along this direction. In the following, we will usually drop the spatial and frequency dependence of the fields for a lighter notation.

With the help of the identity $\nabla \times \nabla \times \mathbf{A} = -\nabla^2 \mathbf{A} + \nabla(\nabla \cdot \mathbf{A})$, taking the curl of Eq. (1.2b) and using (1.3b) and (1.2a), we can write

$$\nabla^2 \mathbf{E} - \nabla(\nabla \cdot \mathbf{E}) + k_0^2 \underline{\underline{\varepsilon_r}} \mathbf{E} = 0. \quad (1.4)$$

Similarly, taking the curl of Eq. (1.2a) and using Eq. (1.2c) we can write

$$\nabla^2 \mathbf{H} + i\omega \nabla \times \varepsilon_0 \left(\underline{\underline{\varepsilon_r}} \mathbf{E} \right) = 0. \quad (1.5)$$

Note that, due to the spatial variation of $\underline{\underline{\varepsilon_r}}$, it is not possible to use Eq. (1.2d) to simplify the last expression.

Eqs. (1.4) and (1.5) are quite complicated to solve, since the anisotropy couples all the polarisations. The solution of these equations in an anisotropic system is usually performed using specific numerical software for the simulation of electromagnetic fields (see 1.4).

For a better understanding of waveguide properties, we can start simplifying the system by considering an isotropic material and considering ε_r as a scalar function. Under this assumption, from Eqs. (1.2d) and (1.3a) we can write²

$$\begin{aligned} \nabla \cdot \mathbf{E} &= -\mathbf{E} \cdot \nabla \varepsilon / \varepsilon \\ &= -\mathbf{E} \cdot \nabla \log \varepsilon \\ \nabla \times \varepsilon \mathbf{E} &= \varepsilon \nabla \times \mathbf{E} + (\nabla \varepsilon) \times \mathbf{E} \\ &= \varepsilon (\nabla \times \mathbf{E} + (\nabla \log \varepsilon) \times \mathbf{E}) \end{aligned}$$

and thus Eqs. (1.4) and (1.5) can be simplified to get

$$\begin{aligned} \nabla^2 \mathbf{E} + \nabla (\mathbf{E} \cdot \nabla \log \varepsilon) + k_0^2 \varepsilon_r(x, y) \mathbf{E} &= 0 \\ \nabla^2 \mathbf{H} + (\nabla \log \varepsilon) \times (\nabla \times \mathbf{H}) + k_0^2 \varepsilon_r(x, y) \mathbf{H} &= 0, \end{aligned} \quad (1.6)$$

where $k_0 = \omega/c$.

With straightforward but tedious vector analysis, one can show that in Eqs. (1.6) the transversal components (\mathbf{E}_\perp , \mathbf{H}_\perp) of the fields are decoupled from their longitudinal components (E_z and H_z). Moreover, since the system is translationally invariant along the z direction, the amplitude of the spatial distribution of the fields cannot depend on the position along z and thus we can look for solutions having the form

$$\begin{aligned} \mathbf{E}(x, y, z) &= \mathbf{E}(x, y) e^{-i\beta z} \\ \mathbf{H}(x, y, z) &= \mathbf{H}(x, y) e^{-i\beta z}. \end{aligned} \quad (1.7)$$

Thus, the system (1.6) can be simplified to

$$\nabla^2 \mathbf{E}_\perp + \nabla (\mathbf{E}_\perp \cdot \nabla \log \varepsilon) + (k_0^2 \varepsilon_r(x, y) - \beta^2) \mathbf{E}_\perp = 0 \quad (1.8a)$$

$$\nabla^2 \mathbf{H}_\perp + (\nabla \log \varepsilon) \times (\nabla \times \mathbf{H}_\perp) + (k_0^2 \varepsilon_r(x, y) - \beta^2) \mathbf{H}_\perp = 0 \quad (1.8b)$$

$$i\beta E_z = \nabla \cdot \mathbf{E}_\perp + \mathbf{E}_\perp \cdot \nabla \log \varepsilon \quad (1.8c)$$

$$i\beta H_z = \nabla \cdot \mathbf{H}_\perp \quad (1.8d)$$

²Using the equality $\nabla \varepsilon / \varepsilon = \nabla \log \varepsilon$.

1.2. Rigorous mathematical description

The first two equations are the eigenvalue equations whose solution provides a set of waveguide modes $\{\mathbf{E}_{\mu,\perp}\}, \{\mathbf{H}_{\mu,\perp}\}$, corresponding to different values of the *propagation constant* β_m while the last two equations can be used to retrieve the longitudinal components of the fields.

In general, the analytical solution of Eq. (1.8) is usually difficult or even impossible, since the term $\nabla(\mathbf{E}_\perp \cdot \nabla \log \varepsilon)$ couples the components of \mathbf{E} . However, this term can be neglected if the fractional change of ε_r over one optical wavelength is small. This is the case of *weakly guiding waveguides*, i.e. waveguides where the refractive index increase in the guiding region is relatively small³. Therefore, in weakly guiding waveguides, Eqs. (1.8a) and (1.8c) can be reduced to

$$\nabla^2 \mathbf{E}_\perp + (k_0^2 \varepsilon_r(x, y) - \beta^2) \mathbf{E}_\perp = 0 \quad (1.9a)$$

$$i\beta E_z = \nabla \cdot \mathbf{E}_\perp \quad (1.9b)$$

and an analogous set of equations for (\mathbf{H}_\perp, H_z) can also be found. Note that now there is no coupling between the field components along x and y , and the z component is coupled via Eq. (1.9b). This approximation is not valid in *strongly guiding waveguides*, also known as high index contrast (HIC) waveguides, i.e. waveguides where the refractive index increase in the guiding region is high, compared to the waveguide cladding⁴.

In weakly guiding waveguides, given that the transversal polarisations are decoupled in Eq. (1.9b), we can write an approximate scalar equation for each polarisation component E_x, E_y in the form

$$\nabla^2 E_s(x, y) + (k_0^2 n(x, y)^2 - \beta^2) E_s(x, y) = 0, \quad s = x, y \quad (1.10)$$

This last equation is often used as a good approximation to the exact vectorial equation (1.6) when considering two dimensional, weakly guiding systems. The solution of Eq. (1.10) provides a set of modes $m = 1, \dots, M$ with well defined electric field distribution $E_m(x, y)$ and propagation constants β_m . It is customary to associate each mode with an *effective index* $n_{eff} = \beta/k_0$. This effective index represents the refractive index “seen” by the mode as it travels along the waveguide and it differs from the refractive index of the material itself since it implicitly contains the non-diffracting nature of light propagation in a waveguide.

It is worth discussing the implications of the simplifications that led to Eq. (1.10). In the case of a slab waveguide, the planar configuration prevents the coupling of the polarisations due to the term $\nabla(\mathbf{E} \cdot \nabla \log \varepsilon)$, since the refractive index changes along only one direction. In this case, it is possible to simplify Eq. (1.6) to the scalar case without any approximation. This leads to the definition of two different sets of modes, the *transverse electric* (TE) modes and the *transverse magnetic* (TM) modes. The TE modes have $E_z = 0$ and thus, from Maxwell’s equations, the non-zero components are E_y, H_x

³Indeed, one can note that $\nabla \log \varepsilon \propto \nabla \log \varepsilon_r = \nabla \log n^2(x, y) = 2\nabla n(x, y)/n(x, y)$ and, for weakly guiding waveguides, $\nabla n(x, y)/n(x, y) < 10^{-2} \mu\text{m}^{-1}$.

⁴This is the case of nanophotonic waveguides, e.g. photonic crystal waveguides, silicon-on-insulator or lithium niobate on insulator waveguides.

and H_z . The TM modes have $H_z = 0$ and thus the non-zero components are E_x , H_y and E_z . In a 2D waveguide, as we already mentioned, the different polarisations are coupled via the refractive index distribution $n(x, y)$; however, in the case of weakly-guiding waveguides, it is possible to find approximate solutions using Eq. (1.10) for modes with $E_z \approx 0$ or $H_z \approx 0$, thus leading to two different sets of modes, the *quasi-TE* (QTE) and *quasi-TM* (QTM) modes. For this reason, the properties of weakly guided waveguides can be understood fairly well since they are similar to the properties of slab waveguides and, for this reason, in the next section we will briefly discuss the properties of 1D waveguides. On the other hand, when this approximation is not valid, like in the case of strongly confining waveguides, the properties of the waveguides can vary drastically and a detailed analysis of their properties via accurate numerical modelling is required.

1.3. Asymmetric slab waveguide

To discuss the main properties of 1D and weakly-guiding 2D waveguides, let's consider the case of the 1D asymmetric slab waveguide. Following the treatment in [2], we consider a system composed of a slab of dielectric material with refractive index n_c and thickness h sandwiched between two dielectric regions with refractive index n_s and n_a . We will consider $n_c > n_s > n_a$ and call the three regions *core*, *substrate* and *cladding*, respectively. Since there is no variation of refractive index along y , we can set to zero all the derivatives along y . In this case, the E_y components of the TE modes of the waveguide are described by Eq. (1.10)

$$\frac{\partial^2}{\partial x^2} E_y(x) + [k_0^2 n(x)^2 - \beta] E_y(x) = 0. \quad (1.11)$$

The other components can be calculated from E_y as $H_x = -\beta/(\omega\mu)E_y$ and $H_z = i/(\omega\mu_0)\partial_x E_y$.

On the other hand, one can show that the H_y components of the TM modes of the waveguides are solutions of

$$n(x)^2 \frac{\partial}{\partial x} \left(\frac{1}{n(x)^2} \frac{\partial}{\partial x} H_y \right) + [k_0^2 n(x)^2 - \beta^2] H_y(x) = 0, \quad (1.12)$$

while E_x and E_z can be calculated from $E_x = \beta/(\omega\epsilon_0 n^2)H_y$ and $E_z = -i/(\omega\epsilon_0 n^2)\partial_x H_y$.

Let's focus on the TE modes first. Due to the geometry of the system, we can solve Eq. (1.11) separately in the core, substrate and cladding and then impose the continuity of the fields to derive the final shape of $E_y(x)$. For this reason, let's consider

$$\frac{\partial^2}{\partial x^2} E_y(x) + [k_0^2 n_a^2 - \beta] E_y(x) = 0, \quad x > h \quad (1.13a)$$

$$\frac{\partial^2}{\partial x^2} E_y(x) + [k_0^2 n_c^2 - \beta] E_y(x) = 0, \quad 0 \leq x \leq h \quad (1.13b)$$

$$\frac{\partial^2}{\partial x^2} E_y(x) + [k_0^2 n_s^2 - \beta] E_y(x) = 0, \quad x < 0. \quad (1.13c)$$

1.3. Asymmetric slab waveguide

From Eq. (1.13) we can already draw some insights regarding the allowed values of β . In particular,

- if $\beta > k_0 n_c$, then $\partial_x^2 E_y$ has the same sign as E_y , resulting in an unphysical solution, since the field diverges for $x \rightarrow \pm\infty$;
- if $k_0 n_s < \beta < k_0 n_c$, then the solution is oscillating in the waveguide core and $E_y \rightarrow 0$ outside the core. Such a mode is called a *guided mode*;
- if $k_0 n_a < \beta < k_0 n_s$, then there is a continuum of allowed modes with oscillating behaviour in the substrate and rapidly decaying in the cladding; such a mode is called a *substrate radiation mode*;
- if $\beta < k_0 n_a$ then the mode is oscillating in all three regions and it is known as *substrate-cover radiation mode*.

In most applications, only the guided modes are of interest. However, radiation modes are involved in the generation of Cerenkov-radiation type phase matching [3] and must be taken into account to properly describe the properties of strongly confining waveguides [4], as briefly discussed in section 7.4.

Restricting our attention to the guided modes ($k_0 n_s < \beta < k_0 n_c$), it can be shown that solutions of Eq. (1.13) can be taken in the form

$$E_y(x) = E_a e^{-\gamma_a(x-h)}, \quad x > h \quad (1.14a)$$

$$E_y(x) = E_c \cos(\kappa_c x - \phi), \quad 0 \leq x \leq h \quad (1.14b)$$

$$E_y(x) = E_s e^{\gamma_s x}, \quad x < 0, \quad (1.14c)$$

where $\gamma_a^2 = \beta^2 - k_0^2 n_a^2$, $\gamma_s^2 = \beta^2 - k_0^2 n_s^2$ and $\kappa_c^2 = k_0^2 n_c^2 - \beta^2$. By imposing the continuity of E_y and $\partial_x E_y$ at the interfaces, the system (1.14) leads to the equations

$$\tan(\kappa_c h - \phi) = \frac{\gamma_a}{\kappa_c} \quad (1.15a)$$

$$\tan \phi = \frac{\gamma_s}{\kappa_c} \quad (1.15b)$$

that can be rewritten as

$$\kappa_c h - \phi - \psi = m\pi, \quad \text{with } \tan \psi = \frac{\gamma_a}{\kappa_c} \text{ and } \tan \phi = \frac{\gamma_s}{\kappa_c} \quad (1.16)$$

Note that this last equation is the same as Eq.(1.1), which has been derived from geometrical considerations. The solution of this equation generates a discrete, finite set of modes β_m . With a similar mathematical treatment, one can write a similar equation for TM modes:

$$\kappa_c h - \phi - \psi = m\pi, \quad \text{with } \tan \psi = \frac{n_c^2 \gamma_a}{n_a^2 \kappa_c} \text{ and } \tan \phi = \frac{n_c^2 \gamma_s}{n_s^2 \kappa_c} \quad (1.17)$$

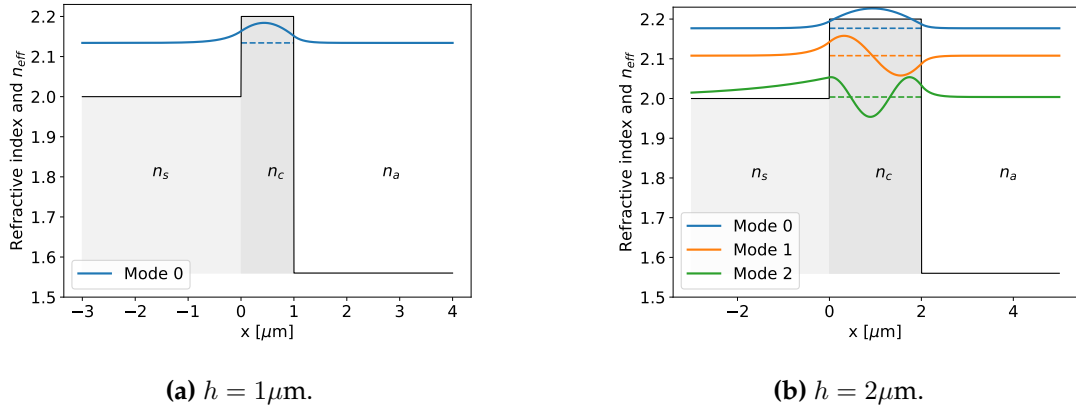


Figure 1.2. – TE modes in a slab waveguide with $n_a = 1.56$, $n_c = 2.2$, $n_s = 2.0$ and for two different thicknesses h . The effective index n_{eff} of each mode is indicated with a dashed line of the respective colour. Note that for $h = 1\mu\text{m}$ the waveguide supports only one mode, while for $h = 2\mu\text{m}$ the waveguide supports three modes. Moreover, higher order modes have a lower n_{eff} . Note also that the n_{eff} of the fundamental mode changes for different waveguide widths.

Two examples of the TE modes of a slab waveguide are shown in Figure 1.2 for two different slab thicknesses h . In Fig. 1.2a, the slab is thin enough to support only a single mode, while in Fig. 1.2b the slab is twice as wide and allows guiding of three modes.

Two main observations here are important: firstly, in the multimode regime, as the mode order increases, the n_{eff} decreases and the mode is less confined in the waveguide; secondly, the n_{eff} of the fundamental mode is dependent on the size of the waveguide and, in particular, it approaches n_c as the waveguide becomes thicker. This behaviour can be better appreciated in Figure 1.3, where the n_{eff} of the first five guided modes of the slab waveguide is plotted against the slab thickness h . These observations suggest that it is possible to modify the effective refractive index of the waveguide mode by varying the geometry of the waveguide: indeed this is the main tool used in section 7 to tailor the properties of the nonlinear waveguides.

The behaviour of the modes of 2D weakly guiding structures is very similar to the 1D case. On the other hand, strongly guiding waveguides are characterised by a much wilder modal behaviour since the polarisations are coupled together. In particular, the typical eigenmodes of single mode, strongly guiding waveguides are hybrid modes where E_x , E_y and E_z can exhibit comparable amplitudes and there is a non negligible field polarised parallel to the propagation direction. An example of such mode can be seen in Figure 7.17. Therefore, the calculation of the modal structure is more complicated and requires numerical methods that will be briefly described in the next section.

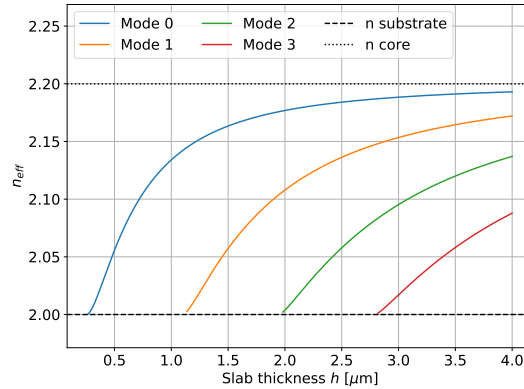


Figure 1.3. – Calculated effective refractive indices n_{eff} of the first four guided modes as a function of the slab thickness h . The refractive index of the waveguide substrate and the core are shown as a reference.

1.4. Numerical methods

A wide variety of numerical methods have been developed over the last 50 years to find solutions of Eq. (1.8). Here, we will briefly review the methods this work.

Marcatili’s method This method [5] is an approximate method that works best for weakly guiding rectangular waveguides. In this method, the guided mode is constituted by two standing waves, one along x and one along y . The field distribution $F(x)$ ($G(y)$) and the respective wavevector k_x (k_y) along x (y) is calculated considering the system as a 1D slab waveguide extending in the y (x) direction. The propagation constant is then given by $\beta^2 = k_0^2 - k_x^2 - k_y^2$ and the spatial distribution of the mode is $E(x, y) = F(x) \cdot G(y)$. As this method neglects the corner regions around the waveguide, it assumes that the field in these regions is negligible. This method is intrinsically unable to treat strongly guiding structures; a modification of the Marcatili’s method to high index contrast (HIC) waveguides has been proposed by Westerveld et al. in [6]. Marcatili’s method and its extension are unable to describe accurately the guiding properties of waveguides in anisotropic materials since, in this case, all the polarisations are coupled. Therefore, an exact calculation of the waveguide modes requires the solution of the full vectorial model.

Finite elements methods Finite element methods (FEMs) are numerical methods to find the solutions of partial differential equations (PDEs) [7]. After reformulating the PDE under consideration into its weak variational form, the domain of the problem is discretised into a mesh and the weak variational problem is solved via polynomial approximation inside each element of the mesh. Since the mesh has no specific geomet-

ric constraint, FEMs are usually apt to solve PDEs on complicated domain structures, as opposed to other methods like finite difference methods. However, the numerical implementation of FEMs is quite complex and simpler and faster methods are usually preferred for the solution of Maxwell's equations.

Finite difference methods Finite difference methods (FDMs) are numerical methods to solve ordinary and partial differential equations (ODEs/PDEs) by approximating the derivatives with finite differences, thus converting the differential equation into a system of algebraic equations [7]. The domain of the ODE/PDE is discretised over a rectangular mesh and the derivatives of the differential equation are approximated using finite differences between the points of the grid. Since this method is based on a rectangular grid, it works best for structures with a simple geometry. However, numerous variants have been developed to describe material interfaces that do not follow the grid mesh. In the context of electromagnetic waves, FDM schemes have been extended to allow the time-dependent solution of Maxwell's equation, leading to the so-called *finite difference time domain* (FDTD) methods. These methods exploit the symmetries of Maxwell's equations to construct the discretisation mesh and reduce the approximation error. For this reason, they are one of the preferred methods for the calculation of propagation of light waves in a wide variety of media, in particular in nanophotonic structures.

Summary

In this chapter, we introduced the concept of waveguides and derived the equations that describe light propagation inside such systems. We analytically solved the eigenmode equation for 1D slab waveguides to gain insights into the modal structure of 1D and weakly guiding 2D waveguides. We concluded providing a quick overview of some numerical methods for the solution of Maxwell's equations.

Nonlinear optics in waveguiding structures

Contents

2.1 Nonlinear material response	13
2.2 Nonlinear coupled-mode theory in waveguides	19
2.3 Understanding and tailoring three wave mixing	27
2.4 Elements of ultrafast quantum optics	34

Nonlinear optical processes are paramount in several areas of physics nowadays because they enable complex manipulation of light. In particular, they have been exploited extensively both in the classical and quantum regime for a wide variety of purposes, e.g. classical single- and multiple-channel frequency conversion [8, 9], optical parametric amplification [10], generation of squeezed states and entangled photons [11–13], frequency conversion for single-photon detection [14–16] and to interface single photons with quantum memories [17–19].

In addition to this, realizing nonlinear processes in integrated waveguides is fundamental in bringing quantum protocols and devices closer to every-day life [20]. As we will see, integrated nonlinear waveguides offer interesting advantages over bulk nonlinear crystals, since they achieve a stronger nonlinear interaction by increasing the field confinement over longer lengths and can be interfaced more easily with fibre networks [21].

In this chapter the mathematical description of the nonlinear processes is discussed and their properties are analysed, with particular focus on the correct formalism to model second order nonlinear processes in waveguides.

2.1. Nonlinear material response

The response of a material subjected to an external electric field can be described macroscopically by the onset of a non-zero dipole moment per unit volume, or *polarisation density*¹, $\mathbb{P}(t)$. To first order, considering an instantaneous response of the material, the induced polarisation density is proportional to the amplitude of the incident electric

¹In the following, we will use the terms *polarisation density* to indicate the dipole moment per unit volume and *polarisation* to indicate the polarisation of the light field.

field

$$\mathbf{P}(t) = \varepsilon_0 \chi^{(1)} \mathbf{E}(t),$$

where $\chi^{(1)}$ is the *linear susceptibility* of the material and can be a scalar (in the case of isotropic material) or a second-rank tensor (in the case of an anisotropic material). Due to the linearity relation, the medium does not allow interaction of electric fields at different frequencies, i.e. the polarisation density will vary in time at the same frequency as the incident electric field.

However, when strong electric fields are present, $\mathbf{P}(t)$ cannot be described any more with a simple linear dependence to the electric field and one needs to consider a higher order expansion for \mathbf{E} :

$$\begin{aligned} \mathbf{P}(t) &= \varepsilon_0 \left[\chi^{(1)} \mathbf{E}(t) + \chi^{(2)} \mathbf{E}(t)^2 + \chi^{(3)} \mathbf{E}(t)^3 + \dots \right] \\ &= \underbrace{\mathbf{P}^{(1)}(t)}_{\mathbf{P}_L(t)} + \underbrace{\mathbf{P}^{(2)}(t) + \mathbf{P}^{(3)}(t) + \dots}_{\mathbf{P}_{NL}(t)}, \end{aligned} \quad (2.1)$$

where $\mathbf{P}_{L/NL}$ indicate the components of the polarisation density that depend linearly/nonlinearly on the electric field.

The presence of higher order terms in the expansions allows the creation of electric fields at different frequencies. In fact, the nonlinear polarisation density acts as a driving current source in Maxwell's equation:

$$\begin{aligned} \nabla \times \mathbf{H}(t) &= \frac{\partial \mathbf{D}(t)}{\partial t} \\ &= \varepsilon_0 \varepsilon_r \frac{\partial \mathbf{E}(t)}{\partial t} + \frac{\partial \mathbf{P}_{NL}(t)}{\partial t} \\ &= \varepsilon_0 \varepsilon_r \frac{\partial \mathbf{E}(t)}{\partial t} + \mathbf{J}(t) \end{aligned}$$

For example, writing the electric field $\mathbf{E}(t)$ as a linear combination of fields at different frequencies $\sum_i \mathbf{E}_i e^{i\omega_i t} + \text{c.c.}$, the quadratic nonlinear response $\mathbf{P}^{(2)}(t)$ will be in the form

$$\begin{aligned} \mathbf{P}^{(2)}(t) \propto & \underbrace{\sum_m \mathbf{E}_m^2 e^{i2\omega_m t}}_{\text{second harmonic generation}} + \underbrace{\sum_{\substack{mn \\ m \neq n}} \mathbf{E}_m \mathbf{E}_n^* e^{i(\omega_m - \omega_n)t}}_{\text{difference frequency generation}} + \\ & \underbrace{\sum_{\substack{mn \\ m \neq n}} \mathbf{E}_m \mathbf{E}_n e^{i(\omega_m + \omega_n)t}}_{\text{sum frequency generation}} + \underbrace{\sum_m \mathbf{E}_m \mathbf{E}_m^*}_{\text{optical rectification}} + \text{c.c.} \end{aligned} \quad (2.2)$$

Therefore, the driving current $\mathbf{J}(t)$ will have components at twice the frequencies of the input field and at all possible sum/difference combinations of said frequencies,

provided the total energy of the system is conserved².

Thus, in materials with a non-zero $\chi^{(2)}$, up to three different frequencies can be coupled together by the second-order nonlinear polarisation density $\mathbb{P}^{(2)}$. For this reason, nonlinear processes in materials with non-zero $\chi^{(2)}$ are also called *three-wave mixing* (TWM) processes. With similar arguments, one can see that materials with $\chi^{(3)}$ nonlinearity allow the coupling of up to four different frequencies (a.k.a. four-wave mixing, FWM), and so on.

In this work, we investigate the properties of waveguides in $\chi^{(2)}$ nonlinear materials and thus in the following we will always refer to TWM processes, unless stated otherwise. Four possible frequency combinations are possible in a classical TWM process:

$\omega_3 = 2\omega_1$	Second Harmonic Generation (SHG)
$\omega_3 = \omega_1 + \omega_2$	Sum Frequency Generation (SFG)
$\omega_3 = \omega_2 - \omega_1$	Difference Frequency Generation (DFG)
$\omega_3 = 0$	Optical Rectification

It is customary to define different types of allowed processes according to the polarisations of the interacting fields. In the literature, there are very different naming schemes, whereby up to eight different TWM processes can be defined. In this thesis, we will adhere to the following nomenclature:

- *type 0* processes are processes where all the three fields have the same polarisation;
- *type I* processes are processes where the two input fields (in the case of SHG, SFG or DFG) or the two generated fields (in the case of PDC) have the same polarisation;
- *type II* processes are processes where the two input fields (in the case of SHG, SFG or DFG) or the two generated fields (in the case of PDC) have the different polarisations.

Considering a quantum treatment of light-matter interaction, a fifth process is possible, *spontaneous parametric downconversion* (SPDC or PDC). This process can be visualised as a special case of the DFG process, where the two input fields are a bright pump and the quantum mechanical vacuum state: the vacuum seeds the DFG process, destroying the pump photon and generating two photons at lower energies. Since all possible frequencies are present in the vacuum state, a continuum of DFG processes are possible, under energy and momentum conservation constraints, as shown in Figure 2.1. In fact, if ω_{pump} is the frequency of the pump field, the vacuum can seed all processes yielding photon pairs at

$$\omega_{pump} \rightarrow \left(\frac{\omega_{pump}}{2} + \delta\omega, \frac{\omega_{pump}}{2} - \delta\omega \right), \quad (2.3)$$

for all $\delta\omega$ that satisfy momentum conservation.

²Note that energy conservation describes only which processes are allowed to occur in a nonlinear process, but does not describe their efficiency. As we will see later on, an efficient nonlinear process requires a second condition, *momentum conservation*.

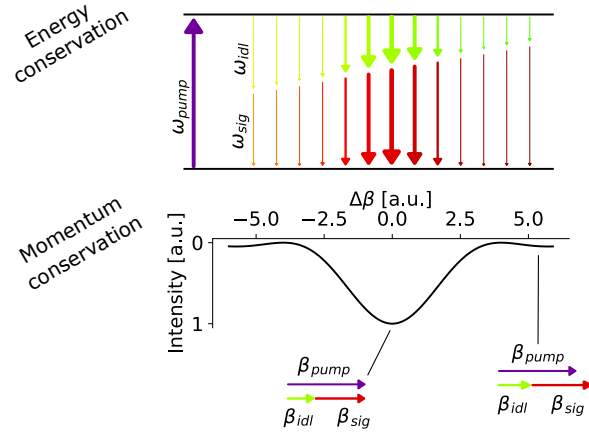


Figure 2.1. – Sketch representing the energy and momentum conservation (see section 2.3) in PDC processes in waveguides. The upper diagram represents the energy levels of the photons involved in the process: a pump photon at frequency ω_{pump} can be destroyed, creating a pair of photons at frequencies ω_{sig} and ω_{idl} , as long as energy is conserved, i.e. $\omega_{pump} = \omega_{sig} + \omega_{idl}$. However, in a dispersive material different frequencies propagate at different speeds and thus the momentum mismatch $\Delta\beta = \beta_{pump} - \beta_{sig} - \beta_{idl}$ defines the probability of the down-conversion process, represented by the width of the arrows of the photon pairs. Macroscopically, this corresponds to the intensity distribution of the process represented in the bottom diagram, as a function of $\Delta\beta$.

The peculiarity of the PDC process is that it can be properly described only within a full quantum optical theory and thus it can generate non-classical states of light. In fact, if properly tailored, it can generate entangled pairs of signal/idler photons, i.e. photons with correlation stronger than classically possible. The correlations, or lack thereof, embedded in the photon pairs generated via PDC can be exploited in a plethora of quantum experiments and technologies, such as testing of Bell's inequality [22], the generation of pure heralded single photons at telecom wavelengths for quantum communications [23] and the production of squeezed states for continuous variables protocols [24].

2.1.1. Second-order nonlinear polarisation density

Let us now derive in detail the description of TWM processes. In a material with nonzero $\chi^{(2)}$, the polarisation density induced by an incident field

$$\mathbf{E}(t) = \frac{1}{2} \sum_{m=1,2,3} (\mathbf{E}_m(\omega_m) e^{i\omega_m t} + c.c.) \quad (2.4)$$

is given by [25]³

$$P_i^{(2)}(\omega_m + \omega_n) = \frac{1}{2} \varepsilon_0 \sum_{jk} \sum_{(mn)} \chi_{ijk}^{(2)}(-\omega_m - \omega_n, \omega_m, \omega_n) E_j(\omega_m) E_k(\omega_n), \quad (2.5)$$

where i, j and k are indices running over the polarisation components of the electric fields and (m, n) denotes a summation over the possible permutations of the frequencies (ω_m, ω_n) such that $\omega_{sum} = \omega_m + \omega_n$ is constant.

As an example, in the case of SHG, $P_i^{(2)}(2\omega)$ can be calculated from Eq. (2.5) observing that $\omega_{m,n}$ can only assume the value ω . Therefore,

$$P_i^{(2)}(2\omega) = \frac{1}{2} \varepsilon_0 \sum_{jk} \chi_{ijk}^{(2)}(-2\omega, \omega, \omega) E_j(\omega) E_k(\omega). \quad (2.6)$$

On the other hand, to calculate the polarisation density component at ω , one needs to consider that $\omega_{m,n}$ can both have the values $\{2\omega, -\omega\}$. Therefore,

$$P_i^{(2)}(\omega) = \frac{1}{2} \varepsilon_0 \sum_{jk} \chi_{ijk}^{(2)}(-\omega, 2\omega, -\omega) [E_j(2\omega) E_k(-\omega) + E_j(-\omega) E_k(2\omega)] \quad (2.7a)$$

$$= \varepsilon_0 \sum_{jk} \chi_{ijk}^{(2)}(-\omega, 2\omega, -\omega) E_j(2\omega) E_k(-\omega) \quad (2.7b)$$

$$= \varepsilon_0 \sum_{jk} \chi_{ijk}^{(2)}(-\omega, 2\omega, -\omega) E_j(2\omega) E_k^*(\omega). \quad (2.7c)$$

In (2.7b), we have exploited the intrinsic symmetry condition

$$\chi_{ijk}^{(2)}(\omega_s, \omega_m, \omega_n) = \chi_{ikj}^{(2)}(\omega_s, \omega_n, \omega_m),$$

whereby j and k are dummy indices and thus interchangeable; in (2.7c), we applied the condition $E(-\omega) = E(\omega)^*$, valid since $E(t)$ is a real-valued function. Note the difference of a factor 2 between Eq. (2.6) and Eq. (2.7c) that arises from the different multiplicity of the frequency involved in the summation (mn) .

In its most general definition, the second order susceptibility $\chi^{(2)}$ is a rank-3, frequency dependent tensor that couples all polarisation of the three fields involved in

³Note that, with respect to reference [25], Eq. (2.5) contains an extra $1/2$ factor. This is due to a different convention for the expression of the electric field (2.4). With our convention, $E(t) = 1/2 (Ae^{i\omega t} + c.c.) = \cos(\omega t)$ while, adopting the convention in [25], $E(t) = (Ae^{i\omega t} + c.c.) = 2 \cos(\omega t)$.

the nonlinear process. However, when the processes under investigation lie far away from the resonant frequencies of $\chi^{(2)}$, as it is the case for all processes analysed in this thesis, the $\chi^{(2)}$ tensor can be greatly simplified, first by neglecting the frequency dependence and then using *Kleinman's symmetry conditions* [25], i.e.

$$\chi_{ijk}^{(2)} = \chi_{jki}^{(2)} = \chi_{kij}^{(2)} = \chi_{ikj}^{(2)} = \chi_{jik}^{(2)} = \chi_{kji}^{(2)}$$

Under Kleinman's symmetry condition, we can thus reduce the notation in Eq. (2.5) introducing the *nonlinear coefficient*

$$d_{il} = \frac{\chi_{ijk}^{(2)}}{2}, \quad (2.8)$$

where l is related to the combined indices j, k by the following relations

$$\begin{array}{l} jk: \quad 11 \quad 22 \quad 33 \quad 23,32 \quad 31,13 \quad 12,21 \\ l: \quad \quad 1 \quad 2 \quad 3 \quad 4 \quad 5 \quad 6 \end{array} .$$

Finally, denoting by X, Y, Z the crystallographic directions, the second-order nonlinear polarisation density can be related to the incident field polarisations via

$$\begin{bmatrix} P_X(\omega_3) \\ P_Y(\omega_3) \\ P_Z(\omega_3) \end{bmatrix} = M\varepsilon_0 \begin{bmatrix} d_{11} & d_{12} & d_{13} & d_{14} & d_{15} & d_{16} \\ d_{21} & d_{22} & d_{23} & d_{24} & d_{25} & d_{26} \\ d_{31} & d_{32} & d_{33} & d_{34} & d_{35} & d_{36} \end{bmatrix} \begin{bmatrix} E_X(\omega_1)E_X(\omega_2) \\ E_Y(\omega_1)E_Y(\omega_2) \\ E_Z(\omega_1)E_Z(\omega_2) \\ E_Y(\omega_1)E_Z(\omega_2) + E_Z(\omega_1)E_Y(\omega_2) \\ E_X(\omega_1)E_Z(\omega_2) + E_Z(\omega_1)E_X(\omega_2) \\ E_X(\omega_1)E_Y(\omega_2) + E_Y(\omega_1)E_X(\omega_2) \end{bmatrix}, \quad (2.9)$$

where M is the *multiplicity factor* and can assume the value 1 or 2, depending on the permutation symmetry of the frequencies involved in the process, as discussed previously for Eq. (2.6) and (2.7). In practice, $M = 1$ for a type 0/I SHG and $M = 2$ in all the other cases.

The different types of nonlinear processes can be easily related to specific components of the \mathbf{d} tensor:

$$\begin{bmatrix} d_{11} & d_{12} & d_{13} & d_{14} & d_{15} & d_{16} \\ d_{21} & d_{22} & d_{23} & d_{24} & d_{25} & d_{26} \\ d_{31} & d_{32} & d_{33} & d_{34} & d_{35} & d_{36} \end{bmatrix},$$

$\underbrace{\hspace{10em}}_{\text{type 0/I}}$
 $\underbrace{\hspace{10em}}_{\text{type II}}$

where the coefficients d_{11}, d_{22} and d_{33} are responsible for type 0 processes.

For a given nonlinear crystal, not all processes are possible. In fact, each crystallographic class is characterised by a specific structure of the nonlinear tensor, thus drastically reducing the number of parameters d_{ij} . The structure of the nonlinear tensor for the two crystals analysed in this thesis (LiNbO₃ and KTP), along with the allowed processes, will be described in detail in sections 3.1 and 3.2.

After having introduced the formalism to properly describe second order nonlinear polarisation density, we can proceed with deriving the equations that provide the evolution of the electric fields inside a second order nonlinear waveguide.

2.2. Nonlinear coupled-mode theory in waveguides

The derivation of the coupled-mode equations is a fairly complex but well-understood topic. Therefore, in the following we will introduce the equation describing the evolution of a continuous wave (CW) waveguide mode in the presence of a nonlinear polarisation density and discuss the system of coupled equation describing TWM processes in waveguides. For the full derivation of such equation, we refer the reader to [1, 3].

Let us consider a waveguide with propagation axis along z ⁴. A *monochromatic* guided mode $\{\mathbf{E}_m, \mathbf{H}_m\}$ can be written as a superposition of the waveguide eigenmodes $\{\tilde{\mathcal{E}}_m, \tilde{\mathcal{H}}_m\}$, i.e.

$$\begin{aligned}\mathbf{E}(x, y, z) &= \sum_m \gamma_m A_m(z) \tilde{\mathcal{E}}_m(x, y) e^{-i\beta_m z} \\ \mathbf{H}(x, y, z) &= \sum_m \gamma_m n_m c \varepsilon_0 A_m(z) \tilde{\mathcal{H}}_m(x, y) e^{-i\beta_m z}.\end{aligned}\quad (2.10)$$

This modal expansion is very convenient for the description of the interaction between different light fields, since the power⁵ I carried by eigenmode m at position z is given by

$$I(z) = |A_m(z)|^2$$

In Eq. (2.10), the constant γ_m is defined as

$$\gamma_m = \sqrt{\frac{2}{n_m c \varepsilon_0}},$$

where $n_m = \beta_m/k_0$ the effective index of the m^{th} mode, and the modes are normalised such that

$$\iint dx dy \left| \tilde{\mathcal{E}}_{\perp}(x, y) \right|^2 = 1 \quad (2.11)$$

As discussed in [3], the equation for the evolution of the field amplitude $A_m(z)$ in the presence of a nonlinear polarisation density \mathbf{P}_{NL} is

$$\frac{dA_m}{dz} = -i\gamma_m \frac{\omega}{4} e^{i\beta_m z} \iint dx dy \tilde{\mathcal{E}}_m^* \cdot \mathbf{P}_{NL,m}. \quad (2.12)$$

Therefore, the evolution of the envelope of the m th eigenmode (at frequency ω_m) depends on the nonlinear polarisation density generated at the same frequency by the other fields present in the waveguide. The complete description of a TWM process requires solving Eq. (2.12) for all the three fields, as they are coupled by the polarisation density terms in the integral, as we will show in the following.

⁴Note that, despite an identical labelling, the (x, y, z) reference system for the electromagnetic field is, in general, independent from the crystallographic axes X, Y, Z .

⁵For monochromatic waves, the intensity $\mathcal{I}(x, y)$ is given by $\mathcal{I} = 1/2 \cdot n c \varepsilon_0 |E|^2$.

2.2.1. Three wave mixing in waveguides

Let us now derive the equations describing the evolution of the amplitudes A_m during a TWM process. Consider a general input field in the form

$$\mathbf{E}(t) = \frac{1}{2} \sum_{i=1,2,3} E_i e^{-i\omega_i t} + c.c \quad (2.13)$$

where $\omega_3 = \omega_1 + \omega_2$ (including the case $\omega_1 = \omega_2$) and

$$E_i(x, y, z) = \gamma_i A_i(z) \tilde{\mathcal{E}}_i(x, y) e^{-i\beta_i z}. \quad (2.14)$$

Since the nonlinear tensor d couples well-defined field polarisations, we will consider here the case where all three fields are linearly polarised. With this convention, equation (2.12) for the three modes at ω_1 , ω_2 and ω_3 becomes

$$\begin{cases} \frac{dA_1}{dz} = -i\gamma_1 \frac{\omega_1}{4} e^{i\beta_1 z} \iint dx dy \tilde{\mathcal{E}}_1^* \cdot P_1 \\ \frac{dA_2}{dz} = -i\gamma_2 \frac{\omega_2}{4} e^{i\beta_2 z} \iint dx dy \tilde{\mathcal{E}}_2^* \cdot P_2 \\ \frac{dA_3}{dz} = -i\gamma_3 \frac{\omega_3}{4} e^{i\beta_3 z} \iint dx dy \tilde{\mathcal{E}}_3^* \cdot P_3 \end{cases} \quad (2.15)$$

With the formalism introduced in the previous section, the polarisation density components for a SFG/DFG process ($\omega_1 \neq \omega_2$) or a type II SHG process ($\omega_1 = \omega_2$) are given by

$$P_1(\omega_1) = 2\varepsilon_0 d(x, y, z) E_2(\omega_2)^* E_3(\omega_3) \quad (2.16a)$$

$$P_2(\omega_2) = 2\varepsilon_0 d(x, y, z) E_1(\omega_1)^* E_3(\omega_3) \quad (2.16b)$$

$$P_3(\omega_3) = 2\varepsilon_0 d(x, y, z) E_1(\omega_1) E_2(\omega_2). \quad (2.16c)$$

For a type 0/I SHG process ($\omega_1 = \omega_2 = \omega$), the polarisation density components are given by

$$P_\omega = 2\varepsilon_0 d(x, y, z) E(\omega)^* E(2\omega) \quad (2.17a)$$

$$P_{2\omega} = \varepsilon_0 d(x, y, z) E(\omega)^2. \quad (2.17b)$$

The difference between these two classes of processes resides in the number of distinct modes of light involved in the TWM process: for SFG, DFG and type II SHG, there are three distinct eigenmodes that differ by frequency ω_i or by polarisation; on the other hand, for type 0 and type I SHG there are only two distinct eigenmodes, as the fields at ω have the same polarisation and thus they belong to the same waveguide mode. This effect is responsible for the lack of the factor 2 in the Eq. (2.17b). Note that in Eqs.(2.16) and (2.17) we consider explicitly the spatial distribution of the nonlinear tensor to take into account variations of the nonlinearity along z and in the transversal plane (x, y) .

2.2. Nonlinear coupled-mode theory in waveguides

Let us now consider the case of SFG, DFG, type II SHG. Substituting the expression for the polarisation densities (2.16) into the system (2.15) we get

$$\begin{cases} \frac{dA_1}{dz} = -i\gamma_1 \frac{\varepsilon_0 \omega_1}{2} \iint dx dy d(x, y, z) \tilde{\mathcal{E}}_1^* E_2^* E_3 e^{i\beta_1 z} \\ \frac{dA_2}{dz} = -i\gamma_2 \frac{\varepsilon_0 \omega_2}{2} \iint dx dy d(x, y, z) \tilde{\mathcal{E}}_2^* E_1^* E_3 e^{i\beta_2 z} \\ \frac{dA_3}{dz} = -i\gamma_3 \frac{\varepsilon_0 \omega_3}{2} \iint dx dy d(x, y, z) \tilde{\mathcal{E}}_3^* E_1 E_2 e^{i\beta_3 z} \end{cases} \quad (2.18)$$

Using the field expansions (2.14) we find

$$\begin{cases} \frac{dA_1}{dz} = -i\gamma_1 \gamma_2 \gamma_3 d_0 \frac{\varepsilon_0 \omega_1}{2} A_2^*(z) A_3(z) g(z) e^{-i\Delta\beta z} \iint dx dy \hat{d}(x, y) \tilde{\mathcal{E}}_1^* \tilde{\mathcal{E}}_2^* \tilde{\mathcal{E}}_3 \\ \frac{dA_2}{dz} = -i\gamma_1 \gamma_2 \gamma_3 d_0 \frac{\varepsilon_0 \omega_2}{2} A_1^*(z) A_3(z) g(z) e^{-i\Delta\beta z} \iint dx dy \hat{d}(x, y) \tilde{\mathcal{E}}_2^* \tilde{\mathcal{E}}_1^* \tilde{\mathcal{E}}_3 \\ \frac{dA_3}{dz} = -i\gamma_1 \gamma_2 \gamma_3 d_0 \frac{\varepsilon_0 \omega_3}{2} A_1(z) A_2(z) g(z) e^{i\Delta\beta z} \iint dx dy \hat{d}(x, y) \tilde{\mathcal{E}}_3^* \tilde{\mathcal{E}}_1 \tilde{\mathcal{E}}_2 \end{cases}, \quad (2.19)$$

where we defined the *phase mismatch* (or wavevector mismatch)

$$\begin{aligned} \Delta\beta &= \beta_3 - \beta_2 - \beta_1 \\ &= 2\pi \left(\frac{n_3(\lambda_3)}{\lambda_3} - \frac{n_2(\lambda_2)}{\lambda_2} - \frac{n_1(\lambda_1)}{\lambda_1} \right). \end{aligned} \quad (2.20)$$

Moreover, we subdivided the nonlinear tensor $d(x, y, z)$ as

$$d(x, y, z) = d_0 \hat{d}(x, y) g(z). \quad (2.21)$$

where $d_0 = \max |d|$ is the magnitude of the nonlinear coefficient, $|\hat{d}(x, y)| \leq 1$ is its normalised transversal distribution and $|g(z)| \leq 1$ is its profile along the propagation axis of the waveguide⁶.

The system of equations (2.19) can be written more compactly as

$$\begin{cases} \frac{dA_1}{dz} = -i\kappa_1 \theta^* A_2^* A_3 g(z) e^{-i\Delta\beta z} \\ \frac{dA_2}{dz} = -i\kappa_2 \theta^* A_1^* A_3 g(z) e^{-i\Delta\beta z} \\ \frac{dA_3}{dz} = -i\kappa_3 \theta A_1 A_2 g(z) e^{i\Delta\beta z} \end{cases} \quad (2.22)$$

where we defined the *coupling coefficient* κ_j and the *field overlap* of the process as θ as

$$\begin{aligned} \kappa_j &= \sqrt{\frac{8\pi^2 d_0^2}{n_1 n_2 n_3 c \varepsilon_0 \lambda_j^2}}, \quad j = 1, 2, 3 \\ \theta &= \iint dx dy \hat{d}(x, y) \tilde{\mathcal{E}}_1(x, y) \tilde{\mathcal{E}}_2(x, y) \tilde{\mathcal{E}}_3^*(x, y). \end{aligned}$$

The system (2.22) completely describes the evolution of the *envelope* of three monochromatic fields oscillating at frequencies ω_1 , ω_2 and $\omega_3 = \omega_1 + \omega_2$ in the presence of a nonlinear polarisation density that couples them.

⁶In an ideal crystal, $g(z) \equiv 1$. However, in the case of crystal imperfections or due to fabrication processes (e.g. periodic poling, see section 3.4), the value of d can depend on the position along the propagation axis.

The evolution of the fields in a type 0/I SHG process is calculated similarly by substituting (2.17) into (2.15), leading to

$$\begin{cases} \frac{dA_\omega}{dz} &= -i\kappa_\omega\theta^* A_{2\omega}(z)A_\omega^*(z)g(z)e^{-i\Delta\beta z} \\ \frac{dA_{2\omega}}{dz} &= -\frac{i}{2}\kappa_{2\omega}\theta A_\omega^2(z)g(z)e^{i\Delta\beta z} \end{cases} \quad (2.23)$$

where

$$\kappa_j = \sqrt{\frac{8\pi^2 d_0^2}{n_\omega^2 n_{2\omega} c \epsilon_0 \lambda_j^2}}, \quad j = \omega, 2\omega$$

$$\begin{aligned} \Delta\beta &= \beta_{2\omega} - 2\beta_\omega \\ \theta &= \iint dx dy d(x, y) \tilde{\mathcal{E}}_\omega^2(x, y) \tilde{\mathcal{E}}_{2\omega}^*(x, y) \end{aligned}$$

These expressions have been derived assuming continuous wave (CW) fields. In the case of pulsed fields, and in particular when considering ultrafast laser pulses, a treatment that takes into consideration the different propagation speeds of the pulse envelopes is necessary [10].

In general, the analytical solution of (2.22) and (2.23) is quite involved [25]. However, simple expressions for the evolution of the fields can be found under reasonable assumptions, as shown in the following.

2.2.2. Evolution of SFG at perfect phase matching with no pump depletion

Let us consider here the TWM interaction in a uniform crystal with constant nonlinear profile $g(z) = 1$, involving a pump field at ω_2 and a weak field at ω_1 under perfect phase matching conditions $\Delta\beta=0$. In this case, the system (2.22) can be solved under the *no pump depletion approximation* (NPDA), i.e. considering the pump field ω_2 much stronger than the others for the entire process.

Under these assumptions, with $A_2(z) = A_{pump} = \sqrt{I_{pump}}$, the system (2.22) reads

$$\begin{cases} \frac{dA_1}{dz} &= -i\kappa_1\theta^* A_{pump}^* A_3 \\ \frac{dA_3}{dz} &= -i\kappa_3\theta A_1 A_{pump}. \end{cases} \quad (2.24)$$

Calculating the derivative of the first equation leads to

$$\begin{aligned} \frac{d^2 A_1}{dz^2} &= -i\kappa_3\theta^* A_{pump}^* \frac{dA_3}{dz} \\ &= \kappa_1\kappa_3|\theta|^2 |A_{pump}|^2 A_1 \\ &= \eta_{norm} I_{pump} A_1, \end{aligned}$$

where we defined the *normalised conversion efficiency*⁷

$$\eta_{norm}^{SFG} = \kappa_1\kappa_3|\theta|^2 = \frac{8\pi^2 d_0^2 |\theta|^2}{n_1 n_2 n_3 c \epsilon_0 \lambda_1 \lambda_3}.$$

⁷As the dimensions of $|\theta|^2$ are m^{-2} , it is customary to define the *interaction area* of the process as $A_{inter} = |\theta|^{-2}$.

2.2. Nonlinear coupled-mode theory in waveguides

The solution of (2.24) with the initial conditions $A_1(0) = \sqrt{I_1(0)}$ and $A_3(0) = 0$ is then

$$\begin{cases} A_1(z) &= A_1(0) \cos\left(\sqrt{\eta_{norm}^{SFG} I_{pump}} z\right) \\ A_3(z) &= -i A_1(0) \sqrt{\frac{\lambda_1}{\lambda_3}} e^{-i(\varphi_\theta + \varphi_{A_{pump}})} \sin\left(\sqrt{\eta_{norm}^{SFG} I_{pump}} z\right), \end{cases} \quad (2.25)$$

where $e^{-i\varphi_\theta} = |\theta|/\theta^*$ and $e^{-i\varphi_{A_{pump}}} = |A_{pump}|/A_{pump}^*$.

The power variation in fields 1 and 3 is thus given by

$$\begin{cases} I_1(z) &= I_{1,0} \cos^2\left(\sqrt{\eta_{norm}^{SFG} I_{pump}} z\right) \\ I_3(z) &= I_{1,0} \frac{\lambda_1}{\lambda_3} \sin^2\left(\sqrt{\eta_{norm}^{SFG} I_{pump}} z\right). \end{cases} \quad (2.26)$$

The factor in the second equation λ_1/λ_3 is fundamental to ensure that the solution (2.26) satisfies energy conservation, as stated by the the Manley-Rowe relations [26]

$$\frac{d}{dz} \left(\frac{I_1}{\omega_1} + \frac{I_3}{\omega_3} \right) = 0 \Leftrightarrow \mathcal{N}_1 + \mathcal{N}_3 = \text{constant}, \quad (2.27)$$

where $\mathcal{N}_{1/3}$ the number of photons in field 1/3.

As an example, the converted power as a function of the position inside the crystal and the pump power I_{pump} is shown in Figure 2.2, for $\eta_{norm} = 0.4 \text{ W}^{-1}\text{cm}^{-2}$. Note that the power oscillates sinusoidally as the pump converts light from field 1 to 3 and then backwards. Moreover, the position z for optimal power transfer from mode 1 to mode 3 depends on the pump intensity: the stronger the pump, the quicker the power is transferred between the two fields.

2.2.3. Phase matching spectrum of SHG processes under NPDA

In the previous section the spatial evolution of the generated field in an SFG process has been calculated under perfect phase matching conditions. It is possible lift this last assumption to calculate the frequency-dependent spectrum of this SFG process. However, the calculations are very laborious [25] and do not provide many physical insight. A clearer understanding can be gained from the derivation of the phase matching spectral distribution for an SHG process.

Under the NPDA, the spectral distribution of the generated SH field at the end of a crystal with length L can be derived integrating the second equation from the system (2.23):

$$\frac{dA_{2\omega}}{dz} = -\frac{i}{2} \kappa_{2\omega} \theta A_\omega^2 g(z) e^{i\Delta\beta z}. \quad (2.28)$$

Then, considering an input field at ω with total power $P_\omega = |A_\omega|^2$ and no input at

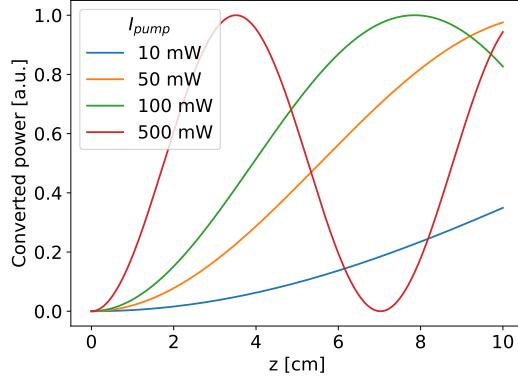


Figure 2.2. – Normalised intensity of the field at ω_3 in a SFG process, as a function of the pump power I_{pump} and the position z along the sample, under the no pump depletion approximation. We have assumed an $\eta_{norm} \approx 40\%/Wcm^2$.

2ω , a direct integration of Eq. (2.28) from $z = 0$ to $z = L$ leads to

$$A_{2\omega}(L) = -\frac{i}{2}\kappa_{2\omega}\theta A_{\omega}^2 \int_0^L g(z)e^{i\Delta\beta z} dz \quad (2.29a)$$

$$= -\frac{\kappa_{2\omega}}{2}\theta A_{\omega}^2 L \operatorname{sinc}\left(\frac{\Delta\beta L}{2}\right) e^{i\frac{\Delta\beta L}{2}}, \quad (2.29b)$$

where we have assumed $g(z) = 1$ since the modes are propagating in an homogeneous crystal.

The total power is given by

$$I_{2\omega}(L) = \eta_{norm}^{SHG} I_{\omega}^2 L^2 \operatorname{sinc}\left(\frac{\Delta\beta L}{2}\right)^2. \quad (2.30)$$

Eq. (2.30) shows that the spectrum of an SHG process, under the NPD approximation and in presence of a constant nonlinearity profile g , has the shape of a sinc^2 profile in $\Delta\beta$ and its intensity scales linearly with the normalised conversion efficiency η_{norm} and quadratically with the sample length L . Similar behaviour can be derived also for the phase matching spectrum of SFG processes as shown in [25].

2.2.4. Final remarks on the conversion efficiency and phase matching shape of TWM processes.

The coefficients

$$\eta_{norm}^{SHG,type0/I} = \frac{\kappa_{2\omega}^2}{4} |\theta|^2 = \frac{2\pi^2 d_0^2}{n_{\omega}^2 n_{2\omega} c \varepsilon_0 \lambda_{2\omega}^2} |\theta|^2 \quad (2.31)$$

$$\eta_{norm}^{SFG} = \kappa_1 \kappa_3 |\theta|^2 = \frac{8\pi^2 d_0^2}{n_1 n_2 n_3 c \varepsilon_0 \lambda_1 \lambda_3} |\theta|^2 \quad (2.32)$$

represent the conversion efficiency per unit length and unit pump power of the TWM process and is usually expressed in $\% \text{ W}^{-1} \text{ cm}^{-2}$.

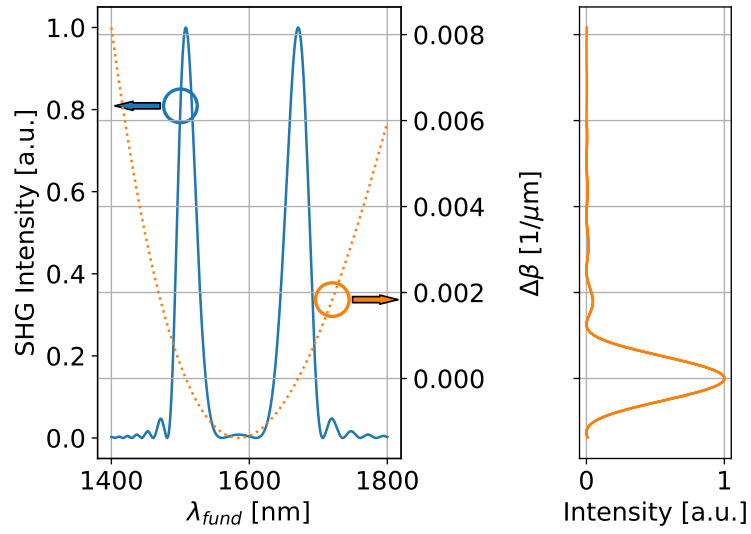
The specific value of η_{norm} depends on several factors, namely the wavelengths of the fields involved, their effective indices, the magnitude of the nonlinear coefficient d and the field overlap $|\theta|^2$. It is evident then that, for a given process, there are only two main ways to improve its efficiency: choosing a material with a high d_0 and increasing the overlap of the fields $|\theta|^2$. While the former method is limited by the different types of materials available, the latter can be optimised since the waveguides can be engineered to maximise the overlap integral $|\theta|^2$.

To conclude this section, two important remarks are necessary concerning the shape of the converted spectrum. Firstly, the spectrum of the light generated in a TWM process has the well-known sinc^2 only as a function of $\Delta\beta$. In fact, writing the phase mismatch as a function of either the frequencies ω or the wavelengths λ of the interacting fields

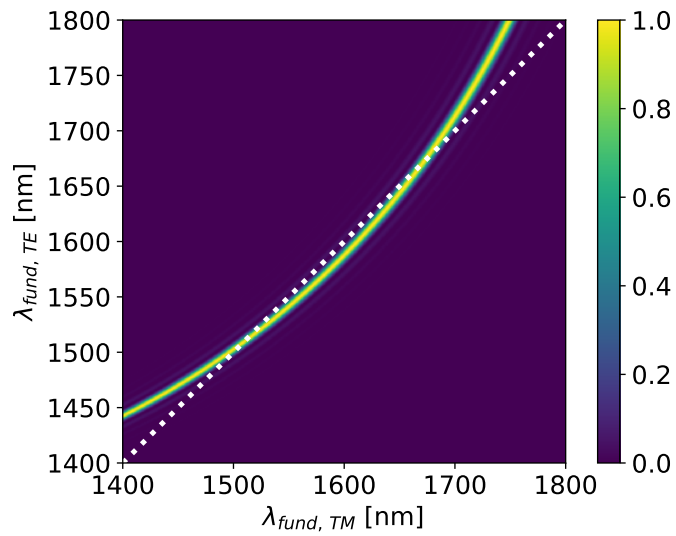
$$\begin{aligned} \Delta\beta &= 2\pi \left(\frac{n_3(\lambda_3)}{\lambda_3} - \frac{n_2(\lambda_2)}{\lambda_2} - \frac{n_1(\lambda_1)}{\lambda_1} \right) \\ &\propto n_3(\omega_3)\omega_3 - n_2(\omega_2)\omega_2 - n_1(\omega_1)\omega_1 \end{aligned}$$

reveals the nonlinear dependence of the phase mismatch on the frequencies (or wavelengths) of the fields. For this reason, the shape of the phasematching spectrum as a function of the wavelength λ (or the frequency ω) can be very different from a sinc^2 .

As an example, the phase matching spectrum for a type II process in a KTP waveguide is shown in Figure 2.3. In Figure 2.3a, the phase matching spectrum of the process as a function of the fundamental wavelength λ_{fund} is shown in a solid blue line in the left plot. The quadratic relation between the phase mismatch $\Delta\beta$ and λ_{fund} is shown by the orange dashed line in the same plot. The presence of two distinct zeros of the $\Delta\beta(\lambda_{fund})$ function generates a double-peaked phase matching spectrum in λ_{fund} , whereas the spectrum as a function of $\Delta\beta$ shows the usual sinc^2 profile, as displayed by the orange solid line in the right plot. Figure 2.3b visualises the reason of such nonlinear dependence: the curvature of the phase matching spectrum in the $\lambda_{fund,TE}$ vs. $\lambda_{fund,TM}$ space is such that an SHG measurement - represented by the white dashed line - intersects the 2D-spectrum twice, thus creating the double-peaked structure shown in Figure 2.3a.



(a) Spectrum of a type II SHG process in a KTP waveguide as a function of the pump wavelength λ_{fund} and the relative $\Delta\beta$.



(b) Phase matching spectrum of a type II SFG process in a KTP waveguide as a function of the wavelengths of the fundamental TE and TM fields. The white dashed line corresponds to the SHG spectrum shown in (a).

Figure 2.3. – Example of the nonlinear dependence between the $\Delta\beta$ and the wavelength of a TWM process in a KTP waveguide.

2.3. Understanding and tailoring three wave mixing

Secondly, the sinc^2 shape comes from the solution of the integral

$$A(\Delta\beta) \propto \int_0^L g(z) e^{i\Delta\beta z} dz \quad (2.33)$$

assuming $g(z) = 1$.

However, for a general $g(z)$, rewriting the former integral as

$$\int_{-\infty}^{+\infty} g(z) \Pi_{[0,L](z)} e^{i\Delta\beta z} dz, \quad \text{with } \Pi_{[0,L](z)} = \begin{cases} 1, & \text{if } z \in [0, L] \\ 0 & \text{elsewhere} \end{cases} \quad (2.34)$$

highlights that the shape of the phase matching spectrum of an ideal waveguide is the Fourier transform \mathcal{F} of the nonlinearity profile $g(z)\Pi_{[0,L](z)}$:

$$\begin{aligned} A(\Delta\beta) &= \int_{-\infty}^{+\infty} g(z) \Pi_{[0,L](z)} e^{i\Delta\beta z} dz \\ &= \mathcal{F} [g(z) \Pi_{[0,L](z)}] (\Delta\beta). \end{aligned}$$

In other words, the sinc^2 spectrum arises because of the box-like shape of the nonlinearity profile, corresponding to the physical sample length: as soon as the light enters the nonlinear material, the nonlinearity assumes a nonzero value and remains constant until light exits the system.

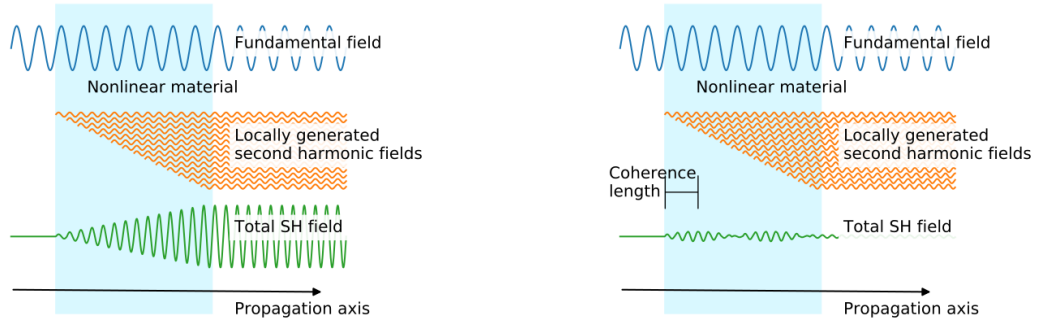
2.3. Understanding and tailoring three wave mixing

In the last section we derived the mathematical description of TWM processes in waveguides. During the derivation, we introduced the phase mismatch $\Delta\beta$ and showed in Eq. (2.34) that the phase term $e^{i\Delta\beta z}$ is responsible for the sinc^2 shape of the phase matching spectrum. It is therefore clear that the phase mismatch plays a critical role in the description of nonlinear phenomena. In the following, we provide a deeper understanding of the physical interpretation of the phase mismatch $\Delta\beta$ and introduce the concept of *quasi-phase matching*.

2.3.1. Birefringent phase matching

To understand the role of $\Delta\beta$ and the phase factor $e^{i\Delta\beta z}$, we need to have a closer look at Eq. (2.12). The evolution of the envelope of the field $\tilde{\mathcal{E}}_3$ is given by

$$\frac{dA_3}{dz} \propto g(z) e^{i\beta_3 z} \iint dx dy \tilde{\mathcal{E}}_3^* \cdot \mathbf{P}_{NL,3}.$$



(a) SHG process in the presence of perfect phase matching, $\Delta\beta = 0$

(b) SHG process in the presence of phase mismatch $\Delta\beta \neq 0$.

Figure 2.4. – Sketch of the physical interpretation of different phase matching conditions. In 2.4a, the SH fields generated at different positions in the crystal are always in phase, since $\Delta\beta = 0$, thus leading to a constant increase of the generated field. In 2.4b, the SH fields generated at different positions are not always in phase, since $\Delta\beta \neq 0$, and thus the overall intensity is limited. Figure inspired from [3].

The guided mode \mathbf{E}_3 propagates along the crystal with a phase velocity of β_3 . At the same time, the excitation of the nonlinear polarisation density \mathbf{P}_3 propagates with a phase velocity of $\beta_1 + \beta_2$, since

$$\mathbf{P}_3 \propto \mathbf{E}_1 \mathbf{E}_2 \propto e^{-i(\beta_1 + \beta_2)z}.$$

Therefore, at position z inside the crystal, the phase difference between the field generated in z by the nonlinear polarisation density and the pre-existent field \mathbf{E}_3 will be $\Delta\varphi = [\beta_3 - (\beta_2 + \beta_1)]z = \Delta\beta z$. The phase factor $e^{i\Delta\beta z}$ then represents the overall dephasing of the field generated at position z with respect to the pre-existent field. Therefore, the integral (2.33) can be interpreted as the coherent sum of the fields generated along the crystal comprising their phase factors.

A simplified sketch of the coherent sum of Eq. (2.33) can be seen in Figure 2.4 in the case of SHG: the fundamental field (in blue) drives the crystal polarisation density that generates a local electric field, shown in orange. The total second harmonic field, obtained by summing the local contributions along z , is shown in green. In the case of perfect phase matching ($\Delta\beta = 0$), since the field produced by the nonlinear polarisation density is always in phase with the fields generated at other positions inside the crystal, the SH field amplitude increases linearly in space, as shown in Figure 2.4a. On the other hand, if there is a phase mismatch between the fields ($\Delta\beta \neq 0$), the waves have regions of constructive and destructive interference, as seen in Figure 2.4b. Thus, the

2.3. Understanding and tailoring three wave mixing

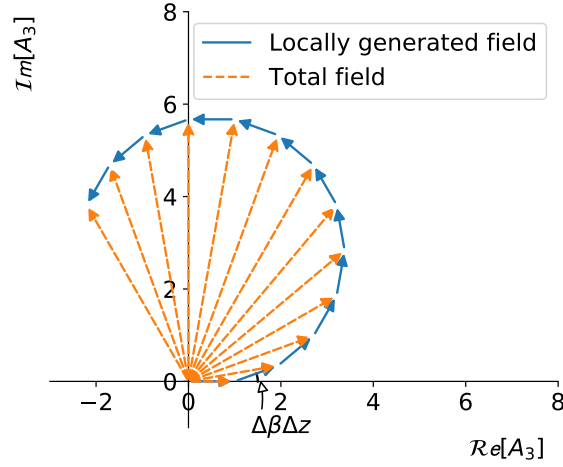


Figure 2.5. – Representation of A_3 in the complex plane. Obviously, the physical process is continuous, not discretised.

SH field amplitudes oscillates, due to the alternation of constructive and destructive interference conditions. The result is an output SH field with reduced intensity, as compared to the one produced under perfect phase matching conditions.

A complete representation of the coherent sum of the fields throughout the nonlinear process can be given by displaying the amplitude A_3 in the complex plane: the amplitude A_3 of the field generated at position z can be represented by the vector $e^{i\Delta\beta z}$ in the complex plane. As shown in Figure 2.5, the integral (2.33) is the vectorial sum of the individual vectors. Since the angle (with respect to the real axis) of the field generated at position z is given by $\Delta\beta z$, for $\Delta\beta \neq 0$, the nonzero angle between each successive generated vector reduces its contribution of each newly generated field component to the total SH field. One can note that, if $z > \pi/\Delta\beta$, the angle of the new components is actually greater than 180° , and thus the newly generated fields will reduce the total SH field. For this reason, one can define the *coherence length* L_C of a process, for a given $\Delta\beta$ as

$$L_C = \frac{\pi}{\Delta\beta}, \quad (2.35)$$

since, for $z > L_C$, the SH field will start to decohere, with respect to the fundamental field. In other words, at $z = L_C$ the total SH field and the local polarisation density are in opposition of phase and start to cancel each other.

Displaying the SH amplitude A_3 in the complex plane helps understanding the shape of the phase matching spectrum as well. To this aim, the evolution of A_3 along the propagation axis, for different $\Delta\beta$ and sample lengths L , is shown in Figure 2.6. In each subplot, the evolution of the complex-valued amplitude A_3 for $\Delta\beta \in [0, 0.003, 0.006, 0.009] \mu\text{m}^{-1}$ is shown for different crystal lengths. In the inset of each subplot,

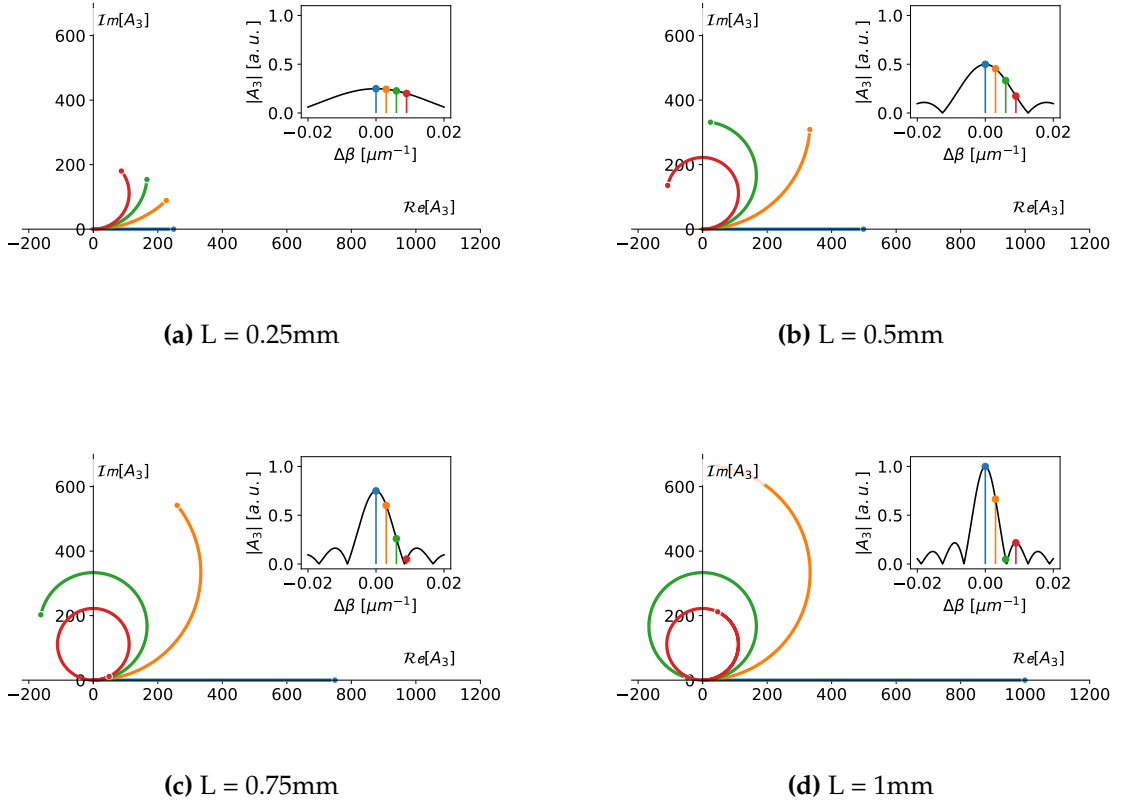


Figure 2.6. – Complex plane representation of a generic SFG process for different crystal lengths and $\Delta\beta$.

the magnitude of the amplitude $|A_3|$ at the end of the crystal is shown, normalised to the amplitude of a 1mm-long sample. The Figure shows the effect of the interplay between the phase mismatch and the crystal length, in determining the magnitude of the amplitude of a TWM process, for a given $\Delta\beta$. In particular, one can note that, for $\Delta\beta = 0$, the magnitude $|A_3|$ grows linearly, as shown by the blue lines in the Figure. This is due to the fact that the contribution of the fields generated at different positions of the sample are all aligned. On the other hand, for $\Delta\beta \neq 0$ (corresponding to the lines in orange, green and red in the Figure), the different contributions add with a slight phase mismatch and thus the amplitude A_3 will draw a circumference (or an arc thereof) whose diameter is inversely proportional to the phase mismatch $\Delta\beta$. From this observation one can see that longer samples will exhibit a smaller bandwidth, as the amplitude A_3 propagates enough to draw a full circle in the complex plane even for small values of $\Delta\beta$.

From this discussion, it is clear that the generation of new light frequencies through

2.3. Understanding and tailoring three wave mixing

nonlinear processes is a restrictive phenomenon, as at least two main conditions have to be met:

- *energy conservation*: only frequencies that preserve the total energy of the system can be coupled via nonlinear processes, i.e. $\omega_3 = \omega_2 + \omega_1$;
- *momentum conservation*: the process needs to be phase matched, i.e. $\beta_3 = \beta_2 + \beta_1$.

To make things worse, due to material dispersion, enforcing energy conservation usually prevents satisfying the momentum conservation. As an example, considering for simplicity a SHG process, momentum conservation implies that

$$\begin{aligned}\Delta\beta = 0 &\Rightarrow n_{2\omega} \cdot 2\omega - (n_{2,\omega} + n_{1,\omega})\omega = 0 \\ &\Rightarrow 2n_{2\omega} = n_{1,\omega} + n_{2,\omega}\end{aligned}\tag{2.36}$$

From this last equality, it is clear that not all type of processes can be phase matched. With the exception of very rare cases, the simplest way to ensure momentum and energy conservation is to perform nonlinear processes in birefringent materials, exploiting the different refractive indices seen by fields polarised along different crystallographic axes. This technique is therefore called *birefringent phase matching*.

Birefringent phase matching requires careful tuning of the parameters involved in the process. In bulk systems, this is often ensured by polarizing the highest frequency field along the axis with the lowest refractive index and then by changing the dispersion of the three fields. This can be accomplished by changing the angle of the crystal with respect to propagation direction of the light beam or by varying the temperature of the crystal. Even though these methods can provide reliable birefringent phase matching, the allowed processes are still dramatically limited by the dispersion characteristics of the nonlinear crystal and thus birefringent phase matching is not flexible enough to allow full process engineering, i.e. achieving a target phase matching spectral shape for a desired frequency combination. To break free from this material constraint it is necessary to engineer the material nonlinearity, as we will discuss in the next section.

2.3.2. Quasi-phase matching

As we have seen in the last section, the field propagating in a waveguide starts to interfere destructively with the newly generated components after a coherence length, $L_C = \pi/\Delta\beta$. In the complex-plane description, after one L_C the vector of the newly generated fields will be characterised by an angle $\Delta\beta z > \pi$ with respect to the fundamental field, as can be seen in Figure 2.5.

Therefore, if a π phaseshift is provided to the newly generated A_3 every time the total envelope aligns with the imaginary axis, the vectors keep adding up constructively, as shown in Figure 2.7. In practice, we want to modify the phase matching integral in Eq.

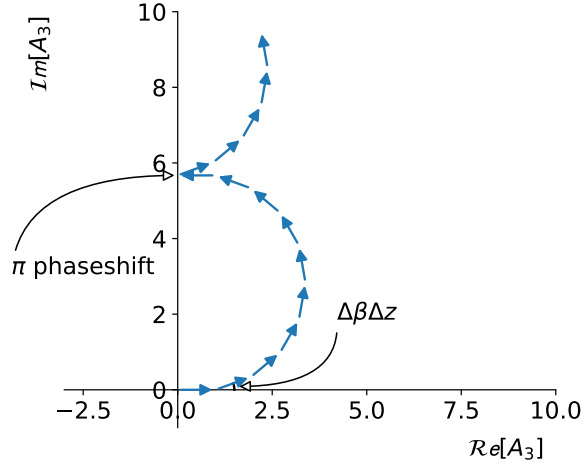


Figure 2.7. – Complex-plane description of quasi-phase matching. Every time the generated field is at its maximum amplitude, i.e. it encounters the imaginary axis, a π phaseshift is applied to the field components generated in the next section of the crystal. This avoids going back to the origin and the field can keep growing until the following phaseshift.

(2.33) to

$$\begin{aligned}
 A(\Delta\beta) &\propto \int_0^{L_C} e^{i\Delta\beta z} dz + \int_{L_C}^{2L_C} e^{i\Delta\beta z + \pi} dz + \int_{2L_C}^{3L_C} e^{i\Delta\beta z + 2\pi} dz + \dots \\
 &= \sum_m (-1)^m \int_{mL_C}^{(m+1)L_C} e^{i\Delta\beta z} dz \\
 &= \int_0^L \Gamma_{\Lambda,0.5}(z) e^{i\Delta\beta z} dz
 \end{aligned}$$

where $\Gamma_{\Lambda,0.5}(z)$ is a square wave with amplitude between $(-1,1)$, pitch $\Lambda = 2L_C$ and duty-cycle $d = 0.5$:

$$\Gamma_{\Lambda,0.5}(z) = \begin{cases} +1, & \text{if } 0 \leq \text{mod}(z, L_C) < 1 \\ -1, & \text{if } 1 \leq \text{mod}(z, L_C) < 2. \end{cases} \quad (2.37)$$

Such a technique to ensure momentum conservation is called *quasi-phase matching*.

2.3. Understanding and tailoring three wave mixing

Comparing this last equation with Eq. (2.33)

$$A_3(\Delta\beta) \propto \int_0^L g(z) e^{i\Delta\beta z} dz,$$

it is evident that the required square wave $\Gamma_{\Lambda,0.5}(z)$ can be implemented modulating the nonlinear profile $g(z)$. Practically, this is done by periodic inversion of the nonlinear tensor d orientation. In fact, expanding the nonlinear profile $d(x, y, z)$ as a Fourier series

$$d(x, y, z) = d_0 \hat{d}(x, y) g(z) = \hat{d}(x, y) \sum_{n \text{ odd}} i \frac{2d_0}{\pi n} e^{i \frac{2\pi}{\Lambda} n z}, \quad (2.38)$$

the integral in Eq. (2.33) describing the intensity of the generated light is transformed into

$$\begin{aligned} A_3(\Delta\beta) &\propto \sum_{n \text{ odd}} i \frac{2d_0}{\pi n} \int_0^L e^{i(\Delta\beta + \frac{2\pi}{\Lambda} n)z} dz \\ &\propto \sum_{n \text{ odd}} i \frac{2d_0}{\pi n} \text{sinc} \left(\frac{(\Delta\beta + \frac{2\pi}{\Lambda} n) L}{2} \right) e^{i \frac{(\Delta\beta + \frac{2\pi}{\Lambda} n) L}{2}}. \end{aligned} \quad (2.39)$$

Inspecting this last equation, one can note that, the modulation of the nonlinearity with $\Gamma_{\Lambda,0.5}(z)$ has the effect of shifting the phase matching spectrum to the new frequencies

$$\Delta\beta \pm \frac{2\pi n}{\Lambda},$$

where n is an odd integer and is called the *process order*. Interestingly, different wavevector mismatches $\Delta\beta$ can be compensated with the same poling period Λ , for an appropriate choice of the order n . This observation can be exploited to realise higher order quasi-phase matching: in the case of processes requiring very small Λ , it is possible to achieve the same process employing a bigger poling period $n\Lambda$, with n odd. However, the amplitude of the process will be reduced by a factor equal to $2/(\pi n)$, as the nonlinear coefficient d_0 is replaced with the *effective nonlinear* coefficient

$$d_{eff}^{(n)} = \frac{2d_0}{\pi n}.$$

The cause of this reduction is clear, when observing Figure 2.7: the generated fields still dephase as they propagate along the crystal and thus, instead of aligning along the real axis, their sum forms a half circle in the complex plane, before being compensated. Therefore, the total field amplitude, calculated as $|A_3|$, is reduced if compared to an ideal birefringent process with identical nonlinear interaction strength.

From a physical point of view, the periodic inversion of the nonlinear profile $g(z)$ can be obtained by periodically inverting the orientation of the $\chi^{(2)}$ tensor every L_C . This inversion is called *periodic poling*. Some fabrication techniques to periodically pole crystals will be reviewed in section 3.4.

2.4. Elements of ultrafast quantum optics

The mathematical description of TWM processes derived in section 2.2.1 assumed that all three fields involved are classical monochromatic fields. However, the correct description of quantum phenomena requires a quantum formulation of the TWM equations. In fact, the theory presented so far cannot take into account two important aspects of many quantum optics experiments:

- being a classical theory, it cannot predict quantum correlations among the three fields at the end of the nonlinear process, and
- assuming monochromatic fields, it cannot describe the effects of the frequency-dependent spectra usually encountered in PDC states and in experiments using pulsed light.

The derivation of TWM processes involving quantum fields is outside the scope of this thesis, and thus we refer the reader to [27–29] for a more thorough derivation. Here, we will report only the main results relevant in this work. For this reason, we will focus our attention to type II PDC processes and frequency conversion (FC) processes, i.e. SFG/DFG.

Assuming a classical pump field and single spatial mode operation in the waveguide, it can be shown that the output state of a type II PDC/FC process can be calculated as

$$|\psi_{out}\rangle_{PDC} = \exp \left[\mathcal{B} \int d\omega_s d\omega_i F(\omega_s, \omega_i) \hat{a}^\dagger(\omega_s) \hat{b}^\dagger(\omega_i) + h.c. \right] |\psi_{in}\rangle \quad (2.40a)$$

$$|\psi_{out}\rangle_{FC} = \exp \left[\mathcal{C} \int d\omega_{in} d\omega_{out} G(\omega_{in}, \omega_{out}) \hat{a}(\omega_{in}) \hat{c}^\dagger(\omega_{out}) + h.c. \right] |\psi_{in}\rangle, \quad (2.40b)$$

where the constants \mathcal{B} and \mathcal{C} provide the strength of the nonlinear process which include the pump power, the spatial field overlap and the nonlinear coefficient d . In Eq. (2.40), the quantum description of the PDC/FC processes is introduced via the creation operators \hat{a}^\dagger , \hat{b}^\dagger and \hat{c}^\dagger , while the frequency-dependent description of the nonlinear interaction is provided by the *joint spectral amplitudes* (JSAs) $F(\omega_s, \omega_i)$ and $G(\omega_{in}, \omega_{out})$. These functions are given by

$$F(\omega_s, \omega_i) = \alpha(\omega_s + \omega_i) \cdot \phi_{PDC}(\omega_s, \omega_i) \quad (2.41a)$$

$$G(\omega_{in}, \omega_{out}) = \alpha(\omega_{out} - \omega_{in}) \cdot \phi_{FC}(\omega_{in}, \omega_{out}) \quad (2.41b)$$

where α is a complex function describing the spectral profile of the pump field and ϕ is the phase matching function.

The joint spectral amplitude can be understood as the transfer function of the process: for a PDC process, it describes the frequency correlations⁸ of the two-photon PDC state; for a FC process, it defines the mapping between the spectrum of the input and output photons.

⁸Which may include entanglement.

2.4. Elements of ultrafast quantum optics

An important tool for the analysis of PDC and FC processes is the Schmidt decomposition of their JSAs [30]. The Schmidt decomposition of a two-dimensional function $f(x, y)$ is a mathematical algorithm that provides two sets of orthonormal functions $\{g_k(x)\}$ and $\{h_k(y)\}$ such that

$$f(x, y) = \sum_k \sqrt{\lambda_k} g_k(x) h_k(y), \quad \sum_k \lambda_k = 1. \quad (2.42)$$

Therefore, the JSA for PDC and FC can be decomposed into

$$F(\omega_s, \omega_i) = \sum_j \sqrt{\lambda_j} g_j(\omega_s) h_j(\omega_i) \quad (2.43a)$$

$$G(\omega_{in}, \omega_{out}) = \sum_j \sqrt{\lambda_j} g_j(\omega_{in}) h_j(\omega_{out}). \quad (2.43b)$$

Thanks to the Schmidt decomposition, Eq. (2.40) can be written as

$$|\psi_{out}\rangle_{PDC} = \otimes_j \exp \left[\mathcal{B} \sqrt{\lambda_j} A_j^\dagger B_j^\dagger + h.c. \right] |\psi_{in}\rangle \quad (2.44a)$$

$$|\psi_{out}\rangle_{FC} = \otimes_j \exp \left[\mathcal{C} \sqrt{\lambda_j} A_j C_j^\dagger + h.c. \right] |\psi_{in}\rangle, \quad (2.44b)$$

where we have defined the *broadband operators*

$$\hat{A}_j^\dagger := \int d\omega g_j(\omega) \hat{a}^\dagger(\omega) \quad (2.45a)$$

$$\hat{B}_j^\dagger := \int d\omega h_j(\omega) \hat{b}^\dagger(\omega) \quad (2.45b)$$

$$\hat{C}_j^\dagger := \int d\omega h_j(\omega) \hat{c}^\dagger(\omega). \quad (2.45c)$$

The broadband operators are a generalisation of the monochromatic creation and annihilation operators and can be interpreted as operators that act on specific pulse modes, i.e. they create or annihilate photons with a broadband spectrum defined by the sets of orthogonal functions $\{g_k\}$ and $\{h_k\}$. Such pulse modes are called *time-frequency modes* (TF modes).

2.4.1. PDC and broadband modes

In the limit of low gain, Eq. (2.44a) for a PDC state with vacuum as input can be written as

$$|\psi\rangle_{PDC} \approx \sum_j \sqrt{\lambda_j} \hat{A}_j^\dagger \hat{B}_j^\dagger |0\rangle. \quad (2.46)$$

Looking at Eq. (2.46), one can see that, in general, the output state of a PDC is constituted by a multitude of PDC sources, each creating photons in their corresponding TF modes: the two output photons will be generated in the TF modes A_j and B_j - and will

therefore have a frequency spectrum $g_j(\omega)$ and $h_j(\omega)$ - with probability λ_j [30]. Such a state is defined as a *multimode state*, since it is constituted by the superposition of many TF modes. Multimode PDC states are characterised by the presence of correlations between the time-frequency modes of the two photons. However, if the JSA is shaped such that only one $\lambda_i = 1$ and the others are zero, then the PDC state is described by

$$|\psi(T)\rangle = \hat{A}_i^\dagger \hat{B}_i^\dagger |0\rangle. \quad (2.47)$$

In this case, the state is generated in only one single-TF mode and therefore no frequency correlations are present between the generated photons. For this reason, such a state is also called *separable* or *decorrelated*, since no entanglement is present in the two-photon state. Moreover, since the system is constituted by only one TF mode, the JSA of a separable state can be written as the product of two functions $F(\omega_s, \omega_i) = g_j(\omega_s)h_j(\omega_i)$.

Decorrelated PDC states are fundamental in generating heralded pure single photons: any heralding measurement that traces out the frequency information of the heralding photon will collapse the heralded photon into a mixed superposition of all the TF modes, unless the state is decorrelated, granting the presence of only one TF mode.

An example of correlated and decorrelated PDC states is shown in Figure 2.8, along with their Schmidt decomposition. Note that the number of Schmidt modes cannot reach 1 due to the slight tilt in the phase matching spectrum and to the presence of the sinc^2 sidelobes.

2.4.2. FC and broadband modes

The description of the FC process in terms of broadband TF modes, under NPDA, is given by Eq. (2.44b)

$$|\psi(T)\rangle_{FC} = \otimes_j \exp \left[\mathcal{C} \sqrt{\lambda_j} A_j C_j^\dagger + h.c. \right] |\psi(0)\rangle.$$

With careful inspection of this equation, we can notice that it is analogous with the quantum optical description of a beamsplitter operation, whose Hamiltonian reads

$$\hat{H}_{BS} = \theta \hat{a}^\dagger \hat{c} + \theta^* \hat{a} \hat{c}^\dagger, \quad (2.48)$$

where θ is a parameter defining the splitting ratio of reflected/transmitted modes in the beamsplitter

$$\hat{a} \rightarrow \cos(\theta) \hat{a} - i \sin(\theta) \hat{c} \quad (2.49a)$$

$$\hat{c} \rightarrow -i \sin(\theta) \hat{a} + \cos(\theta) \hat{c}. \quad (2.49b)$$

We can then conclude that the FC operation is a particular type of beamsplitter operation on the TF modes of the input/output photons, transforming their TF mode

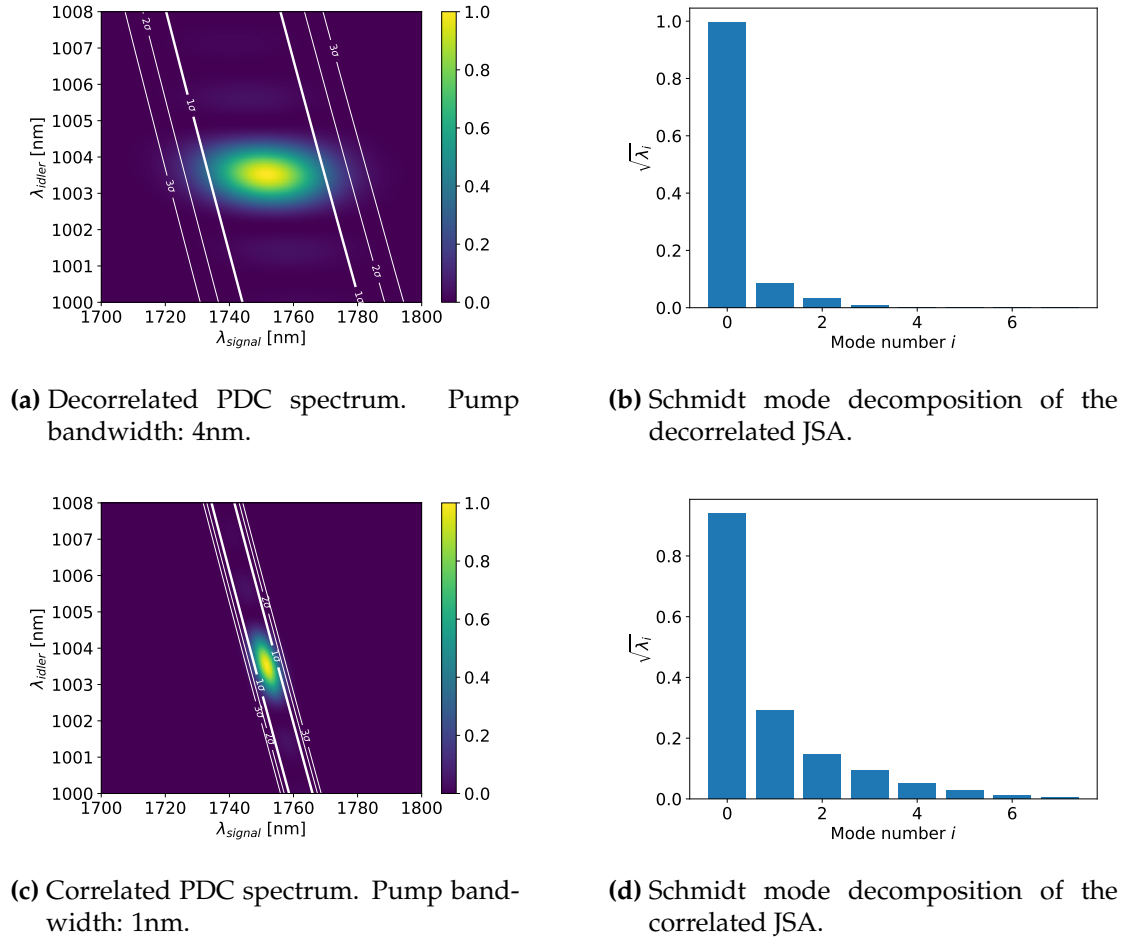


Figure 2.8. – Examples of decorrelated and correlated JSIs obtained by tailoring the pump bandwidth, for a type II PDC process in KTP. This is possible since the process is asymmetric group velocity matched (see section 2.4.3). Since the phase matching is horizontal, increasing the pump bandwidth brings the state towards a more decorrelated condition, thus decreasing the number of Schmidt modes of the system.

components according to

$$\hat{A}_j \rightarrow \cos(\mathcal{C}\sqrt{\lambda_j})\hat{A}_j - i \sin(\mathcal{C}\sqrt{\lambda_j})\hat{C}_j \quad (2.50a)$$

$$\hat{C}_j \rightarrow -i \sin(\mathcal{C}\sqrt{\lambda_j})\hat{A}_j + \cos(\mathcal{C}\sqrt{\lambda_j})\hat{C}_j. \quad (2.50b)$$

Therefore, in the case of single TF-mode operation, the FC process will operate only on a specific TF mode, i.e. it will up/down convert only the spectral components of the input photons that overlap with the TF mode of the process, with an efficiency equal to $\sin(\mathcal{C})^2$.

2.4.3. Decorrelated JSA

In the last two sections, we have seen that a critical requirement for the generation and manipulation of many states of interests in quantum optics application is the realisation of a process characterised by single TF-mode operation. Without entering into the details of JSA engineering [28], one fundamental way to achieve a decorrelated JSA is the engineering of the phase matching angle α in the (ω_1, ω_2) plane. The phase matching angle α is given by

$$\alpha_{PDC} = -\arctan\left(\frac{v_{g,pump}^{-1} - v_{g,signal}^{-1}}{v_{g,pump}^{-1} - v_{g,idler}^{-1}}\right) \quad \text{for PDC} \quad (2.51a)$$

$$\alpha_{FC} = \arctan\left(\frac{v_{g,pump}^{-1} - v_{g,in}^{-1}}{v_{g,pump}^{-1} - v_{g,out}^{-1}}\right) \quad \text{for FC,} \quad (2.51b)$$

where v_g is the group velocity⁹ of the field. In particular, it can be shown that, if the phase matching angle is between 0° and 90° , it is possible to realise decorrelated PDC processes. An example is showed in Figure 2.8a where, in the presence of horizontal phase matching, it is possible to generate a decorrelated PDC state by choosing the correct pump bandwidth.

More specifically, there are two phase matching conditions of particular interest, when designing an ultrafast PDC or FC process. These are known as *symmetric* and *asymmetric* group velocity matching. Symmetric group velocity matching, or sGVM, occurs when the group velocity of the pump field lies at the midpoint between the group velocities of the other two fields. As discussed in [28], the realisation of sGVM phase matching implies an angle of 45° in the (ω_1, ω_2) plane. Notably, this sGVM can be achieved in KTP at 1550nm, thus allowing the realisation of pure, degenerate photon pair generation in the telecom band [23].

Asymmetrical group velocity matching, or aGVM, occurs when the group velocity of the pump field is equal to the group velocity of one of the other two fields. This yields

⁹The group velocity is defined as

$$v_g = \left[\frac{\partial\beta}{\partial\omega}\right]^{-1}.$$

2.4. Elements of ultrafast quantum optics

a phase matching spectrum that is aligned with one of the axes in the (ω_1, ω_2) plane. This phase matching spectrum is incredibly useful for both FC and PDC processes: in a FC process, it enables the realisation of a frequency converter sensitive to the temporal mode of the pump [31], while for PDC states it allows the generation of pure heralded single photons with arbitrary temporal modes [32].

A third, much rarer GVM condition is what the *full* group velocity matching condition (fGVM), where all the three fields have the same envelope speed. Such condition grants very broad phase matching conditions, since the phase matching angle α becomes undefined and the quadratic terms in the $\Delta\beta(\omega_1, \omega_2)$ become relevant. In general, this condition is impossible to realise in standard bulk nonlinear crystal and even in weakly guiding system, since these systems usually exhibit monotonic group velocity curves, whereas fGVM requires the presence of at least a local maximum in the v_g . However, as we will discuss in chapter 7, it is possible to engineer the dispersion of high-index contrast waveguides to find geometries that allow the generation of fGVM states.

Summary

In this chapter, we provided both a classical and quantum description of second order nonlinear processes in waveguides. We introduced the phase mismatch, describing the different phase velocity of the three interacting waves; the normalised conversion efficiency, a parameter providing the theoretical maximum conversion efficiency; the joint spectral amplitude, a two-dimensional transfer function useful in the description of ultrafast quantum processes.

Nonlinear materials and waveguide fabrication

Contents

<p>3.1 Lithium niobate 41</p> <p>3.2 KTP 48</p> <p>3.3 Linear characterisation . 54</p> <p>3.4 Periodic poling 57</p>	<p>The systems analysed in this thesis are non-linear waveguides realised in lithium niobate (LiNbO_3 or LN) and potassium titanyl phosphate (KTP). Therefore, in this chapter we briefly report the properties of these materials that are relevant in this work. Moreover, we describe the types of waveguides discussed in this work, focusing in particular on their fabrication and on the theoretical models used to predict their properties. A brief overview discussing the main parameters used to characterise the performance of waveguides follows. Finally, a section describing the technique used to fabricate periodically poled structures in LN and KTP concludes the chapter..</p>
---	--

3.1. Lithium niobate

Lithium niobate is probably the most important nonlinear material used in state-of-the-art optical telecommunication networks, due to its outstanding acousto-optical, electro-optical and nonlinear optical properties. Fabrication of lithium niobate crystals was first reported in 1928 by Zachariasen [33], while its ferroelectric properties were recognised by Matthias and Remeika [34] in 1949. The crystal does not exist in nature but can be grown using the Czochralski process [35]. Two main types of lithium niobate crystal are commercially available, *stoichiometric* lithium niobate (or SLN) with a 1:1 ratio of Li and Nb ions, and *congruent* lithium niobate (or CNL), with a light Li deficiency ($\text{Li/Nb} \sim 0.946$).

The crystal belongs to the trigonal crystal class, to the $3m$ (C_{3v}) point group and in the $R3c$ space group. It exhibits rotational symmetry along the crystallographic Z-axis (also labelled the optical c -axis), while the crystallographic X and Y axes (optical a - and b - axes) are perpendicular to the c -axis and form a 120° angle. Lacking inversion symmetry, the crystal displays a wide range of nonlinear properties, like ferroelectricity, the electrooptic effect, the piezoelectric effect, photoelasticity and nonlinear optical properties. Thanks to these properties, this material is widely used in telecommunication, mainly in electrooptic or acoustooptic modulators and in surface acoustic wave

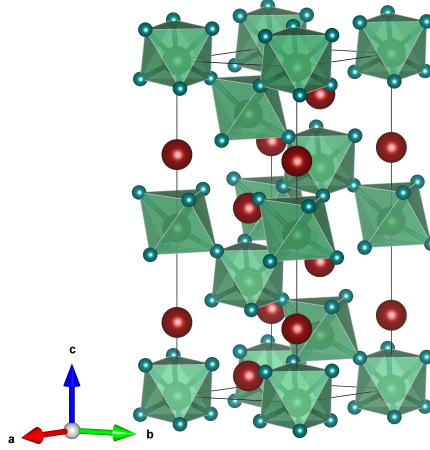


Figure 3.1. – Crystalline structure of LiNbO_3 . Lithium ions are indicated in red, oxygen ions are indicated in green while the niobium ions lie at the centre of the oxygen octahedra.

(SAW) devices.

The crystalline structure, shown in Figure 3.1, is composed by slightly deformed oxygen octahedra surrounding a niobium cation Nb^{5+} . Each octahedron shares the two opposite oxygen atoms with neighbouring octahedra. These $[\text{NbO}_6]$ structures align along the c -axis in an alternating pattern $[\text{NbO}_6] - \text{vacancy} - \text{Li}^+ - [\text{NbO}_6] - \dots$. The lack of inversion symmetry is due to the diagonal structure of the oxygen octahedra, the different Li-O distances and the alternating pattern along the c -axis.

3.1.1. Optical properties

Dispersion properties

Lithium niobate is a dielectric material with a very wide transparency range, since its linear absorption α is $< 0.03\text{cm}^{-1}$ for $\lambda \in [350, 4000]$ nm [36]. The low absorption in the visible and infrared range make this crystal an ideal candidate as a waveguide platform.

Due to its crystalline structure, LN is a negative uniaxial birefringent material with optical axes parallel to the crystallographic c -axis. The *extraordinary* refractive index (along the c -axis) has been found to follow the Sellmeier equation [37]

$$n_e^2(\lambda, T) = A_{1,e} + B_{1,e} \cdot f + \frac{A_{2,e} + B_{2,e} \cdot f}{\lambda^2 - (A_{3,e} + B_{3,e} \cdot f)^2} + \frac{A_{4,e} + B_{4,e} \cdot f}{\lambda^2 - A_{5,e}^2} - A_{6,e} \lambda^2, \quad (3.1)$$

where $f = (T - 24.5)(T + 570.82)$, the temperature T is in degree Celsius and the wavelength λ is in μm . The *ordinary* refractive index (perpendicular to the c -axis) follows the

Ordinary refractive index coefficients		Extraordinary refractive index coefficients	
$A_{1,o}$	4.9048	$A_{1,e}$	5.35583
$A_{2,o}$	0.11775	$A_{2,e}$	0.100473
$A_{3,o}$	0.21802	$A_{3,e}$	0.20692
$A_{4,o}$	0.027153	$A_{4,e}$	100
		$A_{5,e}$	11.3493
		$A_{6,e}$	1.5337×10^{-2}
$B_{1,o}$	2.2317×10^{-8}	$B_{1,e}$	4.6390×10^{-7}
$B_{2,o}$	-2.9671×10^{-8}	$B_{2,e}$	3.8620×10^{-8}
$B_{3,o}$	2.1429×10^{-8}	$B_{3,e}$	-8.9×10^{-9}
		$B_{4,e}$	2.657×10^{-5}

Table 3.1. – Table of the coefficients for the Sellmeier equations (3.1) and (3.2)

Sellmeier equations [38]

$$n_o^2(\lambda, T) = A_{1,o} + \frac{A_{2,o} + B_{1,o} \cdot F}{\lambda^2 - (A_{3,o} + B_{2,o} \cdot F)^2} + B_{3,o} \cdot F - A_{4,o} \lambda^2, \quad (3.2)$$

where $F = (T - 24.5)(T + 549)$, the temperature is in degree Celsius and the wavelength λ is in μm . The values of the parameters in Eqs. (3.1) and (3.2) are given in Table 3.1.

The normalised group velocity curves for bulk LN at room temperature are shown in Figure 3.2. The inspection of these curves shows that it is not possible to realise group velocity matched PDC processes in bulk LN. In fact, from the specific form of the nonlinear tensor reported in the next section, all type I and type II processes require the pump photon to be polarised along the crystallographic X or Y axis. Since the group velocity along these axes is lower than along the z axis, it is impossible to find GVM conditions for PDC processes. It is possible to find aGVM SFG (or DFG) type II processes ($\omega_1 + \omega_2 \rightarrow \omega_3$) where the lowest energy photon at ω_1 is polarised along X or Y and the photon at ω_2 is polarised along Z [28].

Optical nonlinearity

As mentioned above, lithium niobate is a noncentrosymmetric crystal, and therefore has a non-zero $\chi^{(2)}$ that can be exploited for three wave mixing processes. In particular, the nonlinear tensor for lithium niobate reads

$$\underline{d}_{\text{LiNbO}_3} = \begin{bmatrix} 0 & 0 & 0 & 0 & d_{31} & -d_{22} \\ -d_{22} & d_{22} & 0 & d_{31} & 0 & 0 \\ d_{31} & d_{31} & d_{33} & 0 & 0 & 0 \end{bmatrix}, \quad (3.3)$$

where $d_{33} = 27.2 \pm 2.7$ pm/V, $d_{31} = 4.35 \pm 0.44$ pm/V and $d_{22} = 2.1 \pm 0.21$ pm/V [36]. Therefore, it can be seen that the allowed processes in LiNbO_3 are five type 0/I processes (having the field at ω_3 polarised along either the Y or Z crystallographic axis)

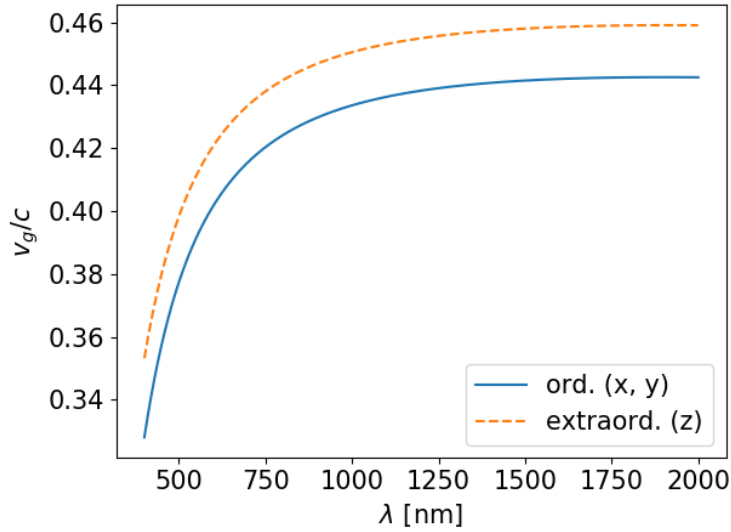


Figure 3.2. – Group velocity curves for bulk LN.

and three type II processes ($YZ \rightarrow Y$, $XZ \rightarrow X$ and $XY \rightarrow X$). The most efficient process is the type 0 process with light polarised along the Z (extraordinary) axis.

Other properties

Lithium niobate is one of the main platforms employed in optical telecommunication system, thanks to its electro- and acoustooptical properties. The electrooptic effect is related to a change in the crystal refractive index ellipsoid when an external field (static or up to radiofrequency) is applied, while the acoustooptic effect manifests as a variation of the refractive index when the crystal is subjected to mechanical strain. Both these effects can be exploited to create acousto- or electrooptic modulators that can be used to modulate the intensity or the phase of light propagating inside LN waveguides.

One of the major drawbacks of LN, as opposed to other nonlinear materials, is its low photorefractive damage threshold in the visible range. Photorefraction is the local change of refractive index induced by a strong light field incident on the crystal. The electric field of the incident light stimulates the motion of ions and electrons in the crystal lattice and can create local electric fields that modify the refractive index through the electrooptic effect [35]. Since the guiding properties of waveguide structures are highly dependent on the refractive index distribution, photorefraction can dramatically disrupt the guiding properties of waveguide, e.g. by locally changing the dispersion relations of the system or the shape of the propagating modes. This has detrimental effects for the realisation of efficient nonlinear optical systems operating at visible frequencies. It is possible to mitigate the effect of photorefraction with dif-

ferent techniques, e.g. with a 5% MgO doping of the waveguide¹ or increasing the crystal temperature above 170°C. However, the additional processing steps or the high operating temperature can be problematic in some applications - e.g., a high operating temperature requires careful thermal insulation and control - and thus other materials with higher photorefractive damage threshold (like KTP, see section 3.2) might offer better performance in these cases.

3.1.2. Diffused waveguide in LN

One of the most common type of waveguides in LN is titanium-indiffused lithium niobate (Ti:LN) waveguides. Ti:LN waveguides have been widely used for classical and quantum applications [12, 13, 31, 39–44] due to having many ideal properties: they exhibit high conversion efficiency - up to 45%/Wcm² for SHG pumped at 1550nm, guide orthogonal light polarisation and thus allow the realisation of type II processes². This enables the realisation of type II PDC in waveguides [45]. Moreover, it is possible to realise bends, coupling regions and active elements such as $\Delta\beta$ -reversed switches and phase shifters, thus allowing the development of a toolbox of integrated components that enables the realisation of on chip generation and manipulation of complex states of light [46, 47]

The standard production of Z-cut³ Ti:LN waveguides is shown in Figure 3.3. Initially, a titanium film with thickness τ is evaporated onto the surface of a 0.5mm-thick LN sample. With standard photolithographic techniques, a series of photoresist stripes with width w are then patterned on top of the titanium film. After etching the exposed titanium and removing the residual photoresist, the sample exhibits titanium stripes with width w and thickness τ . The sample is then loaded in an oven, where the diffusion process takes place in an oxygen-rich environment. The sample is heated to the temperature T for a well defined amount of hours Δt . The temperature has to be high enough to allow the diffusion of the Ti⁴⁺ ions inside the crystalline structure. The temperature T of the diffusion process, its duration Δt and the stripes' thickness τ define the profile of the diffused titanium inside the crystal and thus the waveguides depth, while the stripes' width w define their widths. During the diffusion, lithium oxide diffuses out of the substrate and creates an amorphous structure on the -Z face, that needs to be ground to allow electric periodic poling (see section 3.4). After diffusion has taken place, the sample is removed from the oven and its facets are polished to optical quality. If necessary, after the waveguides are fabricated, the sample can be periodically poled (see section 3.4) for the realisation of quasi phasematched processes.

¹Such doping is not possible in the systems analysed in this thesis, titanium in-diffused LN waveguide (see section 3.1.2).

²This is not possible, for example, in proton exchanged LN waveguides, since these systems cannot guide light polarised along the ordinary axis.

³A Z-cut LN crystal has been cut perpendicularly to the [001] crystallographic axis.

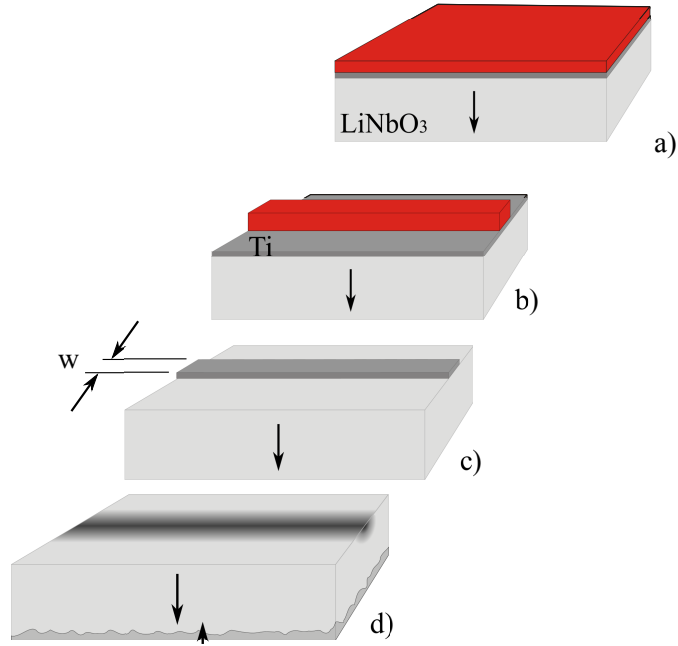


Figure 3.3. – Standard Ti:LiNbO₃ waveguide fabrication technique. From top to bottom: a) deposition of a titanium layer on top of the lithium niobate substrate and spin coating of a photoresist layer; b) photolithographic patterning of the photoresist; c) etching of the titanium to define the Ti stripe to be diffused; d) diffusion of the Ti stripe in the substrate to define the waveguide.

Modelling of Z-cut Ti:LN waveguides

As seen in chapter 1, a guiding structure modifies the refractive index experienced by light propagating inside it. Therefore, precise knowledge of the influence of the fabrication parameters and geometry on the dispersion properties of a waveguide is fundamental for the design of nonlinear processes. In our work, we followed the model proposed by Strake et al. [48] and detailed here in the following.

First, the concentration profile $c(x, y)$ of Ti⁴⁺ ions is described as

$$c(x, y) = c_0 f(u) g(s) \quad (3.4)$$

$$f(u) = \exp(-u^2) \quad (3.5)$$

$$g(s) = \frac{\operatorname{erf}[w/2D_x \cdot (1 + s)] + \operatorname{erf}[w/2D_x \cdot (1 - s)]}{2} \quad (3.6)$$

where $u = y/D_y$, $s = 2x/w$, D_x and D_y are the diffusion depths along the transverse directions, w is the Ti stripe width and c_0 is a parameter related to the Ti-ion content per unit length along the waveguide. The parameter c_0 can be related to the original

3.1. Lithium niobate

Ti stripe thickness τ by the relation $\tau = a_0 c_0 d_y$, where $a_0 = 1.57 \times 10^{-23} \text{ cm}^3$. The diffusion depths D_x and D_y depends on the crystal orientation and are calculated from

$$D = D_{ord/extr,0} \sqrt{\frac{\Delta t}{\Delta t_0}} e^{E_{ord/extr}^{act} \left(\frac{1}{T_0} - \frac{1}{T} \right)},$$

where $T_0 = 1333.15 \text{ K}$, $\Delta t_0 = 9.0 \text{ h}$, $D_{ord,0} = 4.105 \text{ }\mu\text{m}$, $D_{extr,0} = 4.850 \text{ }\mu\text{m}$, $E_{ord}^{act} = 11.234 \times 10^3 \text{ K}$ and $E_{extr}^{act} = 11.054 \times 10^3 \text{ K}$.

The concentration profile $c(x, y)$ is used to calculate the refractive index increase of the ordinary δn_o and extraordinary δn_e refractive indices, with respect to the bulk values:

$$\delta n_x(\lambda, c) = d_x(\lambda) f_x(c), \quad x = e, o. \quad (3.7)$$

The model uses the following values for d and f :

$$f_e(c) = Ec \quad (3.8a)$$

$$f_o(c) = (Fc)^\gamma \quad (3.8b)$$

$$d_e(\lambda) = \frac{0.839\lambda^2}{\lambda^2 - 0.0645} \quad (3.8c)$$

$$d_o(\lambda) = \frac{0.67\lambda^2}{\lambda^2 - 0.13} \quad (3.8d)$$

where λ is expressed in μm . The value of the parameters are $E = 1.2 \times 10^{-23}$, $F = 1.3 \times 10^{-25} \text{ cm}^3$ and $\gamma = 0.55$. Note that the values for F and γ approximate well the measured data only for $c \leq 0.9 \times 10^{-21} \text{ cm}^{-1}$.

The presented model provides a description of the refractive index distribution as a function of the fabrication parameters ($w, \tau, \Delta t, T$), the wavelength λ and the polarisation of the light entering the structure. To extract the effective refractive index of the fundamental modes propagating inside the Ti:LN waveguide, a FEM solver implemented in Python has been used.

The calculated effective indices provide a fairly good estimation of the dispersion of light modes in Ti:LN waveguides in the range between 400-1700nm for most processes of interest. For poling periods below $20\mu\text{m}$, the model has an error below 0.5% while it increases for longer poling period. The greatest error is found for the prediction of birefringent phasematching, where a 50nm offset in the phasematching wavelength is observed.

3.1.3. Thin film LNOI

A second type of LN waveguide investigated in this thesis is thin film lithium niobate on insulator (LNOI) waveguides.

Thin film waveguide technologies are characterised by the presence of a high refractive index contrast between the waveguide and the cladding region. This is usually achieved by inscribing ribs in a high-refractive index, submicrometric thin film material, bonded to a lower refractive index substrate. This geometry provides very high

modal confinement and low bending radii, allowing the realisation of compact devices and thus it is an ideal platform for optical chip fabrication. Moreover, it offers great flexibility in waveguide mode dispersion engineering, since the effective refractive index is highly dependent on the waveguide geometry. For this reason, the landscape of nonlinear processes available in nonlinear thin film waveguides is dramatically different from the one offered by weakly guiding structures realised in the same substrate.

In the last two years, thin film lithium niobate technology has seen an increasingly growing interest. As soon as the first ultra-low loss LNOI waveguides were demonstrated in 2017 [49] many groups started investigating this technology, as it joins all the benefits of standard thin film waveguides with the amazing properties of the lithium niobate platform, namely high electrooptic effect and high optical nonlinearities. Since then, in just two years, many optical components have been demonstrated in LNOI, including electrooptic modulators [50] and SHG/SFG [51, 52].

Fabrication of low loss LNOI waveguides [49] has proved to be particularly complex, since it requires optimised etching procedures to reduce the roughness of the waveguides sidewalls. A sub-micron LN thin film, bonded to a SiO₂ substrate and coated with hydrogen silsesquioxane (HSQ) photoresist, is patterned via electron-beam lithography to achieve high resolution ($\sim 10\text{nm}$) structures. This step is crucial to achieve low loss waveguides, as the resolution of standard vacuum-contact UV photolithography is one or two orders of magnitude lower than E-beam lithography. After photoresist development, the pattern is transferred to the LN film via inductively coupled plasma reactive ion etching (ICP RIE). The etching depth and the shape of the LN rib depend on many parameters, among which are the photoresist thickness and the ion etching rate. Finally, the sample is cleaned from the photoresist remainings and a capping layer (usually SiO₂) can be deposited on the LN rib for protection.

3.2. KTP

Along with lithium niobate, potassium titanyl phosphate is another important material for nonlinear optical processes. It is commonly employed to double the frequency of infrared solid state and diode lasers, as a source to generate light between 600nm-4500nm in optical parametric oscillator and as an active material in electrooptic modulators.

It was first synthesised by Ouvrard in 1890 [53], while its nonlinearity was discovered by Zumsteg *et al.* [54] in 1976. KTP is only one of the components of the isomorphic family of crystals described by the general formula $MTiOXO_4$, where M can be potassium (K), rubidium (Rb), thallium (Tl), ammonium (NH₄) or caesium (Cs), while X can be phosphorus (P) or arsenic (As). All crystals in this family belong to the point group $mm2$ (C_{2v}), space group $Pna2_1$ and possess an orthorhombic structure.

The crystalline structure is shown in Figure 3.4. It is characterised by helical chains of TiO₆ octahedra aligned along the [011] and $[0\bar{1}1]$ directions interconnected by PO₄ tetrahedra. The presence of channels between the TiO₆ octahedra and PO₄ tetrahedra along the [001] axis, i.e. the c -axis, allows the accommodation of K ions. The presence of these channels oriented along the c -axis is responsible for many anisotropical proper-

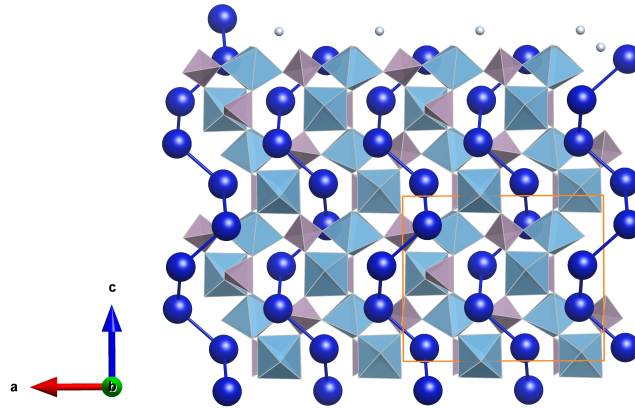


Figure 3.4. – KTP crystalline structure

ties of KTP and its isomorphs. Such anisotropy can be exploited for the realisation of sub-micrometric poling of bulk KTP crystals [55]. The crystallographic a and b axes are perpendicular to each other and lie on a plane orthogonal to the c axis.

As stoichiometric KTP cannot be grown, KTP is characterised by a high concentration of K-vacancies allowing the movement of K ions along the potassium channels. This results in a non negligible ionic conductivity when the crystal is subjected to a high voltage along the c -axis. This is problematic for the realisation of small periodic poling structures. To reduce this ionic current, it is possible to treat a KTP crystal by immersing it in a potassium nitride melt, to increase the concentration on K ions in the crystal [56]. Another option is to insert larger ions (like Rb or Cs) inside the crystalline structure, either by doping or by exchanging them with K ions [57]. Due to the larger atomic radii, these species dramatically reduce the mobility of the ions along the channels, thus reducing the ionic conductivity.

From a physical perspective, KTP is transparent in the range from 350nm to 4500nm, offers relatively large electrooptic and nonlinear coefficients. Differently from LN, KTP exhibits very low photorefraction, possesses a high damage threshold and its dispersion properties change very little with temperature ($dn/dT \leq 1.6 \times 10^{-5}/^{\circ}\text{C}$) These last three properties are especially crucial for the realisation of optical processes in nonlinear waveguides at room temperature. A final key property of this material, that makes it one of the most commonly used nonlinear crystal in quantum optics experiments, is its unique dispersion relations, that allow for symmetric group velocity matching (see section 2.4.3) and thus the generation of a separable photon pair state at telecom wavelength [23].

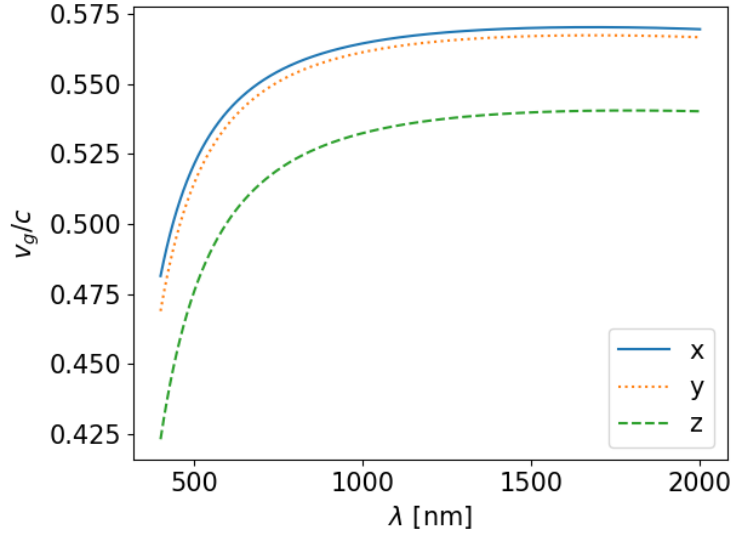


Figure 3.5. – Group velocity curves for bulk KTP.

3.2.1. Optical properties

Dispersion properties

KTP is a biaxial birefringent material and the refractive indices along the X , Y , Z axis (equivalent to the a , b , c axes) are given by [58]

$$n_x^2 = 3.27100 + \frac{0.04140}{\lambda^2 - 0.03978} + \frac{9.35522}{\lambda^2 - 31.45571} \quad (3.9a)$$

$$n_y^2 = 3.45018 + \frac{0.04341}{\lambda^2 - 0.04597} + \frac{16.98825}{\lambda^2 - 39.43799} \quad (3.9b)$$

$$n_z^2 = 4.59423 + \frac{0.09206}{\lambda^2 - 0.04763} + \frac{110.80672}{\lambda^2 - 86.12171}. \quad (3.9c)$$

The normalised group velocity curves for bulk KTP are shown in Figure 3.5. The analysis of these curves reveals a situation very different from bulk LN: among the processes allowed (see next paragraph), it is possible to find both sGVM and aGVM PDC processes, since the pump photon must lie on the faster curves, i.e. it needs to be either X - or Y -polarised. This unique combination of allowed nonlinear process and dispersion properties makes KTP an extremely attractive material for both classical and quantum nonlinear optics applications.

	d_{31}	d_{32}	d_{33}	d_{24}	d_{15}
532nm [59]	1.4	2.65	10.7	2.65	1.4
1064nm [60]	2.4	4.4	16.9	7.9	6.1

Table 3.2. – Values of the nonlinear coefficients for KTP for different wavelengths. All values in pm/V.

Optical nonlinearity

Being a noncentrosymmetrical crystal, KTP possesses second-order nonlinear optical properties. In particular, its nonlinear tensor reads

$$\underline{d}_{\text{KTP}} = \begin{bmatrix} 0 & 0 & 0 & 0 & d_{15} & 0 \\ 0 & 0 & 0 & d_{24} & 0 & 0 \\ d_{31} & d_{32} & d_{33} & 0 & 0 & 0 \end{bmatrix} \quad (3.10)$$

and the values of the nonlinear coefficients are give in Table 3.2.

From the structure of the tensor $\underline{d}_{\text{KTP}}$, the nonlinear processes allowed in KTP are type 0/I processes with ω_3 polarised along Z and the two type II processes $YZ \rightarrow Y$ and $XZ \rightarrow X$.

3.2.2. Rb exchanged waveguides in KTP

Being a nonlinear material with relatively high nonlinear coefficients and high damage threshold, KTP has been investigated as a substrate for the realisation of nonlinear optical waveguides since 1987, when the first fabrication of optical waveguides in KTP was reported by Bierlein *et al.* [61]. In their work, the authors realised planar and channel waveguides in KTP by exchanging the K ions with Rb, Cs or Tl ions. Since then, a few other technologies for the production of KTP waveguides have been attempted, such as He⁺ implanted waveguides [62], femtosecond laser written waveguides [63–65] and, recently, ridge rubidium-exchanged waveguides [66, 67].

Waveguides based on the rubidium exchange process are by far the most common type of KTP waveguides, since they are relatively simple to fabricate, have shown high efficiency and offer the possibility of integrating different electrooptical and nonlinear components on a single chip. They are mainly exploited for their unique dispersion properties, that allow the generation of decorrelated photon pair states in the telecom C-band [23] and O-band [32]. Another advantage of KTP waveguides is the possibility to use them in conjunction with very short poling periods, making them attractive for the generation and manipulation of light in the blue [66, 67].

The standard fabrication of Z-cut channel rubidium-exchanged KTP (Rb:KTP) waveguides is sketched in Figure 3.6. A 1cm-thick, Z-cut KTP substrate is prepared by depositing a titanium layer on the +Z face. Subsequently, a photoresist layer is patterned via UV lithography, creating slits in the photoresist corresponding to the desired waveguide structures. After photoresist development, the titanium layer is etched away,

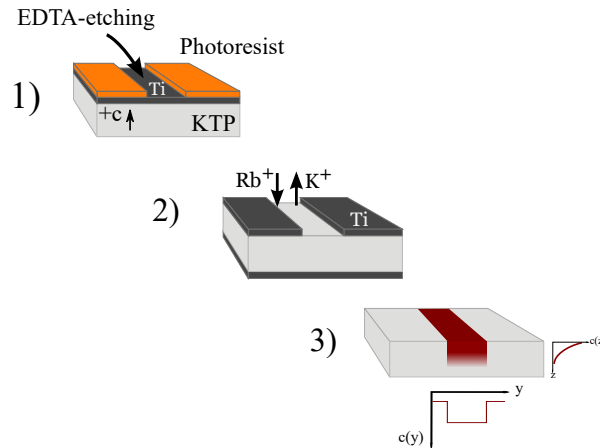


Figure 3.6. – Fabrication of Rb:KTP waveguides. At first, Ti slits, defining the waveguide widths, are patterned via UV photolithography (step 1). The waveguides are realised via Rb-K exchange in a RbNO₃, KNO₃ and Ba(NO₃)₃ melt (step 2). Sample fabrication is completed with a cleaning step and the polishing to optical grade of the in- and out-coupling facets (step 3).

revealing the KTP surface that will experience the Rb exchange. The sample is then immersed in a melt composed of KNO₃, Ba(NO₃)₂ and RbNO₃, where rubidium nitrate is used as a reservoir of Rb ions and barium and potassium nitrate are used to control the speed of the exchange. The exchange is performed at a fixed temperature above 300°C for a well defined amount of time. The melt composition, the exchange time and temperature completely define the exchange process and thus the waveguide properties. After exchange, the sample is removed from the melt and cleaned. After a polishing step to prepare the waveguide facet to optical quality, the sample is ready to be poled, if needed, or directly employed.

Modelling of exchanged waveguides

The modelling of exchanged waveguides in KTP requires the understanding of the diffusion dynamics of the K-Rb exchange. However, as Bierlein *et al.* noted in their original paper [61], the diffusion of Rb in KTP “does not obey simple diffusion kinetics”: the refractive index increase at the surface Δn , due to the Rb exchange, and the waveguide depth seems to be independent of the exchange time (in the range from 0.25-4h) and temperature (in the range 350-400°C). Only very recently there has been developments in understanding the exchange dynamics [68].

Another problem preventing clear understanding and modelling of Rb:KTP waveguides is the scarcity of information regarding the relation between the Rb concentra-

tion profile and the refractive index distribution. In particular, the relation between these two parameters has not been thoroughly investigated for varying melt composition, exchange time and temperature, and thus it is hard to predict the impact of fabrication parameters on the performance of KTP waveguides. For these reasons, *ab initio* modelling of Rb:KTP waveguides still proves to be a hard task.

A waveguide, propagating along the crystallographic X axis and waveguides patterned on either of the Z faces, is usually modelled assuming a 1D diffusion of Rb along the Z axis in presence of an infinite Rb reservoir, providing a complementary error function⁴ erfc concentration profile

$$\begin{aligned} c(z, t) &= c_0 \operatorname{erfc} \left(\frac{z}{2\sqrt{D(T)\Delta t}} \right) \\ &= c_0 \operatorname{erfc} \left(\frac{z}{d} \right) \end{aligned} \quad (3.11)$$

where c_0 is the final concentration of rubidium at the surface, Δt is the exchange time and $D(T)$ is the temperature-dependent diffusion coefficient. A linear dependence of the refractive index on the rubidium concentration is assumed, thus leading to a refractive index increase described by

$$\Delta n(y, z; \lambda) = \Delta n_0(\lambda) \Pi_{[-w/2, w/2]}(y) \operatorname{erfc} \left(\frac{z}{d} \right), \quad (3.12)$$

where Δn_0 is the refractive index increase at the surface, $\Pi_{[-w/2, w/2]}(y)$ is a box function with width w along the y direction. Since the dispersion properties of rubidium doped KTP have not been thoroughly investigated yet, the only model available for $\Delta n_0(\lambda)$ is the one provided by [69] and developed for the waveguides sold by the company AdvR Inc. The refractive index increase is thus given by

$$n_{wg}(y, z; \lambda) = n_{bulk}(\lambda) + \Delta n_0(\lambda) \Pi_{[-w/2, w/2]}(y) \operatorname{erfc} \left(\frac{z}{d} \right) \quad (3.13a)$$

$$\Delta n_0(\lambda) = A + B\lambda + C\lambda^2 + Fe^{-\frac{\lambda \times 10^3 - 350}{G}}. \quad (3.13b)$$

where λ is in μm and the parameters of Δn_0 are reported in Table 3.3.

A few remarks regarding this model are needed. Firstly, the parameters reported here are different from the ones presented in [69] and have been retrieved from private communications with the authors of the paper, who acknowledge that the published parameters are incorrect. Secondly, this model has been optimised for the commercial waveguides, whose fabrication process has not been fully disclosed. Despite providing good estimates for the effective index of the modes of the waveguides fabricated in our

⁴The complementary error function is defined as

$$\operatorname{erfc} = \frac{2}{\sqrt{\pi}} \int_x^{+\infty} e^{-t^2} dt.$$

	A	B	C	F	G
ordinary (n_y)	26.76947	-10.9737	2.29268	2.24595×10^{-2}	44.62477
extraordinary (n_z)	29.0816	-6.5850	2.13894	9.60547×10^{-3}	39.20047

Table 3.3. – Table of the coefficients for the refractive index increase $\Delta n_0(\lambda)$ in Eq. (3.13b).

cleanroom and used in chapter 4, there will be an inevitable discrepancy between the model and the experimental results, since our fabrication is likely to be different to the industrial processing. Another source of discrepancy between Callahan’s model and the experiments reported in chapter 4 is that the model form Callahan assumes an *erfc* diffusion profile while, as already mentioned, this assumption is only a simplification of a much more complex nonlinear diffusion dynamics.

3.3. Linear characterisation of waveguide properties

It is important to assess the quality of a waveguide before it is employed in experiments or in real-world applications. Two of the most important parameters to evaluate before the deployment of a waveguide system are the *propagation losses* and the waveguide-to-fibre *coupling efficiency*: the former describes the intrinsic losses of the system, while the latter characterises how well it can be integrated in a fibre network.

3.3.1. Propagation losses

The losses of an integrated optical devices are a measurement of the ratio between the total input power and the total transmitted power. In particular, it is usual to define the *insertion losses* IL as

$$IL[\text{dB}] = -10 \log_{10} \left(\frac{P_{out}}{P_{in}} \right), \quad (3.14)$$

where P_{in} is total power entering the system and P_{out} is the total power exiting the system. From the point of view of the user of the integrated device, the IL are fundamental since they represent the total, unavoidable added losses due to the usage of the device in an optical setup. However, these losses can usually be decomposed into three different types of losses: *coupling losses* CL , *reflection losses* RL and propagation losses PL :

$$IL [\text{dB}] = CL [\text{dB}] + FL [\text{dB}] + PL [\text{dB/cm}] \cdot l, \quad (3.15)$$

where l is the length of the device.

Coupling losses are due to mismatch between the field entering the optical system and the set of possible eigenmodes supported by the system. Typically, they are due to different spatial distributions of the fields inside and outside the waveguide. In this

case, they are often evaluated as

$$CL[\text{dB}] = -10 \log_{10} (|\Theta|^2), \quad (3.16)$$

where Θ is the field overlap defined as

$$\Theta = \frac{\iint dx dy E_{in} E_{out}^*}{\sqrt{\iint dx dy |E_{in}|^2 \iint dx dy |E_{out}|^2}}. \quad (3.17)$$

Reflection losses are due to the reflections occurring at the interface between two materials having different refractive indices. For this reason, they are usually called also Fresnel losses and, for a single interface, are evaluated as

$$RL[\text{dB}] = -10 \log_{10} (1 - R), \quad (3.18)$$

where R is the reflectivity of the interface.

Finally, the *propagation losses* quantify the amount of light lost due to absorption or scattering, as it travels along the optical system. These losses are usually modelled following the Lambert-Beer law

$$P(L) = P(0)e^{-\alpha l}, \quad (3.19)$$

relating the intensity of light after propagation in a material with length l and linear attenuation coefficient α . The propagation losses, in dB/cm, are related to the attenuation coefficient by

$$\begin{aligned} PL[\text{dB/cm}] &= -\frac{10}{l} \log_{10} \left(\frac{P_{end}}{P_{start}} \right) \\ &= -\frac{10}{l} \log_{10} \left(e^{-\alpha l} \right) \\ &= 10 \log_{10}(e) \cdot \alpha \\ &\approx 4.34\alpha, \end{aligned} \quad (3.20)$$

where α is expressed in cm^{-1} .

Among all these losses, the propagation losses are typically the most important ones when developing an integrated system. In fact, both coupling and reflection losses can be reduced after waveguide fabrication: the former can be reduced by appropriately shaping the input beam to match the eigenmodes of the waveguide and the latter can be reduced using proper antireflective coatings. On the other hand, propagation losses are intrinsic properties of the waveguide system and can only be reduced by optimising the fabrication process.

One of the most common techniques to estimate the propagation losses in waveguides with refractive index much higher than air is the Fabry-Pérot technique [70]. Given the high refractive index contrast with air, the facets of the waveguide are characterised by a non-negligible reflectivity (ca. 8% for KTP), effectively making the waveguide a Fabry-Pérot resonator. The transmission T of the resonator is given by

$$T = \kappa \frac{(1 - R)^2 e^{-\alpha L}}{(1 - \tilde{R})^2 + 4\tilde{R} \sin^2(\Phi/2)}, \quad (3.21)$$

where κ is the coupling efficiency to the waveguide mode, R is the mode reflectivity, $\tilde{R} = Re^{-\alpha L}$ and $\Phi = 2\beta L$ is the optical round trip length of the cavity. Due to the presence of the \sin^2 function, the transmission of the resonator presents periodical maxima and minima, corresponding to instances of constructive and destructive interference of the light field in the resonator. The maxima and the minima of the transmission T can be measured scanning the optical round trip length Φ , e.g. by tuning the wavelength of the incident field or by varying the refractive index of the material changing its temperature.

From the contrast K between the maxima (constructive interference) and the minima (destructive interference) of the transmitted power, defined as

$$K = \frac{I_{max} - I_{min}}{I_{max} + I_{min}}, \quad (3.22)$$

it is possible to retrieve the propagation losses inside the waveguide, if the reflectivity of the facets is known, since

$$\alpha[\text{dB/cm}] \sim \frac{\log_{10}(e)}{L} (\log R - \log K + \log 2). \quad (3.23)$$

From this discussion, it is clear that the main assumption of this technique is the knowledge of the reflectivity of the waveguide facets. Indeed, in general, the reflectivity is considered to be equal to the Fresnel reflectivity under normal incidence

$$R = \left(\frac{n_{eff} - 1}{n_{eff} + 1} \right)^2, \quad (3.24)$$

where n_{eff} is the effective index of mode being measured. This assumption is sufficient in most cases, especially when the waveguide is weakly guiding, has high quality optical facets and the uncertainty in the reflectivity coefficients is higher than the propagation losses. When these conditions are not valid, as in the case of high index contrast waveguides [4], the application of the Fabry-Pérot technique can yield a false estimate of the propagation losses.

Furthermore, the presented method is valid mostly in single mode waveguides. In a multimode waveguide, the different spatial modes are characterised by different effective refractive indices and thus will resonate differently inside the crystal. Therefore, the interference pattern will be very different from the one described in Eq. (3.21) and it is usually very difficult to calculate losses with this technique in a multimode waveguide [71]. However, the measurement of losses in regimes where the waveguide is multimode is crucial, for example when characterising a device for second harmonic generation (see chapter 2). For this reason, during this work, we developed a method based on the Fabry-Pérot technique to estimate the losses in a multimode waveguide. This method is presented in chapter 6.

3.3.2. Waveguide-fibre coupling efficiency

Another important characteristic of an integrated optical device is how well it can be interfaced with existing standard telecommunication components and, in particular,

with standard fibre technology. For the case of integrated waveguides, it is important to assess the difference between the spatial modes propagating in the waveguide and the mode guided in a standard telecom fibre, the so-called waveguide-fibre *coupling efficiency*. This information is crucial for two reasons:

- it provides a measure of the coupling losses (see previous section) when matched to a reference fibre;
- it might be possible to improve it by modifying the waveguide geometry or the fabrication process, and thus it can help in the design of new, optimised devices.

Theoretically, the coupling efficiency is defined as

$$|\Theta|^2 = \left| \frac{\iint dx dy E_{wg} E_{fibre}^*}{\sqrt{\iint dx dy |E_{wg}|^2 \iint dx dy |E_{fibre}|^2}} \right|^2. \quad (3.25)$$

However, calculating this parameter from the definition is quite tricky. The resolution of the imaging systems and the background noise of the camera can bias the evaluation of the integrals in the previous expression. Therefore, a more practical way to estimate the coupling efficiency is to maximise the coupling between the output of a waveguide and a reference fibre and then measure the ratio of the powers before the fibre coupling and at the end of the fibre.

3.4. Periodic poling

In section 2.3.2, we introduced the concept of *quasi-phasematching*, i.e. the method of periodically inverting the $\chi^{(2)}$ nonlinearity of a crystal to satisfy the momentum conservation. The most common technique to achieve quasi-phasematching is to invert the *spontaneous polarisation* P_S of the crystal with the application of an external electric field [72].

The presence of a non-zero spontaneous polarisation P_S is a characteristic of all $\chi^{(2)}$ materials and it is related to their lack of inversion symmetry. By applying an electric field opposite to the spontaneous polarisation and greater than the *coercive field* E_c , one can invert the spontaneous polarisation and thus invert the symmetry of the cell. This has the effect of inverting the sign of the $\chi^{(2)}$ tensor as well.

The coercive field strength is material dependent and is⁵ ≈ 21 kV/mm in congruent LiNbO₃ [73] and 1.7 – 2.1 kV/mm in KTP [74].

First, the +Z-face of a LN sample or the -Z face of a bulk KTP sample are patterned with a photoresist structure reproducing the correct poling grating that needs to be produced. Subsequently, electrodes are deposited on both +Z and -Z faces. To pole the sample, a number electrical pulses with voltage above E_c and well defined width and

⁵The exact value of the coercive field strength is difficult to estimate since it depends on the temperature of the crystal, on the type of electrodes used to contact the crystal and on the type of the signal used to perform the measurement.

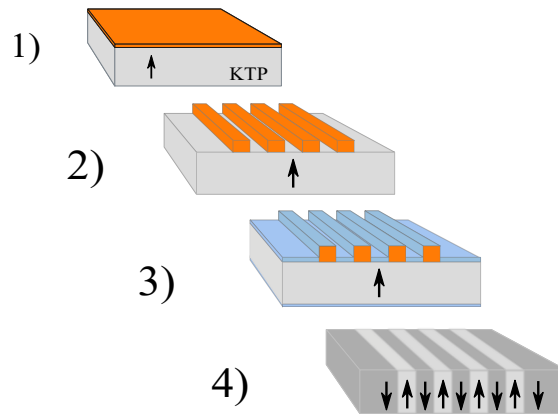


Figure 3.7. – Example of fabrication of periodically poled structures in KTP via electric field poling. Definition of the poling pattern via UV photolithography (steps 1 and 2). Deposition of the electrodes on the top and bottom face of the crystal (step 3). Poling of the sample and cleaning (step 4).

shape are applied to the electrodes. At first, small, localised regions (or *domains*) with inverted P_S are created under the patterned electrode. These are called *enucleation centres*. Then, if the pulse is sufficiently long, or during the following pulses, the inverted domains start to grow and extend towards the opposite electrode with a wedge like shape. When these domains reach the opposite electrode, they continue growing sideways. If too many pulses are applied, the inverted domains start to extend under the photoresist. This undesired effect is called *overpoling* and reduces the efficiency of the quasi phasematched process. A sketch of the processing steps required to electrically pole a bulk KTP crystal is shown in Figure 3.7 as an example.

Summary

In this chapter we reported the main optical and material properties of LN and KTP, the two crystals studied in this thesis. We described the processing steps necessary for the fabrication of titanium in-diffused LN waveguides, LNOI waveguides and rubidium exchanged KTP waveguides, and we provided the theoretical models used to predict their dispersion relations. Next, we discussed the basic parameters of interest when characterising a dielectric waveguide, such as the propagation losses and the mode size. Finally, a small section on the electric field poling explains the technique used in chapter 4 to achieve quasi phasematching.

Part II.

Design of nonlinear processes

Design of nonlinear processes in KTP

Contents

4.1	Frequency conversion IR→UV	61
4.2	Decorrelated PDC source at 1300nm . . .	76

As seen in section 3.2, KTP possess specific properties that make it an ideal technological platform for the realisation of waveguides for quantum optics experiments. In particular, the high resistance to photorefraction makes this crystal ideal for the realisation of efficient PDC

or SFG processes pumped at high intensities. Moreover, the modest refractive index sensitivity to temperature variations implies a high resilience to external temperature fluctuations. Finally, KTP possesses unique dispersion properties, that allow the realisation of decorrelated processes in the IR region. All these factors motivated us to try and establish an in-house fabrication process for the realisation of periodically poled, rubidium exchanged KTP (pp-Rb:KTP) waveguides.

In this chapter, we will present two different waveguide systems that we have fabricated in our cleanroom facility. The first waveguide is a pp-Rb:KTP waveguide for the conversion of light from the IR to the UV. The second system is a Rb:KTP waveguide for the generation of decorrelated PDC states at 1300nm.

4.1. Frequency conversion IR→UV

Almost all quantum communication schemes up to date revolve around the transmission of qubits (and qudits) via a fibre network and the storage and manipulation of such qudits in quantum memories. However, the transmission channels and the quantum memories usually operate over different wavelength regimes: the former provides minimal losses in the telecom C-band (1530-1570nm), while the latter are usually solid state or ion based memories that operate at wavelengths below 1000nm. Therefore, such networks require the realisation and optimisation of a quantum interface converting the *flying* qudits sent along the fibre network into *stationary* qudits stored in the quantum memory. For this reason, the investigation of systems offering noise-free frequency conversion between these two different regimes is paramount for the realisation of quantum networks in the real world.

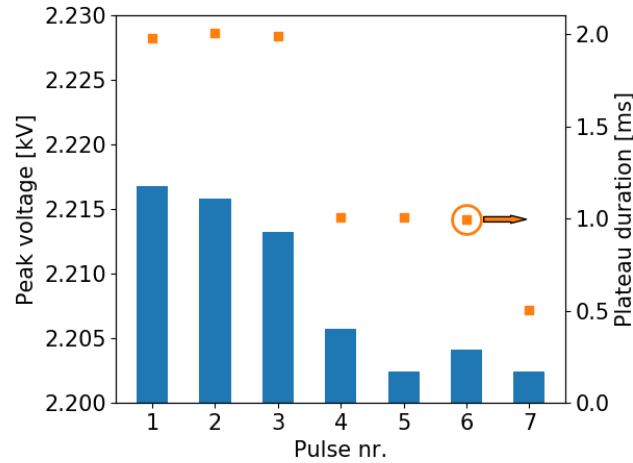


Figure 4.1. – Voltage and duration of the plateaus

Towards this aim, in this section we present a KTP-based frequency converter fabricated in our group, implementing a type 0 SFG process $1564\text{nm} + 532\text{nm} \rightarrow 397\text{nm}$ to interface the telecommunication C-band and one of the UV transition of the calcium ion $^{40}\text{Ca}^+$ memory [75–77].

4.1.1. Sample fabrication

The fabrication of the pp-Rb:KTP waveguides follows the steps detailed in sections 3.2 and 3.4. In particular, we first pole a virgin KTP sample and then realise the Rb exchanged waveguides in the poled crystal.

Periodic poling

Initially, a virgin Z-cut KTP sample with dimensions $6\text{mm} \times 8\text{mm} \times 1\text{mm}$ is patterned as shown in Figure 3.7. In particular, the poling pattern is realised on the -Z face, since the nucleation centres that start the poling process preferentially form on this face.

In the first photolithographic step, the edges of the sample are illuminated and developed to remove bulges in the photoresist occurring due uneven to surface tension at the edges of the sample. This is necessary to guarantee a good adhesion of the chromium mask used to transfer the poling pattern to the photoresist surface. In the second photolithographic step, standard contact vacuum photolithography is used to pattern onto the sample 8 different poling periods ranging from $3.52\mu\text{m}$ to $3.66\mu\text{m}$. For the patterning of the photoresist, we use the MA/BA Mask Aligner from Suss MicroTec GmbH.

Next, after sputtering a thin layer of Au/Pd as electrodes on both the +Z and -Z faces, the sample is placed in a sample holder and connected to the poling equipment, consisting of a pulse generator and a high-voltage amplifier. The sample holder connects

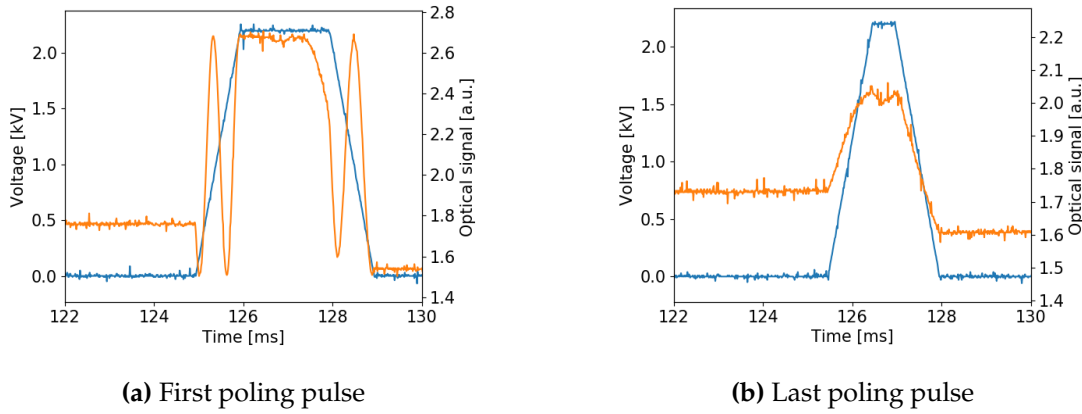


Figure 4.2. – First and last poling pulse.

the patterned face to the amplifier via an electrolyte solution, while the unpatterned face is connected via contact with a Au softpad. The use of an electrolyte solution is necessary to ensure constant contacting of the whole patterned surface, especially in the crevices presented by the small poling pattern. A sequence of 7 pulses is used to invert the spontaneous polarisation and pole the sample. The pulses have a trapezoidal shape, with a linear rise and fall edge lasting for 3ms and a plateau above the coercive field strength ($\approx 2.1\text{kV}$) lasting between 0.5 and 2ms. The plateau duration and voltage are shown in Figure 4.1. The poling dynamics are monitored via optical monitoring techniques [78]: a diagonally polarised light field from a HeNe laser is injected in the sample at 45° to the poling structures, then passes through a polariser oriented parallel to the input field and finally is detected by a photodiode. Due to the electrooptic effect, the polarisation of the injected light is rotated as the electric field changes during the rising and falling edge of the poling pulse. The resulting signal is detected as a sinusoid on the photodiode, as can be seen in Figure 4.2a. Since the direction of rotation induced by the external electric field is dependent on the orientation of the crystal cell, this technique can be used to discriminate when exactly half the crystal is poled: the polarisation rotation induced by the inverted domains will perfectly compensate the rotation induced by the non-inverted ones. Therefore, a flat signal on the photodiode, even in the presence of changing electric field, is the signature of a successful poling of the KTP crystal, as seen in Figure 4.2b.

After removal of the electrodes and surface cleaning, the quality of the poling can be assessed. In particular, the ammonia solution used for cleaning the sample acts as a soft etchant¹ and attacks the +Z and -Z faces with different etching rates. In this way, it is possible to visualise the poling pattern written in the bulk crystal and to monitor its quality, as seen in Figure 4.4. The analysis of the poled surface reveals that the duty

¹More aggressive solutions can be employed to achieve deeper selective etching for a better visualisation of the different domains orientations, at the cost of an increase in the waveguide losses.

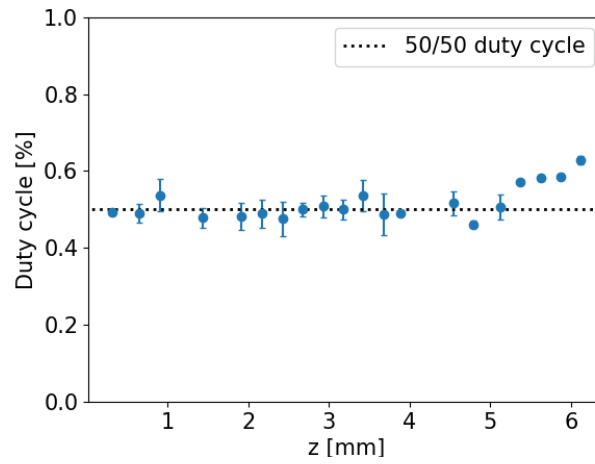


Figure 4.3. – Duty cycle

cycle of the poled sample is quite homogeneous over its entire length, thus indicating a good quality of the poling, as reported in Figure 4.3.

Waveguide fabrication

We start the fabrication of waveguides in PPKTP bulk crystal by evaporating a 100nm-thick titanium layer on the original -Z face of the KTP crystal. Subsequently, a photore-

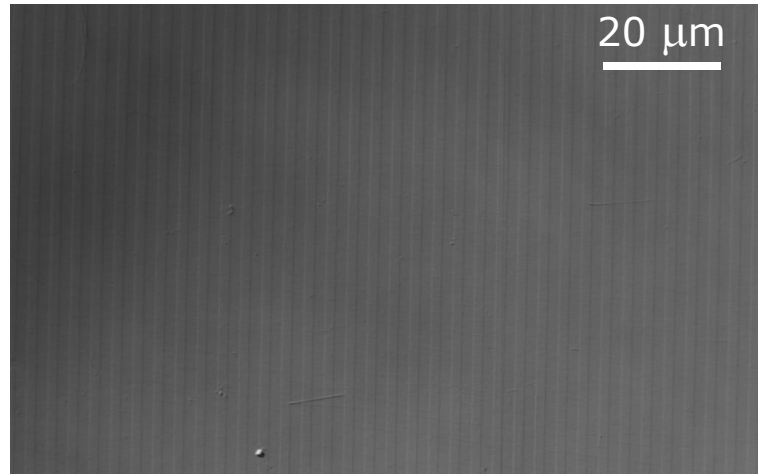


Figure 4.4. – Poling pattern on the virgin KTP.

sist layer (AZ4533 from *Microchemical*) is deposited on the Ti-layer and patterned with the waveguide structures. Analogous to the patterning of the poling periods, we first remove the bulges at the edge of the sample and subsequently pattern the slits corresponding to waveguide structures using the *vacuum contact* mode of the photolithography machine. The waveguide mask consists of a series of 8 groups of 12 waveguides with nominal widths varying from $1.5\mu\text{m}$ to $4.5\mu\text{m}$. However, due to inaccuracies during the photolithographic step, the sample produced for the frequency conversion process exhibits slits approximately $1.1\mu\text{m}$ wider than the mask. After photoresist development, the metallic layer is exposed through the slits in the photoresist structure. An EDTA-based etching solution is used to etch the exposed Ti surfaces. After photoresist removal and cleaning of the patterned surface, a protective Ti layer is deposited on the face opposite to the patterned one to ready the sample for Rb-exchange.

Rb-exchanged waveguides are realised by immersing the sample in a melt composed of RbNO_3 , $\text{Ba}(\text{NO}_3)_2$ and KNO_3 , heated at 330°C for 1h. The temperature is monitored via a thermocouple immersed in the melt. After the exchange, the sample is removed and cleaned. A final chemical-mechanical polishing step is required to prepare the input and output waveguide facets to optical quality.

After these two processing stages, the final length of the sample is equal to 6.4mm.

4.1.2. Linear characterisation

As a first assessment of the sample performance, the propagation losses and the mode sizes at 1550nm are characterised. Knowledge of the propagation losses allows one to evaluate the quality of the fabrication and to later compensate the measured conversion efficiencies for the losses of the input signal at 1550nm, while mode characterisation helps to design an optical setup that maximised the coupling efficiency of the IR field in the waveguide.

Propagation losses

As detailed in section 3.3.1, a common technique to estimate propagation losses in weakly guiding waveguides is via the Fabry-Pérot method. The application of this technique was pioneered for the estimation of losses in Ti:LN waveguides. In particular, in these waveguides the resonator is scanned by varying the temperature of the sample and monitoring the transmitted power at a fixed wavelength, supplied by a narrow CW laser. The change of the refractive index modifies the optical length of the cavity, therefore providing a mean for scanning its resonance condition.

However, this technique has proven to be inefficient in KTP. In fact, when performing the loss measurement via temperature tuning, we discover that often the overall transmitted power rapidly decreases over time, thus preventing a reliable estimation of the fringing contrast. This is probably due to different thermal behaviour between LN and KTP, in particular to the very low sensitivity of KTP refractive index to temperature changes.

For this reason, we establish a different procedure for scanning the Fabry-Pérot resonances to measure the losses in KTP waveguides. In particular, we find that loss measurement via wavelength tuning is a valid alternative that provides estimates with relatively low variance. In this technique, the cavity optical length is scanned by varying the frequency of a CW input laser, using the setup shown in Figure 4.5. The tunable IR laser used for the loss measurement is a EXFO TUNICS and the measurements are performed scanning the wavelength in a 300pm range around $\lambda_0=1550\text{nm}$ in steps of 1pm. This small resolution is necessary since the cavity free spectral range is in the order of

$$\Delta\lambda_{FSR} = \frac{\lambda_0^2}{2n_g L} \approx 60\text{pm} \quad (4.1)$$

and thus a wavelength resolution below 10pm is necessary to correctly sample the cavity frequency response. The transmitted power is recorded as a function of the wavelength and the fringing contrast is used to calculate the losses of the waveguides. The losses of all the waveguides in the sample under investigation are presented in Figure 4.6. In particular, the IR losses of the waveguide used in the SFG experiments are estimated to be 2.3 ± 0.1 dB/cm.

Mode measurement

The measurement of the mode profiles is performed launching the amplified spontaneous emission of an erbium-doped fibre amplifier (EDFA) into the waveguides. A polariser before the waveguides is used to select the polarisation of the injected light. The mode exiting the waveguide is imaged onto a *Xenics Xeva640* IR camera using a 100x microscope objective.

The distribution of the modes full width at half maximum (FWHM) along the horizontal (x) and vertical (y) direction plotted against the nominal waveguide width is shown in Figure 4.7. One can note that the FWHM along x follows almost linearly the waveguide width as expected, since the confinement along x is due to the sharp refractive index transition from Rb-exchanged KTP to pure KTP and the width of the confining region is determined by the dimension of the slit on the mask. On the other hand, the FWHM along y decreases for increasing waveguide widths. This can be related to two main effects: firstly, due to the geometry of the system, the field distribution is not separable along x and y and therefore the depth of the mode is related to its width; secondly, later investigations [68] will show that, surprisingly, the waveguide diffusion depths depend on their widths and, in particular, they tend to decrease for increasing waveguide width. This explains the trend observed in the mode measurement. The IR modes of the waveguide used for the SFG experiment are shown in Figure 4.8. The mode profile along x exhibits an annular structure and some fringes on its left side. This might be due to small damage at the output facet of the waveguide. From these images, assuming a flat phase front exiting the sample facet, using Eq. (3.25) it is possible to estimate the coupling efficiency with standard SMF28 telecom fibre (having mode field diameter² $\text{MDF} = 10.8\mu\text{m}$) and the maximum theoretical coupling efficiency with

²The mode field diameter MDF of a light field corresponds to the $1/e^2$ diameter of its intensity profile

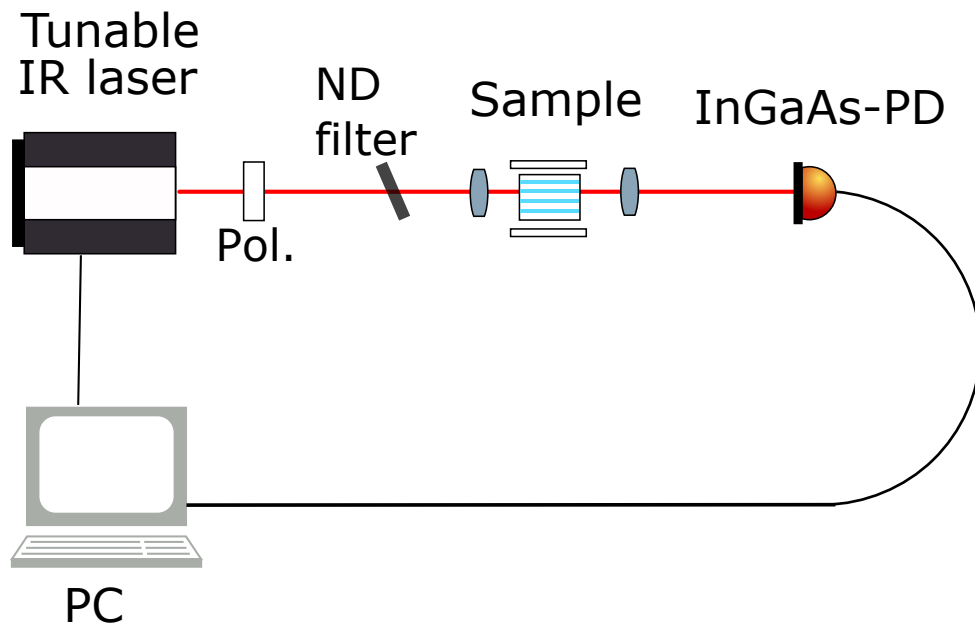


Figure 4.5. – Setup for the measurement of propagation losses in KTP waveguides via wavelength tuning. The output of a tunable laser (EXFO Tunics) is launched into the investigated waveguide with a C-coated aspheric lens (8mm-long focal length) with a well-defined polarisation, set via a polariser in front of the waveguide. The light exiting the waveguide is collected with another C-coated aspheric lens and collimated on a InGaAs photodiode. The photodiode readout is measured with an amperemeter and recorded on a computer, while the wavelength of the laser is swept to characterise the frequency response of the sample. A neutral density filter placed before the waveguide is used to reduce the impact of possible cavity resonances between the uncoated waveguide facet and other optical elements.

a properly tailored Gaussian mode. The estimated coupling efficiencies are reported in table 4.1.

4.1.3. Frequency conversion measurement

The setup for the characterisation of the sample phase matching and for the measurement of the frequency conversion performance is shown in Figure 4.9.

The IR radiation is provided by a fibre-coupled EXFO TUNICS laser, tunable from

(equivalent to the $1/e$ diameter of the field profile).

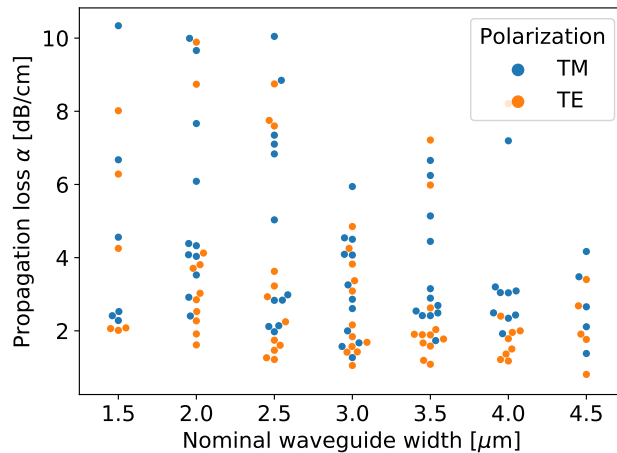


Figure 4.6. – Loss distribution for the sample under investigation. The waveguide used for the frequency conversion experiment has a nominal width of $1.5\mu\text{m}$, corresponding to $\alpha = 2.3 \pm 0.14$ dB/cm. The datapoints are scattered around their nominal waveguide width for better visualisation.

	TE mode	TM mode
Coupling to SMF28	67.0%	75.0%
Max coupling	87.8%	89.0%
	MFD= $5.98\mu\text{m}$	MFD= $5.08\mu\text{m}$

Table 4.1. – Estimated coupling efficiency of the measured IR modes with an SMF28 and with a Gaussian field providing optimal coupling.

1480nm to 1660nm, while the green radiation is provided by a Coherent Verdi V5. Both lasers are computer controlled, allowing an automated variation of the pump and signal power, as well as automatic tuning of the IR wavelength. For a finer power and polarisation control, a sequence of half-waveplate, polarisation beam splitter (PBS) and half-waveplate is used at the output of the Verdi. Similarly, a combination of a fibre polarisation controller, a PBS and a half-waveplate are used in the IR arm of the setup. The two beams are overlapped over a shortpass dichroic mirror (Thorlabs DMSP1180) and injected in the sample with a C-coated 8mm-long aspheric lens (Thorlabs C240TME-C). Before merging the green and the IR, a telescope is necessary to modify the green beam diameter to improve the coupling to the waveguide.

The sample is placed on a 5mm-long, self-built, temperature-stabilised stage. The temperature controller is a *profile TED420* that stabilises the temperature to $\pm 10\text{mK}$.

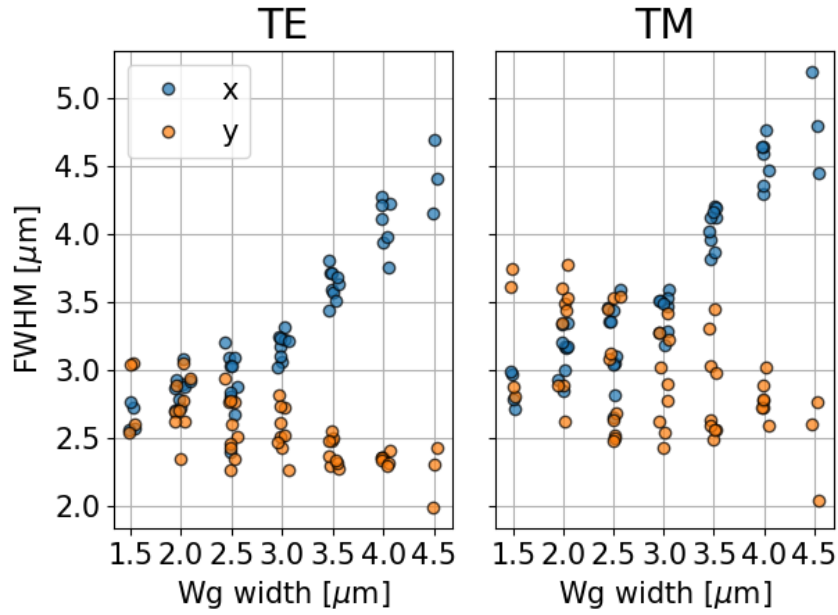


Figure 4.7. – Intensity FWHM (full width at half maximum) of the spatial modes of the waveguides in the sample, for waveguide having different nominal widths. The datapoints are scattered around their nominal waveguide width for better visualisation.

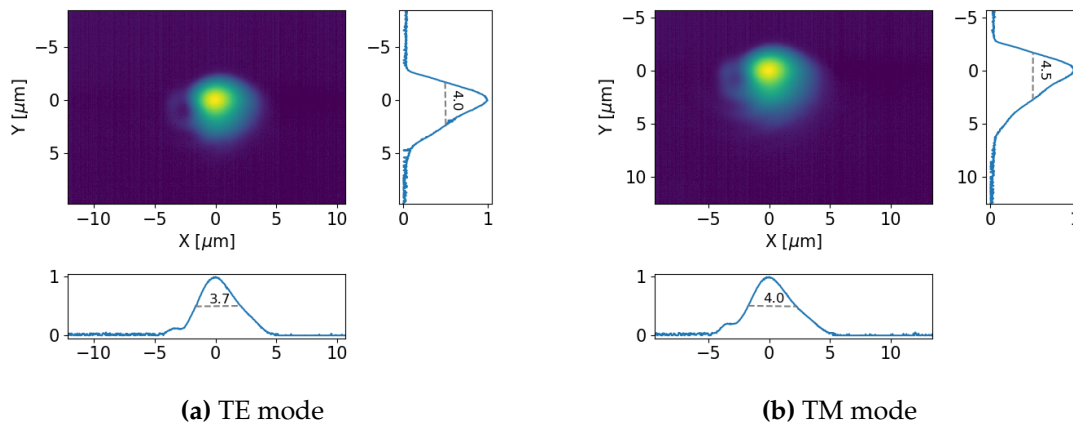


Figure 4.8. – TE and TM modes of the waveguide used for the SFG experiment.

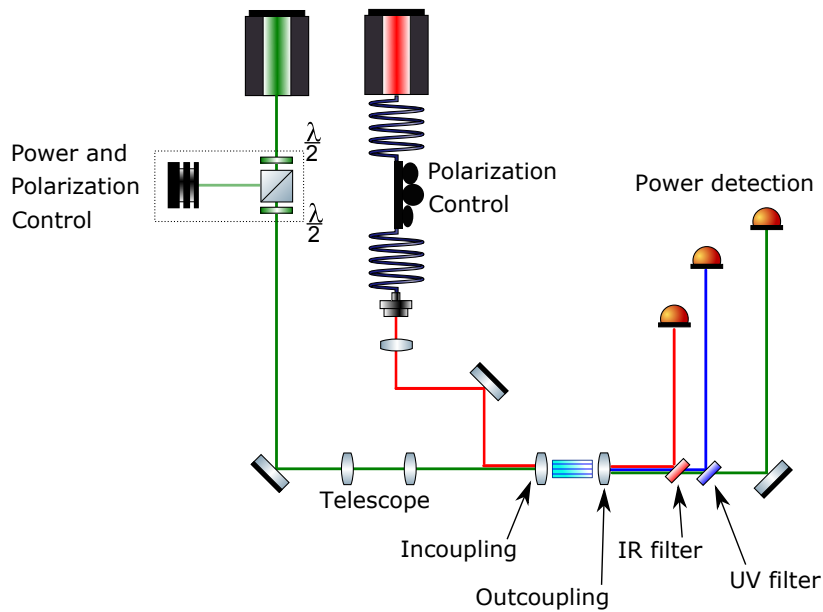


Figure 4.9. – Measurement setup for the nonlinear characterisation of the sample and for the measurement of the conversion efficiency. The detailed description of the employed components is reported in the main text.

For most of the experiments, the temperature of the sample is kept stable at 25°C. The input fields and the upconverted UV light are collected by an A-coated 8mm-long aspheric lens (*Thorlabs A240TME-A*). The transmission of the outcoupling lens is measured to be $96.1 \pm 7\%$ for the UV, $99.1 \pm 7\%$ for the green and $64.3 \pm 7\%$ for the IR. After the outcoupling lens, a short pass dichroic mirror (*Thorlabs DMSP650*) is used to separate the IR radiation from the other two fields, while the UV is separated from the green using a dichroic mirror with edge at 427nm (*Semrock LaserMUX427*). The power of the three fields is recorded simultaneously using three Thorlabs powermeter heads, namely *S121C* for the green, *S132C* for the IR and *S130VC* for the UV field.

After analysing the phase matching spectra of all the waveguides present on the sample, we focus our attention to the one that exhibited efficient phase matching close to the target process. This waveguide has a nominal width of $1.5\mu\text{m}$, a width after fabrication³ of $2.6\mu\text{m}$ and a poling period $\Lambda = 3.62\mu\text{m}$. In this waveguide, the phase matching

³Due to overdeveloping during the photolithography of the sample, the waveguides are roughly $1\mu\text{m}$ wider than the nominal width of the employed mask.

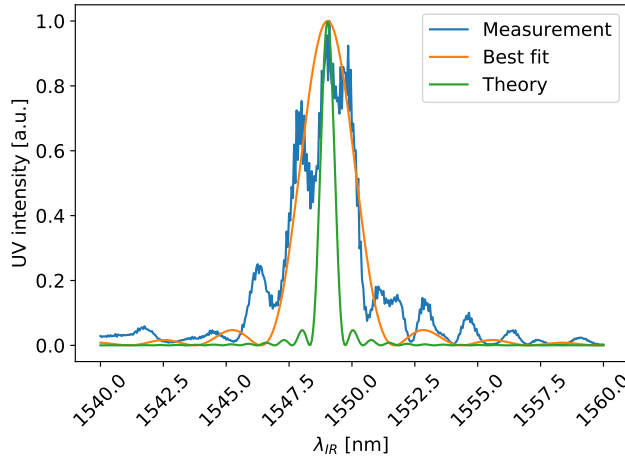


Figure 4.10. – Measured and simulated phase matching spectra of the SFG signal. The blue line represent the measured data. The orange line is the best fit of the data, yielding an effective length of 1.7mm. The green line represent the theoretically expected spectrum, considering the full length of the poling region.

between the fundamental IR, green and UV modes occurs at $\lambda_{IR} = 1549.05\mu\text{m}$. The respective field distributions are shown in Figure 4.11.

The measured phase matching spectrum of this waveguide is shown in Figure 4.10, along with the predicted spectrum for the interaction length $L = 6.4\text{mm}$. One can note that the predicted spectrum is much narrower than the measured one. Fitting the phase matching with

$$I(\lambda_{IR}) = \text{sinc} \left(\frac{\Delta\beta(\lambda_{IR}, \lambda_{green})L_{eff}}{2} \right)^2$$

provides an effective length $L_{eff} = 1.7\text{mm}$, resulting in a spectral bandwidth almost four times wider than the theoretical prediction. We attribute the increased bandwidth to fabrication imperfections that reduced the overall effective length of the poled region. This assumption is consistent with the shape of the measured phase matching: its asymmetry and the prominent side lobes are tell-tale signs that the waveguide poling and/or dispersion properties vary along the sample. In addition to this, later studies will reveal that the fabrication procedure adopted for the realisation of this waveguide, namely poling the sample before waveguide fabrication, can lead chemical poling of the waveguide, resulting in the partial erasing of the poling profile, thereby explaining the increased bandwidth and low efficiency [79].

After the alignment of the IR and the green fields into the waveguide, we quantify the conversion efficiency of the system as a function of the green pump power, using the following protocol:

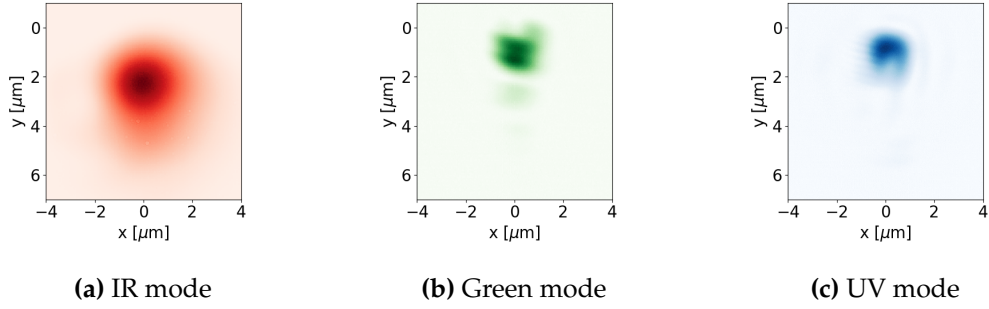


Figure 4.11. – Spatial modes of the fields involved in the three wave mixing process.

- set the pump power to P_{pump} ;
- optimise the coupling of the green and IR field to the waveguide by maximising the converted UV power;
- scan the IR wavelength λ_{IR} around the phase matching peak with a 1pm resolution to retrieve the wavelength of the maximum conversion efficiency;
- measure the converted UV light with four different IR input powers in the range between 1 and 8 mW.

In this way, for each pump power P_{pump} , we are able to retrieve the conversion efficiency

$$\eta = \frac{P_{UV}}{P_{IR}}$$

using a linear regression on the measured datapoints, after compensating for the propagation losses and the transmission of the setup. Estimating the losses for the green and UV fields is a hard task, because the waveguide is highly multimode at these frequencies⁴. An upper bound for the losses at smaller wavelengths has been inferred from the measured insertion losses: the losses for the green field are below 5.1 ± 0.8 dB/cm, while the losses of the UV field are below 6.6 ± 0.5 dB/cm.

We characterise the conversion efficiency as a function of P_{pump} for pump powers from 4mW to 324mW. The results are shown in Figure 4.12: the datapoints represent the measured conversion efficiency, calculated taking into account the transmission losses in the optical setup and the estimated propagation losses of the three fields, while the

⁴Simulations showed that our waveguide supports around five TM modes at 532nm and more than twenty at 397nm.

4.1. Frequency conversion IR→UV

dashed line is the best fit of the theoretical conversion efficiency curve (2.26)

$$\eta = \frac{P_{UV}}{P_{IR}} = \sin\left(\sqrt{\eta_{norm} P_{pump} L_{eff}}\right)^2$$

$$\approx \eta_{norm} P_{pump} L_{eff}^2,$$

where the approximation holds in the low conversion efficiency regime. From the linear fit, we estimate a normalised conversion efficiency $\eta_{norm}=122\pm 3\%/W\text{ cm}^2$ assuming a $L_{eff}=1.7\text{mm}$, as retrieved from the phase matching bandwidth. Due to the overall low conversion efficiency of the system, it was impossible to estimate the conversion efficiency by measuring the depletion of the IR signal.

The theoretical normalised conversion efficiency can be estimated using Eq. (2.32)

$$\eta_{norm} = \frac{8\pi^2 d_{eff}^2}{n_1 n_2 n_3 c \epsilon_0 \lambda_1 \lambda_3} |\theta^2|,$$

where $d_{eff} = \frac{2}{\pi} d_{33} = 10.76\text{ pm/V}$ is the effective nonlinearity for a QPM type 0 process, $n_{1/2/3}$ are the refractive indices at 397nm, 532nm and 1564nm, $\lambda_{1/3}$ are equal to 397nm and 1564nm, respectively, and the overlap integral $\theta \approx 140000\text{m}^{-1}$ can be evaluated from numerical simulations. With these numbers, the theoretical conversion efficiency is $\eta_{norm,theo} \approx 160 \pm 40\%W^{-1}\text{ cm}^{-2}$, where the error on the theoretical estimate was calculated assuming conservative estimates for the uncertainties of θ and d of 5% and 10%, respectively. These estimates are justified since it is hard to exactly evaluate the field overlap in the real waveguide, mainly due to uncertainties of the relative position of the modes, noise in the camera images and imperfect theoretical waveguide models, and because the reported value for the nonlinearity d varies by roughly 10% in the literature.

The measured normalised conversion efficiency is close to the theoretical expectations, when the effective length of the sample L_{eff} is considered. This indicates that the nonlinear properties of the KTP are preserved during the fabrication process. However, the reduced effective length and the shape of the phase matching suggest that the fabrication needs to be improved to produce more homogeneous waveguides to increase the conversion efficiency.

Figure 4.12 shows that the conversion efficiency measurements, despite following a roughly linear trend, are quite noisy and do not increase monotonically. We attribute this behaviour to the variation of coupling condition of the input fields at different pump powers. In fact, even though KTP waveguides are resistant to photorefractive damage, the high modal confinement of the pump field can locally heat up the waveguide, thus causing local thermal effects like thermal expansion or variation of the dispersion conditions. The effect of increasing pump powers on the overall conversion process is characterised by measuring the shift of the phase matching wavelength as a function of the pump power. The measurements, shown in Figure 4.13, reveal that the pump power induces a wavelength shift equal to $\Delta\lambda_{pm}/\Delta P_{pump}=3.2\pm 0.1\text{ pm/mW}$.

The nonlinear characterisation is completed with the characterisation of the phase matching wavelength dependence on the temperature of the sample. To this aim,

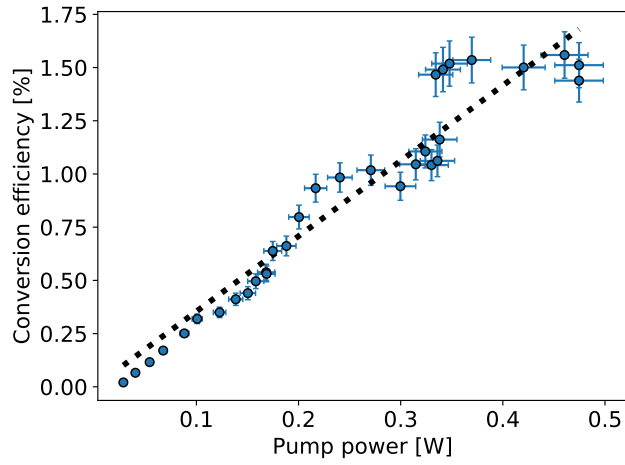


Figure 4.12. – Measured conversion efficiency (corrected for the estimated propagation losses) as a function of the pump power P_{pump} . The dashed line represents the best fit using Eq. (2.26), corresponding to a normalised conversion efficiency is $\eta_{norm} = 122\%W^{-1}cm^{-2}$, assuming a 1.7mm effective length. The data errorbars are calculated from the 5% uncertainty in the power reading of the powermeters.

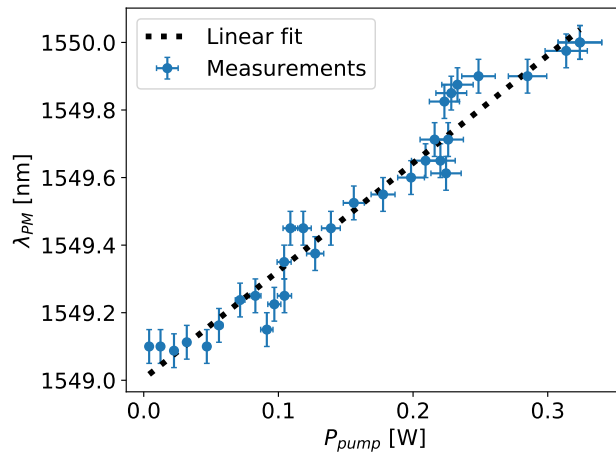


Figure 4.13. – Relation between the phase matching wavelength λ_{PM} and the pump power P_{pump} for the SFG process.

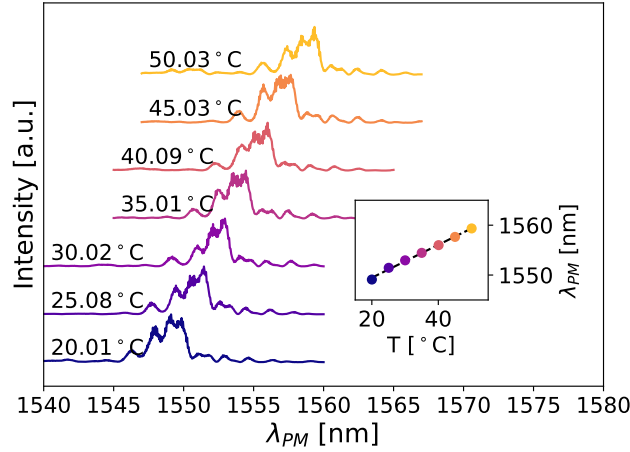


Figure 4.14. – Variation of the phase matching spectrum as a function of the sample temperature. In the main plot, the phase matching spectra corresponding to different temperatures of the sample are plotted. The shape of the spectrum is basically preserved at all temperature and the different spectra are simply shifted towards longer wavelengths at higher temperature. The inset shows the linear dependence between the phase matching wavelength and the sample temperature.

the phase matching spectrum is measured for sample temperatures between 20°C and 50°C at low pump power. The results of these measurement are shown in Figure 4.14. The phase matching wavelength λ_{PM} depends linearly on the sample temperature with a slope equal to $\Delta\lambda_{pm}/\Delta T = 0.33 \pm 0.01$ nm/K, thus showing a limited tunability, as expected. This characterisation shows that it is impossible to reach the desired process (1564nm + 532nm → 397nm) around room temperature with the current sample. However, from the measured phase matching wavelength and the bulk dispersion curves for KTP, we can predict that a poling period of $\Lambda = 3.67$ μm should bring the process closer to the desired transition without the need for temperature tuning. Finally, comparing the measured phase matching shift for different pump powers and for different sample temperatures, we can infer that the pump field locally heats the waveguide according to $\Delta T/\Delta P_{pump} = 9.7 \pm 0.4$ K/W.

This nonlinear characterisation provides values of normalised conversion efficiency η_{norm} , $\Delta\lambda_{pm}/\Delta P_{pump}$, $\Delta\lambda_{pm}/\Delta T$ and $\Delta T/\Delta P_{pump}$ close to the values reported for a very similar process in a commercial sample [80], revealing that the properties of our waveguides are close to those that are commercially available. However, the low efficiency η of the sample proved to be a major limitation and improvement in the sample fabrication is still necessary to use this system as a quantum frequency converter.

4.2. Decorrelated PDC source at 1300nm

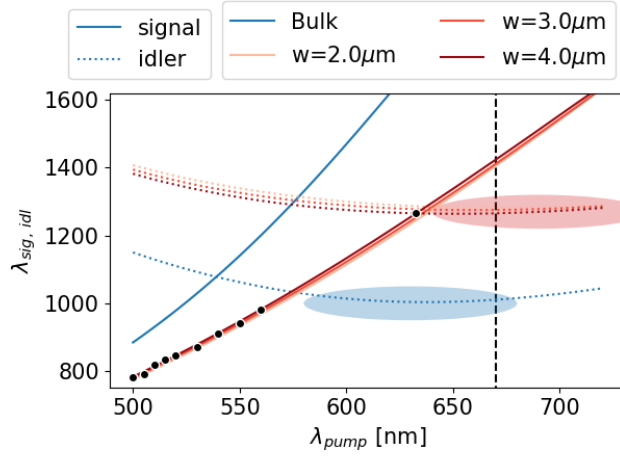
One of the main benefits of employing KTP as a nonlinear material is the possibility of realising decorrelated, degenerate sources in the telecom range, a very interesting resource for quantum optics applications [23]. However, in current waveguide technology, such a process is possible only under quasi-phase matching conditions. Unfortunately, the erasing of the poling profile occurring during the waveguide fabrication [79] is currently preventing us from fabricating samples implementing this processes. Therefore, while researching new fabrication processes that would prevent this effect, we investigate the realisation of decorrelated birefringent processes in unpoled Rb:KTP waveguides.

As a first step, we calculate the effective refractive index n_{eff} of our waveguides by implementing in FemSIM [81] the model presented in section 3.2.2. The model requires two geometric parameters, namely the waveguide depth and its width; the waveguide width is varied between 1.5 and 4.5 μm , according to the structures available on the lithography mask; the waveguide depth is determined to be between 8 μm and 12 μm via EDX measurements performed by our colleagues on an analogous sample [68], with narrower waveguides having deeper diffusion depth, as mentioned in section 4.1.2

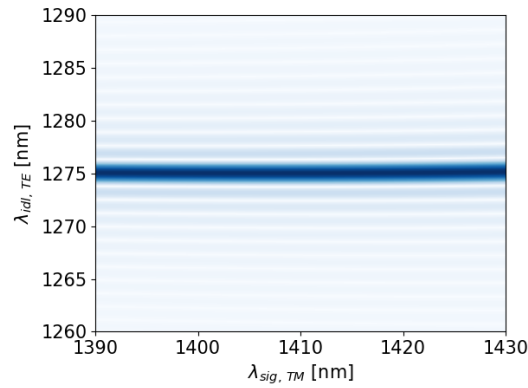
The birefringent phase matching conditions for a type II PDC process ($o \rightarrow eo$) pumped between 500nm and 700nm are outlined in Figure 4.15a, for both cases of bulk system and our waveguides. One can note that the guiding provided by the structure shifts the phase matched process to longer wavelengths with respect to the bulk crystal. Moreover, variations of the waveguide geometry only have a minor impact on the phase matching conditions, as wider waveguides shift the phase matching to slightly shorter wavelengths.

The analysis of the phase matching curves in Figure 4.15a reveals that the dispersion relations of KTP allow the realisation of a birefringent aGVM process, indicated by a region where the signal wavelength varies linearly while the idler wavelength is constant, as the pump wavelength is changed. In bulk KTP, such aGVM condition is met for signal and idler wavelengths around 1600nm and 1000nm, respectively, as shown by the blue region highlighted in the Figure.

Interestingly, the variation of the dispersion induced by the waveguide has the effect of shifting the pair of group velocity-matched signal and idler wavelengths to 1270nm (red shaded region in the Figure) and 1400nm. This combination is much more appealing for the realisation of a PDC source, since it corresponds to the generation of photon pairs in the telecom O- and E- bands. One important characteristic of an aGVM PDC source is the possibility of generating heralded pure single photon states in arbitrary temporal modes, i.e. transferring the spectrum of the pump to the signal photons without affecting the spectrum of the idler, as shown by the joint spectral intensity (JSI) presented in Figure 4.16. The Figure shows the JSI of the PDC process pumped with pulses having a first order Hermite-Gaussian spectrum: the spectrum of the signal photon, obtained by tracing out the JSI with respect to the idler, is approximately a first order Hermite-Gaussian mode as well, while the idler photon spectrum is independent from the shape of the pump.



(a) Birefringent phase matching conditions for bulk KTP and for waveguides with different widths. The shaded areas mark the regions of aGVM process in bulk and waveguide samples.



(b) Phase matching spectrum for the birefringent, aGVM PDC process pumped at 670nm for a 3 μ m-wide waveguide.

Figure 4.15. – Study of the birefringent phase matching conditions in KTP bulk and waveguides.

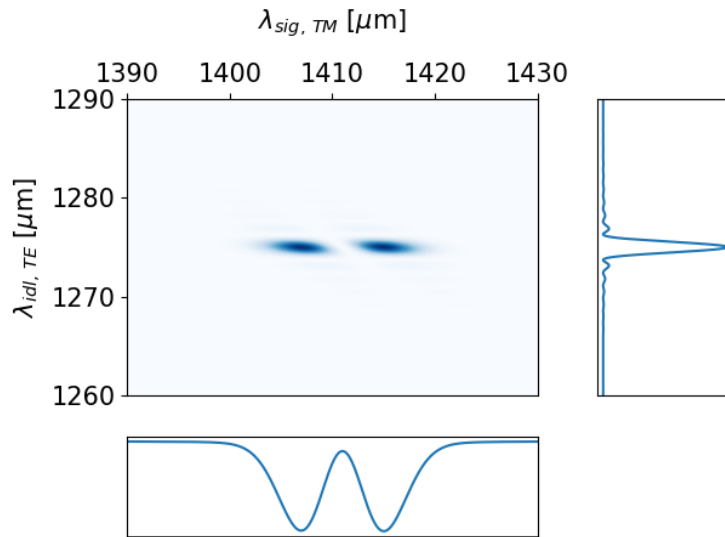


Figure 4.16. – JSI of the aGVM PDC process in a 16mm-long Rb:KTP waveguide, pumped with a first-order Hermite-Gaussian pump having a 1.5nm bandwidth. The lateral plots show the marginal spectra of the signal (bottom) and idler (right) photons. The number of Schmidt modes this state is ≈ 1.18 , since the side lobes of the phase matching spectrum increase the correlations between signal and idler. However, filtering the sidelobes with a narrow bandpass filter on the idler photons can reduce the number of Schmidt modes to ≈ 1.05 .

Motivated by these theoretical considerations, we fabricate an unpoled Rb:KTP waveguide with a length of 16 mm following the process outlined in section 4.1.1. In this new sample, the propagation losses at 1550nm, shown in Figure 4.17, are lower than the ones reported for the previous sample. Fewer number of processing steps required to fabricate this sample reduce the inevitable waveguide damage caused by the handling of the sample during the fabrication. The characterisation of the FWHM of the waveguides in the sample is shown in Figure 4.18. The modes of the two samples are quite comparable. In particular, in this sample the modes of narrow waveguides are much deeper than those of wider ones, as $1.5\mu\text{m}$ waveguides were shown to have much deeper diffusion profiles [68].

The phase matching properties of the sample are characterised by our colleague V. Ansari via PDC and SHG measurements. In particular, the SHG measurement is performed by injecting a broadband pulse from an OPO into the waveguide and recording the SH spectrum, while the PDC measurement is performed by injecting frequency-doubled OPO pulses and measuring the PDC signal photons on a single-photon-sensitive spectrometer (*Andor*), as detailed in [32]. In this way, we are able to retrieve the phase

4.2. Decorrelated PDC source at 1300nm

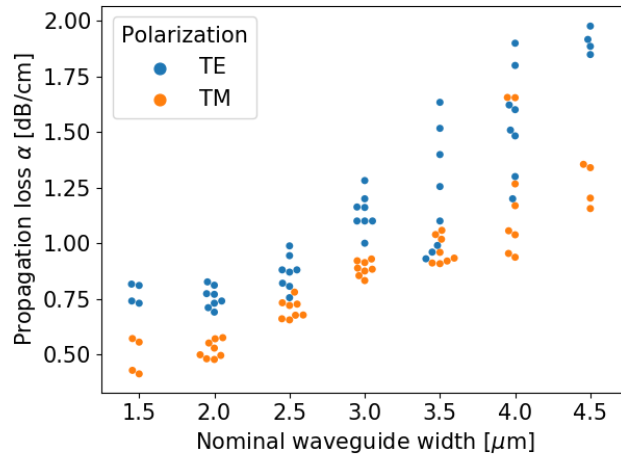


Figure 4.17. – Propagation losses of the unpoled Rb:KTP sample.

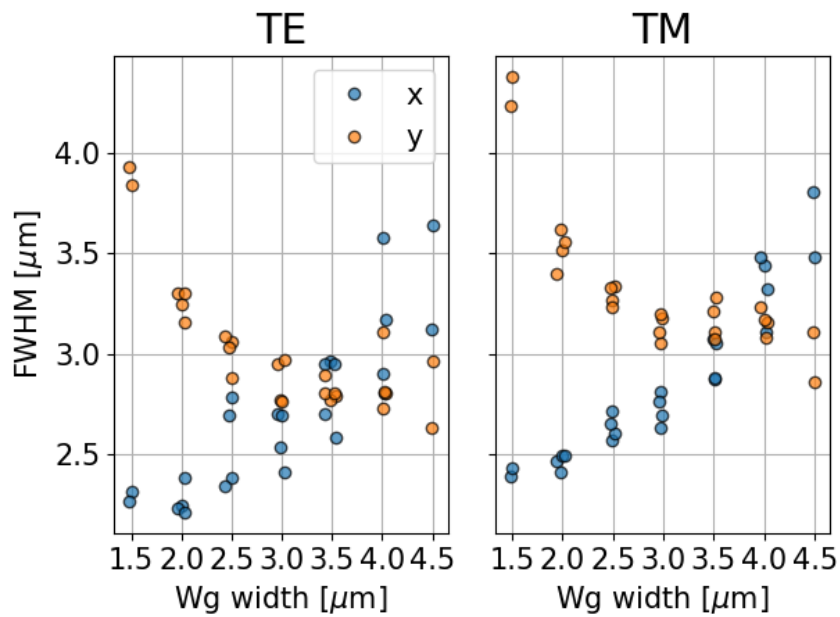


Figure 4.18. – Intensity FWHM (full width at half maximum) of the spatial modes of the waveguides in the sample, for waveguide having different nominal widths. The datapoints are scattered around their nominal waveguide width for better visualisation

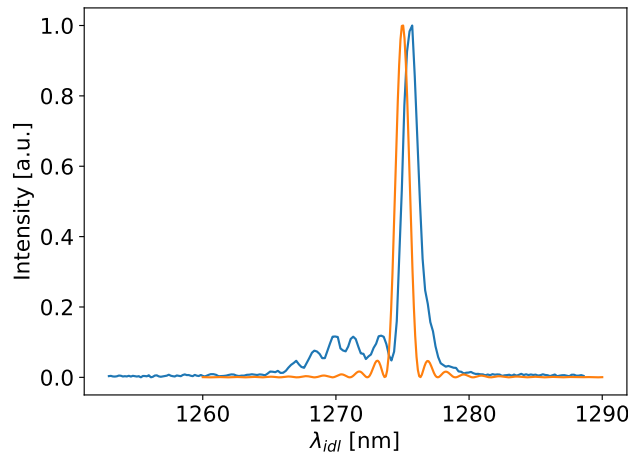


Figure 4.19. – Measured spectrum of the idler photon, as compared to the theoretical prediction. The asymmetric side lobes indicate the presence of variations in the dispersion properties of the waveguide along the propagation axis.

matching wavelengths for the PDC and SHG processes as a function of the pump wavelength and experimentally verify the validity of the model used to simulate the waveguides properties. Subsequent measurements realised by V. Ansari and E. Roccia verify the possibility of realising a source of pure heralded single photons with programmable temporal modes [32].

In the context of this thesis, the most interesting measurement performed is the characterisation of the idler photon spectrum. In Figure 4.19, the idler photon spectrum, as measured via a time of flight spectrometer [82] is compared to the theoretically expected one. Apart from the small offset of the peak wavelength - which is due to small inaccuracies of the theoretical model, the asymmetry of the measured spectrum and the presence of a pronounced side-lobe towards shorter wavelengths cannot be predicted by the theory presented in section 2.2. These features are characteristics of phase matching spectra of crystals whose dispersion properties change along the propagation axis of the investigated process [83]. This is certainly due to errors in the waveguides itself because there are no other sources, such as poling, where this effect could arise.

The realisation that fabrication errors can heavily influence the nonlinear performance of our devices motivates us to develop a comprehensive model relating the properties of the fabrication process to the nonlinear performance of a device, as described in detail in chapter 5.

Summary

In this chapter we reported the fabrication and characterisation of two rubidium-exchanged KTP waveguide systems for quantum optics experiments. The first waveguide was designed as a quantum interface between telecom photons and a memory operating in the UV range. The classical characterisation of the first prototype showed promising result. However, improvement in the fabrication steps are required increase its efficiency. The second waveguide was designed as a decorrelated type II PDC source. Characterisation of this source verified the validity of our theoretical model for this class of waveguides. Moreover, we verified that this source allows the heralding of pure single photons with arbitrary pulse shapes. The finding reported in this chapter constitute important steps towards establishing an in-house fabrication and engineering of rubidium-exchanged KTP waveguides.

Effect of inhomogeneities in nonlinear systems

Contents

5.1	Qualitative model	84
5.2	Phase matching in inhomogeneous waveguides.	90
5.3	Reconstruction of sample inhomogeneity	105
5.4	Correction of fabrication imperfection	111
5.5	General theory of waveguide inhomogeneities	115

The realisation of nonlinear processes with ideal phase matching properties is paramount for quantum optics experiments. However, small imperfections during the fabrication and/or operation of a nonlinear waveguide degrade the final performance of the device, as briefly discussed at the end of previous chapter. Of particular interest here are all the factors that cause a variation (temporary or permanent) of the refractive index properties along the waveguide: for example, the finite resolution of the photolithographic system leads to small errors in the patterning of the waveguide structures,

or uneven temperature distribution of the sample during operation can lead to an inhomogeneous refractive index distribution along the waveguide. These inhomogeneities result in variable momentum mismatch conditions along the waveguide and thus will degrade the phase matching spectrum.

In this chapter, we will present a framework to analyse the impact of such inhomogeneities and to include them in the design of nonlinear waveguides. In particular, we will describe two different models: the first one is a qualitative model that gives simple rules to safely design waveguide systems taking into account the effect of fabrication errors; the second one is a quantitative model that helps predict the effect of inhomogeneities on a specific application. Using this second framework, we studied the effects of different types of noise spectra in Ti:LiNbO₃ waveguides and characterised our fabrication process. Despite discovering the presence of fabrication imperfection in KTP waveguides, we used Ti:LiNbO₃ waveguides as case studies due to the availability of more precise models and a longer tradition in fabricating and characterising these systems. At the end of the chapter, a general framework is provided, showing that the impact of imperfections in a nonlinear device can be treated independently from the technological platform itself.

Most of the material presented in this chapter has been published in publication I

and appears as a preprint in publications II and III. The author of this thesis is the main contributor in all three publications.

5.1. Qualitative model

In this section, we derive a simple model describing the effect of inhomogeneities on the efficiency of a nonlinear process, assuming that the inhomogeneity is constant along the sample length. In other words, we postulate that the variation of refractive index of the waveguide with respect to the ideal case is constant along the waveguide. Under this assumption, the effective refractive index n_{eff} is constant and the waveguide is said to be *homogeneous*. This assumption simplifies the treatment of phase matching in waveguide structures and in the rest of this section we will consider this scenario. The analysis of spatially-varying $n_{eff}(z)$ will be analysed in detail in section 5.2.

As seen in chapter 2.2.1, the phase matching spectrum $\phi(\Delta\beta)$ of the process is given by [25]

$$\phi(\Delta\beta) \propto \frac{1}{L} \int_0^L e^{i\Delta\beta z} dz \Rightarrow \phi(\Delta\beta) \propto \text{sinc}\left(\frac{\Delta\beta L}{2}\right) e^{i\frac{\Delta\beta L}{2}}, \quad (5.1)$$

where L is the crystal length and

$$\Delta\beta = 2\pi \left(\frac{n_{eff,3}(\lambda_3)}{\lambda_3} - \frac{n_{eff,2}(\lambda_2)}{\lambda_2} - \frac{n_{eff,1}(\lambda_1)}{\lambda_1} - \frac{1}{\Lambda} \right)$$

Following the approach presented in [84], we consider a homogeneous waveguide designed for a specific TWM process. For simplicity, we analyse the influence of a single parameter having a nominal value f_0 . Such a parameter can represent, for example, the waveguide width, depth, exchange temperature, operation temperature etc. Due to imperfections, the nominal parameter f_{nomin} can be off from the designed one by $\delta f = |f_{nomin} - f_0|$. The deviation δf will modify the n_{eff} of the waveguide, which in turn has an impact on $\Delta\beta$. For this reason, a deviation δf from the design parameter will shift the position of the phase matching curve $\phi(\Delta\beta)$ and reduce the overall efficiency of the process, as shown in Figure 5.1.

It is thus fundamental to provide an upper bound for δf , such that the efficiency of the designed process does not fall below a well defined threshold. Therefore, we can bound $|\delta f| \leq \delta f_{max}$ such that the efficiency of the target process remains greater than 50% of the ideal value:

$$\text{sinc} \frac{\Delta\beta(\delta f) L}{2} \geq 0.5 \Rightarrow \left| \frac{\Delta\beta(\delta f) L}{2} \right| \leq \Gamma, \quad (5.2)$$

where $\Gamma \approx 1.39$ is the half-width at half maximum of $\text{sinc}(x)^2$. Expanding $\Delta\beta$ in a Taylor series

$$\Delta\beta = \Delta\beta(f_0) + \partial_f \Delta\beta|_{f_0} \cdot \delta f + o(\delta f^2),$$

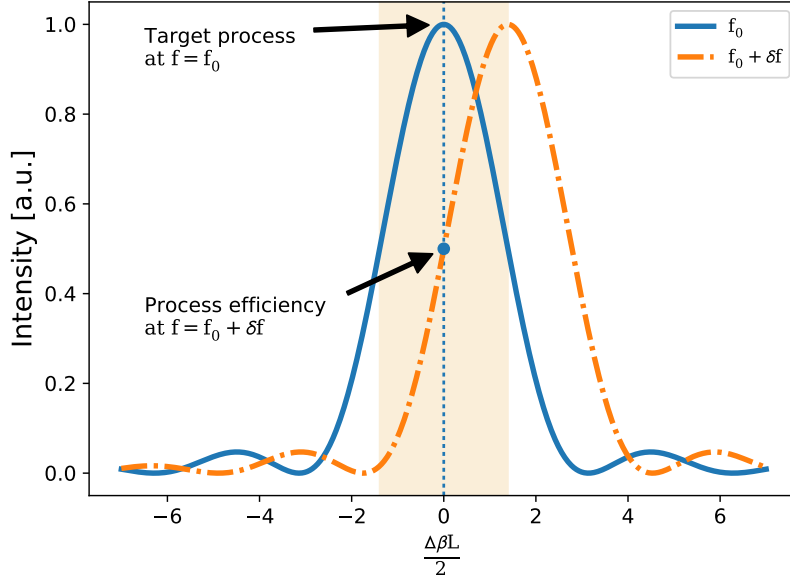


Figure 5.1. – Illustration of the effect on the phase matching spectrum of a uniform variation δf of the waveguide fabrication parameter f . The solid blue line shows the intensity of a desired nonlinear process for a waveguide with fabrication parameter f_0 , plotted against the dimensionless parameter $\frac{\Delta\beta L}{2}$. A variation δf of the fabrication parameter will shift the phase matching curve (dashdotted orange line). For shifts greater than the HWHM of the phase matching spectrum, the efficiency of the target process, represented by the dashed blue line, drops below 50%. This condition is used to establish a simple criterion to indicate when the fabrication error δf moves the process outside the chosen tolerance limits.

and noticing that, for the target process, $\Delta\beta(f_0) = 0$, we can approximate Eq. (5.2) to first order as

$$\left| \partial_f \Delta\beta|_{f_0} \cdot \delta f \right| \frac{L}{2} \leq \Gamma. \quad (5.3)$$

The parameter $\partial_f \Delta\beta$ can be referred to as the *process sensitivity* to parameter f because it relates the length of a waveguide to the maximum deviation allowable. In fact, assuming a maximum deviation of δf_{max} , from Eq. (5.3) we can determine the maximum waveguide length L_{max} to ensure that the process efficiency is greater than 50%

$$L_{max} = \frac{2\Gamma}{|\partial_f \Delta\beta| \cdot \delta f_{max}}. \quad (5.4)$$

It is therefore clear that any deviation from the nominal design parameters poses an

unavoidable constraint on the waveguide length, no matter how small. In particular, this means that the ultimate length of a nonlinear waveguide is theoretically bounded by the precision of the fabrication process.

However, one can see that if $|\partial_f \Delta\beta|$ approaches 0, then δf_{max} tends to infinity. Under this condition, the waveguide becomes first-order insensitive to the deviations of the parameter f from the nominal value. The condition $\partial_f \Delta\beta = 0$ is known as *noncritical phase matching* and has been investigated in detail in previous works [84, 85].

Note that this model can be generalised to include the effect of more than one fabrication parameter by considering the following Taylor expansion

$$\Delta\beta = \Delta\beta(\mathbf{f}_0) + \nabla_{\mathbf{f}} \Delta\beta|_{\mathbf{f}_0} \cdot \delta\mathbf{f} + o(\delta\mathbf{f}^2), \quad (5.5)$$

where the variations of the fabrication parameters have been represented by the vector \mathbf{f} . Thus, Eq. (5.3) can be generalised to

$$|\nabla_{\mathbf{f}} \Delta\beta|_{\mathbf{f}_0} \cdot \delta\mathbf{f}| \frac{L}{2} \leq \Gamma \quad (5.6)$$

$$\left| \sum_i \frac{\partial \Delta\beta}{\partial f_i} \Big|_{\mathbf{f}_0} \delta f_i \right| \frac{L}{2} \leq \Gamma. \quad (5.7)$$

Obviously, the inclusion of multiple sources of imperfection greatly complicates the treatment of the system.

Two main conclusions can be drawn from the analysis presented in this section. Firstly, for a desired process, there is an inverse proportionality between maximum waveguide length and fabrication and operation errors. This means that the technological accuracy poses a well defined limit on the maximum length of the waveguides. The second conclusion is that technological imperfections can be mitigated if the *process sensitivity* is minimised through careful waveguide design, thereby approaching noncritical phase matching [84, 85]. It is worth stressing that these conclusions are independent of the specific waveguide technology or waveguide geometry and therefore can be applied to all systems described by the integral in Eq. (5.1). While the model has been derived for a constant error δf , which will not usually be the case, its predictions still provide a valid qualitative description of device performance in the presence of imperfections, as we will show in the following sections.

5.1.1. Numerical analysis of $|\partial_w \Delta\beta|$ for Ti:LN waveguides

We now apply the qualitative model discussed in the last section to titanium in-diffused lithium niobate (Ti:LN) waveguides in order to study the technological limits of this platform.

Analysing the fabrication steps involved in the production of Ti:LN waveguides (see section 3.1.2), it is evident that fabrication errors can occur at many different steps: for example, inhomogeneous illumination conditions can affect the patterning of the titanium stripes during photoresist exposure, or temperature gradients in the diffusion oven can lead to inhomogeneous diffusion of the titanium. The result of all these

imperfections are local deviations of the waveguide profile with respect to the ideal, homogeneous case.

Here we use Eq. (5.4) to study qualitatively the fabrication limits of Ti:LN waveguides. To simplify the treatment, we choose to consider only one source of error, namely variation of the width w of the Ti stripe (from now on we will refer to w simply as the waveguide width). In order to estimate $\partial_w \Delta\beta$, the effective refractive index of the guided modes as a function of the wavelength, polarisation and waveguide width is needed. We employ a finite element solver written in Python implementing the model described in [48] to calculate the Sellmeier equations of waveguides produced with different widths w . The process sensitivity $\partial_w \Delta\beta$ as a function of w for different processes is shown in Figure 5.2 for a number of processes of interest for quantum applications, namely:

1. type 0 PDC, 775nm→1550nm, $Z \rightarrow ZZ$, as in e.g. [13];
2. type II PDC, 775nm→1550nm, $Y \rightarrow YZ$, analogous to [21];
3. the quantum pulse gate (QPG), 1550nm+860nm→553nm, $YZ \rightarrow Y$, as in e.g. [31, 86];
4. the resonant PDC source described in [42], 532nm→890nm+1320nm, $Y \rightarrow ZY$;
5. counter-propagating PDC, 765nm→1510nm+1550nm, $Z \rightarrow ZZ$.

Recall that the waveguide is first-order immune to noise if the condition $\partial_w \Delta\beta = 0$ is met. Among the processes considered, only the resonant PDC source is non-critically phase matched in a regime where the waveguide is single-mode at telecom wavelengths, i.e. for $5\mu\text{m} \leq w \leq 7\mu\text{m}$. The type 0 PDC process is noncritically phase matched for $w=13\mu\text{m}$, but the waveguide is spatially multimode for this width. This is unfortunate as single-mode operation is often required for interfacing with telecommunication networks [21].

Another important observation is that each process has a different sensitivity; even the ones involving similar wavelengths exhibit very different behaviour, e.g. type 0 and type II PDC. Therefore, the process sensitivity has to be investigated independently for every process under consideration. Using the calculated process sensitivities, we can estimate the maximum tolerable width error depending on the desired sample length using Eq. (5.4). The results for analysed process are displayed in Figure 5.3, where relation (5.4) is plotted for different waveguide widths w . Note that some lines are missing, since they are noncritically phase matched.

An estimate of the waveguide width error δw is given by the ultimate resolution of the illumination technologies. Standard vacuum contact lithographic techniques are limited to resolutions around 0.5-0.8 μm [87] and one might therefore expect waveguide width errors δw in the same range. E-beam lithography can improve the precision by up to two orders of magnitude. However, techniques with higher precision often present other disadvantages, such as higher costs, increased processing time or difficulty in writing long structures, and thus a trade-off must be found.

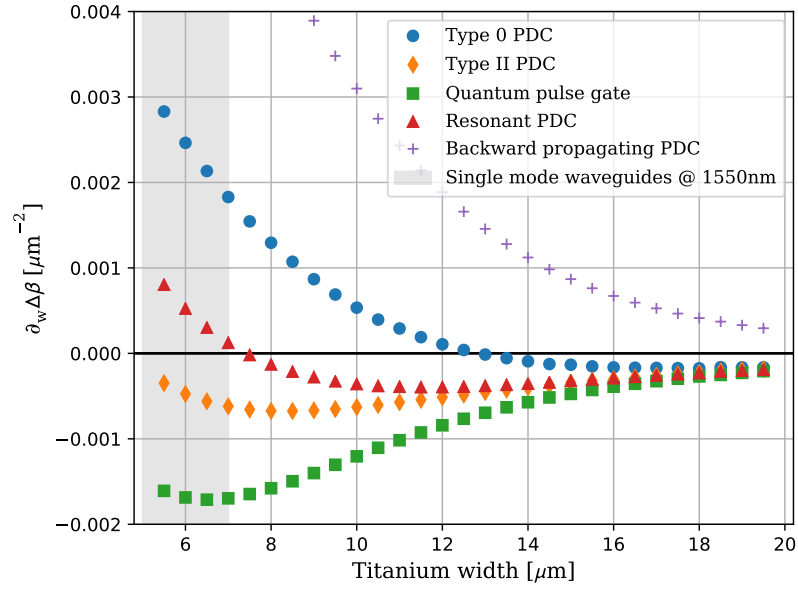
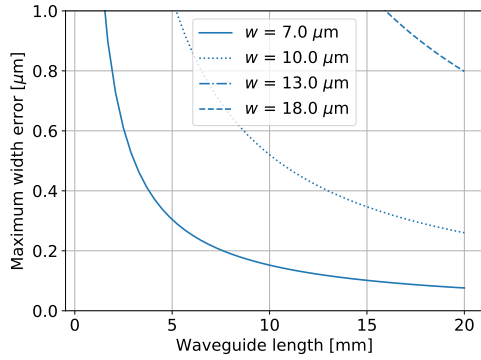


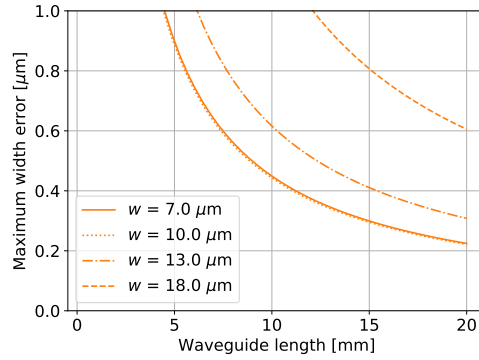
Figure 5.2. – Calculated sensitivity $\partial_w \Delta\beta$ of different processes to variations of the Ti stripe width for Ti:LN waveguides. The processes analysed are: type 0 PDC, type II PDC, quantum pulse gate, resonant PDC and counter-propagating PDC. Details of the processes are provided in the main text.

In this section, we presented a simple, qualitative model to estimate the interplay between device length and fabrication imperfections of a nonlinear waveguide. In the next section, we will present a method to quantitatively study the impact of fabrication imperfections on the performance of a nonlinear system.

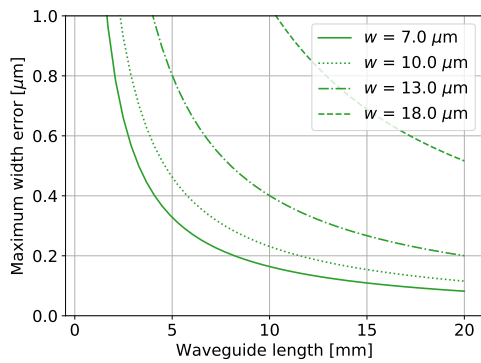
5.1. Qualitative model



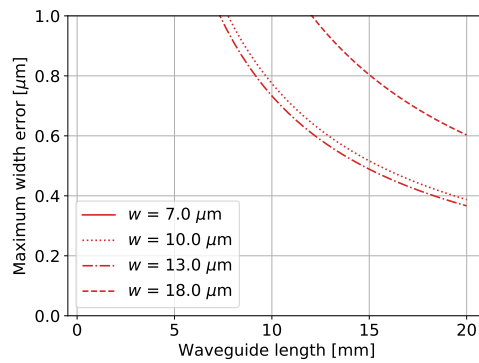
(a) type 0 PDC 775nm→1550nm



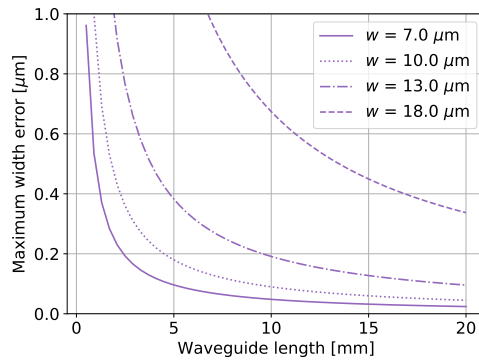
(b) type II decorrelated PDC



(c) Quantum pulse gate



(d) Resonant PDC



(e) Counterpropagating PDC

Figure 5.3. – The dependence of the maximum width error on the chosen waveguide length is shown for the processes studied in Figure 5.2. This dependence is shown for different waveguide widths. The plots show that the maximum allowable width error decreases as $1/L$ and that wider waveguides are less sensitive to the width error. Note that the $13\mu\text{m}$ line in Figure 5.3a and the $7\mu\text{m}$ line in Figure 5.3d are not present because they are first-order immune to noise.

5.2. Phase matching in inhomogeneous waveguides.

5.2.1. Mathematical modelling of waveguide inhomogeneities

The analysis conducted in the previous sections considered only homogeneous waveguides. However, in reality the variation of the nominal parameters is likely to be randomly distributed along a waveguide. In such a case, the waveguide is said to be *inhomogeneous* and the refractive index distribution varies along z . In this case, a spatially-varying parameter $f(z)$ is mapped to a momentum mismatch $\Delta\beta(z)$ that varies along the waveguide and Eq. (5.1) does not hold anymore.

The derivation of a correct expression that includes the longitudinal variation $\Delta\beta(z)$ is not trivial. Since we are mainly interested in the shape of the phase matching spectrum, we will neglect here the additional losses (due to coupling to other guided modes or radiation modes) introduced by the waveguide inhomogeneity [1]. Under this assumption, the waveguide eigenmodes can be approximated to

$$\mathbf{E}(x, y, z) = \mathcal{E}(x, y) e^{i \int_0^z \beta(\xi) d\xi}, \quad (5.8)$$

where the phase factor $\int_0^z \beta(\xi) d\xi$ describes the total phase accumulated by the eigenmode as it travels in along the waveguide.

Under this approximation, Eq. (2.22) is rewritten as

$$\frac{dA_3}{dz} = -i\kappa_3\theta A_1 A_2 g(z) e^{i \int_0^z \Delta\beta(\xi) d\xi}.$$

Here, $\Delta\beta z$ is replaced with

$$\int_0^z \Delta\beta(\xi) d\xi = \int_0^z (\beta_3(\xi) - \beta_2(\xi) - \beta_1(\xi) - \beta_G) d\xi, \quad (5.9)$$

where $\beta_{1/2/3}(z)$ is the spatially-dependent propagation constant of the field 1, 2 and 3 and $\beta_G = 2\pi/\Lambda$ is the additional momentum provided by the poling period. This integral is necessary to properly account for the phase retardation accumulated by the field while travelling along a material with variable dispersion. With this substitution, the phase matching amplitude ϕ is given by [88, 89]

$$\phi \propto \frac{1}{L} \int_0^L e^{i \int_0^z \Delta\beta(\xi) d\xi} dz. \quad (5.10)$$

Integration of Eq. (5.10) is usually possible only numerically and by assuming specific profiles for the momentum mismatch variation $\Delta\beta(z)$ along the waveguide. As we will see, assuming a z -dependent $\Delta\beta$ will impact the phase matching spectrum, which will not result in the usual sinc^2 shape [83, 90–92].

In the past, investigation of waveguides with variable dispersion profiles has been restricted to classical SHG systems assuming simple profiles for $\Delta\beta(z)$ [83]. However,

5.2. Phase matching in inhomogeneous waveguides.

randomly distributed inhomogeneities may dramatically affect the desired quantum state produced in waveguide systems. For example, degradation of the shape of the phase matching spectrum can increase the number of Schmidt modes in a decorrelated system, thus reducing its separability. Therefore, in the remaining sections we study the effect of randomly variable dispersion relations in waveguides designed for quantum processes. In particular, we will focus on the impact of fabrication errors on the final phase matching properties of a nonlinear waveguide. In particular, we study the phase matching properties of inhomogeneous Ti:LN waveguides as a function of the Ti stripe width w and its maximum error δw . It must be noted, however, that the discussion can be extended to any parameter that affects the momentum mismatch of the nonlinear process in the waveguide, e.g. the temperature profile of the sample during an experiment.

Numerical modelling

For the numerical integration of Eq. (5.10), knowledge of the effective refractive index $n_{eff}(\lambda)$ of the waveguide for variable waveguide widths is required. Therefore, using a FEM solver implemented in Python, we computed $n_{eff}(\lambda)$ for waveguide widths w in the range $[5.5, 22]\mu\text{m}$ in steps of $0.5\mu\text{m}$, using the model presented in section 3.1.2. These retrieved dispersion relations are used to calculate the momentum mismatch along the waveguide

$$\Delta\beta(z) = 2\pi \left(\frac{n_{eff,3}(\lambda_3, z)}{\lambda_3} - \frac{n_{eff,2}(\lambda_2, z)}{\lambda_2} - \frac{n_{eff,1}(\lambda_1, z)}{\lambda_1} \right) \quad (5.11)$$

as a function of the waveguide width for the different processes analysed.

For the numerical integration of Eq. (5.10), we developed and published the Python package PyNumericalPhasematching [93]. In this package, it is possible to calculate the phase matching spectrum of both homogeneous and inhomogeneous waveguides. Moreover, it can integrate Eq. (5.10) as a function of $\Delta\beta$, or as a function of one or two independent wavelengths, if suitable dispersion equations are provided. The simulations presented in the rest of this chapter have been performed using PyNumericalPhasematching.

To simulate a single instance of a waveguide of length L , a mesh of N points spaced by $\Delta z = 50 \mu\text{m}$ is first generated. A random waveguide profile with the desired noise spectrum is then generated as follows:

1. Create a vector of spatial frequencies $f_k = -\frac{1}{2\Delta z} \dots \frac{1}{2\Delta z}$ in steps of $\Delta f = \frac{1}{L}$.
2. Generate the spectrum of the noise $C_k = f_k^{-\gamma} e^{i\phi_k}$ for $k \in [\frac{N}{2}, \frac{N}{2}]$, where $\gamma = 0$ for AWG noise and $\gamma = 1$ for pink noise and ϕ_k is a random variable uniformly distributed in $[0, 2\pi]$. In order to ensure a real-valued noise profile, we pose the condition $\phi_k = -\phi_{-k}$.
3. Take the inverse fast Fourier transform of the spectrum $\{C_k\}$ and normalise it to have a mean value of w and maximum deviation of $|\delta w|$.

Different random instances of the same noise spectrum are generated simply by randomly sampling the phase ϕ_k . Once the width profile $w(z)$ is generated, we calculate the spatially-dependent momentum mismatch $\Delta\beta(z)$ using the width-dependent Sellmeier equations previously derived. Finally, equation 5.10 is discretised as

$$\phi = \frac{\Delta z}{L} \sum_{n=0}^N e^{i\Delta z \sum_{m=0}^n (\Delta\beta_m - \frac{2\pi}{\Lambda})} \quad (5.12)$$

and the phase matching spectrum is evaluated by computing $\Delta\beta(z_m)$ at each mesh point z_m , given the local waveguide width $w(z_m)$. Note that Eq. (5.12) already provides the phase matching spectrum normalised per unit length and $|\phi|^2$ will always have a maximum value of 1 (in the case of ideal phase matching) or lower.

5.2.2. Analysis of different types of noises

For simplicity, we investigate fabrication errors $\delta w(z)$ characterised by two types of noise spectra, namely additive white gaussian (AWG) and $1/f$ noise. AWG noise describes uncorrelated noise fluctuations along the waveguide, while $1/f$ noise is characterised by spatial correlations and accounts for long range drifts in the production parameters. For example, one might expect such long range correlations from illumination inhomogeneities during the photolithography or temperature gradients during the titanium diffusion. In Figure 5.4 we show an example of the effect of these two types of noise on the spectrum of a $7\mu\text{m}$ wide Ti:LN waveguide. Even though the two noises have the same amplitude, they have very different phase matching spectra: AWG noise does not appreciably worsen the spectrum shape, while $1/f$ noise broadens the spectrum and increases the side lobes heights.

For a better understanding of the main differences between the two types of noise, we study in detail the performance of a 20mm-long, $7\mu\text{m}$ -wide waveguide designed for a type 0 second harmonic generation (SHG) pumped at 1550nm. We investigate the degradation of the conversion efficiency for values of the fabrication error $\delta w \in [0, 1.0]\mu\text{m}$ for both types of noise. The results of the simulations are presented in Figure 5.5. The two types of noise have very different impact on the maximum achievable conversion efficiency: AWG noise has a negligible influence, while $1/f$ noise can drastically decrease it. Furthermore, the reduction of conversion efficiency is accompanied by an increase of the phase matching bandwidth, especially for errors $\delta w > 0.25\mu\text{m}$, whose broadened phase matching spectra are shown in the insets of Figure 5.5.

The same analysis has been performed for the other processes characterised in Figure 5.2 and the results are similar: AWG noise consistently has a negligible impact on the average maximum conversion efficiency, while $1/f$ noise rapidly degrades the performance of the device as δw increases. These results are well in agreement with previous studies on different systems. The presence of AWG noise on the poling grating of periodically-poled waveguides has been previously analysed in [90–92] and showed only a minor influence on the maximum conversion efficiency. Moreover, a comparison between correlated and uncorrelated noise has been investigated in photonic crys-

5.2. Phase matching in inhomogeneous waveguides.

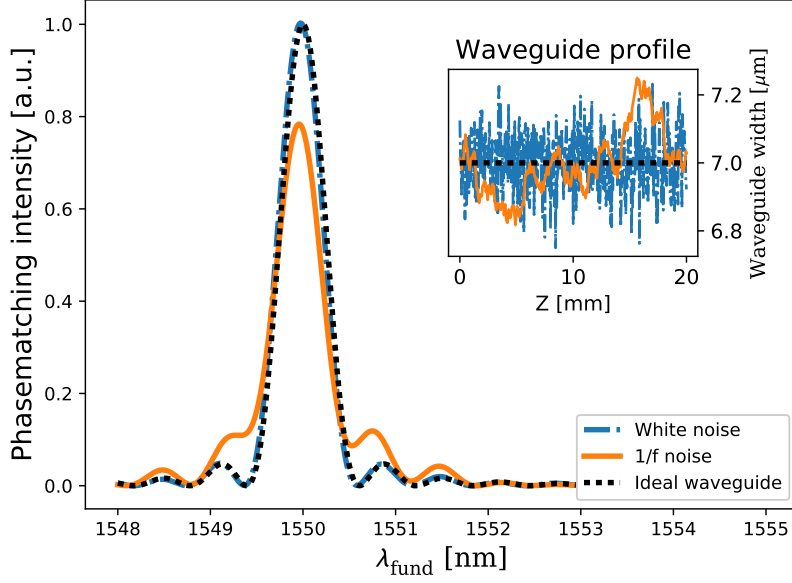


Figure 5.4. – Example of the effect of different noise profiles on the phase matching intensity spectrum. In the main plot, the phase matching spectra of the waveguides without noise (black dotted line), with additive white gaussian noise (blue dash-dotted line) and with $1/f$ noise spectrum (orange solid line) are shown. In the inset, the respective waveguide width profiles are reported. The device under consideration is a 20mm-long Ti:LiNbO₃ waveguide for type 0 PDC 775nm \rightarrow 1550nm, characterised via the reverse process, SHG.

tal fibres, showing that imperfections with long range correlations drastically effect the parametric gain of nonlinear processes [94]. In the rest of the chapter, we will focus our attention exclusively on the effects of $1/f$ noise, since this is the main cause of distortions of the phase matching spectrum.

Having established a framework suitable for the study of waveguide inhomogeneities, we can now compare the approximate results derived in section 5.1 with numerical simulations. An important result was the ability to predict the design of non-critically phase matched waveguides. In particular, we calculated that a type 0 PDC process pumped at 775nm is noncritically phase matched for $w = 13\mu\text{m}$. This result is confirmed by evaluating the conversion efficiency of the reverse process, a type 0 SHG pumped at 1550nm, as a function of the waveguide width w and the error δw in the presence of $1/f$ noise. Indeed, Figure 5.6 shows that a $13\mu\text{m}$ -wide waveguide is practically immune to $1/f$ noise when close to noncritical phase matching. Moreover, from the calculations reported in Figure 5.3a, we expect that a $7\mu\text{m}$ -wide, 20mm-long waveguide will be sensitive to noise values $\delta w \geq 0.1\mu\text{m}$. As shown in Figure 5.6, for

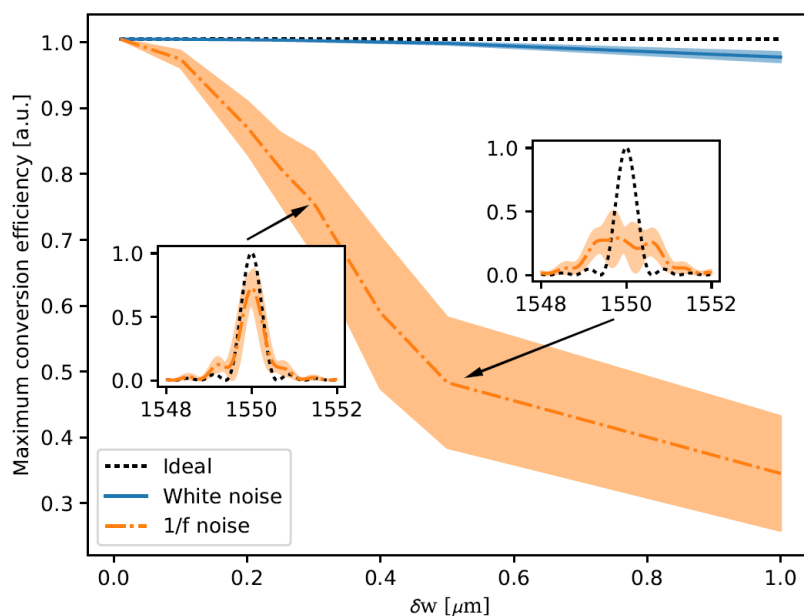


Figure 5.5. – Maximum efficiency of a nonlinear process as a function of the waveguide width error for the ideal waveguide (black dotted line), a waveguide with AWG noise (blue dash-dotted line) and $1/f$ noise (orange solid line). Shaded regions correspond to the standard deviation resulting from the simulation of 40 different systems for each datapoint. The insets show the comparison between the average phase matching intensity in the presence of $1/f$ noise and the ideal phase matching spectrum (in black, dotted line). The shaded area represents the standard deviation of the simulated intensity spectra. A broadening of the average phase matching spectrum, more prominent side lobes and reduction of the efficiency are evident. The device under consideration is a 20mm-long Ti:LiNbO₃ waveguide for type 0 PDC 775nm \rightarrow 1550nm, characterised via the reverse process, SHG.

5.2. Phase matching in inhomogeneous waveguides.

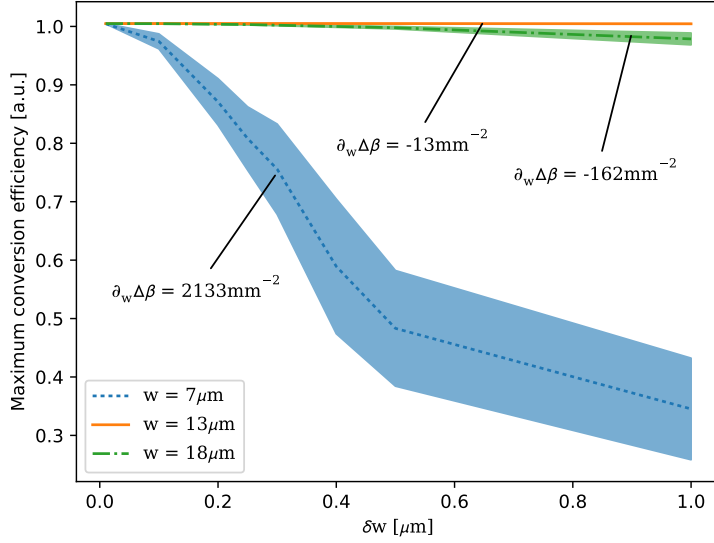


Figure 5.6. – Maximum efficiency of a nonlinear process as a function of the waveguide width error, in the presence of $1/f$ noise. The three different curves are calculated for nominal widths of $7\mu\text{m}$ (blue dotted line), $13\mu\text{m}$ (orange solid line) and $18\mu\text{m}$ (green dashed line). Shaded regions are the standard deviation resulting from the simulation of 40 different systems for each datapoint. Note that the $13\mu\text{m}$ waveguide is non-critically phase matched and so is virtually immune to the presence of noise. The device under consideration is a 20mm -long $\text{Ti}:\text{LiNbO}_3$ waveguide for type 0 PDC $775\text{nm} \rightarrow 1550\text{nm}$, characterised via the reverse process, SHG.

$\delta w \geq 0.1\mu\text{m}$, the maximum efficiency rapidly degrades below 90% of the ideal maximum. This confirms that the simplified model can provide reliable qualitative information about the waveguides' sensitivity to noise and thus the evaluation of the process sensitivity is can provide useful technological boundaries for the process quality of waveguide production.

The theory presented so far is now applied to three different systems of interest in quantum optics. In fact, we will show that it is necessary to consider the impact of fabrication errors in these systems to correctly model and estimate their performance. In section 5.2.3 we analyse the effect of waveguide inhomogeneities on the maximum squeezing attainable in a waveguided system; in section 5.2.4 we estimate how noise reduces the maximum number of bins in a frequency-bin encoding (FBE) scheme; in section 5.2.5 we study the effect of waveguide width noise on the bandwidth compression factor of a frequency conversion device.

5.2.3. Impact of fabrication errors in squeezing generation.

We first consider a waveguide structure designed to produce continuous-wave (CW) single-mode squeezed states in a single-pass configuration. These states are the foundation for continuous-variable (CV) quantum optics: they can be used as a basis for CV quantum computing [24], they have been used to generate complex quantum states such as EPR entanglement [95] and CV cluster states [96], and they have been used in sensing and metrology in order to improve the sensitivity of measurements, e.g. in gravitational-wave astronomy [97].

Reduction of the normalised conversion efficiency

We consider here a $7\mu\text{m}$ -wide Ti:LN waveguide pumped at 775nm that produces type 0 squeezing at 1550nm in a single-pass configuration. It can be shown that both the losses of the fundamental field and the strength of the nonlinear process are critical to the amount of squeezing produced [98]. We begin by neglecting the losses, thereby exclusively investigating the effect of waveguide width imperfections on the strength of the nonlinear process. The strength of the nonlinear process can be found by performing second harmonic generation in such a sample, from which one can calculate the normalised conversion efficiency using

$$\eta_{norm} = \frac{P_{SH}}{P_{FF}^2 L^2}. \quad (5.13)$$

A common misconception is that, due to its definition, η_{norm} is independent of length. However, the qualitative model presented in Figure 5.3a shows that longer waveguides are more susceptible to fabrication imperfections, therefore we expect η_{norm} to be dependent on waveguide length.

To calculate η_{norm} in the presence of fabrication errors, we numerically simulate the phase matching spectra of the system for different sample lengths $L \in [10, 60]\text{mm}$ and width error magnitude $\delta w \in [0, 0.5]\mu\text{m}$. For each parameter combination, we calculate the maximum conversion efficiency of 40 randomly generated systems to estimate the average normalised conversion efficiency. From Figure 5.7, it is evident that the normalised conversion efficiency is critically dependent on both L and δw . The simulations reveal that both η_{norm} and the waveguide length of each sample are necessary to provide a fair comparison of the performance of different devices. Furthermore it can be seen that the normalised conversion efficiency drops from $49\% \text{W}^{-1} \text{cm}^{-2}$ to $40\% \text{W}^{-1} \text{cm}^{-2}$ for 10mm -long waveguides and below $15\% \text{W}^{-1} \text{cm}^{-2}$ for 60mm -long waveguides. These values are in agreement with experimental evidence reported in [99], where the second harmonic conversion efficiency is reduced to $12\% \text{W}^{-1} \text{cm}^{-2}$ for 88mm -long waveguides. Therefore, it is clear that η_{norm} is not a good parameter to compare the performance of samples with different lengths.

5.2. Phase matching in inhomogeneous waveguides.

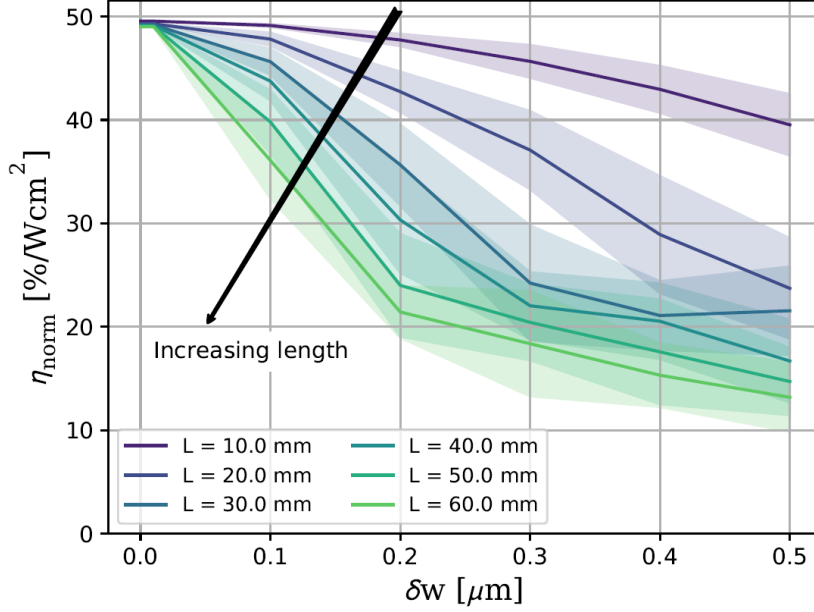


Figure 5.7. – Normalised conversion efficiency as a function of the error on the waveguide width, for lossless samples of varying lengths. It can be seen that both the length of the sample and the magnitude of the width error have a strong impact on the normalised conversion efficiency, even in the absence of losses. The device under consideration is a $7\mu\text{m}$ -wide Ti:LiNbO₃ waveguide for type 0 PDC $775\text{nm} \rightarrow 1550\text{nm}$, characterised via the reverse process, SHG. The shaded areas correspond to the standard deviation of the simulated data.

Maximum squeezing achievable

From the calculated normalised conversion efficiencies, one can estimate the amount of squeezing that can be produced in this device. Following [98], the maximum squeezing S achievable in a single-pass CW waveguide is given by

$$S = \left(e^{-2\sqrt{\eta_{\text{norm}} P_{\text{in}} L} e^{-\alpha L}} \right) + 1 - e^{-\alpha L}, \quad (5.14)$$

where P_{in} is the input pump power of the squeezer and α is the loss for the squeezed field. We assume a negligible effect of the losses for the 775nm pump. We consider $P_{\text{in}} = 500\text{mW}$ at 775nm and propagation losses α equal to 0.1 dB/cm , a safe estimate of the average losses measured in Ti:LN waveguides [13]. The squeezing S produced as a function of L and δw is shown in Figure 5.8. It can be seen that, for a given δw , there exists a waveguide length that maximises the squeezing produced. Moreover, this optimal length increases as the magnitude of the width error increases. This is due to a complex interplay between the nonlinear interaction strength and the losses;

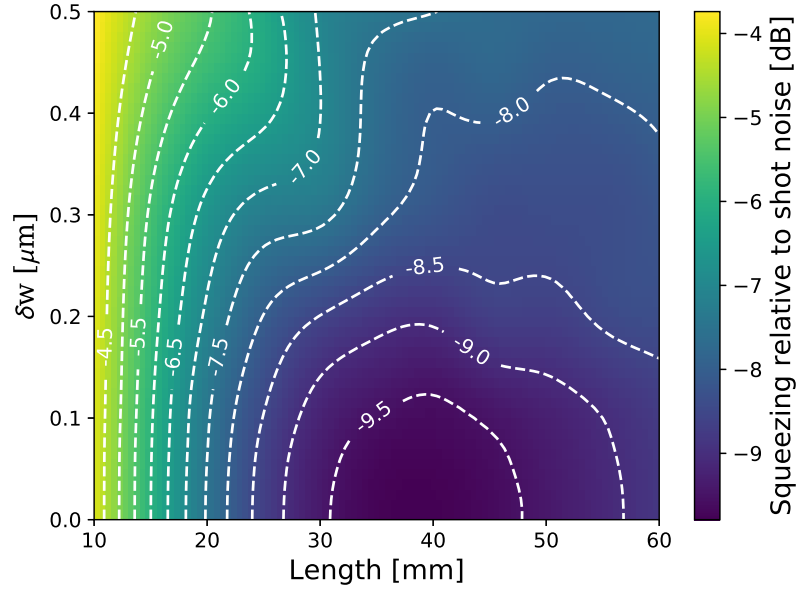


Figure 5.8. – Squeezing relative to shot noise exiting the waveguide for samples with different lengths and widths error. The process is pumped with 500mW of CW input at 775nm. Losses for the fundamental field are assumed to be 0.1 dB/cm. The device under consideration is a 7 μ m-wide Ti:LiNbO₃ waveguide for type 0 PDC 775nm \rightarrow 1550nm

as the waveguide length increases, the positive effect of an increase in the interaction length is counteracted by an increase in the total losses and a simultaneous reduction of the normalised conversion efficiency. The simulations show that the system under investigation (with 500mW of pump power) can produce around -9.5 dB of squeezing, choosing a waveguide with an optimised length of 40mm, if the error is below $\delta w \leq 0.1\mu\text{m}$.

To reduce the impact of fabrication errors, one can consider the use of noncritically phase matched systems. For the system under consideration, this can be done by choosing a 13 μ m-wide waveguide, as shown in Figures 5.3 and 5.6. In this case we expect a normalised conversion efficiency that is independent of the waveguide length and the fabrication imperfections. Note that insensitivity to fabrication imperfections is equivalent to having no fabrication imperfection. Therefore, the squeezing produced in a noncritically phase matched waveguide corresponds to the values at $\delta w = 0\mu\text{m}$ in Figure 5.8, neglecting a minor deviation in η_{norm} due to differences in the overlap of the interacting fields in the wider waveguide.

5.2.4. Impact of fabrication errors on quantum information encoding.

Frequency-bin encoding (FBE) is an attractive scheme for the implementation of quantum information processing protocols because it offers an unbounded space for high-dimensional encoding compatible with standard fibre networks. Furthermore, FBE can be implemented using PDC sources, which are a versatile and tunable platform that has been developed for many years.

Here, we study the limitations of Ti:LN waveguides as pulsed PDC sources for FBE and evaluate the impact of fabrication imperfections on such systems. We consider a type 0 PDC source in a Ti:LN waveguide, pumped at 775nm, generating pairs of frequency-bin entangled photons in the telecom C-band, between 1530nm and 1570nm. The physical device is analogous to the one presented in [100]. Typically, PDC sources for FBE are pumped with CW light [100, 101], however, pulsed systems provide advantages in terms of synchronisation between the communicating parties. Therefore, we consider a pulsed pump laser with a pump bandwidth broader than the phase matching spectral bandwidth.

FBE benefits from having a large number of encoding bins; however, it is also important to minimise cross-talk between them. As a compromise between these two factors, we define the frequency-bin bandwidth Δb as the full width at half maximum (FWHM) of the phase matching spectrum and we assume that each bin is separated by $\Delta b/2$, as illustrated in Figure 5.9. From this definition, given the available frequency band $\Delta\lambda$, one can calculate the number of available bins n_{bins}

$$n_{bins} = \frac{\Delta\lambda}{1.5\Delta b}, \quad (5.15)$$

where $\Delta\lambda = 40nm$ is the bandwidth of the telecom C-band. The number of available bins is then used as a figure of merit for the system. The bin bandwidth Δb is extracted from the phase matching spectrum by fitting it with a Gaussian and taking the FWHM of the fit.

This analysis is applied for varying sample lengths L and width error magnitudes δw and the results of the calculations are shown in Figure 5.10. Solid lines represent 7 μm -wide waveguides, while dashed ones represent 13 μm -wide waveguides. Shaded areas represent the standard deviation of the data, as calculated from the simulation of 40 random samples for each datapoint. Note that, in the presence of a spectrum with multiple peaks and sidelobes, it can be difficult to define a main peak for the Gaussian fit. This sometimes results in an underestimation of the phase matching bandwidth, leading to a higher number of bins in comparison to the noiseless case (for example, this effect can be seen in Figure 5.10 around $\delta w=0.1\mu m$ for $L = 60mm$). The simulations show that it is possible to implement more than 70 bins in a 60mm-long, provided that fabrication errors are minimal. However, for the 7 μm -wide waveguides, the number of bins available in longer waveguides drops rapidly with increasing width error to a minimum of approximately 10. The reason is that longer samples theoretically have much narrower phase matching bandwidth and these are much more susceptible to

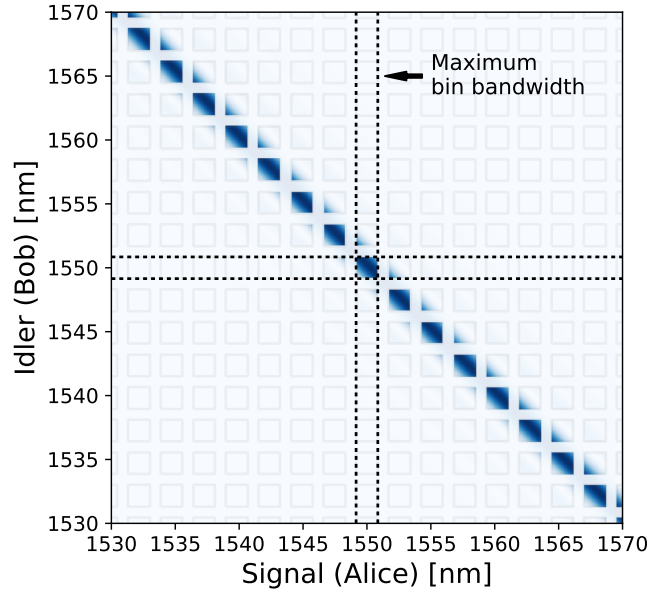


Figure 5.9. – Joint spectral intensity of an ideal, type 0, decorrelated parametric downconversion (PDC) process, pumped with a 775nm lasers. The pump bandwidth is chosen to match the phase matching bandwidth. For frequency-bin encoding, a simple criterion to ensure low cross-talk between the different frequency bins is to define the bin size equal to the FWHM of the phase matching bandwidth, and distance between bins equal to half the FWHM as shown by the overlaid grid.

fabrication errors. Therefore, in the presence of large fabrication errors, the maximum number of bins becomes, on average, independent of the sample length. In contrast, the $13\mu\text{m}$ -wide waveguides do not show a reduction in the number of bins as the noise increases, as can be seen from the dashed lines in Figure 5.10. This is due to the fact that they are noncritically phase matched and therefore immune to fabrication errors.

5.2.5. Impact of fabrication errors on the performance of a bandwidth compressor.

Interfacing components operating at different wavelengths is a critical challenge for quantum optical networks. Reduction of transmission losses is paramount in most applications and therefore transmission in the telecom C-band is desired, where losses are minimal. However, many quantum devices operate outside this frequency band and therefore efficient frequency conversion between these bands is required. Furthermore,

5.2. Phase matching in inhomogeneous waveguides.

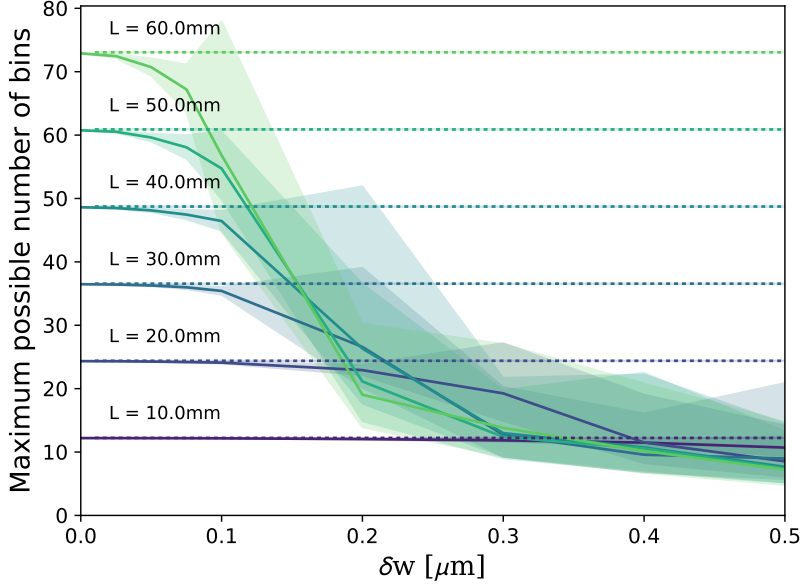


Figure 5.10. – Maximum number of bins available for a frequency-encoded HDQKD protocol. A $1/f$ noise spectrum with maximum error δw has been considered. The bins is set to be equal to the phase matching spectrum FWHM and the distance between the channels is half the FWHM. Solid lines are for a $7\mu\text{m}$ -wide waveguide, dashed line for a $13\mu\text{m}$ -wide waveguide. The shaded areas correspond to the standard deviation of the simulated data. Since the $13\mu\text{m}$ -wide waveguide is noncritically phase matched, the standard deviation is practically zero and barely visible in the figure.

it is often necessary to efficiently match the bandwidth of different quantum devices. Both bandwidth matching and frequency conversion can be efficiently achieved in the integrated quantum pulse gate (QPG), a device that implements type II sum frequency generation (SFG) in a waveguide [86].

The integrated QPG in [86] was implemented in a $7\mu\text{m}$ -wide, 27mm-long Ti:LN waveguide, designed to convert single photons from the telecom C-band to 550nm. The measured bandwidth compression factor (BCF) was $\Delta\nu_{in}/\Delta\nu_{out} = 7.47 \pm 0.01$, where $\Delta\nu_{in/out}$ is the spectral bandwidth of the input and output photons. In this device, the compression factor is directly related to the phase matching bandwidth: the narrower the bandwidth, the higher the compression factor. We have already shown in section 5.2.4 that fabrication imperfections can increase the phase matching bandwidth of a given process. Therefore, we expect that the compression factor will reduce in the presence of fabrication imperfections.

As no theoretical estimate for the expected BCF is provided in [86], it is crucial to the-

oretically investigate the performance of this system and how they degrade in presence of fabrication imperfections. For this reason, we consider a $7\mu\text{m}$ -wide waveguide with different lengths L and varying magnitude δw of $1/f$ noise on the waveguide width. The input bandwidth is set to $\Delta\nu_{in} = 963 \pm 11$ GHz, while the output bandwidth $\Delta\nu_{out}$ is defined as the FWHM of a Gaussian fit to the phase matching spectrum, following the method of [86].

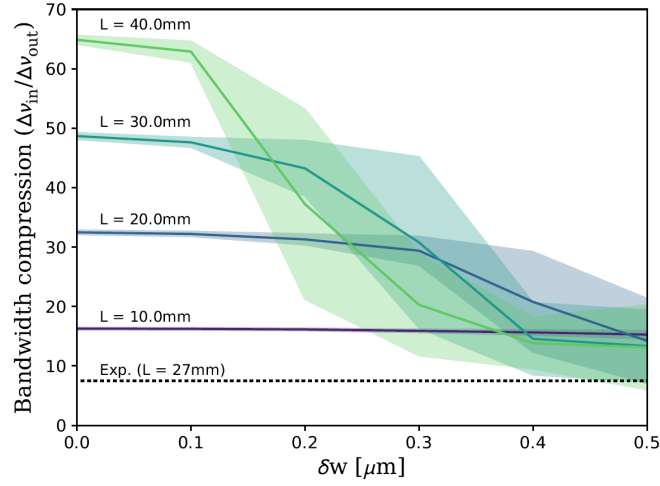
Each datapoint has been simulated 40 times and the results are shown in Figure 5.11a. The calculated BCFs are represented in solid lines, while the shaded regions represent the standard variation of the simulated data. Simulations show that a 40mm-long sample provides a BCF of ~ 6 , in the absence of fabrication imperfections. This corresponds to an output bandwidth of ~ 15 GHz or, equivalently, a 30ps-long pulse, under the approximation of Gaussian phase matching spectrum.

In Figure 5.11a the BCF measured in [86] for their 27mm-long waveguide is shown with a dashed line. It is immediately evident that the measured compression factor is well below the theoretically predicted value. In fact, calculations show that a 27mm-long sample should provide a compression factor close to 45 in the absence of imperfections; however, the experiment measured a compression factor of only 7.45. Such a reduction would only be expected in the presence of width error $\delta w \geq 0.4\mu\text{m}$, as illustrated in the Figure.

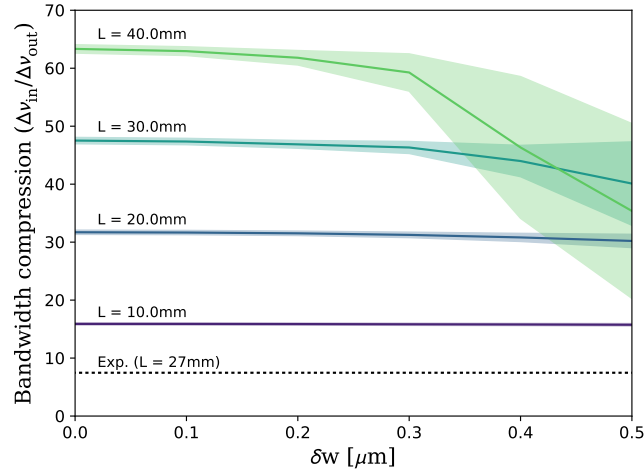
Allgaier *et al.* [86] also characterised the phase matching spectrum of their device and the measurement showed deviations from the expected sinc^2 profile, as shown in Figure 5.12. These deviations indicate the presence of non-negligible fabrication imperfections, recalling that Figure 5.5 showed that the presence of $1/f$ noise leads to more prominent side lobes and an asymmetric phase matching profile. Assuming a $1/f$ -noise profile and $\delta w = 0.4\mu\text{m}$, simulations have been able to reproduce the asymmetry and the prominent side lobes present in the measured phase matching spectrum, as can be seen comparing the measured and simulated spectra in Figure 5.12b and Figure 5.12c respectively.

The limited compression and the shape of the phase matching spectrum lead us to conclude that the presence of fabrication imperfections limits the performance of the device presented in [86]. As previously discussed, one method to overcome these limitations is to design the process to be noncritically phase matched. Although Figure 5.2 shows that noncritical phase matching cannot be found for the QPG, it is possible to reduce the process sensitivity by increasing the waveguide width. Figure 5.11b shows the calculated BCFs for a $13\mu\text{m}$ -wide waveguide as the length and the magnitude of the noise are varied. The results show a greatly reduced sensitivity to noise, as large fabrication errors have a lower impact on the BCF. These systems would reliably permit BCFs above 40, resulting in pulses with bandwidths below 25 GHz. Interestingly, these bandwidths correspond to pulses longer than 20ps at 550nm, a regime that is often difficult to reach. These results highlight the fact that proper system design can have a drastic impact on the final performance of such devices.

5.2. Phase matching in inhomogeneous waveguides.

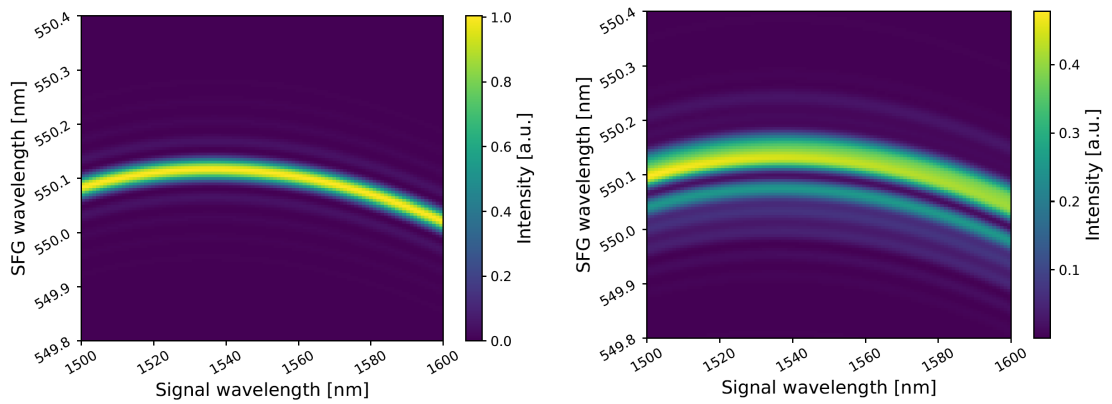


(a) Bandwidth compression for a $7\mu\text{m}$ -wide waveguide.



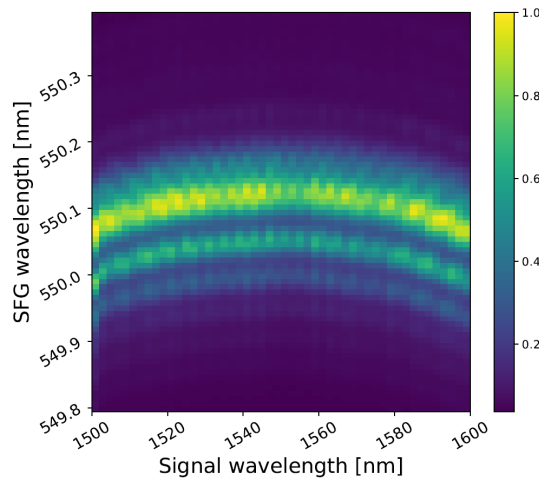
(b) Bandwidth compression for a $13\mu\text{m}$ -wide waveguide.

Figure 5.11. – Bandwidth compression factor resulting from the up-conversion of 963 GHz-broad telecom photons, using the quantum pulse gate [86]. The compression factor has been calculated for different waveguide width errors δw and lengths L , in presence of noise with $1/f$ noise spectrum. Moreover, two different nominal width have been investigated, namely $w = 7\mu\text{m}$ in Figure 5.11a and $10\mu\text{m}$ in Figure 5.11b. The solid lines correspond to the average bandwidth compression factors, while the shaded areas indicate their standard deviation. The experimental value reported in [86] is also shown as a dashed black line in both plots for comparison.



(a) Ideal phase matching spectrum.

(b) Simulated phase matching spectrum for a noisy waveguide ($\delta w = 0.4\mu\text{m}$)



(c) Phase matching spectrum measured in [86]

Figure 5.12. – Theoretical versus experimental performance of the bandwidth compression device presented in [86]. In Figure 5.12a the ideal phase matching spectrum is shown and can be compared with the measured phase matching one shown in Figure 5.12c. A phase matching spectrum similar to the measured one can be produced assuming a $1/f$ noise on the waveguide width and a maximum width error $\delta w = 0.4\mu\text{m}$, as shown in Figure 5.12b.

5.3. Reconstruction of sample inhomogeneity

To verify the validity of the model presented in section 5.2 and to fully characterise the quality of our fabrication process, we reconstruct the phase matching properties of an 83mm-long Ti:LN sample. The sample under investigation is diced down into ~ 10 mm-long pieces, whose individual phase matching spectra, as well as the phase matching profile of intermediate lengths, are characterised. The shift of the phase matching spectrum along the waveguide is mapped and used to retrieve the phase matching variation. Via numerical modelling, we are able to relate the measured variation to fabrication parameter errors and from this show that the estimated errors agree with the fabrication errors predicted in the previous section. i.e. $\delta w \approx 0.2 - 0.4 \mu\text{m}$. Finally, from the measured waveguide inhomogeneities, we are able to reconstruct the original phase matching spectrum of the sample.

5.3.1. Experiment

The system under investigation is a set of seven 83mm-long nonlinear waveguides fabricated by in-diffusing Ti ions in a z-cut LiNbO₃ crystal. The waveguides are designed to be single-mode in the telecom C band, with their nominal width w equal to $7 \mu\text{m}$, and are periodically poled with a period $\Lambda = 16.8 \mu\text{m}$. This allows a type 0, $ee \rightarrow e$ degenerate SHG process pumped at 1528.4nm at room temperature and at 1550nm at 200 °C.

The nonlinear process is completely determined by the phase mismatch $\Delta\beta$ of the involved light fields

$$\Delta\beta(z, \lambda) = 2\pi \left(\frac{n_e(z, \lambda/2)}{\lambda/2} - 2 \frac{n_e(z, \lambda)}{\lambda} - \frac{1}{\Lambda} \right), \quad (5.16)$$

where $n_e(z, \lambda)$ is the extraordinary refractive index of LiNbO₃ at the position z and at the pump wavelength λ . We explicitly consider the variation of the refractive index along the propagation axis z to include the effect of fabrication imperfections, such as inhomogeneities in the waveguide width, depth, operating temperature, poling pattern or a combination thereof.

In the case of small refractive index variations, one can approximate momentum mismatch variations to be wavelength independent [89] and introduce the *decoupling approximation*

$$\Delta\beta(z, \lambda) \approx \Delta\beta_0(\lambda) + \sigma\delta\beta(z), \quad (5.17)$$

where the momentum mismatch has been decomposed into the sum of $\Delta\beta_0(\lambda)$, describing the momentum mismatch of the process in absence of inhomogeneities, and $\sigma\delta\beta(z)$, that encompasses the variation of $\Delta\beta$ due to inhomogeneities in the system. The noise amplitude σ is defined as

$$\sigma = \max_z |\Delta\beta(z) - \overline{\Delta\beta_0}|, \quad (5.18)$$

where $\overline{\Delta\beta_0}$ is the mean $\Delta\beta_0$ in the ideal, noiseless sample. This definition is chosen such that $|\delta\beta(z)| \leq 1$.

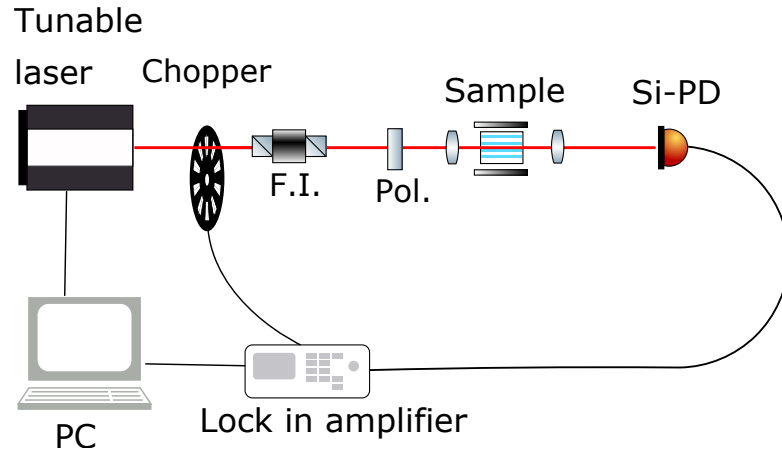


Figure 5.13. – Measurement setup for the characterisation of the phase matching spectrum. Full description in text.

In this case, the output intensity spectrum of the SH process provided by Eq. (5.10) can be rewritten as

$$I(\lambda) \propto \left| \int_0^L e^{i\Delta\beta_0(\lambda)z} e^{i\sigma \int_0^z \delta\beta(\xi)d\xi} dz \right|^2. \quad (5.19)$$

If the waveguide is sufficiently short, the impact of the variations $\sigma\delta\beta(z)$ is relatively weak and does not appreciably distort the phase matching spectrum, as discussed in the previous sections; in particular, for the process under investigation, we expect to see nearly ideal phase matching spectra for waveguides shorter than 1cm. Waveguide inhomogeneities are still expected, however, to affect positioning of the centre of the spectrum. Therefore, it should be possible to retrieve the mismatch variation profile $\sigma\delta\beta(z)$ along the waveguide by dicing a long sample down to ~ 1 cm-long pieces and monitoring the shift in the position (in wavelength) of the phase matching spectrum.

At first, the phase matching spectra of the initial 83cm-long waveguides are measured in the setup illustrated in Figure 5.13. The sample is first stabilised in temperature to around $25 \pm 0.1^\circ\text{C}$ as unwanted temperature shifts are indistinguishable from true waveguide imperfections, since both will act to shift the centre of the phase matching profile. The waveguides are then pumped with approximately 3mW from a tunable 1550nm laser (*EXFO Tunics*) and the wavelength of the pump is scanned in 1pm steps. The generated SH field is then detected using a Si-PIN photodiode. To increase the signal-to-noise ratio of the measurement the pump field is run through a chopping blade, and the photocurrent from the photodiode is fed into a lock-in amplifier (*Ametek Scientific Instrument 7265*).

As expected, the spectra of the long waveguides are distorted due to the presence of waveguide inhomogeneities, as can be seen in Figure 5.15. A ~ 1 cm-long piece was then cut from one end of the original sample and the resulting surfaces were polished.

5.3. Reconstruction of sample inhomogeneity

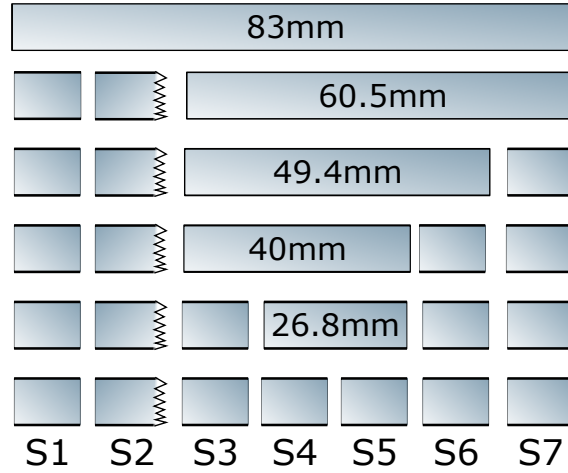


Figure 5.14. – Sequence of sample dicing. All the final sections are ~ 10 mm long. While polishing the 70mm-long sample, roughly 8mm of sample snapped from the left side and thus no phase matching spectrum could be recorded for S2 and for the 70mm-long sample.

Similar to the measurement for the original long sample, both resulting lengths were then temperature stabilised and the phase matching spectra of the waveguides in each section were again recorded. This process was repeated until the full sample was finally cut down into 7 pieces of approximately 1cm long, as shown in Figure 5.14. Note that some of the length is lost in the dicing and polishing of the sample as well as a small piece that was damaged during dicing.

In the previous sections, we discussed that, for a given process, the impact of fabrication imperfection is approximately inversely proportional to the sample length. This is confirmed by the measurement presented in Figure 5.15, showing the phase matching spectra measured from a single waveguide as it was gradually cut into shorter and shorter pieces. As expected, one can see that the measured phase matching spectra gradually approach the ideal sinc^2 -like shape as the sample is shortened down to 1cm.

From the phase matching profile of each 1cm-long piece a more quantitative investigation is undertaken. Figure 5.16 shows the measured phase matching profiles for all 1cm pieces across a single waveguide. For reference, the dashed curve shows the expected sinc^2 profile fitted only for the central wavelength. The central phase matching wavelength λ_{pm} is found from the data as the average of the measured wavelengths weighted by the corresponding measured intensities. Since the sample is temperature stabilised, the deviation of λ_{pm} from the target phase matching wavelength $\bar{\lambda}_{pm} = 1528.4\text{nm}$ is a measure of the waveguide inhomogeneities. With the help of Eq. (5.16), one can quantify the phase mismatch amplitude σ_i with respect to the ideal

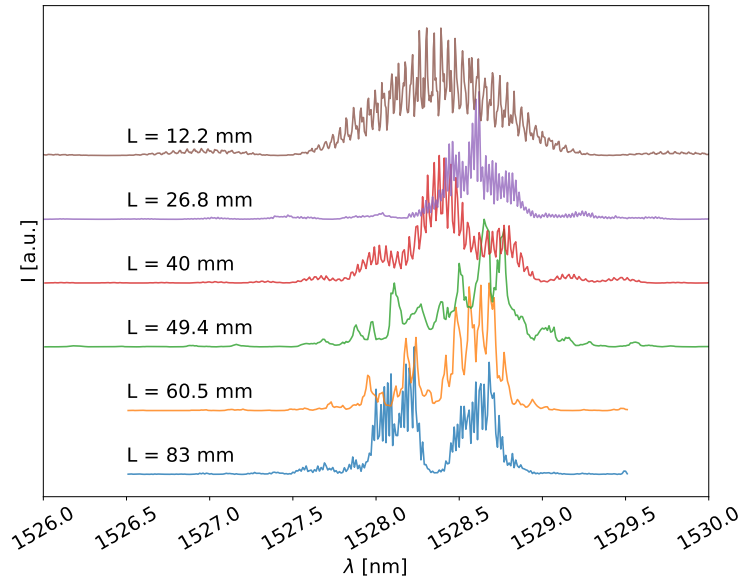


Figure 5.15. – Type 0 SHG phase matching spectra of a single waveguide for different waveguide lengths. Note that, as expected, the phase matching spectrum broadens as the sample becomes shorter and its shape tends towards the ideal sinc^2 profile. The oscillations are due to the presence of Fabry-Perot oscillations from the uncoated end facets.

phase matching for each 1cm-long section and reconstruct an approximate phase mismatch profile along the waveguide as

$$\Delta\beta(z) \approx \Delta\beta_0(\lambda) + \begin{cases} \sigma_1 & \text{in the 1}^{st} \text{ section} \\ \sigma_2 & \text{in the 2}^{nd} \text{ section} \\ \dots & \\ \sigma_n & \text{in the } n^{th} \text{ section} \end{cases}, \quad (5.20)$$

thereby approximating $\sigma\delta\beta(z)$ with a step function.

This characterisation is repeated for all remaining waveguides and the central phase matching wavelengths found in the 1cm-long samples for all waveguides are shown in Figure 5.17. It is immediately apparent that all the measured waveguides show a similar trend, whereby λ_{pm} increases along the sample length. Additionally, λ_{pm} changes quite dramatically between the different sections, with an average maximum variation of 0.6nm. This corresponds to a maximum noise amplitude of σ variation of $\sim 442 \text{ m}^{-1}$.

Using the model presented in [48], one can relate the shift of the phase matching wavelength to a variation of the waveguide properties. For simplicity, we assume that only variations in the waveguide width contribute to phase matching variations along

5.3. Reconstruction of sample inhomogeneity

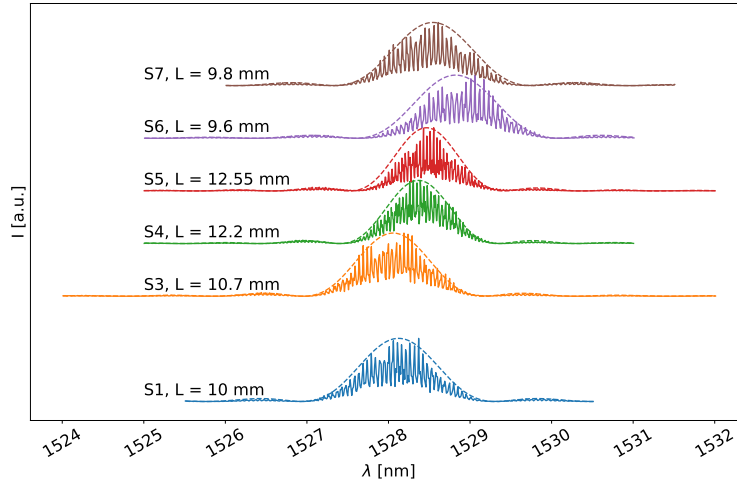


Figure 5.16. – Measured phase matching spectra for the different 1cm-long pieces in a single waveguide (WG1). The dashed lines correspond to the theoretical spectra fitted only for central wavelength. The shift of the phase matching centre is due to local variation of the waveguide properties and is used to derive the phase matching variation along the sample. Section S2 is missing since it broke during the dicing stage.

the sample. For the waveguides under consideration, a variation of $\delta\beta \sim 440\text{m}^{-1}$ corresponds to a width inhomogeneity $\delta w \sim 0.25\mu\text{m}$, in close agreement with the theoretical estimation presented in the first half of this chapter. Interestingly, the retrieved δw is close to the width error estimated in [89] ($\delta w \sim 0.2\mu\text{m}$) with a completely different measurement technique, for a very different process realised in RPE-LN waveguides. The only similarity between the two systems is the employment of a wet-etching based photolithographic step for waveguide patterning. This is perhaps an indication that the main cause of waveguide imperfections resides in the photolithographic step.

Finally, it should be possible to reconstruct the original phase matching spectrum given the measured δw profile along the sample. The performance of this reconstruction will of course be limited by the resolution of the measured δw profile and hence only the profile of the full length sample is reconstructed. We interpolate the measured data points with a piecewise linear interpolation to avoid numerical artifacts that are seen to arise from the choice of higher order polynomials fits. Thus, we obtain an approximate waveguide width profile $w(z)$ and the respective phase mismatch variation $\delta\beta(z)$. Eq. (5.19) is then used to calculate the expected phase matching spectrum of the original, full-length sample. In approximately half of cases, the reconstruction of the phase matching spectrum was successful and showed very similar features to the phase matching spectrum that was initially measured from the full-length sample, as shown in Figure 5.18. Note that, in contrast to previous work in PCF fibres [102], no

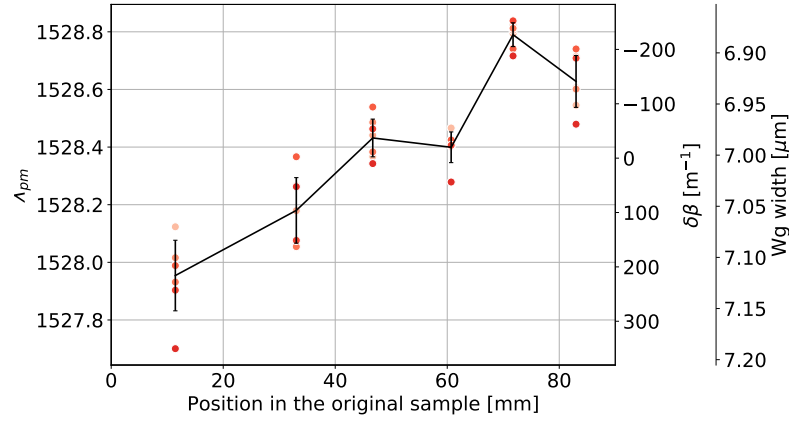


Figure 5.17. – Measured variation in the phase matching wavelength λ_{pm} across all waveguides for each 1cm-long sample. The black solid line is the average λ_{pm} shift. The corresponding phase mismatch variation $\delta\beta$ and waveguide width w can be read on the right axes. Here, we assume that only the width variation is responsible of the whole phase mismatch $\delta\beta$ variation.

fitting has been performed to reproduce the measurement of the original sample. This shows that, in most cases, the phase matching properties of the investigated process in Ti:LN waveguide can be considered constant within 1cm. Finally, we believe that the reconstruction method has still room for improvement: it is likely that the inability to reconstruct properly the spectrum of some waveguides is due to an insufficient spatial resolution for λ_{pm} . We believe this also explains some deviations between the theoretical and the measured phase matching spectra in Figure 5.18. With ulterior subdivision it should be possible to track more accurately the variation of λ_{pm} and thus the waveguide inhomogeneity profile.

5.4. Correction of fabrication imperfection

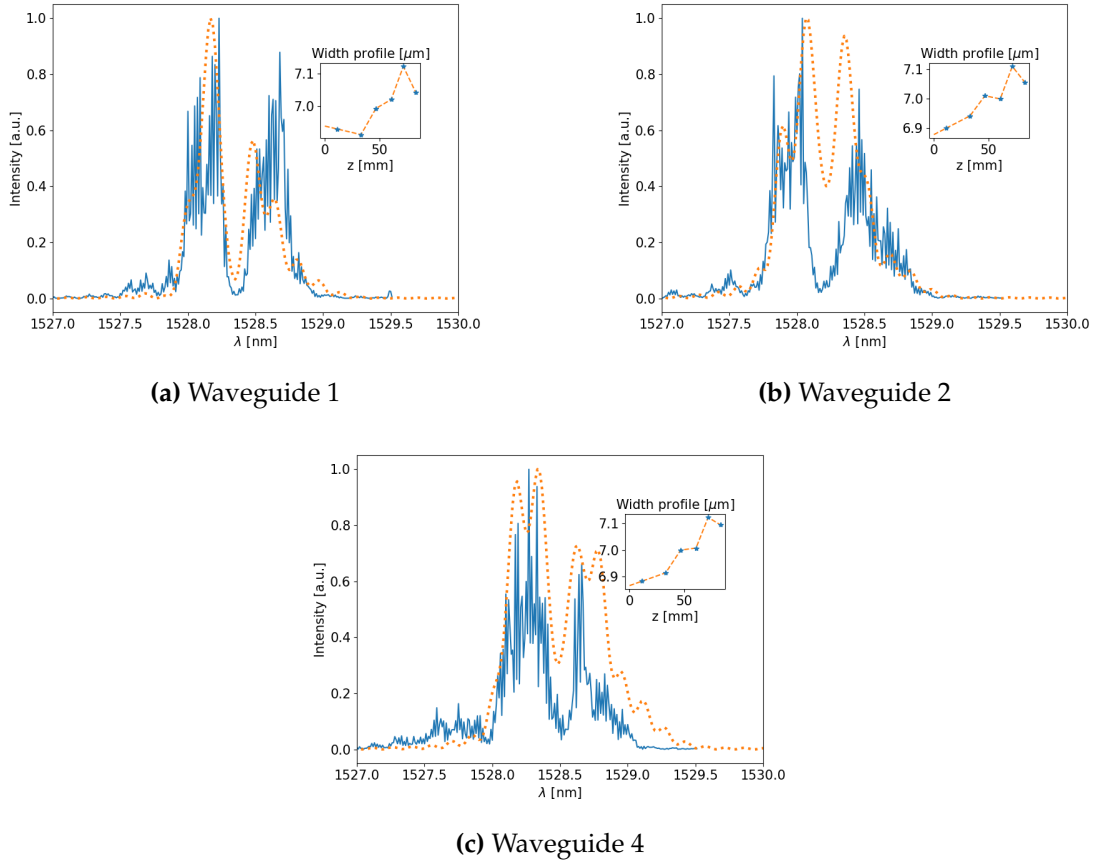


Figure 5.18. – Phase matching spectra reconstructed from the measured data points (in dashed orange lines) and comparison with the measured one (in solid blue lines). In the inset, the inferred waveguide widths and the linear interpolation used to reconstruct the phase matching spectra are shown.

5.4. Correction of fabrication imperfection

The discussion presented so far highlighted that it is always possible to find a maximum waveguide length L_{max} such that fabrication imperfections do not appreciably affect the phase matching spectrum. For example, in the case of type 0 SHG in Ti:LN waveguides, this length is approximately 1cm, as shown with the measurements of the last section.

This observation suggests a possible way to compensate fabrication imperfection in post-processing. In fact, any fabrication imperfection introduces a phase matching error $\delta\beta_{pre}(z)$ along the waveguide. To first approximation, we can consider this to be wavelength-independent, as it is only a small change of the refractive index of a weakly

guiding waveguide. Imposing in postprocessing an external phase matching variation $\delta\beta_{post}(z)$, the total phase mismatch along the waveguide is

$$\delta\beta(z) = \delta\beta_{pre}(z) + \delta\beta_{post}(z) \quad (5.21)$$

Therefore, if $\delta\beta_{post}(z) = -\delta\beta_{pre}(z)$, the phase matching spectrum of the imperfect waveguide would be an ideal sinc^2 . The observation that the phase matching relations can be considered homogeneous within a section of length L_{max} reveals that it is sufficient to compensate the phase matching only over regions longer than L_{max} . This can be done in different ways, e.g. tuning the refractive index via thermal tuning. Indeed, it has been already shown that it is possible to modify the dispersion properties of the waveguide via temperature tuning [103]. Therefore, by carefully tuning the dispersion of waveguide sections with length $L \leq L_{max}$, it should be possible to correct the phase mismatch introduced by the fabrication imperfections.

To show that this is theoretically possible, we simulate a LN waveguide implementing a type 0 SHG, $1550\text{nm} \rightarrow 775\text{nm}$, as described in section 5.2. In particular, we consider a $7\mu\text{m}$ -wide, 10cm -long waveguide with a width error $\delta w = 0.25\mu\text{m}$. We then calculate the phase matching spectrum of this system, when a non uniform external temperature profile is set. Finally, we show that it is possible to reconstruct a nearly ideal phase matching spectrum by tailoring the temperature profile using a very simple algorithm.

5.4.1. Simulation of the inhomogeneous system and its correction

To simplify the treatment, we perform the whole simulation in terms of $\Delta\beta$. This is valid since the $\Delta\beta$ of the selected process behaves almost linearly as a function of the wavelength, temperature or waveguide width, especially if only small wavelength ranges ($\pm 10\text{nm}$) around 1550nm are considered.

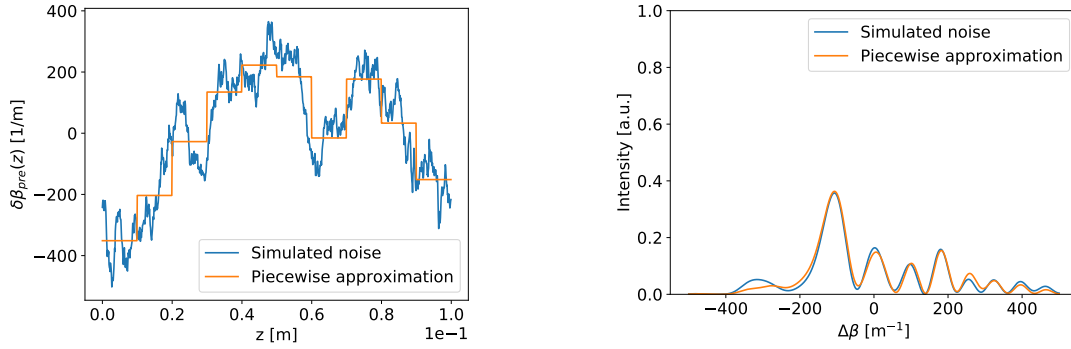
As a first step, we calculate the process sensitivity to the waveguide width $\partial_w \Delta\beta$ and to the operating temperature $\partial_T \Delta\beta$. These coefficients are useful to convert the width error $\delta w(z)$ and temperature correction $\delta T(z)$ profiles in terms of phase mismatch variation as

$$\begin{aligned} \delta\beta_w(z) &\approx \partial_w \Delta\beta \cdot \delta w(z) \\ \delta\beta_T(z) &\approx \partial_T \Delta\beta \cdot \delta T(z). \end{aligned}$$

The width sensitivity $\partial_w \Delta\beta$ was already evaluated at the beginning of this chapter, while the temperature sensitivity $\partial_T \Delta\beta$ can be calculated using the bulk dispersion relation described in section 3.1. This is valid since waveguide geometry mainly impacts the refractive index as a function of the wavelength. The sensitivity parameters are evaluated as

$$\begin{aligned} \partial_w \Delta\beta &\approx 0.002\mu\text{m}^{-2} && \text{at } w = 7\mu\text{m} \\ \partial_T \Delta\beta &\approx 55 \times 10^{-6}(\mu\text{m} \cdot ^\circ\text{C})^{-1} && \text{at } T = 25^\circ\text{C}. \end{aligned}$$

5.4. Correction of fabrication imperfection



(a) Phase mismatch error corresponding to a inhomogeneous width profile with a $1/f$ noise and maximum amplitude of $0.25\mu\text{m}$.

(b) Initial phase matching spectrum of the noisy waveguide. The chosen range of $\Delta\beta$ is equivalent to $\lambda \in [1540, 1560]\text{nm}$.

Figure 5.19. – The blue lines show the simulated profile and phase matching spectrum of a $7\mu\text{m}$ -wide, 10cm -long Ti:LN waveguide implementing a type 0 SHG ($1550\text{nm} \rightarrow 775\text{nm}$) process. The orange line represent the discretised waveguide profile approximating the real noise and the respective phase matching spectrum. The comparison between the two spectra highlights that the features of the noisy waveguide derive by the presence of long range correlation that can be modelled accurately with a step function.

with a maximum error of respectively 1.9% and 0.34% in the range $\lambda \in [1540, 1560]\text{nm}$.

With the help of PyNumericalPhasematching, we simulate a 10cm -long waveguide with $1/f$ noise profile $\delta w(z)$ having a maximum width variation of $0.25\mu\text{m}$, consistent with the fabrication errors previously retrieved in this chapter. The phase mismatch error, parametrised in terms of

$$\delta\beta_{pre}(z) = \delta\beta_w(z) = \partial_w \Delta\beta \cdot \delta w(z), \quad (5.22)$$

is shown in Figure 5.19a, while the relative phase matching spectrum is shown in Figure 5.19b as a function of $\Delta\beta$. One can note that, due to the presence of waveguide inhomogeneities, the phase matching spectrum does not resemble the ideal sinc^2 profile and its maximum intensity is 40% of the ideal one.

As we have seen in the previous sections, the process under consideration has a $L_{max} \approx 1\text{cm}$. Therefore, we can consider the waveguide as composed of ten 1cm -long homogeneous regions, whose phase relations change from section to section but are constant within each of them. As can be seen in Figure 5.19, this approximation is sufficient to reconstruct almost perfectly the phase matching spectrum of the noisy waveguide.

The proposed algorithm to correct the phase matching spectrum of an inhomogeneous waveguide is very simple. The temperature of each waveguide section is varied within a predefined range, while keeping the other sections constant at their previous set temperature. During this temperature sweep, the phase matching spectrum intensity maximum is monitored. If a new maximum is found, the relative temperature settings are stored and used as starting point for the optimisation of the next waveguide section. The idea behind this algorithm is that the phase matching intensity can increase only if the section being tuned improves its coherence with the rest of the sample. Gradually tuning each section ideally will flatten the noise profile and restore the ideal phase matching spectrum.

To numerically evaluate the validity of this algorithm, we write a Python script that creates a temperature profile distribution $\delta T(z)$, given the temperature of the individual sections of the waveguide. In particular, $\delta T(z)$ is calculated as a step function representing the set temperature in each of the sections, convoluted with a Gaussian kernel¹ in order to simulate a smooth temperature profile in a simple way. Then, for a given $\delta T(z)$, the relative phase mismatch variation

$$\delta\beta_{post}(z) = \delta\beta_T(z) = \delta T(z) \cdot \partial_T \Delta\beta \quad (5.23)$$

is calculated. Finally, we evaluate the phase matching spectrum of the resulting sample having a noise profile

$$\begin{aligned} \delta\beta(z) &= \delta\beta_{pre}(z) + \delta\beta_{post}(z) \\ &= \delta\beta_w(z) + \delta\beta_T(z). \end{aligned}$$

We compare it to the best phase matching spectrum retrieved until the current iteration and retain the temperature profile $\delta T(z)$ that provides the spectrum with the highest efficiency. For a correct reconstruction of the phase matching spectrum we tune one section at a time and retain the $\delta T(z)$ profile that maximises the phase matching spectrum.

In Figure 5.20, the result of eight optimisation runs on the waveguide presented in Figure 5.19 are shown. The resulting temperature profile $\delta T(z)$ necessary to compensate the fabrication errors is shown in Figure 5.20a. In Figure 5.20b, the final $\delta\beta(z)$ after compensation can be seen. The Figure shows that the reconstruction algorithm converges to a temperature profile that compensates the long range deviations of the original phase matching error profile $\delta\beta_{pre}(z)$; indeed, the final $\delta\beta(z)$ more closely resembles the case of a waveguide with Gaussian noise, whose phase matching spectrum is only mildly degraded, as shown in section 5.2. The phase matching spectrum of the optimised waveguide is illustrated in Figure 5.20c. It can be seen that the ideal sinc² is almost fully reconstructed. The small offset of the sinc is due to the offset resulting from the optimisation algorithm. Once the ideal profile is retrieved, a constant shift of the temperature profile can be used to retune the process to the correct wavelength.

¹The σ of the kernel is $2\mu\text{m}$. It is chosen by hand to provide a smooth temperature function resembling a physically meaningful one. For better results, it would be necessary to solve the heat diffusion equation in the LN crystal, for every given temperature profile.

5.5. General theory of waveguide inhomogeneities

This simulation shows that the proposed algorithm is able to correct the phase matching spectrum of waveguides affected by fabrication errors. Albeit retrieved for a specific process, we believe that the algorithm can be applied to virtually any waveguide to improve the quality of the phase matching spectrum in postprocessing.

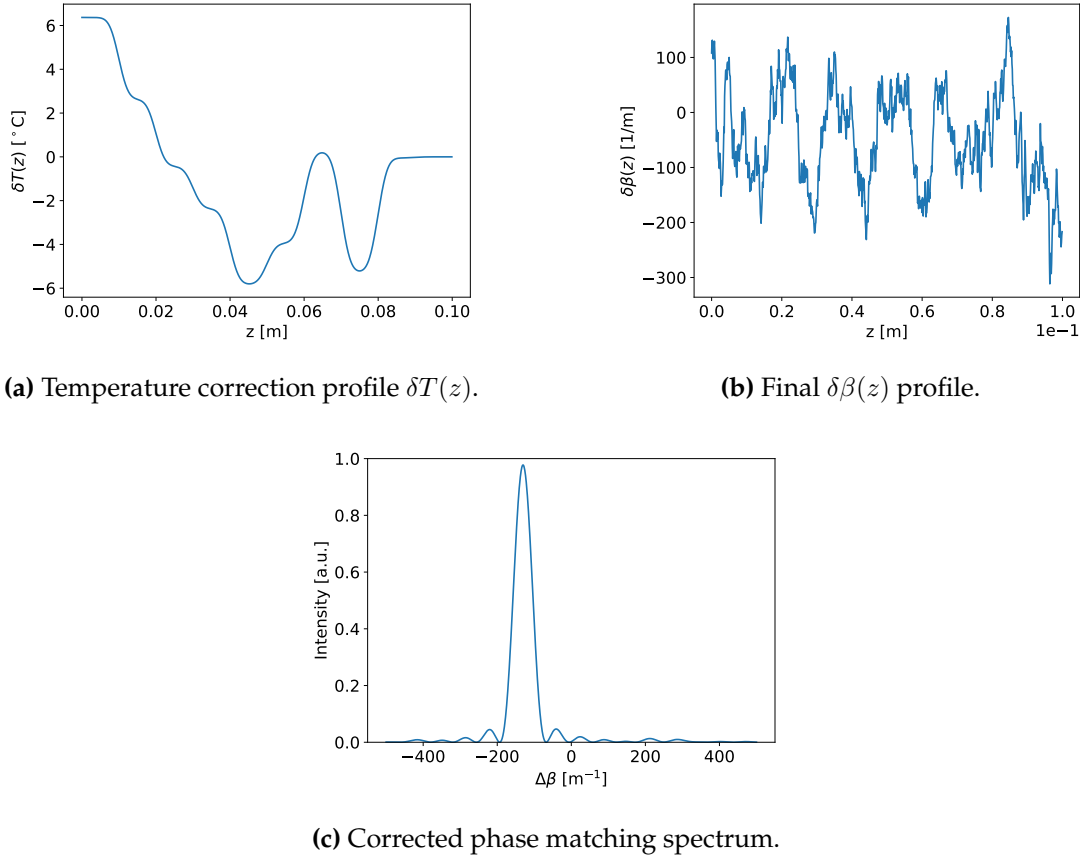


Figure 5.20. – Simulated temperature correction profile and final phase matching spectrum the waveguide reported in Figure 5.19.

5.5. General theory of waveguide inhomogeneities

The effect of fabrication imperfections on the phase matching spectrum of nonlinear process has attracted attention in the past decades. Many studies, including the one presented so far, have discussed to different degrees the relation between fabrication errors in waveguides [83, 84, 88, 90–92, 104, 105] and in fibres [78, 94, 102, 106] and their spectral performance. Comparing all these studies, we note striking similarities among their results: all the analysed systems exhibit a close connection between the device length, the amount of imperfections and the overall performance of the non-

linear process. This observation suggests the existence of a scaling law, common to all nonlinear systems, determining the length where the process becomes sensitive to the imperfections present in the system.

In the following, we show that, under some minor approximation, such a scaling law indeed exists and derive a general, system-independent framework to understand the effect of imperfections on the performance of a wide class of nonlinear systems.

5.5.1. Mathematical formulation

Consider a nonlinear process in a system of length L characterised by a momentum mismatch

$$\Delta\beta = \sum_i s_i \beta_i = \sum_i s_i \frac{2\pi n_i(\lambda_i)}{\lambda_i} + \beta_G, \quad (5.24)$$

where β_i , n_i and λ_i are the propagation constant, the refractive index and the wavelength of the i -th field, $s_i = \pm 1$ is a sign that depends on the type of process considered and β_G is the poling period wavevector - if needed; for example, Eq. (5.24) reduces to $\Delta\beta = \beta_3 - \beta_2 - \beta_1$ for a copropagating, birefringent three wave mixing. Note that Eq. (5.24) is valid for any general wave mixing process.

As previously discussed, the phase matching spectrum of the nonlinear process, normalised per unit length, is defined as

$$\phi = \frac{1}{L} \int_0^L e^{i \int_0^z \Delta\beta(\xi) d\xi} dz, \quad (5.25)$$

where z denotes the propagation axis along the system and scaling constants have been neglected since they do not affect the shape of the phase matching spectrum. Note that Eq. (5.25) sets the ideal maximum efficiency is 1. Typically, the complex phase matching amplitude ϕ is expressed as a function of the wavelengths or the frequencies of the fields involved in the process. This however prevents a direct comparison of different systems, since $\Delta\beta$ depends nonlinearly on these parameters, as shown in Eq. (5.24). Therefore, in the following, we will consider the complex phase matching amplitude ϕ as a function of the $\Delta\beta$.

Under ideal fabrication and operation conditions, the momentum mismatch $\Delta\beta$ is constant along the sample. However, fabrication imperfections and/or non-ideal operating conditions affect the phase mismatch of the process and they can be described as a position-dependent $\Delta\beta(z)$. If the variation of the momentum mismatch is sufficiently small such that it can be considered frequency-independent [89], we can use the *decoupling approximation* introduced in Eq. (5.17)

$$\Delta\beta(z) \approx \Delta\beta_0(\lambda) + \sigma\delta\beta(z). \quad (5.26)$$

With the decoupling approximation and a change of variables $z/L \rightarrow z'$ and $\xi/L \rightarrow \xi'$,

5.5. General theory of waveguide inhomogeneities

the integral in (5.25) can be rewritten as:

$$\phi(\Delta\beta_0 L) = \int_0^1 e^{i\Delta\beta_0 L z'} \cdot e^{i\sigma L \int_0^{z'} \delta\beta(L\xi') d\xi'} dz', \quad (5.27)$$

where the first exponential term leads to the usual sinc dependence of the phase matching amplitude ϕ on the mismatch $\Delta\beta_0$, while the second exponential term describes the effect of the noise $\sigma\delta\beta(z)$ on the system. Eq. (5.27) can also be understood as the Fourier transform of the rectangular function representing the crystal, multiplied by a phase factor introduced by the imperfections.

Setting $\sigma = 0$ in Eq. (5.27) yields

$$\phi(\Delta\beta_0 L) = \int_0^1 e^{i\Delta\beta_0 L z'} dz',$$

which shows that the phase matching spectrum of all noiseless systems is identical, bar a scaling factor given by the length of the system.

A similar scaling law can be found for the second integral in Eq. (5.27). In fact, the exponent

$$\sigma L \int_0^{z'} \delta\beta(L\xi') d\xi' dz',$$

representing the non-flat phase introduced by waveguide variations, highlights that all systems with the same *noise-length product* σL and noise profile $\delta\beta(z)$, defined for $z \in [0, L]$, will exhibit the same phase matching spectrum. This allows us to study the effect of variations of the momentum mismatch on a system with unit length and then extrapolate the results to systems with any length, provided the correct scaling $\Delta\beta_0 \rightarrow \Delta\beta_0 L$ and $\sigma \rightarrow \sigma L$ is applied.

5.5.2. Simulation of inhomogeneous systems

In the previous section it was shown that the phase matching spectrum $\phi(\Delta\beta_0)$ is fully characterised by the noise-length product σL and the noise profile $\delta\beta(z)$. Therefore, in the following we study the impact of these two parameters on the profile of the phase matching spectrum.

The scaling law

$$\begin{aligned} \Delta\beta_0 &\rightarrow \Delta\beta_0 L \\ \sigma &\rightarrow \sigma L \end{aligned}$$

presented in the previous section allows us to consider a general nonlinear system with $L = 1\text{m}$ and $\sigma \in [0.001, 1000] \text{m}^{-1}$ without loss of generality. With the help of the package `PyNumericalPhasematching`, we model $\delta\beta(z)$ as a stochastic process with a $1/f$

spectral density to describe the long range correlations that can arise due to fabrication imperfections and/or under non-ideal operating conditions of the nonlinear system, as discussed in section 5.2.2. For each value of σL , we randomly generate 100 different $\delta\beta(z)$ profiles and calculate the relative phase matching spectra as a function of $\Delta\beta_0$ using a piecewise approximation [102] of Eq. (5.27):

$$\phi(\Delta\beta_0) = \sum_{n=1}^N \text{sinc}\left(\frac{\Delta\beta_n \Delta z_n}{2}\right) e^{i\frac{\Delta\beta_n \Delta z_n}{2}} \cdot e^{i\sum_{m=1}^{n-1} \Delta\beta_m \Delta z_m}, \quad (5.28)$$

where Δz is the mesh discretisation along the z axis, such that $\sum_n \Delta z_n = L$, and $\Delta\beta_n = \Delta\beta_0 + \delta\beta(z_n)$.

To quantify the difference between the phase matching amplitudes ϕ_{noisy} of a system with imperfections and ϕ_{ideal} of an ideal one, i.e. where $\delta\beta(z) = 0$, we introduce the fidelity \mathcal{F} , defined as

$$\mathcal{F} = \frac{\max_{\tau} \int_{-\infty}^{+\infty} I_{ideal}(\Delta\beta_0) I_{noisy}(\Delta\beta_0 - \tau) d\Delta\beta_0}{\int_{-\infty}^{+\infty} I_{ideal}^2(\Delta\beta_0) d\Delta\beta_0}, \quad (5.29)$$

where $I = |\phi|^2$. In Eq. (5.29), the two curves are normalised such that $\int |\phi_{noisy}|^2 d\Delta\beta = \int |\phi_{ideal}|^2 d\Delta\beta$, since this quantity is conserved in the presence of momentum mismatch variation [107]. Using this definition, the fidelity approaches 1 if the effect of noise on the phase matching spectrum is negligible and tends to 0 if the contribution of the noise is dominant.

We calculate the fidelity \mathcal{F} for the simulated phase matching spectra and the results are plotted in Figure 5.21. The results can be well approximated by a Lorentzian-like fitting curve, shown in Figure 5.21 with a solid orange line:

$$\mathcal{F}(\sigma L) = \frac{1}{[1 + A \cdot (\sigma L)^B]^C}, \quad (5.30)$$

with $A = 5.4 \pm 0.3 \times 10^{-3}$, $B = 2.12 \pm 0.04$, $C = 0.35 \pm 0.02$.

The simulations show that systems with $\sigma L \leq 10$ have a fidelity close to 1, while for $\sigma L > 10$ the average fidelity rapidly drops below 0.5. Therefore, we can assume that the inequality

$$\sigma L \leq 10 \quad (5.31)$$

defines as a general design principle for these systems.

5.5.3. General design rule for nonlinear systems

We now move away from the abstract description in terms of $\Delta\beta$, to study how fabrication imperfections directly relate to the phase matching spectrum and to show how the condition $\sigma L \leq 10$ aids in designing a given nonlinear process. For simplicity, we assume that all the imperfections are due to a single system parameter f . For example, f can represent the local temperature of the system during operations, the width

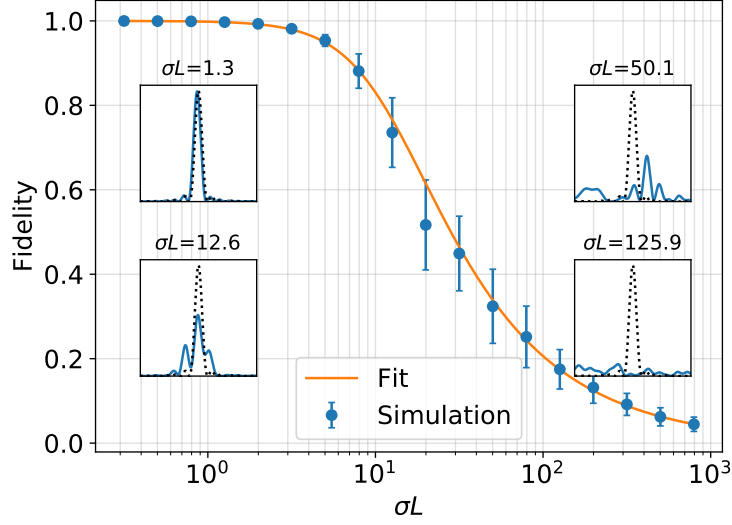


Figure 5.21. – Simulated reduction in fidelity \mathcal{F} as the noise-length product σL of a nonlinear system increases. Errorbars indicate the standard deviations calculated from 100 randomly generated samples. The solid orange line corresponds to the best fit of the average fidelity and follows the relation given by Eq. (5.30). The insets show examples of simulated phase matching spectra (solid blue line) compared to the ideal phase matching spectra (dotted black line), for chosen σL values.

of a waveguide or the holes' diameter in a PCF. With a suitable model of the system, one can relate the noise amplitude σ to the variation of the parameter f with a Taylor expansion $\sigma \approx |\partial_f \Delta\beta| \delta f$. Therefore, the condition $\sigma L \leq 10$ can be rewritten as

$$\sigma L \leq 10 \Rightarrow \delta f \cdot L \leq \frac{10}{|\partial_f \Delta\beta|}. \quad (5.32)$$

In this form, the trade-off between the physical parameters characterizing the sample, namely its length L and the error δf , is explicitly revealed. Note that Eq. (5.32) is extremely similar to Eq. (5.4). The former has been derived via statistical analysis on a many different systems, while the latter has been derived from considerations on the phase matching spectrum of an ideal waveguide.

If $|\partial_f \Delta\beta|$ is known, with the help of Eq. (5.32) one can bound the maximum length of the system to the maximum error during fabrication/operation in order to ensure high fidelity. This can provide crucial information during the design of samples and experiments: if the error δf cannot be further reduced, then the maximum length of the system to achieve high fidelity is bounded by Eq. (5.32); viceversa, if the length of

the sample is constrained by the experiment, then the error δf has to be minimised to satisfy Eq. (5.32).

As an example, we consider the restraints set by Eq. (5.32) on the four wave mixing, seeded parametric downconversion process in a PCF described in [102]. In the paper, the authors show that a 3m-long fibre presents a very distorted phase matching spectrum, while a 15-cm long piece of the same fibre is characterised by a much cleaner but still imperfect spectrum. In particular, they investigate the effects of the variation of the pitch Λ of the holes and their diameter d around the ideal design parameters $\Lambda_0 = 1.49\mu\text{m}$ and $d = 0.6414\mu\text{m}$. Using the Sellmeier equations provided in [108], we can estimate the effect of the variation of these parameters by calculating the partial derivatives

$$\begin{aligned} |\partial_{\Lambda}\Delta\beta|_{\Lambda_0,d_0} &\approx 2 \times 10^{-4} \mu\text{m}^{-2} \\ |\partial_d\Delta\beta|_{\Lambda_0,d_0} &\approx 1.5 \times 10^{-2} \mu\text{m}^{-2} \end{aligned} \quad (5.33)$$

Since $\partial_d\Delta\beta$ is two orders of magnitude higher than $\partial_{\Lambda}\Delta\beta$, the resulting phase matching spectrum is much more sensitive to variations of the holes' diameter d rather than to variations in the pitch.

From the observation that the reported phase matching spectrum is already degraded for PCF longer than 30cm (which implies that $\sigma L \geq 10$); from this, we can infer that the original 3m-long PCF had a $\sigma L \geq 100$. Using Eq. (5.30) the expected fidelity for this noise-length product is below 0.2, thereby explaining the distorted phase matching spectrum measured in [102]. Finally, combining Eqs. (5.32) and (5.33), we can estimate that it is necessary to limit $\delta\Lambda$ (δd) below 1.1% (0.078%) to achieve phase matching spectra with a high fidelity in a 3m-long fibre, clearly a challenging task.

5.5.4. Comparison with simulations of different physical systems

The *decoupling approximation* introduced in Eq. (5.17) relies on the assumption that the refractive index variation due to imperfections can be considered independent of the wavelength [89]. To show that this approximation is indeed valid in many cases of interest, we now compare the results presented in Figure 5.21 with simulations of a number of systems affected by different sources of imperfections, all presenting a $1/f$ noise spectrum.

The investigated systems are:

- (a) TM-polarised, type 0 SHG (1550nm \rightarrow 775nm) in Z-cut Ti:LN channel waveguides, with nominal width $w = 7\mu\text{m}$ and errors δw in the waveguide width;
- (b) type II SHG (1550nm \rightarrow 775nm) in Z-cut Rb:KTP channel waveguides, with nominal waveguide width $w = 3\mu\text{m}$, diffusion depth $d=8\mu\text{m}$ and errors δw in the waveguide width;
- (c) type II, collinear SFG (1550nm+875nm \rightarrow 559nm) in a Z-cut bulk LN crystal, operated at 190°C with an inhomogeneous temperature profile with maximum excursion δT ;

5.5. General theory of waveguide inhomogeneities

- (d) four wave mixing SFG (1545nm+805nm→1058.5nm) in a PCF [102]; the fibre nominal pitch is $\Lambda = 1.49\mu\text{m}$ and the holes' diameter is 641.4nm with a noise which has a maximum excursion of δd .

The lengths of the simulated devices and the fabrication errors are reported in Table 5.1.

For each system (a-d), we calculate the phase matching spectrum and the fidelity \mathcal{F} of 20 randomly generated samples for every combination of the parameters in Table 5.1. To aid in visualisation, a randomly chosen subset of the calculated values of \mathcal{F} is presented in Figure 5.22. It is apparent that the fidelity of the simulated processes closely follows the model derived in the previous section, despite having different noise sources and being realised in vastly disparate physical systems. This shows that the model presented provides a general framework to analyse the effects of inhomogeneities on the phase matching performance of a wide range of nonlinear systems.

In chapter 7, we will use this model to understand the fabrication constraints on lithium niobate on insulator devices.

(a)	$L = 5, 10, 40, 80 \text{ mm}$ $\delta w = 0.05, 0.1, 0.25, 0.5 \mu\text{m}$
(b)	$L = 5, 10, 15, 20, 25, 30 \text{ mm}$ $\delta w = 0.05, 0.1, 0.2, 0.3, 0.5 \mu\text{m}$
(c)	$L = 5, 10, 20, 40 \text{ mm}$ $\delta T = 0.1, 0.2, 0.5, 1.0, 2.0 \text{ }^\circ\text{C}$
(d)	$L = 0.5, 1, 2, 3 \text{ m}$ $\delta d = 0.64, 6.41, 64.14, 641.44 \text{ pm}$

Table 5.1. – Fabrication parameters used for the simulation of (a) Ti:LN waveguides, (b) channel Rb:KTP waveguide, (c) bulk LN crystal and (d) photonic crystal fibre. Details about the processes are provided in the main text and in the appendix.

Summary

In this chapter we presented two models for the analysis of fabrication imperfections in TWM systems and applied them to study the properties of Ti:LN waveguides. Dicing a sample into 1cm-long pieces and measuring their phase matching spectra, we verified the predictions of these models and, at the same time, we characterised our fabrication process. This analysis provided also useful insights to devise new techniques to correct in post-processing the fabrication imperfections. Finally, we presented a general theory describing the effect of fabrication imperfections on any type of nonlinear device.

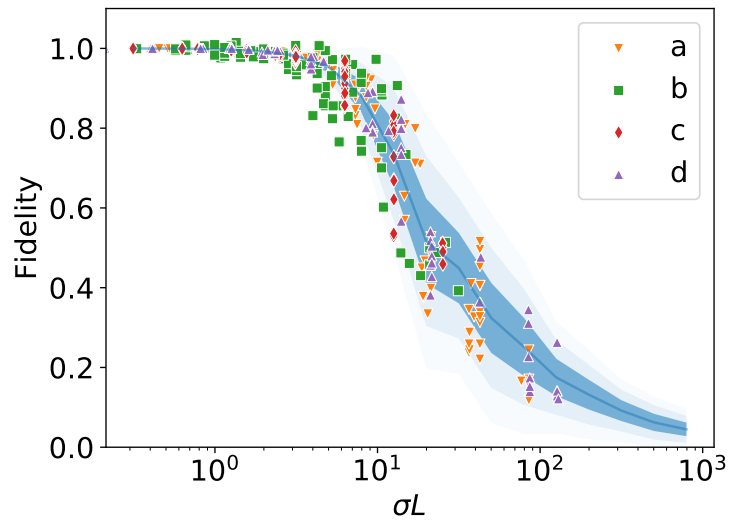


Figure 5.22. – Fidelity \mathcal{F} simulated for different real systems in the presence of $1/f$ noise on a fabrication/operation parameter. The solid blue line represents the average fidelity as estimated by the general model, while the shaded areas correspond to 1,2 and 3 standard deviations. The processes reported here are a) SHG type 0 in Ti:LN waveguides, b) SHG type II in Rb:KTP waveguides, c) collinear SFG type II in bulk LN crystal and d) four-wave mixing SFG in PCF.

Second harmonic losses

Contents

6.1 Measurement Strategy and Theory	124
6.2 Fitting procedure	127
6.3 Results	128

In section 3.3.1, we discussed the Fabry-Pérot technique for the estimation of propagation losses in single mode waveguides. Unfortunately, this resonance-based method is generally unsuitable in waveguides that are spatially multi-mode for the probe field. This is due to

the fact that it is experimentally very difficult to couple light into the waveguide such that only a single propagation-mode of the waveguide is excited. These different spatial modes have disparate dispersion properties, leading to different free spectral ranges (FSRs) for the various spatial modes. The resulting transmitted power will consist of multiple resonance conditions with unknown magnitude and phase, generally making the problem intractable. Under certain conditions the losses can still be obtained from such a measurement, but this requires the fulfillment of a number of conditions which are, in general, not satisfied [71].

For this reason, devices implementing multi-colour processes, such as difference or sum-frequency generation, typically have their losses characterised at the longest wavelength, where the waveguide is single-mode. This value is often used to estimate or bound the losses at shorter wavelengths. However, one cannot know *a priori* the exact relationship between the losses at different wavelengths. This is problematic when the losses at the shorter wavelength/s are critical, or example in frequency converters that aim to produce a field close to the transparency cut-off region of a particular material [80].

In this chapter we present a method for loss characterisation in such systems by measuring the phase matching spectrum of the second harmonic (SH) process as the pump (fundamental) wavelength is varied over the phase matching spectrum. The highly intricate measured phase matching spectrum is compared to theory in order to bound the second harmonic losses using a mean squared error method. This method also allows for selective measurement of the losses of the different spatial modes, as the different spatial modes have different dispersion and therefore different phase matching spectra. This allows one to probe the second harmonic losses for *the spatial mode of one's choosing* by centering the wavelength of the fundamental pump field to the various phase matching profiles of the second harmonic modes. The approach is quite general and in principle could be extended to other processes such as sum frequency generation and

type II second-harmonic generation processes.

The results presented in this chapter appear in publication IV, where the author of this thesis is the main contributor.

6.1. Measurement Strategy and Theory

In the standard low-finesse Fabry-Pérot loss measurement [70], the power transmitted through a waveguide is recorded when scanning a probe field over wavelengths where the system is single-mode. This method requires that one knows the reflectance of the end facets to a high precision. Given this condition, the interference effects observed in the transmitted power can be used to determine the losses inside the resonator at the same wavelength as the probe field.

The general strategy employed in the method presented here is that, in addition to first determining the losses at the fundamental wavelength using the standard method, we also measure the interferometric fringing that one observes in the generated second harmonic field when scanning the pump over the wavelengths where phase matching occurs. One can then fit the obtained phase matching spectrum to a model of this system and gain information about the losses of the second harmonic field. A single spatial-mode for the second harmonic field is guaranteed due to the fact that the single-mode pump field is phase matched to only a single second harmonic spatial-mode over the wavelength region of interest. The unique dispersion properties of different spatial modes generally ensures that this is the case.

The system is modeled using an extension of the second harmonic generation theory presented by Berger [109]. In this method, the internal second harmonic fields are first described and thereafter solved simultaneously in order to find a self-consistent cavity solution. In order to arrive at an analytic expression it is assumed that the pump field, at the fundamental frequency, is not depleted by the nonlinear process. This assumption is trivial to establish experimentally by correctly choosing the power in the pump field. It may be possible to remove this restriction by considering a numerically based iterative approach [110]. However, this will further complicate the treatment and will not provide an analytic expression.

The circulating fundamental field *amplitude* travelling in the cavity in the forward direction $A_\omega^f(0)$ is given by the usual Fabry-Pérot resonance condition

$$A_\omega^f(0) = A_{in} \frac{\tau_{\omega,0}}{1 - \rho_{\omega,0}\rho_{\omega,L} \cdot e^{-i2k_\omega L} \cdot e^{-\alpha_\omega L}} \quad (6.1)$$

where k_ω [m^{-1}] is the wavevector of the fundamental field, α_ω [m^{-1}] are the intensity losses for the fundamental field, $\rho_{\omega,0/L}$ is the complex reflectivity for the input/output facet at ω and $\tau_{\omega,0}$ is the complex transmission of the input facet at ω . Energy conservation ensures that $|\rho_\omega|^2 + |\tau_\omega|^2 = 1$. Note that from these definitions one can also express the circulating fundamental field *amplitude* travelling in the backwards direction, $A_\omega^b(L) = \rho_{\omega,L} A_\omega^f(0) e^{ik_\omega L}$.

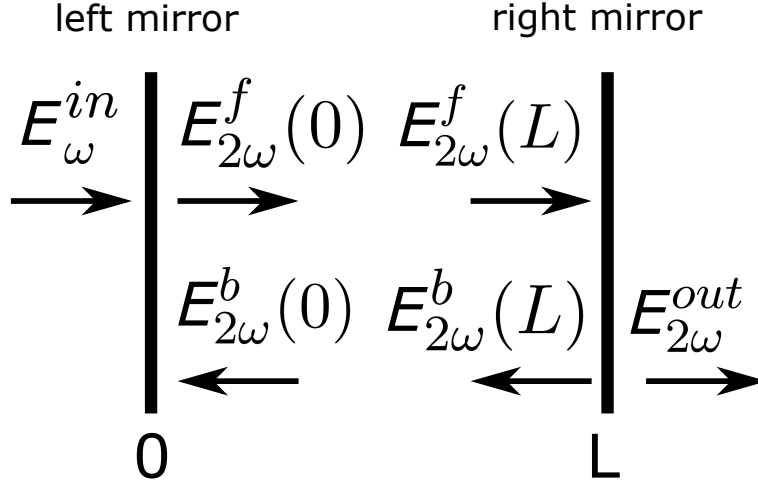


Figure 6.1. – Sketch detailing the forward and backward propagating waves used for theoretical treatment of the waveguide resonator.

With the non-pump depletion approximation, the generated second harmonic field *amplitude*, in presence of losses $\alpha_{2\omega}$, can be calculated from Eq. (2.28) as

$$\frac{dA_{2\omega}}{dz} = i\gamma[A_\omega e^{-\alpha_\omega z/2}]^2 e^{i\Delta k z} - \frac{\alpha_{2\omega}}{2} A_{2\omega}, \quad (6.2)$$

where $A_{\omega/2\omega}(z)$ is the fundamental/second harmonic field amplitude at position z , $\alpha_{2\omega}$ [m^{-1}] represents the (intensity) losses of the second harmonic field, $\gamma = \kappa_{2\omega}\theta/2$ is the nonlinear coupling coefficient determining the strength of the nonlinear process, $\Delta k = 2k_\omega - k_{2\omega} + k_{QPM}$ [m^{-1}] is the wave vector mismatch between the fundamental and second harmonic field, where $k_{QPM} = 2\pi/\Lambda$ is the grating vector due to periodic poling (with period Λ) and $k_{2\omega}$ [m^{-1}] is the wave vector of the second harmonic field. Note that we included in Eq. (6.2) the effect of the losses in the fundamental field by considering a spatially dependent fundamental amplitude in the form $A_\omega e^{-\alpha_\omega z/2}$.

Integration of Eq. (6.2) with initial conditions $(A_\omega(z_0), A_{2\omega}(z_0))$ over a crystal length L yields the component of the second harmonic amplitude after passing through the length z due to the nonlinear interaction

$$\begin{aligned} A_{2\omega}(z) &= SH_z(A_\omega(z_0), A_{2\omega}(z_0)) \\ &= 2i\gamma \frac{e^{(\alpha_{2\omega} - 2\alpha_\omega + 2i\Delta k)z/2} - 1}{\alpha_{2\omega} - 2\alpha_\omega + 2i\Delta k} A_\omega^2 e^{-\alpha_{2\omega}z/2} + A_{2\omega} e^{-\alpha_{2\omega}z/2}. \end{aligned} \quad (6.3)$$

To derive an expression for the circulating second harmonic field amplitude, one defines the second harmonic field *amplitudes* travelling in the forward direction at the left and right sides of the sample, $A_{2\omega}^f(0)$ and $A_{2\omega}^f(L)$, and in the backwards direction at the left and right sides of the sample, $A_{2\omega}^b(0)$ and $A_{2\omega}^b(L)$, respectively, as illustrated

in Figure 6.1. The relation between these four amplitudes can be described by the following system:

$$A_{2\omega}^f(L) = SH_L \left(A_{2\omega}^f(0), A_{2\omega}^f(0) \right) e^{ik_{2\omega}L} \quad (6.4a)$$

$$A_{2\omega}^b(L) = \rho_{2\omega,0} A_{2\omega}^f \quad (6.4b)$$

$$A_{2\omega}^b(0) = SH_L \left(A_{2\omega}^b(L), A_{2\omega}^b(L) \right) e^{ik_{2\omega}L} \quad (6.4c)$$

$$A_{2\omega}^f(0) = \rho_{2\omega,L} A_{2\omega}^b, \quad (6.4d)$$

where $A_{2\omega}^b(L) = \rho_{\omega,L} A_{2\omega}^f(0) e^{-ik_{\omega}L} e^{-\alpha_{\omega}L/2}$. The total circulating second harmonic field at steady-state can be found by simultaneously solving these equations, thereby ensuring self-consistency of the SH field amplitude.

Solving this set of equations, propagating through the right side mirror in order to find the second harmonic field exiting the cavity and substituting Eq. (6.1) we find the output second harmonic field amplitude as

$$\begin{aligned} A_{2\omega}^{out} &= \tau_{2\omega,L} A_{2\omega,L}^f \\ &= \tau_{2\omega,L} \gamma (A_{2\omega}^{in})^2 \frac{\tau_{\omega,0}^2}{(1 - \rho_{\omega,0} \rho_{\omega,L} e^{-2ik_{\omega}L - \alpha_{\omega}L})^2} \times \\ &\quad iL \operatorname{sinc} \left(\frac{(\Delta k - i\alpha_{2\omega}/2 + i\alpha_{\omega})L}{2} \right) e^{\frac{(\Delta k - i\alpha_{2\omega}/2 + i\alpha_{\omega})L}{2}} \times \\ &\quad \frac{1}{1 - \rho_{2\omega,0} \rho_{2\omega,L} e^{-i2k_{2\omega}L - \alpha_{2\omega}L}} \times \\ &\quad \left(1 + \rho_{2\omega,0} \rho_{\omega,L}^2 e^{-ik_{2\omega}L} e^{-i2k_{\omega}L} e^{-\alpha_{2\omega}L/2 - \alpha_{\omega}L} \right) e^{-\alpha_{2\omega}L/2 - ik_{2\omega}L}. \end{aligned} \quad (6.5)$$

This equation is split into four terms in order to highlight the factors that contribute to the observed interference fringes, as noted by Berger [109]. The **first term** represents the Fabry-Pérot interference of the fundamental field; the **second term** is the spectrum of the second harmonic signal generated in a single pass; the **third term** is the Fabry-Pérot interference of the second harmonic field; the **final term** represents the phase mismatch between the nonlinear polarisation and the second harmonic field over half of a cavity round trip or, equivalently, the phase between the forward and backwards propagating second harmonic waves.

The second harmonic power exiting the system when pumped at wavelength λ is then calculated squaring Eq. (6.5), $I_{2\omega}(\lambda) = |A_{2\omega}^{out}(\lambda)|^2$.

The profile of $I_{2\omega}(\lambda)$ depends on the complex facet reflectivities $\rho = |\rho|e^{i\phi}$ at $z = 0$ and $z = L$, the fundamental and SH losses $\alpha_{\omega/2\omega}$ and on the cavity length L . Qualitatively, one can observe that these parameters affect the shape of $I_{2\omega}(\lambda)$ in different ways: the length L of the sample affects the width of the spectrum and the free spectral range (FSR) of the primary frequency component of the fringing, the contrast of the fringes depends on the magnitude of both the fundamental and second harmonic losses and the complicated internal structure of the fringing is dependent on the facet

reflectivities and the crystal length. In the following section it is shown that it is possible to find an optimised fit to these free variables, thereby providing an estimate of the value of $\alpha_{2\omega}$.

6.2. Fitting procedure

The fit of the theory to the measured data is undertaken in steps in order to constrain the range of some of the parameters to physically acceptable values. First, both the model $I_{2\omega}(\lambda)$ and the measured data $I_{meas}(\lambda)$ are normalised to have unitary maximum intensity. Next, the loss of the fundamental field α_{ω} is fixed to the value measured using the standard low-finesse loss technique [70]. This measurement is performed scanning the fundamental field over wavelengths slightly shifted away from phase matching so that the second harmonic process does not influence the measurement. Next, the length L_0 of the sample is retrieved from the free spectral range of the fundamental field. In particular, by Fourier transforming $I_{meas}(\lambda)$, the length L_0 is estimated from the FSR or the primary frequency components, corresponding to the interference of the fundamental field given by Eq. (6.1). Subsequently, the central phase matching wavelength λ_{pm} is estimated from the data using a weighted average of the recorded wavelengths, where the second harmonic spectral intensity is used as weights. From λ_{pm} , the poling period Λ_0 that best centres the phase matching spectrum is chosen.

After determining the center values of these parameters, the theoretical phase matching spectrum $I_{2\omega}(\lambda)$ is then fitted to the measured data $I_{meas}(\lambda)$. As there are a total of 9 free parameters to be optimised¹, the fit of these quantities is performed in two steps. At first, assuming $\alpha_{2\omega} = \alpha_{\omega}$, the phases ϕ are optimised. The optimal ϕ are used as initial parameters in the second step of the fit, where the model $I_{2\omega}(\lambda)$ is fitted again to the measured data. At this stage, the length L , the poling period Λ_0 , the second harmonic losses $\alpha_{2\omega}$, the modules and phases of the facet reflectivities $\rho_{\omega/2\omega,0/L}$ are considered as fitting parameters. The length L is constrained to a $500\mu\text{m}$ range around L_0 , the poling period Λ_0 is constrained to be within 1% of Λ_0 , while the phases retrieved in the first step of the optimisation are used as initial parameters for the fitting algorithm.

The fitting routine solves a nonlinear least square minimisation problem using Python's routine `scipy.optimize.least_squares`. The least square minimisation routine minimises the mean squared error (MSE) between the model $I_{2\omega}(\lambda)$ and the data $I_{meas}(\lambda)$, i.e.

$$MSE = \frac{1}{2N} \sum_{i=1}^N |I_{2\omega}(\lambda_i) - I_{meas}(\lambda_i)|^2,$$

where N is the number of measured datapoints. Due to the complexity of the model, the initial values for the reflectivities of the facets and $\alpha_{2\omega}$ are initialised with random weights and the minimisation is repeated 10 times to find the best set of parameters. To obtain physically meaningful results, we bound the parameters of the fit during the

¹Four reflectivity amplitudes $|\rho|_{\omega/2\omega,0/L}$, four reflectivity phases $\phi_{\omega/2\omega,0/L}$ and $\alpha_{2\omega}$

minimisation. In particular, the phases of ρ are constrained between $[0, 2\pi]$ and the reflectivities are set to the calculated Fresnel value and are allowed to vary slightly. Moreover, as some measured spectra showed asymmetries attributable to waveguide inhomogeneities [105], only the central lobe of the second harmonic spectrum was used during the fit.

Note that the length and the poling period are allowed to vary slightly in this fit in order to allow some flexibility, required due to phase matching distortions in the measured data. Furthermore, the mirror reflectivities ρ are treated as complex numbers in order to account for an unknown phase shift on reflection at the end facets of the sample. This phase shift can take into account the unknown phase shifts present in a quasi-phase matched sample: in such samples, the length of the first and final domains are generally unknown and will impart an unknown phase shift on the two fields, which can be absorbed by the phase term in the complex reflectivities.

As a final note, the model presented in Eq. (6.5) requires the refractive indices of both the fundamental and second harmonic fields as the fundamental pump field is varied - the Sellmeier equation. For the titanium indiffused waveguides investigated here these dispersion relations have been calculated as detailed in section 3.1.2.

6.3. Results

We apply the described measurement technique in order to retrieve the losses of a 31.2mm long $7\mu\text{m}$ -wide titanium indiffused waveguide quasi-phase matched (with a $16.8\mu\text{m}$ poling period) for type 0 second harmonic generation in the TM00 spatial mode when pumped with a fundamental field at 1525nm. This system also supports second harmonic generation in the TM01 mode at around 1480nm. The losses α_ω of each of these phase matching processes at the fundamental wavelength are first found slightly off phase matching. At around 1525nm the fundamental field losses were found to be 0.21 ± 0.04 dB/cm and at around 1481nm the losses were found to be 0.24 ± 0.07 dB/cm.

Subsequently, the phase matching spectra of the second harmonic field are recorded as the fundamental wavelength is scanned over the phase matching profile for the TM00 and TM01 second harmonic modes, using the setup shown in Figure 6.2. The measured phase matching spectra and the fits found using the procedure described in the previous section are illustrated in Figure 6.3a.

An excellent qualitative fit between the measured profile and the theory is observed. The frequency of the fringing and the envelope of this central region overlap well. In particular, the insets show zoomed-in regions of the fits that highlight the fact that even the highly complex structure of the interferences is reproduced by the theory. It can be seen, however, that the presence of waveguide imperfections affects the fit of the “side lobes” of the profile. The minimisation routine results in losses of 1.2 ± 0.2 dB/cm for the TM00 second harmonic mode and losses of 1.3 ± 0.1 dB/cm for the TM01 mode, where the errorbar have been derived considering a 1% variation of the MSE.

In order to check the validity of the fit, in particular the performance of the chosen

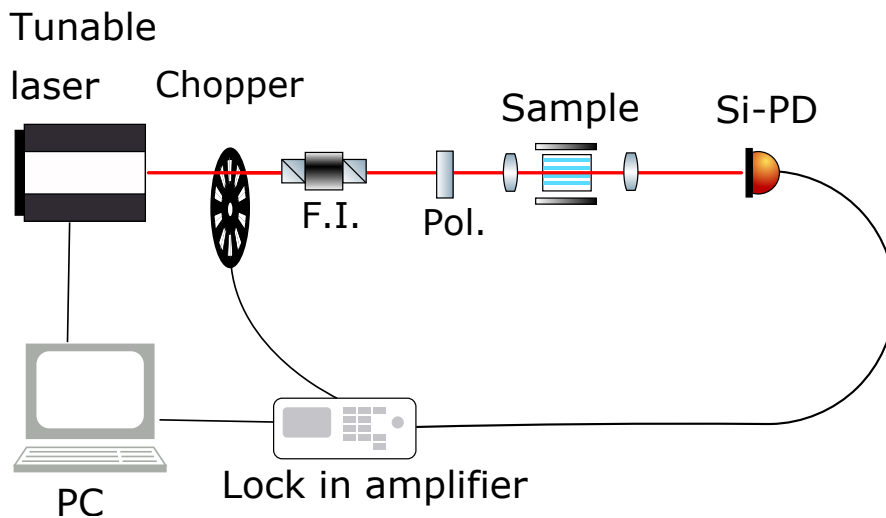


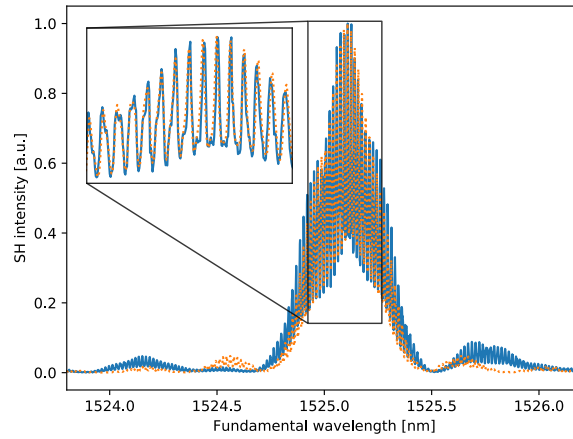
Figure 6.2. – Setup for the measurement of the second harmonic. The light from an IR laser tunable in the range 1460nm-1640nm (EXFO TUNICS) passes through a chopper used in conjunction with a lock-in amplifier to enhance the second harmonic readout. The IR field then passes through a Faraday isolator (F.I.) that suppresses any backreflection from the sample. A polariser is used in front of the sample to set the input polarisation of the fundamental field. Anti-reflection (AR) coated 8mm focal length aspheric lenses are used for the in- and out-coupling. Finally, the second harmonic light is measured via a silicon photodiode connected to a lock-in amplifier.

minimisation routine, we also show the variation of the MSE for both of these fits as the second harmonic losses are varied, holding all other parameters constant. The MSE's found thusly are illustrated in Figure 6.4.

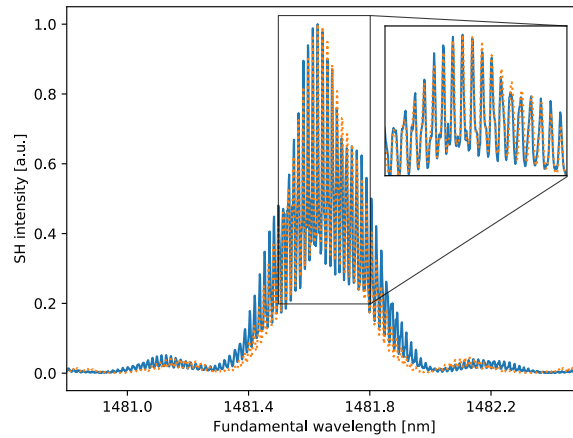
The fitting technique employed here is highly sensitive on the shape of the MSE as a function of $\alpha_{2\omega}$. In particular, the MSE must exhibit a global minimum for the fit to converge to a reasonable value for the SH losses, as is the case for the waveguide analysed in Figure 6.3 and 6.4.

However, a global minimum for the MSE was not always observed. This was seen when investigating a 10mm long waveguide from a second $7\mu\text{m}$ -wide titanium indiffused waveguide. The process under investigation was again a quasi-phase matched, type 0 second harmonic generation in the TM_{00} spatial mode with $\Lambda_0=16.8\mu\text{m}$. This waveguide was found to have losses $\alpha_{\omega}=0.12\pm 0.02\text{dB/cm}$ near to the phase matching wavelength of 1527nm. Using the method described in the previous section, the fit yielded vanishingly small (below 10^{-4} dB/cm) second harmonic losses.

However, as displayed in Figure 6.5, a visual inspection of the fit for different values of $\alpha_{2\omega}$ reveals that, qualitatively, the measured spectrum can be reproduced very well



(a) TM00



(b) TM10

Figure 6.3. – Measured (blue line) and theoretical fit (orange dotted) for the TM00 and TM10 second harmonic mode phase matching spectra.

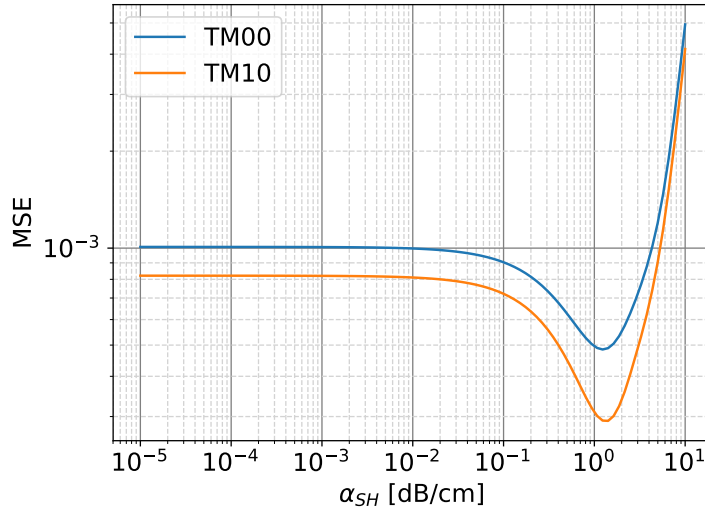


Figure 6.4. – Mean squared error of the sum squared residuals between the model and the data for the TM00 and TM01 second harmonic modes.

with losses up to $\alpha_{2\omega} \leq 0.1$ dB/cm. Furthermore, it can be seen that the fit noticeably degrades at the higher losses of 10dB/cm. The analysis of the MSE for varying second harmonic losses reveals the problem. In contrast to the previously investigated waveguide, the MSE for this waveguide does not show a global minimum. In fact, the MSE asymptotes towards its lowest values at vanishingly small second harmonic losses. In this case, even though the minimisation routine fails to provide an estimate for the SH losses, the inspection of the MSE as a function of $\alpha_{2\omega}$ can still help in determining an upper bound on the losses by choosing a threshold value in relation to the asymptote. For example, setting a 1% threshold for the variation of the MSE with respect to its minimum value provides an upper bound of $\alpha_{2\omega} \leq 0.13$ dB/cm for the second harmonic losses in this waveguide.

It is unclear why a global minimum for the MSE is not found in certain cases. It is likely that the chosen cost function is not sufficiently sensitive to small changes in the second harmonic losses, particularly in the presence of experimental imperfections. A more advanced fitting scheme may be able to predict the second harmonic losses with reduced uncertainty, but this is left as future work.

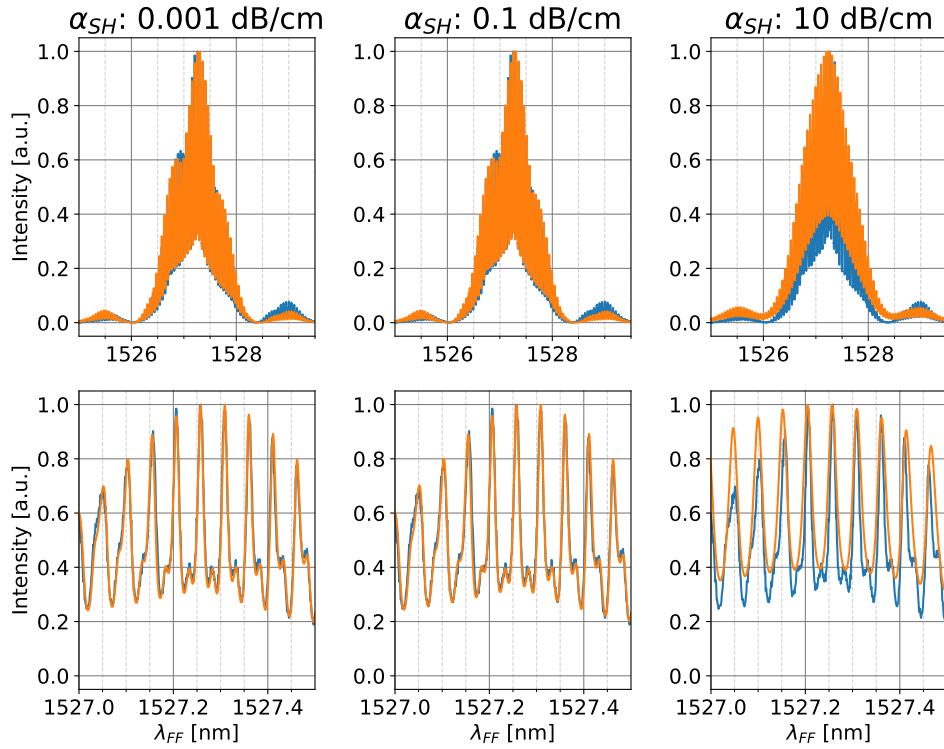


Figure 6.5. – Central portion of the measured (blue) and fitted (orange) phase matching profiles. It can be qualitatively seen that the fit works very well for low losses but that both the structure and envelope of the fit for higher second harmonic losses is degraded. The bottom row shows a zoom-in on the region around 1527.2nm, highlighting the ability of the model to fit the fine structure of the measured spectrum.

Summary

In this chapter we have outlined a new method for characterizing the loss of spatially multi-mode waveguides. A model is introduced that describes the expected phase matching spectrum of the generated second harmonic power, including interferences due to the Fabry-Pérot effect from the end facets. Experimental data is obtained by scanning the wavelength of the fundamental pump field over the phase matching spectrum corresponding to one spatial mode of the second harmonic field. The presented technique is then applied to two waveguides. In one case a reasonable estimate of the losses is found, and in the other an upper bound on the second harmonic losses is obtained. Furthermore, it is shown that the losses of the waveguide for different spatial modes can be determined by changing the central wavelength of the fundamental pump field. The presented approach is very general and can be extended to other nonlinear processes in virtually any high quality waveguide system.

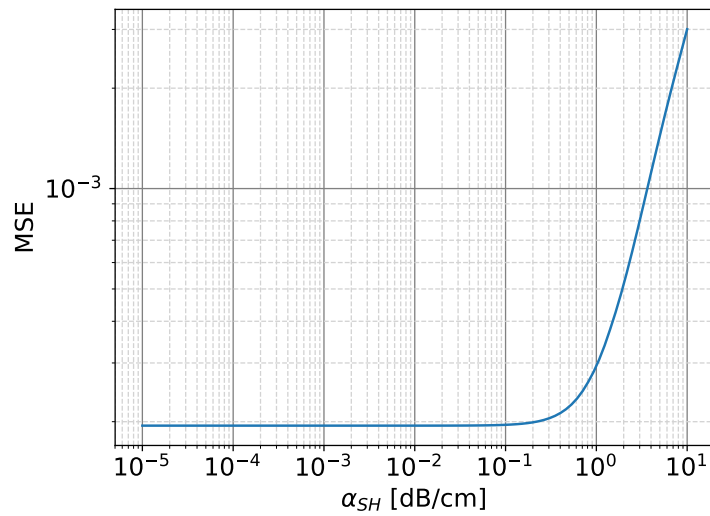


Figure 6.6. – Mean squared error between the measured and fitted central portion of the phase matching profiles as the second harmonic losses are increased. It can be clearly seen that the mean squared error increases rapidly with losses greater than around 0.1 dB/cm. Of note is that the mean squared error does not increase with vanishingly small second harmonic losses.

Design of nonlinear processes in LNOI

Contents

7.1 Dispersion relations of LNOI waveguides . .	135
7.2 Process engineering in LNOI waveguides . .	143
7.3 Pure degenerate PDC states in LNOI	151
7.4 Analysis of facet reflectivity	161

In section 3.1.3, we briefly discussed a new technology that has been rising in importance in the last two years, lithium niobate on insulator (LNOI) [49, 52, 111–113]. This new platform promises to revolutionise the integrated nonlinear optic world since it combines the high nonlinearity and low losses of the LN platform with the very high modal confinement provided by high index contrast waveguides. This allows the realisation of integrated nonlinear

optical devices with normalised conversion efficiency up to *three orders of magnitude higher* than the current standard LN waveguides and with a footprint *thousands of times smaller* than currently possible [112].

However, being a very new platform, systematic investigation is necessary to fully explore its capabilities and its limits. For this reason, in this chapter we investigate the dispersion relation of LNOI waveguides for different waveguide geometries and explore the possible application of this platform as a quantum optic device for the generation and manipulation of quantum states of light.

7.1. Dispersion relations of LNOI waveguides

7.1.1. Modelling of LNOI waveguides

A typical LNOI structure and its parameters can be seen in Figure 7.1. The waveguide geometry is completely defined by the rib width w , the rib height h , the thin film thickness τ and the sidewall angle θ . The substrate is SiO_2 and optionally a capping layer (usually of the same material) can be included in the model. For the realisation of LNOI waveguides, an X-cut substrate is preferred as it provides a simpler poling process: the poling of an X-cut sample can be performed via finger electrodes patterned on the top of the sample [112], while the poling of a Z-cut crystal requires the positioning of one

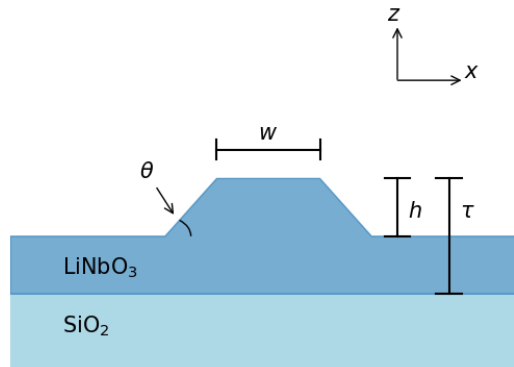


Figure 7.1. – LNOI structure. In a X-cut sample, the crystallographic c axis is aligned parallel to the x axis, while in a Z-cut sample it is aligned along the z axis.

of the poling electrodes between the LN and the SiO_2 , thus creating a highly absorptive layer very close to the waveguide.

Even though their simple geometry is well suited for Marcattili's method for the estimation of the dispersion properties (see section 1.4), the high index contrast (HIC) of LNOI waveguides prevents the applications of such scalar method and requires a full vectorial treatment of the problem. Moreover, although extensions to Marcattili's method have been developed to model HIC waveguides [6], these approximations cannot be directly applied to LNOI since their current formulation does not take into account the birefringence of the material. For these reasons, in this thesis we evaluated the properties of these waveguides using Lumerical FDTD and MODE Solutions [114]: the former implements a finite difference, time domain method to calculate the propagation of light inside the waveguide structure, while the latter uses a finite difference (FDE) scheme to calculate the eigenmodes of a waveguide structure. As briefly outlined in section 2.4, the engineering of quantum optical integrated devices is based on the correct modelling of the dispersion relations of the device and on the understanding of how they can be manipulated, in particular to realise GVM processes. Therefore, to investigate the nonlinear processes available in LNOI waveguides and to assess which GVM PDC processes are allowed in this platform, a detailed analysis of the dispersion relations of LNOI waveguides and their dependence on the waveguide geometry is necessary.

7.1.2. Numerical derivation of the dispersion relations

The investigation of the dispersion relations of LNOI waveguides as a function of their geometry is performed using the MODE Solution package in Lumerical. To avoid numerical artefacts, the simulation mesh is optimised to ensure that the n_{eff} calculated at infrared wavelengths (around 1600nm) is mesh-independent. The mesh used in the calculation of the guided modes consists in a $6\mu\text{m} \times 6\mu\text{m}$ simulation domain, centred on the waveguide and discretised in steps of $\Delta x = 100\text{nm}$ and $\Delta z = 100\text{nm}$. A refined mesh, with $\Delta x_{ref} = 10\text{nm}$ and $\Delta z_{ref} = 5\text{nm}$, centred on the waveguide is necessary to accurately model the field inside the waveguide. This refined mesh extends 100nm beyond the waveguide boundaries since this ensures a sufficiently fine mesh at the boundaries of the waveguide, where the discontinuities of the magnetic and electric field needs to be tracked accurately. Finally, the simulation domain is surrounded by perfectly matching layers (PML) using the default boundary conditions present in MODE Solutions for the simulation of a perfectly absorbing layer. This is necessary to avoid numerical artefacts due to the finite extent of the simulation domain.

After the mesh optimisation, we calculate the n_{eff} of the fundamental TE and TM modes for different sets of fabrication parameters for 30 wavelengths $\lambda \in [0.4, 2.5]\mu\text{m}$ in four different scenarios:

- fully etched waveguides without capping layer (FE), $w \in [0.5, 1.9]\mu\text{m}$ and $\tau \in [450, 700]\text{nm}$;
- fully etched waveguides with capping layer (FEC), $w \in [0.5, 1.9]\mu\text{m}$ and $\tau \in [450, 700]\text{nm}$;
- partially etched waveguides without capping layer (PE), $w \in [0.5, 1.9]\mu\text{m}$, $h \in [450, 650]\text{nm}$ and $\tau = 650\text{nm}$.
- partially etched waveguides with capping layer (PEC), $w \in [0.5, 1.9]\mu\text{m}$, $h \in [450, 650]\text{nm}$ and $\tau = 650\text{nm}$;

The waveguide width w is scanned in steps of $0.2\mu\text{m}$ while its height h and the thin film thickness τ are scanned in steps of 50nm.

We neglect the impact of the rib angle θ as the current dry-etching techniques do not provide easy ways to tune this parameter. For this reason, all the simulated geometries have a rib angle $\theta = 67^\circ$, equivalent to the value measured for the vast majority of LNOI waveguides [52, 115]. Finally, we performed all the calculations assuming the operating temperature is kept stable at 190°C to reduce photorefractive effects [35]. Anyway, a different operation temperature introduces, at first order, only an offset in the dispersion relations but does not change their shape. Therefore, we expect all the discussions concerning the group velocity of the waveguides to be approximately temperature independent.

From the datapoints $n_{eff}(\lambda)$, we fit the dispersion of each waveguide geometry to

the following empirical model

$$n_{effective}^{e/o}(\lambda, T) = n_{bulk}^{e/o}(\lambda, T) + A^{e/o}\lambda^3 + B^{e/o}\lambda^2 + C^{e/o}\lambda + D^{e/o}\sqrt{\lambda} + E^{e/o} + F^{e/o}\log \lambda, \quad (7.1)$$

where $n_{bulk}^{e/o}$ are the bulk Sellmeier equations for LiNbO₃, described in section 3.1. This model has been optimised to fit both n_{eff} and $dn_{eff}/d\lambda$ as well as possible. The error in the fitting is $|n_{fit} - n_{data}| < 0.0015$ for all the data points, corresponding to a relative error below 0.1%. The quality of the fit worsens slightly at longer wavelengths, around >1800nm. Ideally, the coefficients A to F depend on the waveguide geometry and thus a parametrisation as function of w , τ and h can be sought. However, all attempts to parametrise these coefficients as functions of the waveguide geometry failed, as they led to poor fitting of the simulated n_{eff} . For this reason, we report in appendix A the full set of coefficients A-F retrieved for the different waveguide geometries analysed.

7.1.3. Dependence of the dispersion relation on the waveguide geometry: a qualitative analysis

As outlined in section 2.4, many interesting quantum processes are characterised by the presence of group velocity matching between at least two of the fields involved in the interaction. Therefore, the inspection of the normalised group velocities¹

$$\begin{aligned} \tilde{v}_g(\lambda) &= \frac{1}{c} \left(\frac{\partial \beta}{\partial \omega} \right)^{-1} \\ &= \left[n(\lambda) - \lambda \frac{\partial n(\lambda)}{\partial \lambda} \right]^{-1}, \end{aligned} \quad (7.2)$$

provides a first idea how the waveguide geometry influences the waveguide dispersions. Moreover, it is helpful to identify the geometries that could offer interesting and novel phase matching spectra. The curves of the group velocities for the investigated systems are shown in Figures 7.2-7.5.

In uncapped samples (see Figures 7.2 and 7.4), it can be seen that the group velocities are very sensitive to the fabrication parameters. As a general rule of thumb, the dispersion of the TM mode is mostly dependent on the slab thickness τ while the dispersion of the TE mode is affected by the waveguide width w . On the other hand, in capped samples (see Figures 7.3 and 7.5) the group velocities tend to be weakly dependent on the waveguide widths. This is unsurprising, since the capping layer reduces the refractive index contrast between the waveguide and its surrounding. Moreover, the TE modes seem to depend very mildly on the waveguide height. The limited engineerability of capped LNOI waveguide has been noted also in some recent literature [113].

¹Corresponding to the inverse of the group index n_g .

7.1. Dispersion relations of LNOI waveguides

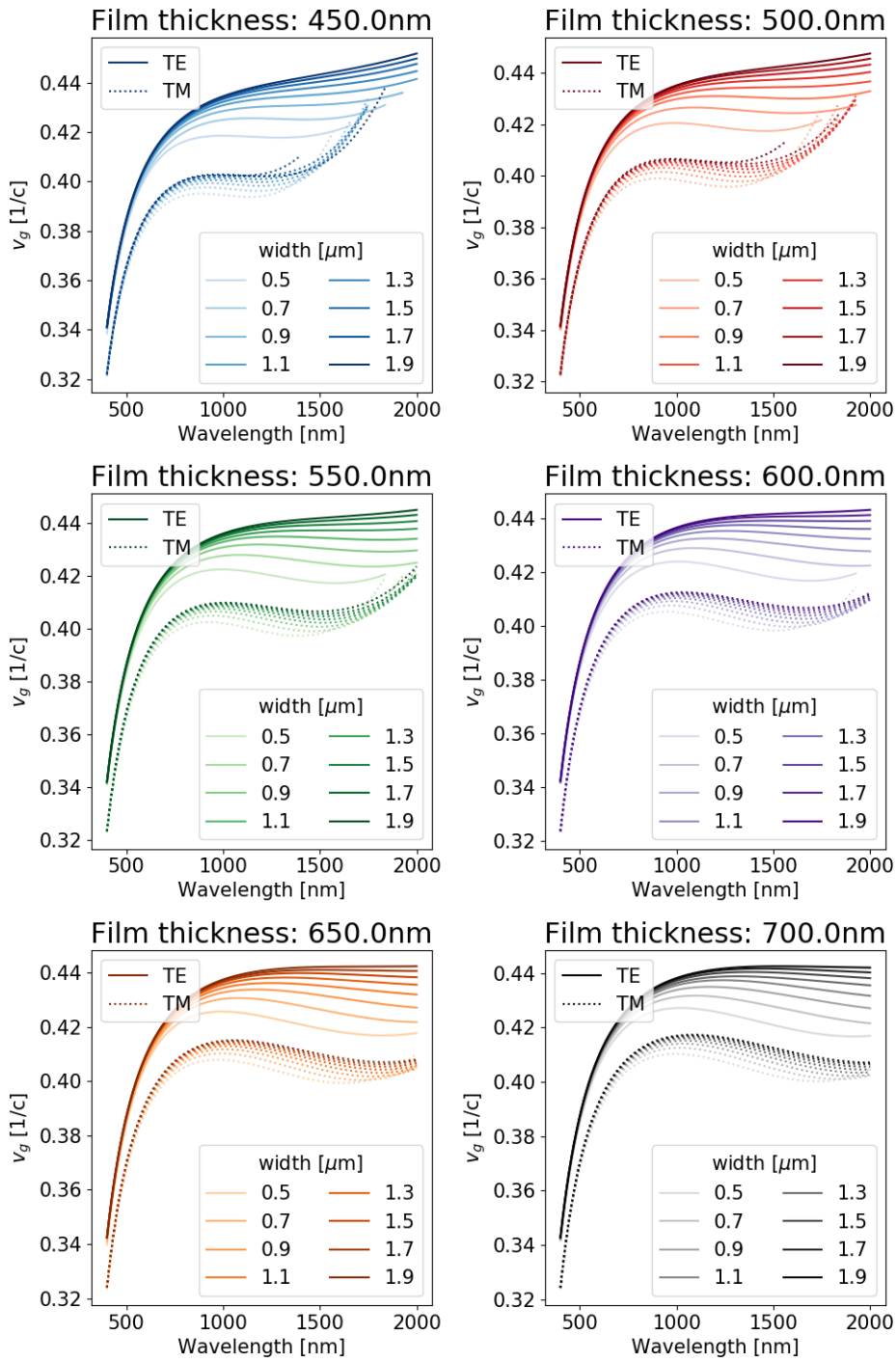


Figure 7.2. – Group velocity curves for fully etched (FE) waveguide structures.

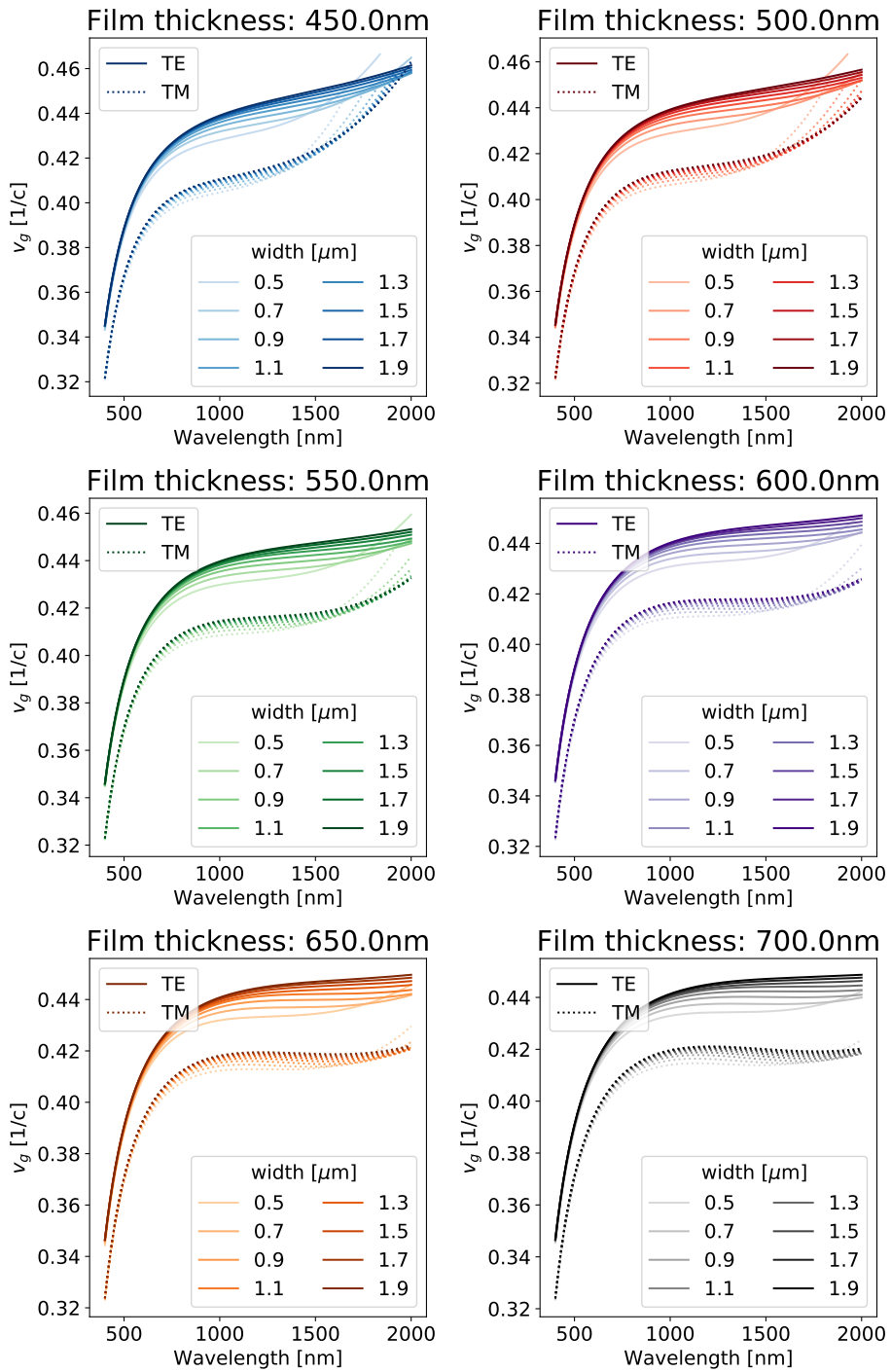


Figure 7.3. – Group velocity curves for fully etched, capped (FEC) waveguide structures.

7.1. Dispersion relations of LNOI waveguides

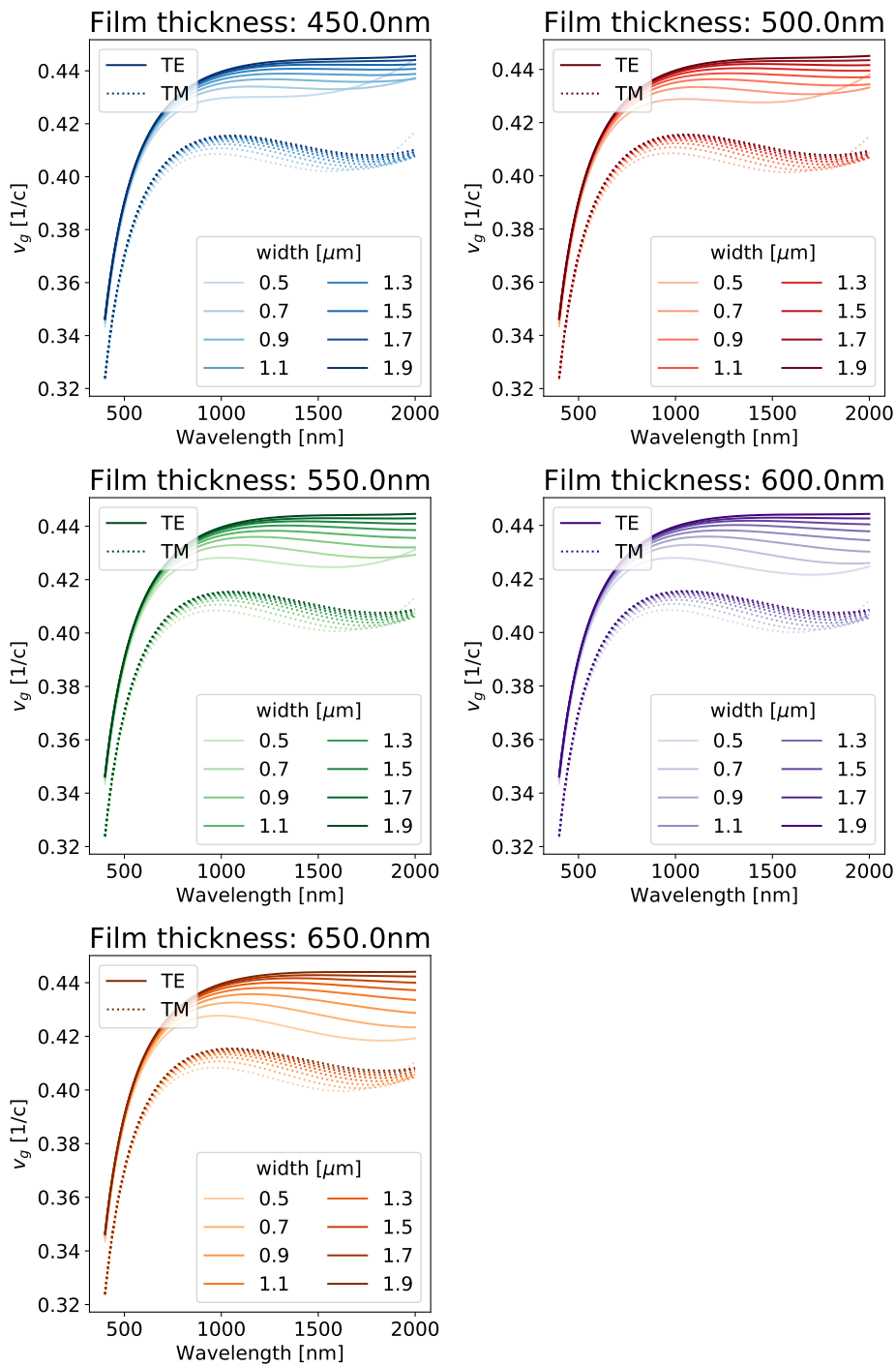


Figure 7.4. – Group velocity curves for partially etched (PE) waveguide structures with thin film thickness $\tau = 650\text{nm}$.

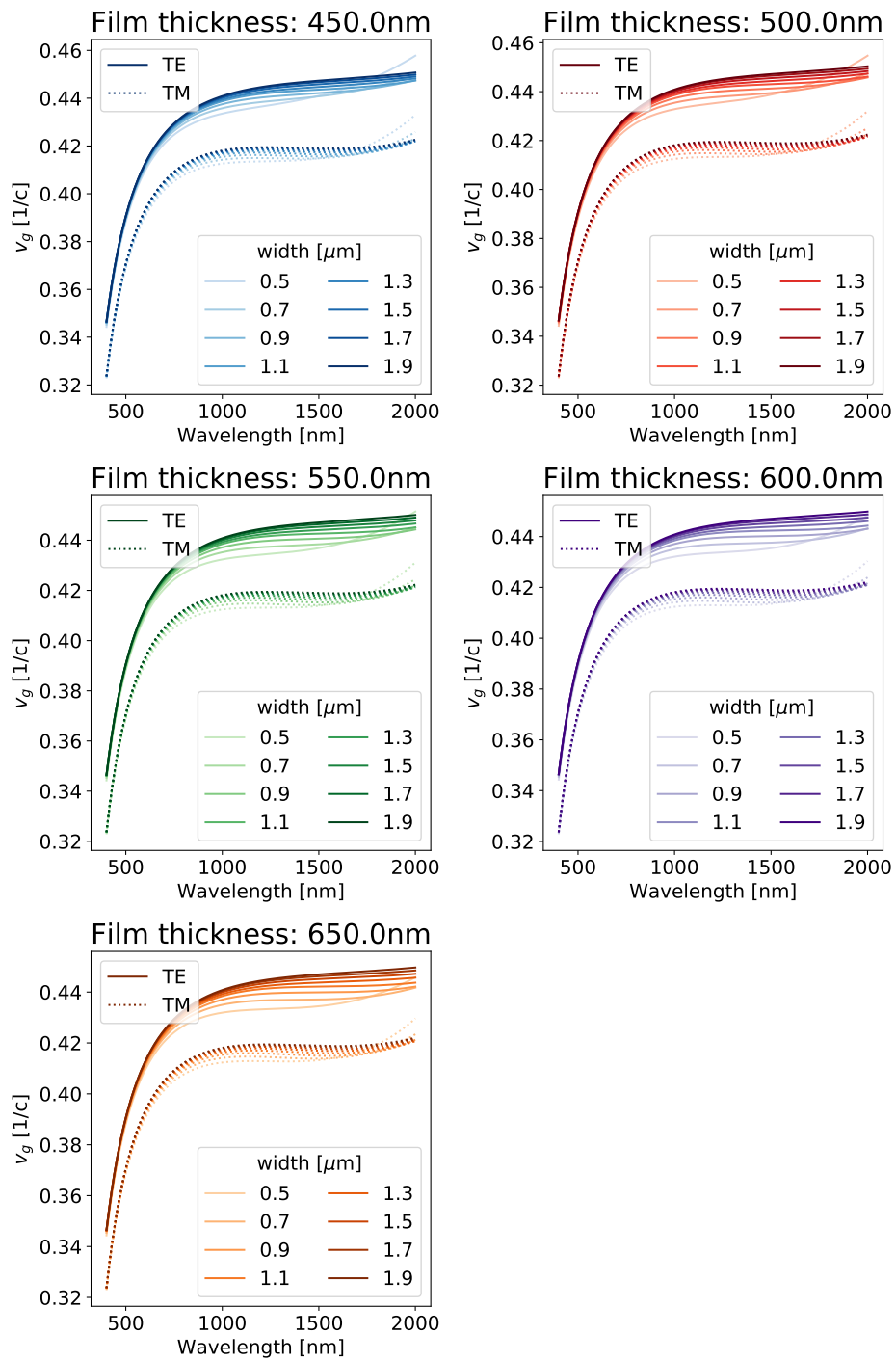


Figure 7.5. – Group velocity curves for partially etched, capped (PEC) waveguide structures with thin film thickness $\tau = 650\text{nm}$.

For the analysis of the GVM processes available in LNOI it is important to remember that, as described in section 3.1, all type I and type II processes allowed in LN require the pump photon to be polarised along the x crystallographic axis, corresponding to the TM mode in X-cut LNOI. Since TM polarised photons belong to the slower curve, GVM processes are allowed only if there is a local maximum around 1000nm. Similarly, an fGVM type 0 process is possible only if the group velocity curve displays a local maximum (or a very broad flat region), as this allows the three interacting photons to have the same group velocity.

With these considerations in mind, the presence of local maxima in many TM curves reveals that it should be possible to realise group velocity matched processes in LNOI, in particular in PE waveguides. This observation motivates the need for a deeper understanding of the influence of the fabrication parameters on the dispersion relations and on the group velocities of the guided modes.

7.2. Process engineering in LNOI waveguides

7.2.1. $\Delta\beta$ contour lines: a novel method of analysis

A quantitative study of all the possible nonlinear processes in the simulated systems is quite complex, since it requires the investigation of the phase matching properties as a function of the four design parameters defining the waveguide geometry (w , h , τ and the presence of a capping layer) as well as the poling period Λ . Moreover, the complex shape of the group velocity curves in LNOI makes it difficult to find stable GVM conditions. The reason is that the numerical minimisation routines used to find wavelength combinations exhibiting GVM can yield inconsistent results, since it is hard for a computer to evaluate equality conditions like $v_{g, signal}(\lambda_1) = v_{g, pump}(\lambda_2)$. For these reasons, we study the processes by directly analysing the shape of the wavevector mismatch $\Delta\beta$ as a function of two independent wavelengths λ_1 and λ_2 . This type of analysis is not commonly used to investigate phase matched processes; however, it provides a complete overview of all the possible processes for a specific waveguide geometry and is therefore an ideal method to investigate and compare different systems at a glance.

As seen in chapter 2, the wavevector mismatch $\Delta\beta$ is directly connected to the spectrum of the nonlinear process by the function

$$I(\lambda_1, \lambda_2) = \text{sinc} \left(\frac{(\Delta\beta(\lambda_1, \lambda_2) - \frac{2\pi}{\Lambda}) L}{2} \right)^2. \quad (7.3)$$

Here, the wavelength-dependent wavevector mismatch $\Delta\beta$ is defined as

$$\Delta\beta_{PDC}(\lambda_1, \lambda_2) = 2\pi \left(\frac{n_3(\lambda_3)}{\lambda_3} - \frac{n_2(\lambda_2)}{\lambda_2} - \frac{n_1(\lambda_1)}{\lambda_1} \right) \quad \text{with } \lambda_3^{-1} = \lambda_2^{-1} + \lambda_1^{-1} \quad (7.4a)$$

$$\Delta\beta_{FC}(\lambda_1, \lambda_2) = 2\pi \left(\frac{n_2(\lambda_2)}{\lambda_2} - \frac{n_3(\lambda_3)}{\lambda_3} - \frac{n_1(\lambda_1)}{\lambda_1} \right) \quad \text{with } \lambda_3^{-1} = \lambda_2^{-1} - \lambda_1^{-1} \quad (7.4b)$$

for PDC and frequency conversion processes, respectively².

Careful inspection of Eq. (7.3) reveals that the maxima of the phase matching spectrum correspond to the zeros of its argument $\Delta\beta(\lambda_1, \lambda_2) - 2\pi/\Lambda$, i.e.

$$\phi(\lambda_1, \lambda_2) = 1 \Leftrightarrow \Delta\beta(\lambda_1, \lambda_2) = \frac{2\pi}{\Lambda}. \quad (7.5)$$

Therefore, given a system characterised by a wavevector mismatch $\Delta\beta$, the choice of the poling period Λ selects all the phase matched processes lying on the lines parametrised by

$$\Delta\beta(\lambda_1, \lambda_2) = \frac{2\pi}{\Lambda}. \quad (7.6)$$

A visual example of this relationship is shown in Figure 7.6. In Figure 7.6a, the contour lines of a generic $\Delta\beta(\lambda_1, \lambda_2)$ are plotted, while the spectrum of the process characterised by the poling period $\Lambda = 2\pi/1.2$ [a.u.] is shown in Figure 7.6b. From the inspection of this Figure, one can note that the density of the contour lines of $\Delta\beta$ is related to the phase matching bandwidth. In fact, a higher density of the contour lines corresponds to a smaller bandwidth of the process, since the $\Delta\beta$ changes more dramatically for small wavelength variations. The comparison of Figures 7.6b and 7.6c, where the sample length is varied by an order of magnitude, highlights that the sample length does not affect the shape of the contour lines but change the bandwidth of the process, as expected.

The analysis of the contour lines of $\Delta\beta(\lambda_1, \lambda_2)$ therefore provides a direct overview of all the possible processes available for a given waveguide geometry and process type. Moreover, it allows a clear identification of the available GVM processes: in fact, the $\Delta\beta$ contour lines align with the axes in aGVM processes, have a positive slope in sGVM processes or present closed contour lines in proximity of fGVM processes³.

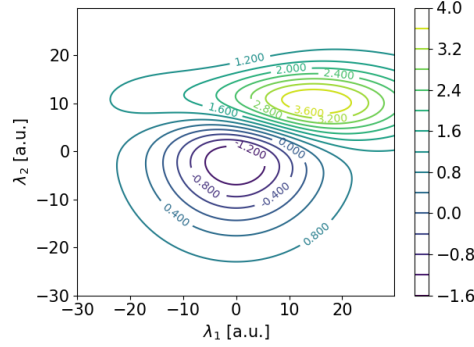
Armed with this intuition, we can easily study the phase matching properties of all simulated systems by inspecting the contour lines of $\Delta\beta(\lambda_1, \lambda_2)$ for PDC and FC processes. Given the huge number of systems analysed, it is impractical to provide here the contour plots for all geometries and processes. Instead, we will use this method to briefly discuss the impact of waveguide geometry on the engineering of two different PDC processes.

7.2.2. Engineering of PDC processes in LNOI waveguides

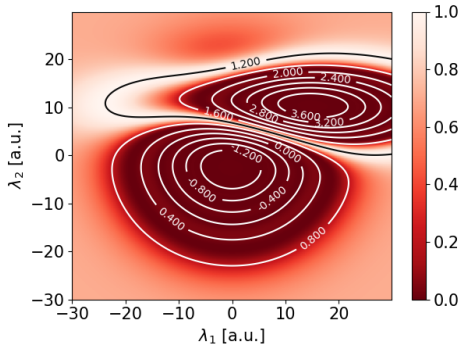
To showcase the strength of the contour line method described in the previous section, we investigate two different nonlinear processes in LNOI waveguides, namely a type II (o \rightarrow eo) and a type I (e \rightarrow oo) PDC process, for different waveguide classes (FE, FEC, PE, PEC) and fabrication parameters w , τ and h .

²Note the exchange between λ_2 and λ_3 between PDC and FC processes.

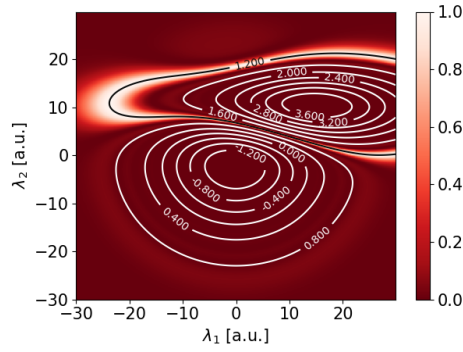
³These regions are associated with fGVM processes since, for these processes, the first nonzero components of the Taylor expansion of $\Delta\beta(\lambda_1, \lambda_2)$ are the second order terms and thus the relative contour lines are closed.



(a) Contour lines of $\Delta\beta(\lambda_1, \lambda_2)$.

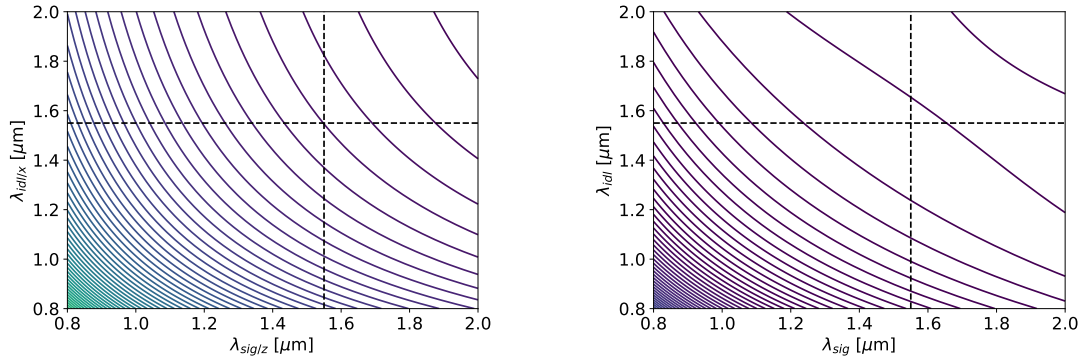


(b) Phase matching with $\Lambda = 2\pi/1.2$ and $L = 1$. All quantities are adimensional.



(c) Phase matching with $\Lambda = 2\pi/1.2$ and $L = 10$. All quantities are adimensional.

Figure 7.6. – Representation of the analysis of the phase matching properties based on the contour lines of the $\Delta\beta$ function. In Figure 7.6a, the contour lines for a generic $\Delta\beta(\lambda_1, \lambda_2)$ function are shown. In Figures 7.6b and 7.6c, the phase matching functions ϕ for different choices of $\Delta\beta_0$ and L . It can be seen that the contour lines define the position of the the phase matching maxima, the poling period Λ selects a specific contour line, while the parameter L only changes the bandwidth of the process.



(a) Isolines of available type II PDC processes ($Y \rightarrow YZ$) in bulk LN.

(b) Isolines of available type I PDC processes ($Z \rightarrow XX$) in bulk LN.

Figure 7.7. – Plots of the contour lines of $\Delta\beta$ for type II and type I PDC processes in bulk LN crystals. The contour lines are linearly spaced in $\Delta\beta \in [0.42, 5] \mu\text{m}^{-1}$.

The contour lines of the two processes realised in a bulk LN crystal are displayed in Figure 7.7. They show that both processes are characterised by spectra with negative phase matching angles α . The situation is dramatically different in LNOI waveguides, as demonstrated by the contour lines shown in Figures 7.8 and 7.9 for sixteen waveguide geometries. In these Figures, each row corresponds to a specific waveguide class, while each column is characterised by the same set of fabrication parameters. From the Figures it is evident that the material dispersion is heavily modified by the geometry of the waveguide, resulting in very different phase matching behaviours from their bulk counterparts. In particular, one can notice from Figure 7.8 that uncapped waveguides (corresponding to the first and third rows) allow the realisation of aGVM type II PDC processes centred around 1550nm. Such processes are impossible in bulk LN crystals and weakly guiding LN waveguides. This highlights the appeal of LNOI as a revolutionary platform for integrated quantum optics devices, due to the great flexibility offered to engineer the desired nonlinear processes.

Figure 7.8 also reveals the effects of different fabrication parameters, for each waveguide class. For example, it can be seen that the angle of the type II process generating IR photons can be easily tuned from negative to positive values in FE waveguides (first row). A similar behaviour is present in PE waveguides (third row). In this case, however, the ability to tune the refractive index properties is reduced due to the presence of a residual LN slab beside the waveguide. Figure 7.8 also shows that the introduction of a capping layer tends to yield processes much more similar to those present in bulk LN - especially for PEC waveguides. The reason is that the capping layer reduces the refractive index contrast between the waveguide core and its cladding, thus approaching a weakly guiding regime where the modal dispersion is determine mainly by the

material properties and not by the waveguide geometry.

Similar conclusions can be derived for the type I PDC process shown in Figure 7.9: FE and PE waveguides exhibit phase matching spectra highly dependent on the waveguide class and dimensions, while the dispersion properties change less drastically in capped waveguides. Interestingly, the $\Delta\beta$ contour lines of the type I PDC process in FE, FEC and PE waveguides exhibit regions of local minima along the main diagonal.

Examples of the phase matching spectra that can be obtained selecting different Λ for the same waveguide structure are shown in Figures 7.10 and 7.11 for 1mm-long FEC waveguides with $(w, h) = (0.7, 0.65) \mu\text{m}$ and $(1.9, 0.45) \mu\text{m}$ respectively. In the first Figure, three different spectra associated to three different poling period $\Lambda = 3.95 \mu\text{m}$, $4 \mu\text{m}$ and $4.01 \mu\text{m}$ are displayed. The relative $\Delta\beta$ contour line plots are shown in the second row, third column of Figure 7.9. Figure 7.10 highlights that, even within a single waveguide design, wildly different phase matching spectra can be achieved simply tuning the poling period Λ .

Figure 7.11 shows the spectra of other interesting type I PDC processes in a different waveguide geometry for two different poling periods. In Figure 7.11a an fGVM region at 1600nm along the main diagonal is phase matched with $\Lambda = 2.862 \mu\text{m}$. This region could be used for the generation of broadband, degenerate, decorrelated photon pairs in the telecom band. Changing the poling period to $\Lambda = 2.88 \mu\text{m}$ it is possible to obtain the phase matching spectrum shown in Figure 7.11b, exhibiting regions with vertical phase matching angles. These correspond to aGVM processes generating photon pairs around 1500nm and 1150nm. For the same poling, another region with a phase matching angle of roughly $+45^\circ$ can be found. In this case, decorrelated photon pairs at 1550nm and 1350nm can be generated via an sGVM process.

The examples in Figures 7.10 and 7.11 show that very small variations of poling period are sufficient to dramatically change the phase matching spectrum. This highlights that the phase matching conditions in LNOI waveguides are extremely sensitive to any factor that affects the dispersion of the waveguides. Therefore, submicrometric fabrication imperfection and temperature variations during the operation of the sample will dramatically degrade the quality of the phase matching spectrum, as their effects will be similar to having a different poling period. This reveals that the manufacturing and handling of LNOI waveguides requires a much higher level of precision than their traditional weakly guiding counterparts.

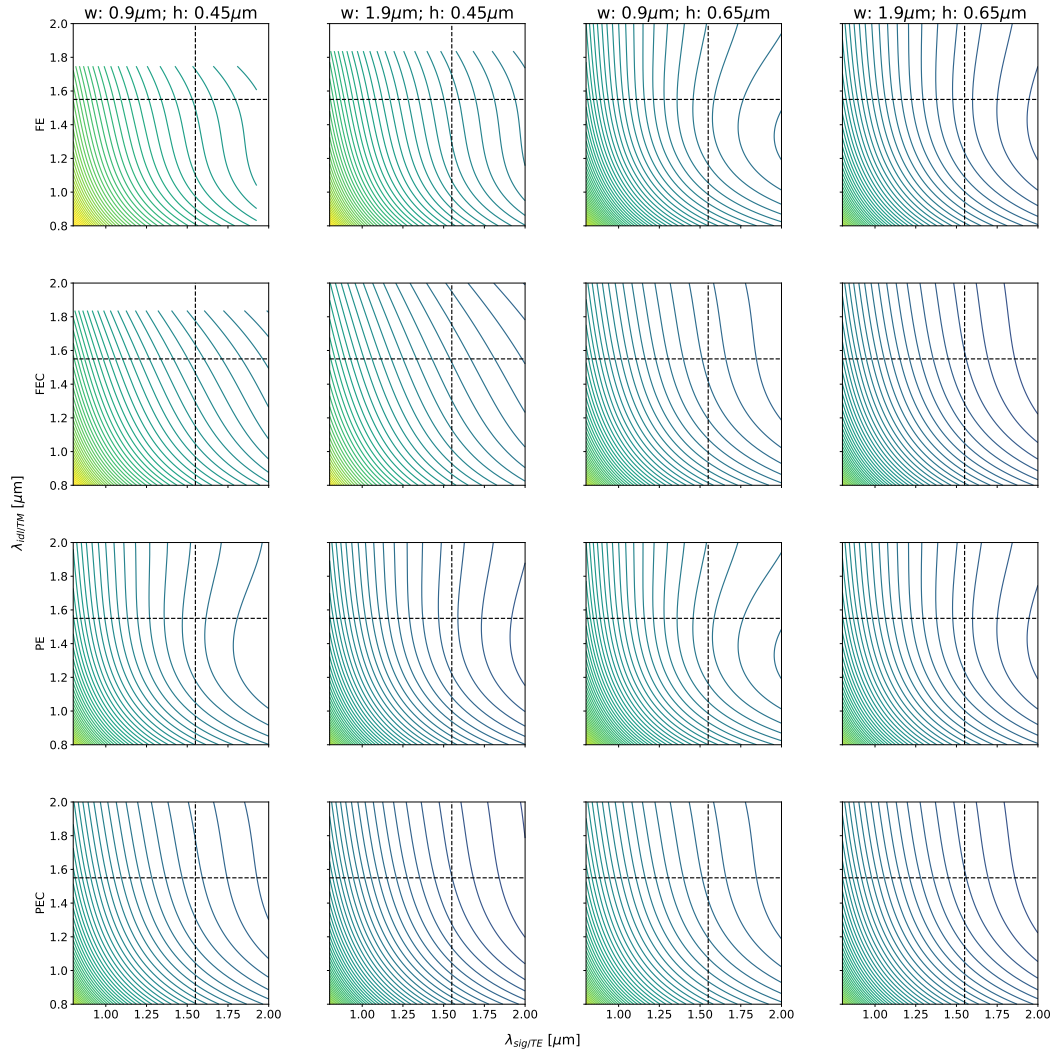


Figure 7.8. – Contour lines of $\Delta\beta$ for type II PDC processes (TE \rightarrow TE+TM) available in X-cut LNOI waveguides. Each row displays the isolines for the same waveguide class (fully etched, fully etched capped, partially etched and partially etched capped). Each column displays the isolines for different waveguide widths w and heights h . The contour lines are linearly spaced in $\Delta\beta \in [0.42, 5] \mu\text{m}^{-1}$. The dashed black lines are drawn in correspondence of $\lambda = 1550 \text{ nm}$, since we are particularly interested in processes where one of the photons lie in the telecom C-band. The abrupt interruption of the contour lines in some of the plots denotes the region when the fundamental mode is not properly guided any more.

7.2. Process engineering in LNOI waveguides

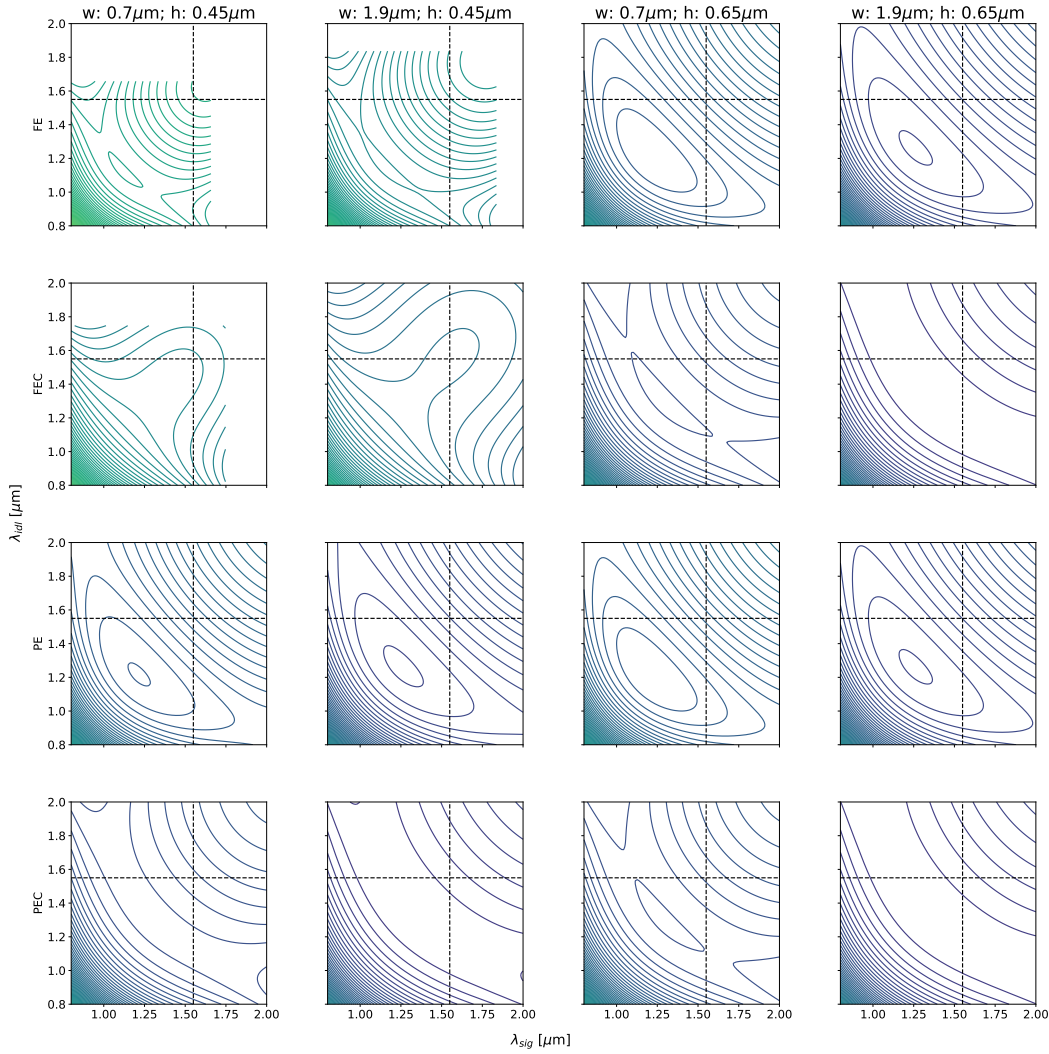


Figure 7.9. – $\Delta\beta$ isolines for type I PDC processes ($TE \rightarrow TM+TM$) available in X-cut LNOI waveguides. Each row displays the isolines for the same waveguide type (fully etched, fully etched capped, partially etched and partially etched capped). Each column displays the isolines for different waveguide widths w and heights h . The contour lines are linearly spaced in $\Delta\beta \in [0.42, 5] \mu\text{m}^{-1}$. The dashed black lines are drawn in correspondence of $\lambda = 1550 \text{ nm}$, since we are particularly interested in processes where one of the photons lie in the telecom C-band. The abrupt interruption of the contour lines in some of the plots denotes the region when the fundamental mode is not properly guided any more.

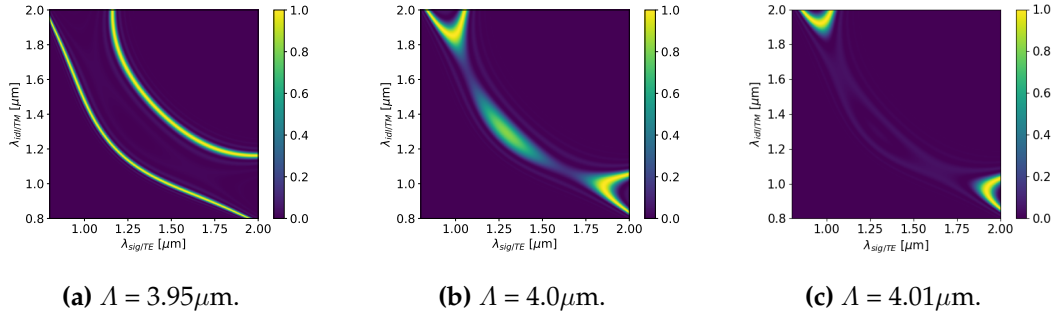


Figure 7.10. – Type I phase matching spectra of a FEC waveguide with $w = 0.7\mu\text{m}$, $h = 650\text{nm}$ and $L = 1\text{mm}$. The different subfigures show the phase matching spectra for different poling periods.

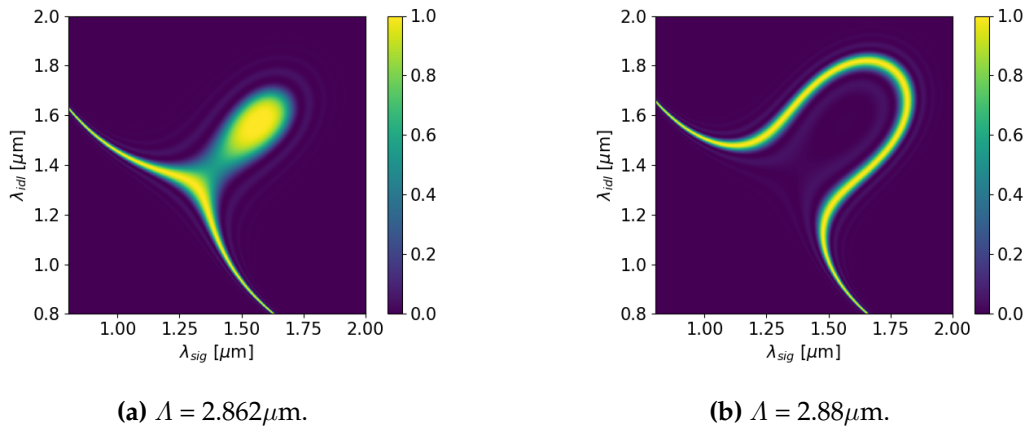


Figure 7.11. – Type I phase matching spectra of a FEC waveguide with $w = 1.9\mu\text{m}$, $h = 450\text{nm}$ and $L = 1\text{mm}$. The different subfigures show the phase matching spectra for different poling periods.

7.3. Engineering degenerate, decorrelated type II PDC process in LNOI structures

With the help of the contour line method discussed in the previous section, we perform a broad search over all the simulated waveguide classes and geometries, looking for novel phase matching processes. As evident from the contour lines in Figure 7.8, one of the most interesting processes available in LNOI waveguides is the degenerate, decorrelated type II PDC process pumped at 775nm. The unprecedented possibility of generating degenerate, decorrelated states in the telecom C-band in LN requires a thorough study to identify the optimal waveguide designs for the fabrication of such an interesting PDC source.

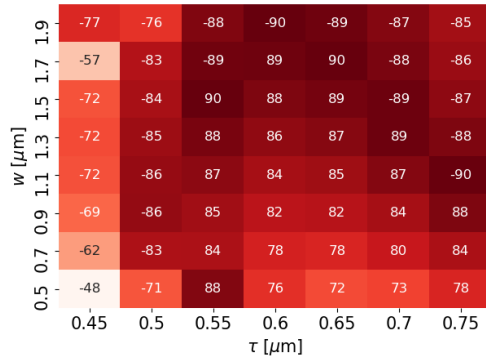
7.3.1. Identification of the design parameters

The process under investigation is an aGVM type II PDC process pumped at 775nm with a TM-polarised field, generating photon pairs at 1550nm in orthogonal polarisations. The analysis of the $\Delta\beta$ contour lines reported in Figure 7.8 reveals that this process is only possible in FE and PE waveguides. Therefore, in the following sections we will exclusively investigate these two waveguide classes.

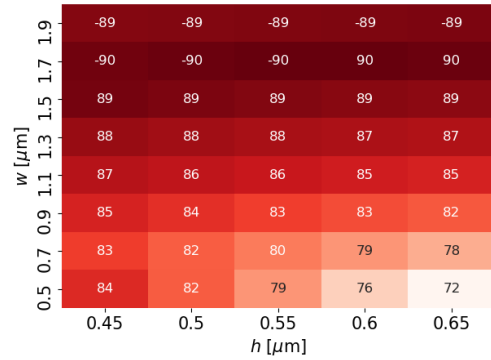
At first, the dependence of the phase matching angle α on the different fabrication parameters is studied to gain a first idea of the fabrication parameters allowing the desired process. The results are shown in Figure 7.12. This analysis reveals that, in FE waveguides, waveguide widths $w \geq 0.7\mu\text{m}$ and film thicknesses $\tau \geq 550\text{nm}$ are sufficient to ensure approximately vertical phase matching angles. The situation is very different in PE waveguides, where the phase matching angle is almost independent on the waveguide height: in these systems, widths $w \geq 0.9\mu\text{m}$ ensures phase matching angles close to 90° for any of the chosen waveguide height.

It is already interesting to notice that these two waveguide classes show different sensitivity to different fabrication parameters. This is important when taking into consideration the impact of fabrication errors, since it helps understanding which fabrication parameters might have a greater impact on the resulting phase matching spectrum. For example, we can expect PE waveguide to be more sensitive to the waveguide width w as opposed to the rib height h , since the phase matching angle is almost height-independent.

Similar trends are observed when plotting the poling period required to phase match the process under investigation. Inspection of Figure 7.13 shows that the poling period of FE waveguides changes between $1.75\mu\text{m}$ and $3.75\mu\text{m}$ and it is highly dependent on the waveguide parameters. On the other hand, the poling period necessary in PE waveguides varies between $2.5\mu\text{m}$ and $3.4\mu\text{m}$ and it is almost independent on the waveguide height h .

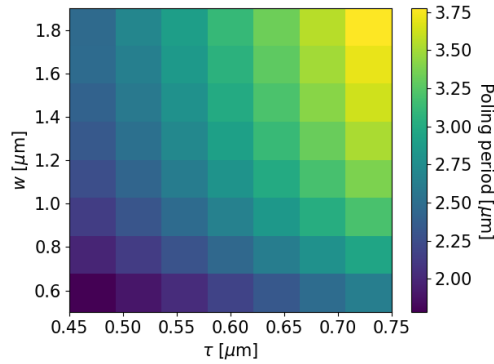


(a) Phase matching angle α_{PM} in FE waveguides.

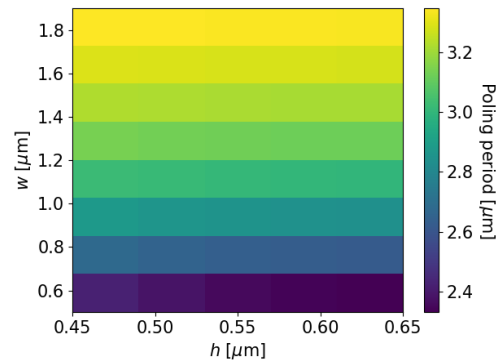


(b) Phase matching angle α_{PM} in PE waveguides.

Figure 7.12. – Phase matching angle α for the degenerate, decorrelated type II PDC process 775nm→1550nm in FE and PE waveguides, as a function of the fabrication parameters. The colormap represents $|\alpha|$.



(a) Poling period Λ for the 775nm→1550nm process in FE waveguides.



(b) Poling period Λ for the 775nm→1550nm process in PE waveguides.

Figure 7.13. – Poling period Λ for the degenerate, decorrelated type II PDC process 775nm→1550nm in FE and PE waveguides, as a function of the fabrication parameters.

7.3.2. Sensitivity of the PDC process to fabrication errors

Evaluation of the sensitivity coefficients

A successful design of the decorrelated PDC source requires a more precise analysis of the impact of fabrication errors on the phase matching spectrum of the final process. To this end, the sensitivity parameters for FE and PE waveguides⁴ are calculated and plotted in Figure 7.14. Comparing the process sensitivity to the waveguide width $\partial_w \Delta\beta$ in FE and PE waveguides (see Figures 7.14a and 7.14c), one can note that the two classes exhibit a similar behaviour, especially for large waveguide widths. This can be explained by the different confinement conditions of the guided modes for varying waveguide width: the guided modes of wider waveguides are more confined inside the waveguide and thus they are much less affected by small variations of the waveguide geometry.

Focusing the attention to FE waveguides, Figures 7.14a and 7.14b show that the process sensitivity to the film thickness $\partial_\tau \Delta\beta$ is one order of magnitude higher than the process sensitivity to the width. This suggests that the nonlinear performance of the waveguide will be highly dependent on the homogeneity of the thin-film thickness. On the other hand, in PE waveguides $\partial_h \Delta\beta \approx -\partial_w \Delta\beta$. This means that the effect of fabrication imperfections depends on the interplay between the waveguide width and height, as discussed in the next section.

Impact of errors on device length

With the process sensitivities for different waveguide classes and geometries at hand, it is possible to evaluate which waveguide designs are more resilient to fabrication errors, using the theory presented in section 5.5. In this way, a restricted set of optimal waveguide designs can be identified for future experimental investigations. As discussed above, different waveguide geometries are characterised by different process sensitivities. For this reason, there will be one optimal set of fabrication parameters that minimises the impact of the errors on the phase matching spectrum, for given fabrication errors.

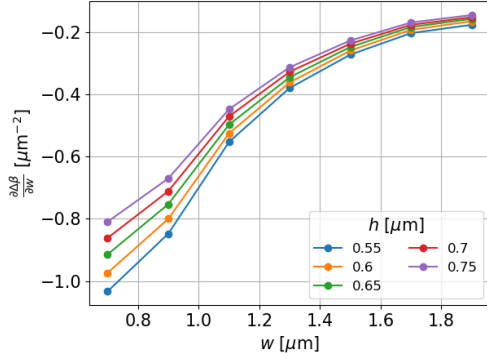
Let us consider, for example, the optimisation of the design of FE waveguides, for a given pair of fabrication errors $(\delta w, \delta\tau)$. As discussed in section 5.3, the presence of fabrication errors in the system introduces a variation of the momentum mismatch $\Delta\beta$ from its ideal value $\Delta\beta_0$. Recall that in 5.3 we defined the *noise amplitude* σ of a given process as the maximum deviation between $\Delta\beta$ and the mean of $\Delta\beta_0$.

For the case under investigation, the σ can be expressed as a function of the fabrication parameters w and τ as

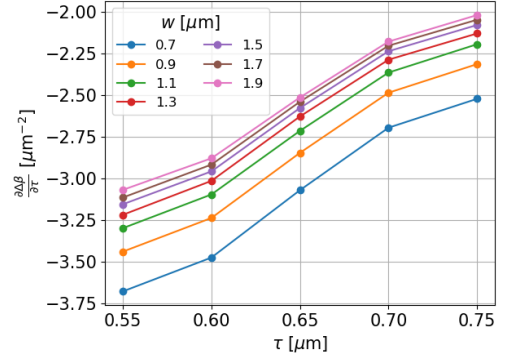
$$\sigma_{FE}(w_0, \tau_0) = \left| \partial_w \Delta\beta|_{w_0, \tau_0} \delta w + \partial_\tau \Delta\beta|_{w_0, \tau_0} \delta\tau \right|. \quad (7.7)$$

The optimal fabrication parameters (w_{opt}, τ_{opt}) can be found by minimising the noise amplitude σ_{FE} over the set of the fabrication parameters (w, τ) . In a similar way, a

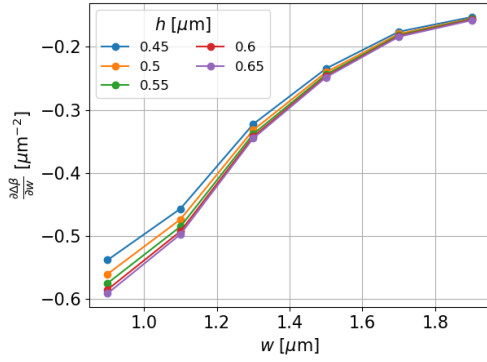
⁴For simplicity, we consider here the geometries providing $|\alpha| \geq 80^\circ$.



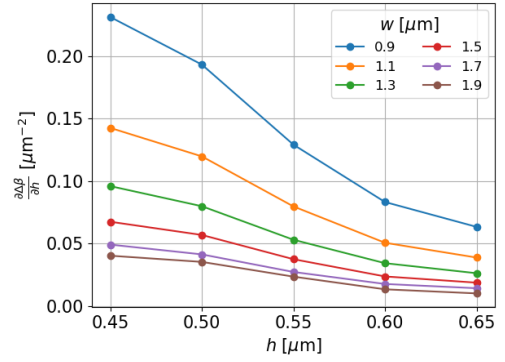
(a) Width sensitivity (FE waveguides).



(b) Thickness sensitivity (FE waveguides).



(c) Width sensitivity (PE waveguides).



(d) Height sensitivity (PE waveguides).

Figure 7.14. – Process sensitivity to waveguide width and thickness for the type II aGVM process 775nm→1550nm.

lower bound for the noise amplitude σ_{PE} for a PE waveguide can be calculated minimising

$$\sigma_{PE}(w_0, h_0) = \left| \partial_w \Delta\beta|_{w_0, h_0} \delta w + \partial_h \Delta\beta|_{w_0, h_0} \delta h \right|. \quad (7.8)$$

It is crucial to observe that, in this analysis, the noise amplitudes σ in Eqs. (7.7) and (7.8) depend on two independent variables, namely $(\delta w, \delta \tau)$ for FE systems and $(\delta w, \delta h)$ for PE systems. In this case, both the magnitude of the fabrication imperfections and their relative sign are important, since the errors on the two parameters can compensate each other. For this reason, the minimisation of Eqs. (7.7) and (7.8) is performed considering both positive and negative $\delta w, \delta \tau$ and δh

The minimisation of σ provides a lower bound σ^{min} for the noise amplitude in FE and PE waveguides. From σ^{min} , it is possible to evaluate the maximum length L_{max} for the investigated systems, such that they still provide a good phase matching spectrum.

7.3. Pure degenerate PDC states in LNOI

In fact, recalling the fabrication inequality (5.32) $\sigma L \leq 10$, the maximum length L_{max} can be calculated as

$$L_{max} = \frac{10}{\sigma_{min}}. \quad (7.9)$$

Since σ_{min} depends on the amount of fabrication errors δw , $\delta\tau$ or δh , the optimal waveguide design providing the maximum length L_{max} depends on the fabrication errors occurring during the manufacturing process. Therefore, proper characterisation of the fabrication process and its errors allows the design and production of optimised LNOI devices.

The result of this analysis on FE and PE waveguides is summarised in Figure 7.15. In the Figure, the maximum lengths L_{max} and the best fabrication parameters w_0 , τ_0 and h_0 for FE and PE waveguides for different amount of errors δw , $\delta\tau$ and δh are reported.

As expected, for FE waveguides the maximum length and the optimal design parameters are highly dependent on the amount of fabrication errors present in the system. The maximum length L_{max} can vary by four orders of magnitude, demonstrating the high sensitivity of this class of waveguides. On the other hand, PE waveguides present a very peculiar behaviour: in these systems, the optimal design always corresponds to $w_0 = 1.9\mu\text{m}$ and $h_0 = 0.45\mu\text{m}$. There is only one exception, for values of fabrication errors $(\delta w, \delta h) = (0.01, 0.1)\mu\text{m}$. In this case, the optimal design is given by $(w_0, h_0) = (1.3, 0.6)\mu\text{m}$ and the relative L_{max} is more than two orders of magnitude higher than for the other designs. The reason for this sudden behaviour is due to the interplay between waveguide design, process sensitivities and fabrication errors: for $(w_0, h_0) = (1.3, 0.6)\mu\text{m}$, the expected σ_{PE} is given by

$$\sigma_{PE}(\delta w, \delta h) \approx -0.343\delta w + 0.0342\delta h.$$

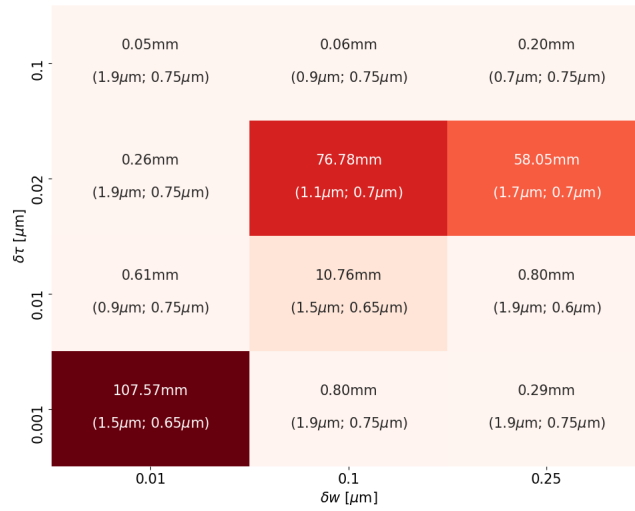
One can see from this equation that, in PE waveguides with $(w_0, h_0) = (1.3, 0.6)\mu\text{m}$, errors on the width can cancel out errors on the height, if they have the correct relative magnitude. Therefore, for $(\delta w, \delta h) = (0.01, 0.1)\mu\text{m}$, the minimum noise amplitude σ_{PE} tends to 0, making the waveguides almost insensitive to the noise present in the system.

7.3.3. Estimation of the conversion efficiency for the type II PDC process

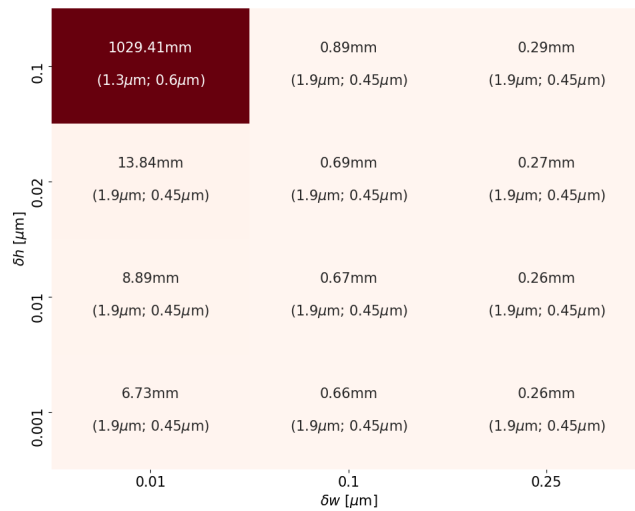
Having estimated the best possible waveguide lengths L_{max} for the systems under investigation, it is finally possible to calculate the expected efficiency of the process, including the effects of fabrication errors. In fact, the expected maximum conversion efficiency, normalised per unit power, η can be estimated as

$$\eta = \eta_{norm} L_{max}^2 \quad (7.10)$$

where η_{norm} is the normalised conversion efficiency of the PDC process and L_{max} is the maximum waveguide length calculated in the previous section. The evaluation of η allows the estimation of the maximum conversion efficiency achievable in the analysed



(a) Maximum length achievable in FE waveguides for different errors in the waveguide width δw and thin film thickness $\delta\tau$. The number in parentheses indicate the fabrication parameters (w ; τ) providing the longest waveguides for each fabrication error.



(b) Maximum length achievable in PE waveguides for different errors in the waveguide width δw and height δh . The number in parentheses indicate the fabrication parameters (w ; h) providing the longest waveguides for each fabrication error.

Figure 7.15. – The plots report the maximum lengths of LNOI waveguides in order to ensure ideal phase matching spectra for the analysed type II PDC process. For a given pair of fabrication errors, the maximum length is derived using the theory presented in chapter 5 and using the process sensitivities reported in Figure 7.14.

7.3. Pure degenerate PDC states in LNOI

type	w [μm]	h [μm]	τ [μm]	$ \theta ^2$ [$1/\mu\text{m}^{-2}$]	A_{eff} [μm^2]	η_{norm} [% $\text{W}^{-1} \text{cm}^{-2}$]
FE	0.7	0.75	0.75	1.017550	0.982752	240 ± 50
FE	0.9	0.75	0.75	0.939691	1.064179	220 ± 40
FE	1.9	0.75	0.75	0.614474	1.627407	134 ± 27
FE	1.1	0.70	0.70	0.856380	1.167706	200 ± 40
FE	1.7	0.70	0.70	0.661350	1.512058	149 ± 30
FE	1.5	0.65	0.65	0.704752	1.418938	164 ± 33
FE	1.9	0.60	0.60	0.574267	1.741351	137 ± 28
PE	1.9	0.45	0.65	0.592872	1.686704	136 ± 28
PE	1.3	0.60	0.65	0.767189	1.303459	180 ± 40

Table 7.1. – Table of the efficiencies in LNOI

systems. Moreover, following the discussion presented in section 5.2.3, evaluating η provides a fair metric for the comparison of these new systems with the established technological platforms.

Calculation of η

The calculation of η requires, along with L_{max} , an estimation of the normalised conversion efficiency η_{norm} . From the theory discussed in section 2.2.1, the normalised conversion efficiency can be calculated as

$$\eta_{norm} = \frac{8\pi^2 d_{31,eff}^2 |\theta|^2}{n_1 n_2 n_3 c \epsilon_0 \lambda_{FF} \lambda_{SH}}, \quad (7.11)$$

where θ is the overlap integral among the *normalised transversal components* $\tilde{\mathcal{E}}_{\perp}(x, y)$ of the three electric fields and the distribution of the nonlinearity in the waveguide plane. Details for the calculations of the overlap integral θ are discussed in the following section, since the systems under investigation present some important differences when compared to the weakly guiding systems considered when deriving Eq. (7.11) in chapter 2.

The normalised conversion efficiencies η_{norm} for the optimal waveguide designs found in the previous section are reported in Table 7.1. These η_{norm} can be compared to the normalised conversion efficiencies of the standard weakly guiding waveguides reported in Table 7.2. The comparison shows that the estimated η_{norm} in LNOI waveguides are almost two orders of magnitude higher than the ones achievable in standard systems.

However, a very different picture appears when the constraints on the waveguide length posed by fabrication errors are taken into consideration. Figure 7.16 reports the estimated η for the maximum waveguide lengths⁵ L_{max} of the analysed LNOI wave-

⁵In three cases, the maximum length L_{max} is well above 5cm. Since achieving these lengths is infeasible for the standard high-resolution lithography, we limited these extreme cases to waveguide lengths of 1cm.

	d [pm/V]	$ \theta ^2$ [μm^{-2}]	η_{norm} [% $\text{W}^{-1} \text{cm}^{-2}$]	η [% W^{-1}]
KTP type II (L=2cm)	2.65	2.25×10^{-2}	2.86	11.45
LN type II (L=3.5cm)	4.35	1.08×10^{-2}	1.92	23.57

Table 7.2. – Table of the efficiencies for standard systems

guide geometries. Comparing the values reported in the Figure with the conversion efficiencies η of the processes in the standard waveguides the expected maximum conversion efficiency of LNOI system is often well below the one provided by current weakly guiding systems.

These observations suggest one final consideration. One of the main advantages claimed by many LNOI supporters is the huge nonlinearities η_{norm} achievable in these waveguides. However, when fabrication errors are considered, the ultimate efficiency of these devices can be way inferior to the expected value. In fact, our analysis shows that LNOI waveguides might exhibit η comparable or lower than the current weakly guiding technologies. Nevertheless, LNOI waveguides provide the unique benefits of achieving much smaller footprints and much higher process engineerability.

Calculation of the field overlap θ

As mentioned in the previous section, the calculation of the overlap integral θ presents some intricacies for the LNOI waveguides under investigations. In fact, due to the presence of a non-negligible component of the electric field along the propagation direction, the estimation of the θ and η_{norm} using the theory⁶ reported in section 2.2 requires particular attention.

The normalisation condition (2.11) for waveguide eigenmodes

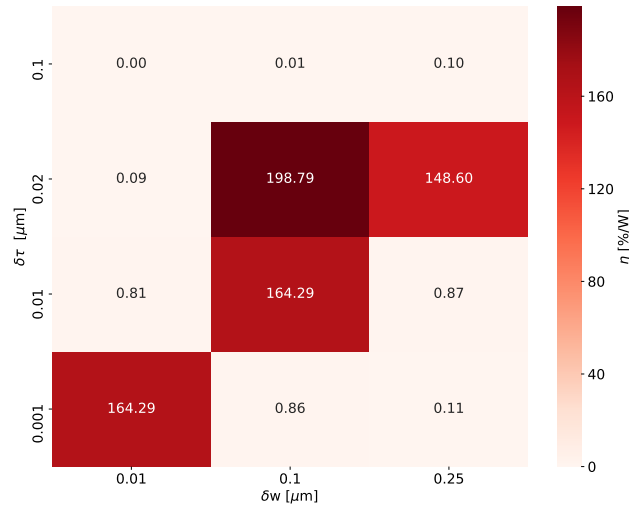
$$\iint dx dz \left| \tilde{\mathcal{E}}_{\perp}(x, z) \right|^2 = 1$$

assumes that the optical power is carried entirely by the transversal components of the electric field. However, in these strongly guiding waveguides a non-negligible portion of the field is polarised along the propagation axis, especially for the infrared modes. This behaviour can be seen from the eigenmode reported in Figure 7.17 for one of the waveguide geometries considered in the previous section. In this case, the normalisation condition (2.11) is not valid anymore, since it overestimates the contribution of the transversal field to the efficiency of the process. For this reason, we replace the normalisation condition (2.11) with

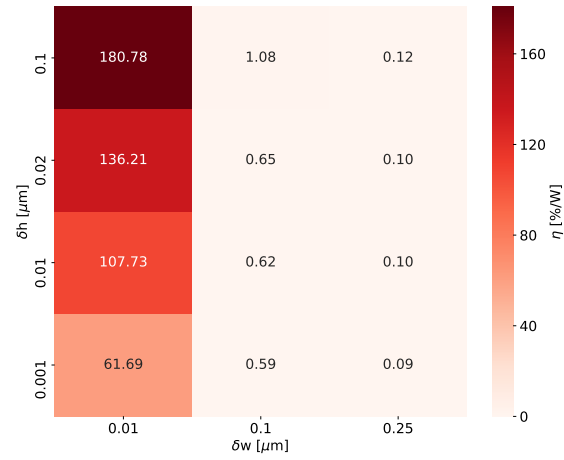
$$\iint dx dz \left| \tilde{\mathcal{E}}_{\perp}(x, z) \right|^2 + \left| \tilde{\mathcal{E}}_z(x, z) \right|^2 = 1. \quad (7.12)$$

⁶In [112], the authors use different equations for the estimation of the normalised conversion efficiency. However, as the source of those equations is missing, it is very hard to compare reliably the two methods.

7.3. Pure degenerate PDC states in LNOI

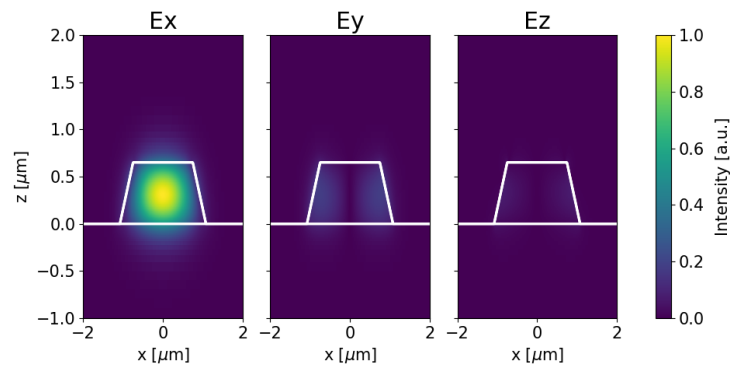


(a) Highest expected conversion efficiency η [%/W] for FE waveguides.

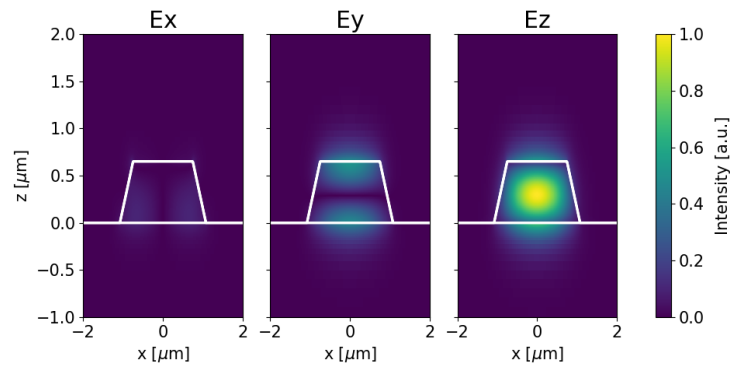


(b) Highest expected conversion efficiency η [%/W] for PE waveguides.

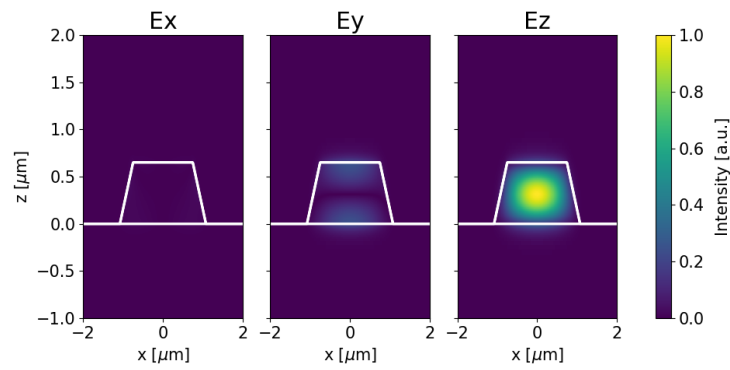
Figure 7.16. – The plots report the conversion efficiency $\eta = \eta_{norm} L_{max}^2$ of the LNOI systems investigated in Figure 7.15 and Table 7.1. The maximum waveguide length is limited to 1cm.



(a) TE 1550



(b) TM 1550



(c) TM 775

Figure 7.17. – Fundamental modes used to evaluate the efficiency of FE.

Therefore, the overlap integral θ is evaluated as

$$\begin{aligned}\theta &= \iint dx dz \hat{d}(x, z) \tilde{\mathcal{E}}_{\perp,1}(x, z) \tilde{\mathcal{E}}_{\perp,2}(x, z) \tilde{\mathcal{E}}_{\perp,3}^*(x, z) \\ &\approx^7 \iint dx dz \hat{d}(x, z) \tilde{\mathcal{E}}_{z,1550nm TM}(x, z) \tilde{\mathcal{E}}_{x,1550nm TE}(x, z) \tilde{\mathcal{E}}_{x,775nm TE}^*(x, z),\end{aligned}$$

where the three field distributions are normalised as

$$\begin{aligned}\tilde{\mathcal{E}}_{z,1550nm TM}(x, z) &= \frac{\mathcal{E}_{z,1550nm TM}(x, z)}{\sqrt{\iint dx dz |\mathcal{E}_{\perp,1550nm TM}(x, z)|^2 + |\mathcal{E}_{z,1550nm TM}(x, z)|^2}} \\ \tilde{\mathcal{E}}_{x,1550nm TE}(x, z) &= \frac{\mathcal{E}_{x,1550nm TE}(x, z)}{\sqrt{\iint dx dz |\mathcal{E}_{\perp,1550nm TE}(x, z)|^2 + |\mathcal{E}_{z,1550nm TE}(x, z)|^2}} \\ \tilde{\mathcal{E}}_{x,775nm TE}(x, z) &= \frac{\mathcal{E}_{x,775nm TE}(x, z)}{\sqrt{\iint dx dz |\mathcal{E}_{\perp,775nm TE}(x, z)|^2 + |\mathcal{E}_{z,775nm TE}(x, z)|^2}}.\end{aligned}$$

Finally, it is important not to forget the presence of the normalised nonlinear distribution

$$\hat{d}(x, z) = \begin{cases} 1 & \text{inside the LN region} \\ 0 & \text{elsewhere} \end{cases}$$

in the calculation of θ . Due to the sharp transition between LN and air (or SiO₂), the tails of the guided modes do not lie in the nonlinear material and therefore they do not contribute to the TWM process. Neglecting the spatial distribution of the nonlinearity leads to an overestimation of the overlap integral θ and of the normalised conversion efficiency η_{norm} .

7.4. Analysis of facet reflectivity

As previously outlined, high index contrast waveguides can exhibit wild behaviours, when compared to weakly guiding structures. In the first part of this chapter, we studied the effect of waveguide geometry on the dispersion relations of LNOI waveguides, noting that the strong guiding regime allows for a much more flexible engineering of nonlinear processes. Here, we want to briefly discuss a second, important characteristic of HIC waveguides, that is often overlooked: the reflectivity of the end facets.

Previously, we have observed that, for weakly guiding waveguides, the power reflectivity coefficients R for a given spatial mode at the waveguide-air interface is usually approximated by the Fresnel coefficient

$$R = \left(\frac{n_{eff} - 1}{n_{eff} + 1} \right)^2. \quad (7.13)$$

⁷This approximation is valid since there is only one main polarisation component in the transversal plane.

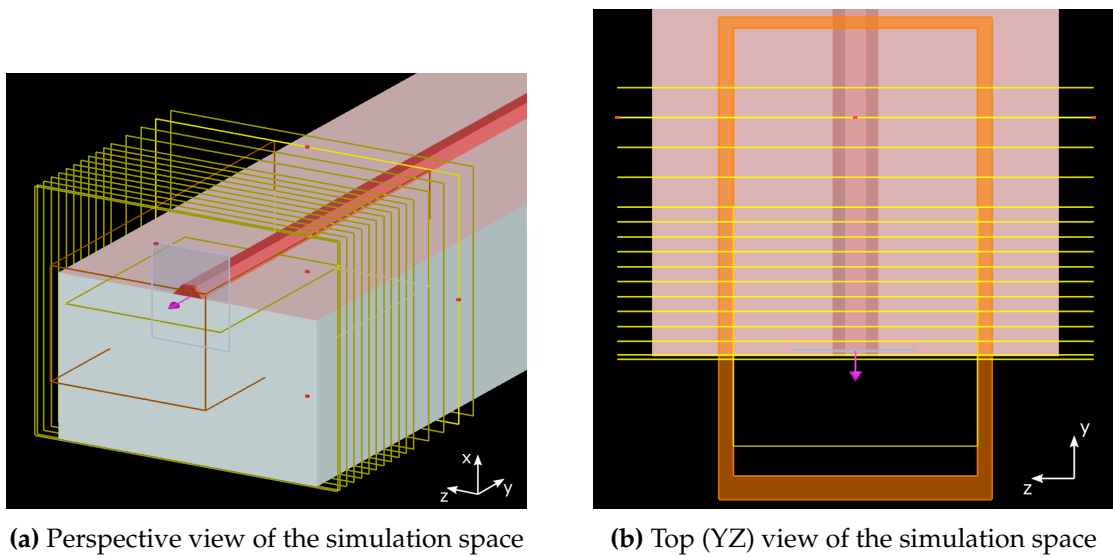


Figure 7.18. – Simulation region for the evaluation of the facet reflectivity. The domain mesh, indicated with an orange outline, has dimensions of $7\mu\text{m}$ (x) \times $15\mu\text{m}$ (y) \times $6\mu\text{m}$ (z). The drawings have different scaling along each axis for better visualisation of the simulation region.

This approximation is not valid in a strongly guiding waveguide. Indeed, as discussed in [4], approximating the reflectivity of the facets of a HIC waveguide with the Fresnel coefficient can lead to considerable errors. This is problematic in all the applications where a correct evaluation of the facets reflectivity is necessary, e.g. to correctly evaluate the propagation losses using the Fabry-Pérot method or to design dielectric coatings to improve the coupling to the device.

Different methods exist in the literature to estimate the reflectivity coefficient of HIC structures [4, 116–118] without the use of FDTD simulations. However, all of them assume an isotropic dielectric (or semiconductor) and most of them consider a simplified 1D slab waveguide. Therefore, all these methods are not directly suited for the study of facet reflectivity in LNOI structures.

For this reason, we perform a preliminary study of the facet reflectivity of LNOI waveguides using FDTD simulations, via the FDTD Solution module in Lumerical. The massive requirements in terms of computational power and time prevented us from performing a full analysis. Further exploration on this topic is left as future work.

The geometry of the simulation is set up as shown in Figure 7.18. The system under investigation is a FE LNOI waveguide with $\tau = 600\text{nm}$, $\theta = 63^\circ$ and $w \in [0.5, 1.5] \mu\text{m}$. The simulation space is a rectangle with dimensions $7\mu\text{m} \times 15\mu\text{m} \times 6\mu\text{m}$, denoted by the orange box in the Figure. The simulation mesh type is set to conformal variant 0, a setting that allows Lumerical to accurately take into account dielectric boundaries that

lie within a rectangular mesh unit. The mesh accuracy factor is set to 2, corresponding to a relatively coarse mesh that allows relatively short simulation times (in the order of 0.5h). The dt stability factor is set to 0.8 (corresponding to a time step of 0.038 fs) and the minimum mesh step is set to 0.25nm. These settings ensured simulation convergence, despite the relatively coarse mesh. The boundaries of the simulation domain are set to PML, using Lumerical standard values. The maximum simulation time is set to 1ps.

The source field, corresponding to the fundamental TE mode of the waveguide, is defined in the dark grey plane intersecting the waveguide 0.2 μ m before the waveguide facet and is launched towards the waveguide end facet, as indicated by the purple arrow. It is modelled as a pulse⁸ with a Gaussian spectrum in ω , with wavelengths spanning from 1.0 μ m to 2.0 μ m.

We monitor the evolution of the field in the waveguide using 15 power monitors perpendicular to the transversal axis of the waveguide, denoted by the yellow squares in the Figure. These monitors record the total power of the light field passing through the monitor, with a wavelength resolution of 20nm. One monitor is placed 100nm after the waveguide end facet. This monitor, denoted as *T monitor*, is used to record the total power transmitted out of the waveguide. The other 14 monitors, *R0* to *R13*, are placed inside the waveguide, behind the source plane. The monitor *R0* is located 500nm inside the waveguide. Monitors *R0* to *R9* are regularly spaced with a pitch of 500nm, while the remaining monitors are spaced by 1 μ m.

To study the reflection mechanisms in LNOI structure, we analyse the total power measured in each power monitor throughout the simulation, for different waveguide widths. The results are shown in Figure 7.19, where only the outputs of some monitors are shown⁹, along with the Fresnel reflection coefficient as inferred from Eq. (7.13) using the simulated n_{eff} . To check the consistency of the simulation, we verify that the sum of the powers measured by *R0* and *T* is 1, due to energy conservation.

The results of the simulation show that the reflection of our LNOI waveguides follows a behaviour that is not described by the simple Fresnel coefficient. In particular, the reflection coefficient is always higher than Fresnel one. Moreover, it can be seen that the total power is not conserved in the simulation domain: as the mode propagates further away from the waveguide-air interface some energy is lost, since light reflected by the waveguide facet is coupled to radiation modes. This behaviour is stronger at wavelengths above 1400nm and settles after $\sim 8\mu$ m.

This effect can be seen by the plots in Figure 7.20. The Figure tracks the distribution of the magnitude $|E|$ of the reflected field at different positions along a 1 μ m-wide waveguide, for $\lambda = 2000$ nm. In Figure 7.20a, it can be seen that the reflected field is not confined to the waveguide, but has very deep tails in the substrate and above the waveguide. As the field travels away from the waveguide facet, these tails fade, carrying away part of the reflected power. The system reaches a steady state after approximately 8 μ m, as shown in Figure 7.20f. In the simulation, more than $2/3$ of the reflected

⁸The power of FDTD simulations is the capability of performing frequency-dependent analysis by injecting pulsed light and then Fourier transforming the monitored results.

⁹We avoided showing the complete dataset for all monitors to improve the readability of the plots. The data from the missing monitors show the same trend as the one reported here.

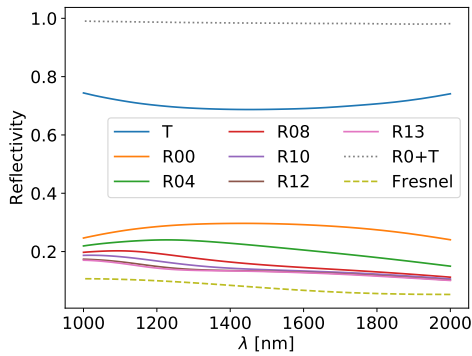
power has been coupled to radiation modes and lost from the waveguide.

These preliminary results show that the topic of LNOI facet reflectivity is extremely complex and needs to be investigated in detail. The effects shown here have crucial repercussions on the design of anti-reflection coatings and on the characterisation of LNOI samples via the standard Fabry-Pérot technique. In this regard, the results presented here seem to invalidate some recent published results [119] that calculate the reflectivity of LNOI waveguides using the simple Fresnel coefficient. In fact, an erroneous estimation of the facet reflectivity can introduce significant error when retrieving the propagation losses of a LNOI waveguide. This can be seen in Figure 7.21, where the error between the actual losses and the inferred losses of the fundamental mode (at $\lambda = 1550\text{nm}$) of a LNOI waveguide is shown as a function of the sample length, for different waveguide widths. One can see that the error is always greater than 1dB/cm and it rapidly increases for shorter samples. This trend highlights that this measurement technique is not suitable for the estimation of propagation losses in LNOI waveguides, without a careful evaluation of the reflectivity of the waveguide facets.

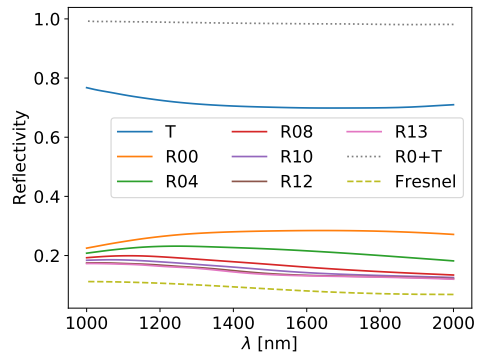
Summary

In this chapter, we discussed some of the main properties of LNOI waveguides with the help of numerical simulations. We calculated the dispersion relations of LNOI waveguides in X-cut LN thin films for different waveguide geometries and used them to investigate the possibility of engineering novel PDC sources in LNOI waveguides. During this investigation, we developed a novel method to study and visualise nonlinear processes in waveguide. Using this method, we highlighted some interesting processes available exclusively in LNOI waveguides. Interested by the possibility of realising a degenerate, decorrelated type II PDC source in LNOI waveguides, we studied the properties of this process. In particular, we focused our interest in estimating the maximum theoretical conversion efficiency in these systems, when fabrication errors are taken into consideration. Finally, we briefly presented the problem of correctly estimating the facet reflectivity in LNOI waveguides.

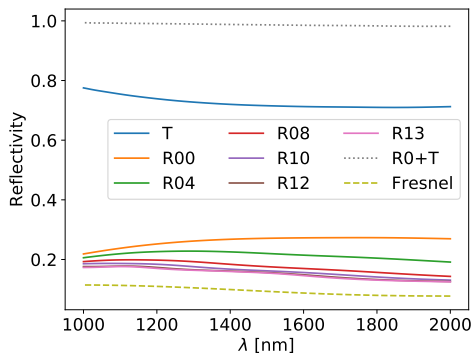
7.4. Analysis of facet reflectivity



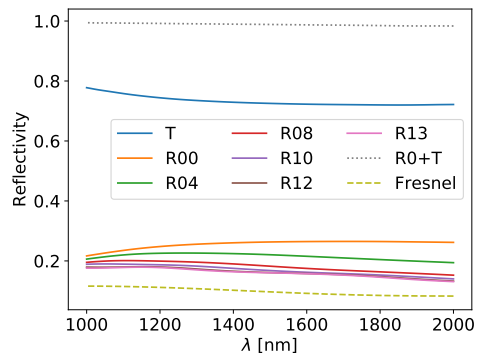
(a) $w = 0.5\mu\text{m}$.



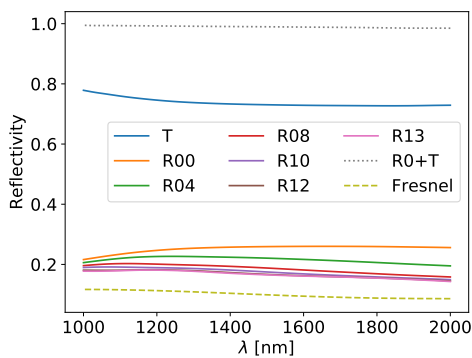
(b) $w = 0.75\mu\text{m}$.



(c) $w = 1.0\mu\text{m}$.

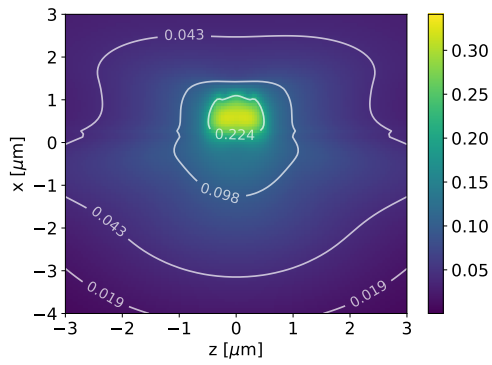


(d) $w = 1.25\mu\text{m}$.

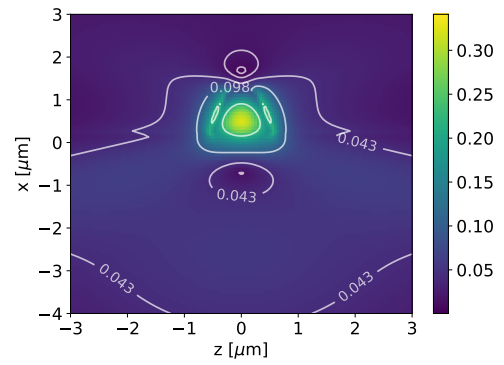


(e) $w = 1.5\mu\text{m}$.

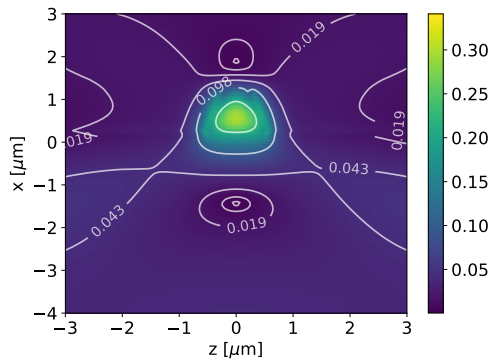
Figure 7.19. – Field power measured by different monitors, for different waveguide widths.



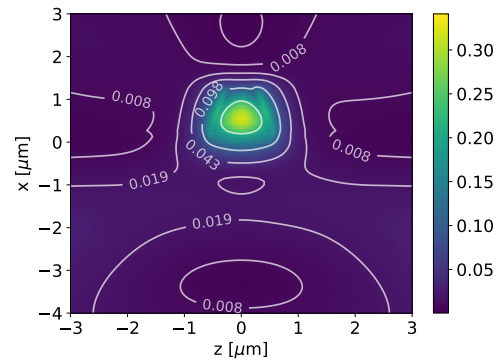
(a) Monitor R0 ($y = 0.5\mu\text{m}$).



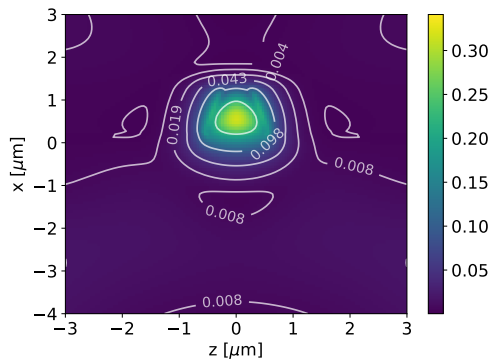
(b) Monitor R2 ($y = 1.5\mu\text{m}$).



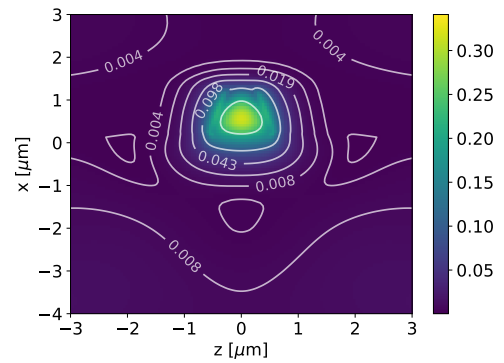
(c) Monitor R4 ($y = 2.5\mu\text{m}$).



(d) Monitor R8 ($y = 4.5\mu\text{m}$).



(e) Monitor R10 ($y = 6\mu\text{m}$).



(f) Monitor R12 ($y = 8\mu\text{m}$).

Figure 7.20. – Field distribution $|E(z, x)|$ of the reflected field recorded at different monitors for $\lambda=2000\text{nm}$ for a $1\mu\text{m}$ -wide waveguide.

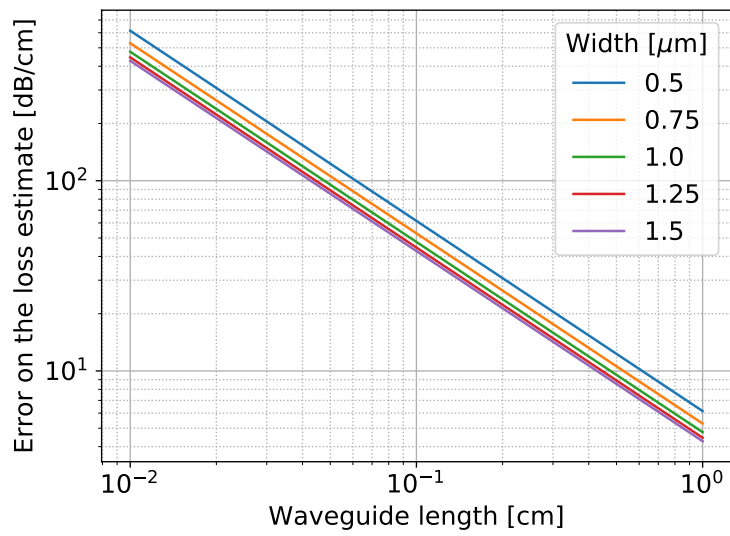


Figure 7.21. – The plot shows the error $\alpha_{real} - \alpha_{inferred}$ when estimating the propagation losses at 1550nm of a LNOI waveguide using the Fabry-Pérot technique, for different sample length and waveguide widths.

Conclusions

The usage of integrated nonlinear devices for quantum optics applications is continuously increasing due to the advantages they offer with respects to the more traditional bulk crystals. Integrated systems are inherently phase stable, offer much higher nonlinear efficiencies due to the smaller modal confinement and can be interfaced much more easily with current fibre optical systems. Most of the current know-how of integrated nonlinear devices derives from the design of devices intended for classical applications. However, the requirements of quantum optics applications can be very different from the classical optics one. For example, while many classical applications require the optimisation of device efficiency, many quantum optics protocols have stronger constraints on the spectral properties of the nonlinear process. For this reason, it is important to assess the performance of current technological platforms bearing in mind their quantum optics applications. At the same time, it is fundamental to investigate new types of materials and technologies, as these can exhibit properties more suitable for quantum optics applications than the current established technologies. The work of this thesis addresses these aspects both theoretically and experimentally.

In chapter 4, we discussed a number of quantum optics applications of self-made KTP waveguides. In particular, we described the fabrication and characterisation of two devices for quantum optics applications, namely a frequency converter and a PDC source. On the one hand, we showed that the fabrication of the frequency converter requires further improvements for successful application as a quantum interface between quantum memories and the fibre network. On the other hand, we showed that the unique dispersion properties of KTP waveguides offer the possibility of realising a heralded source of pure single photons with arbitrary temporal profiles. In chapter 5, we reported a detailed study of the effect of fabrication imperfections on the performance of LN waveguides. We showed that the distribution of these imperfections along the waveguide is crucial in determining the degradation of its performance, particularly when their application in quantum optics protocols is taken into account. In the same chapter, we presented a general framework for the description and the analysis of the impact of fabrication imperfections on the performance of a wide variety of nonlinear optical systems, e.g. optical waveguides, photonic crystal fibres, hollow-core fibres, nanophotonic waveguides, etc. In chapter 6, we discussed a new method for the measurement of the propagation losses of a multimode nonlinear waveguide. Finally, in chapter 7, we reported one of the first in-depth analyses of the characteristics of LNOI waveguides. We discussed the effect of different geometries on the dispersion

properties of these waveguides and analysed the impact of fabrication imperfections on the generation of PDC states in this system.

The work in this thesis lays a strong foundation for continued development of integrated technologies, particularly in the quantum domain. In particular, the general framework presented in chapter 5 will aid in the analysis of imperfections in nonlinear systems will help the optimisation of the design of current integrated technologies and will speed up the implementation of efficient quantum optical protocols in new technological platforms. Similarly, this thesis has provided a concrete starting point for the investigation of novel devices in LNOI through dispersion engineering, which will help the development of this relatively new technological platform.

Part III.

Appendix

A

Coefficients for LNOI waveguides

In the following, we provide the coefficients used to calculate the effective refractive index of LNOI waveguides using the following equation

$$n_{effective}^{e/o}(\lambda, T) = n_{bulk}^{e/o}(\lambda, T) + A^{e/o}\lambda^3 + B^{e/o}\lambda^2 + C^{e/o}\lambda + D^{e/o}\sqrt{\lambda} + E^{e/o} + F^{e/o} \log \lambda,$$

where $n_{bulk}^{e/o}$ are the bulk Sellmeier equations for LiNbO₃ reported in section 3.1. These coefficients have been retrieved via a nonlinear least square fit between the equation above and the n_{eff} simulated with the MODESolution solver in Lumerical [114], as described in section 7.1.

Fully etched capped LNOI waveguide coefficients

w	τ	h	pol	λ_{max}	A	B	C	D	E	F
0.5	0.45	0.45	e	1.837	$5.593 \cdot 10^{-2}$	-0.146	-0.644	1.345	-0.843	-0.253
0.5	0.45	0.45	o	1.658	0.198	-0.913	2.637	-5.092	2.887	0.693
0.5	0.5	0.5	e	1.926	$6.458 \cdot 10^{-2}$	-0.277	0.287	-0.552	0.269	$2.927 \cdot 10^{-2}$
0.5	0.5	0.5	o	1.837	0.147	-0.712	2.005	-3.896	2.21	0.527
0.5	0.55	0.55	e	2.016	$6.148 \cdot 10^{-2}$	-0.304	0.608	-1.224	0.67	0.133
0.5	0.55	0.55	o	1.926	0.129	-0.692	2.239	-4.408	2.516	0.605
0.5	0.6	0.6	e	2.105	$5.983 \cdot 10^{-2}$	-0.338	0.989	-2.067	1.186	0.27
0.5	0.6	0.6	o	2.105	$9.844 \cdot 10^{-2}$	-0.55	1.728	-3.432	1.962	0.469
0.5	0.65	0.65	e	2.105	$2.852 \cdot 10^{-2}$	$-8.503 \cdot 10^{-2}$	-0.655	1.612	-1.056	-0.318
0.5	0.65	0.65	o	2.195	$8.437 \cdot 10^{-2}$	-0.504	1.703	-3.43	1.973	0.474
0.5	0.7	0.7	e	2.195	$3.397 \cdot 10^{-2}$	-0.166	$2.512 \cdot 10^{-2}$	$8.692 \cdot 10^{-2}$	-0.123	$-7.15 \cdot 10^{-2}$
0.5	0.7	0.7	o	2.284	$7.172 \cdot 10^{-2}$	-0.452	1.597	-3.258	1.882	0.454
0.7	0.45	0.45	e	2.016	$3.211 \cdot 10^{-2}$	$-7.59 \cdot 10^{-2}$	-0.646	1.305	-0.816	-0.248
0.7	0.45	0.45	o	1.747	0.148	-0.676	1.761	-3.484	1.995	0.479
0.7	0.5	0.5	e	2.016	$3.552 \cdot 10^{-2}$	-0.145	-0.112	0.199	-0.157	$-7.618 \cdot 10^{-2}$
0.7	0.5	0.5	o	1.926	0.115	-0.57	1.525	-3.01	1.718	0.409
0.7	0.55	0.55	e	2.105	$3.215 \cdot 10^{-2}$	-0.147	$-9.237 \cdot 10^{-3}$	$5.384 \cdot 10^{-3}$	$-4.183 \cdot 10^{-2}$	$-4.545 \cdot 10^{-2}$
0.7	0.55	0.55	o	2.105	$9.046 \cdot 10^{-2}$	-0.476	1.275	-2.516	1.432	0.337
0.7	0.6	0.6	e	2.195	$2.701 \cdot 10^{-2}$	-0.129	$-3.102 \cdot 10^{-2}$	$5.488 \cdot 10^{-2}$	$-6.719 \cdot 10^{-2}$	$-4.974 \cdot 10^{-2}$
0.7	0.6	0.6	o	2.195	$8.053 \cdot 10^{-2}$	-0.468	1.474	-2.949	1.69	0.403
0.7	0.65	0.65	e	2.284	$2.486 \cdot 10^{-2}$	-0.12	-0.109	0.352	-0.281	-0.114
0.7	0.65	0.65	o	2.284	$6.968 \cdot 10^{-2}$	-0.435	1.487	-3.009	1.733	0.415
0.7	0.7	0.7	e	2.284	$2.144 \cdot 10^{-2}$	-0.108	-0.101	0.321	-0.256	-0.104
0.7	0.7	0.7	o	2.374	$5.951 \cdot 10^{-2}$	-0.393	1.409	-2.883	1.668	0.401
0.9	0.45	0.45	e	2.105	$2.452 \cdot 10^{-2}$	$-8.65 \cdot 10^{-2}$	-0.204	0.173	$-9.056 \cdot 10^{-2}$	$-4.954 \cdot 10^{-2}$
0.9	0.45	0.45	o	1.837	0.108	-0.452	0.792	-1.656	0.966	0.229
0.9	0.5	0.5	e	2.195	$2.256 \cdot 10^{-2}$	$-8.533 \cdot 10^{-2}$	-0.242	0.411	-0.268	-0.102
0.9	0.5	0.5	o	2.016	$8.827 \cdot 10^{-2}$	-0.416	0.857	-1.723	0.987	0.23
0.9	0.55	0.55	e	2.195	$1.989 \cdot 10^{-2}$	$-8.235 \cdot 10^{-2}$	-0.212	0.39	-0.26	$-9.949 \cdot 10^{-2}$

0.9	0.55	0.55	o	2.105	$8.23 \cdot 10^{-2}$	-0.452	1.303	-2.616	1.501	0.357
0.9	0.6	0.6	e	2.284	$1.396 \cdot 10^{-2}$	$-4.599 \cdot 10^{-2}$	-0.405	0.842	-0.536	-0.17
0.9	0.6	0.6	o	2.284	$6.579 \cdot 10^{-2}$	-0.382	1.111	-2.232	1.278	0.301
0.9	0.65	0.65	e	2.374	$2.061 \cdot 10^{-2}$	-0.117	$8.745 \cdot 10^{-2}$	-0.158	$4.751 \cdot 10^{-2}$	$-2.35 \cdot 10^{-2}$
0.9	0.65	0.65	o	2.284	$6.234 \cdot 10^{-2}$	-0.402	1.422	-2.903	1.678	0.403
0.9	0.7	0.7	e	2.374	$1.599 \cdot 10^{-2}$	$-8.644 \cdot 10^{-2}$	$-7.676 \cdot 10^{-2}$	0.219	-0.181	$-8.235 \cdot 10^{-2}$
0.9	0.7	0.7	o	2.374	$5.314 \cdot 10^{-2}$	-0.362	1.34	-2.76	1.601	0.385
1.1	0.45	0.45	e	2.105	$1.637 \cdot 10^{-2}$	$-4.563 \cdot 10^{-2}$	-0.315	0.38	-0.208	$-7.921 \cdot 10^{-2}$
1.1	0.45	0.45	o	1.926	$7.556 \cdot 10^{-2}$	-0.254	-0.141	0.142	$-5.476 \cdot 10^{-2}$	$-2.205 \cdot 10^{-2}$
1.1	0.5	0.5	e	2.195	$9.861 \cdot 10^{-3}$	$-5.949 \cdot 10^{-3}$	-0.555	0.968	-0.569	-0.171
1.1	0.5	0.5	o	2.105	$6.642 \cdot 10^{-2}$	-0.277	0.188	-0.407	0.231	$4.236 \cdot 10^{-2}$
1.1	0.55	0.55	e	2.284	$1.497 \cdot 10^{-2}$	$-6.112 \cdot 10^{-2}$	-0.213	0.352	-0.228	$-8.943 \cdot 10^{-2}$
1.1	0.55	0.55	o	2.195	$6.613 \cdot 10^{-2}$	-0.348	0.808	-1.635	0.937	0.217
1.1	0.6	0.6	e	2.374	$1.184 \cdot 10^{-2}$	$-4.509 \cdot 10^{-2}$	-0.291	0.562	-0.36	-0.123
1.1	0.6	0.6	o	2.284	$6.012 \cdot 10^{-2}$	-0.356	1.054	-2.142	1.233	0.291
1.1	0.65	0.65	e	2.374	$1.985 \cdot 10^{-2}$	-0.128	0.281	-0.618	0.334	$5.249 \cdot 10^{-2}$
1.1	0.65	0.65	o	2.374	$5.286 \cdot 10^{-2}$	-0.34	1.129	-2.313	1.336	0.318
1.1	0.7	0.7	e	2.463	$1.264 \cdot 10^{-2}$	$-7.009 \cdot 10^{-2}$	$-7.781 \cdot 10^{-2}$	0.188	-0.154	$-7.348 \cdot 10^{-2}$
1.1	0.7	0.7	o	2.463	$4.563 \cdot 10^{-2}$	-0.312	1.106	-2.284	1.323	0.316
1.3	0.45	0.45	e	2.195	$1.464 \cdot 10^{-2}$	$-4.765 \cdot 10^{-2}$	-0.2	0.11	$-4.276 \cdot 10^{-2}$	$-3.64 \cdot 10^{-2}$
1.3	0.45	0.45	o	1.926	$6.923 \cdot 10^{-2}$	-0.228	-0.188	0.2	$-7.956 \cdot 10^{-2}$	$-2.644 \cdot 10^{-2}$
1.3	0.5	0.5	e	2.284	$1.008 \cdot 10^{-2}$	$-2.05 \cdot 10^{-2}$	-0.378	0.58	-0.336	-0.112
1.3	0.5	0.5	o	2.105	$6.121 \cdot 10^{-2}$	-0.254	0.144	-0.348	0.205	$3.723 \cdot 10^{-2}$
1.3	0.55	0.55	e	2.374	$1.717 \cdot 10^{-2}$	$-9.609 \cdot 10^{-2}$	0.125	-0.422	0.246	$3.44 \cdot 10^{-2}$
1.3	0.55	0.55	o	2.195	$6.118 \cdot 10^{-2}$	-0.323	0.74	-1.522	0.877	0.203
1.3	0.6	0.6	e	2.374	$1.031 \cdot 10^{-2}$	$-4.126 \cdot 10^{-2}$	-0.236	0.422	-0.271	$-9.946 \cdot 10^{-2}$
1.3	0.6	0.6	o	2.284	$5.593 \cdot 10^{-2}$	-0.334	0.992	-2.036	1.175	0.278
1.3	0.65	0.65	e	2.463	$6.672 \cdot 10^{-3}$	$-1.449 \cdot 10^{-2}$	-0.408	0.85	-0.539	-0.17
1.3	0.65	0.65	o	2.374	$4.9 \cdot 10^{-2}$	-0.318	1.055	-2.175	1.259	0.3
1.3	0.7	0.7	e	2.463	$1.218 \cdot 10^{-2}$	$-7.423 \cdot 10^{-2}$	$2.75 \cdot 10^{-2}$	$-7.099 \cdot 10^{-2}$	$9.745 \cdot 10^{-3}$	$-2.922 \cdot 10^{-2}$
1.3	0.7	0.7	o	2.463	$4.223 \cdot 10^{-2}$	-0.292	1.033	-2.143	1.244	0.296
1.5	0.45	0.45	e	2.195	$6.563 \cdot 10^{-3}$	$1.174 \cdot 10^{-2}$	-0.497	0.701	-0.382	-0.12
1.5	0.45	0.45	o	1.926	$6.399 \cdot 10^{-2}$	-0.202	-0.26	0.318	-0.141	$-4.038 \cdot 10^{-2}$
1.5	0.5	0.5	e	2.284	$1.091 \cdot 10^{-2}$	$-3.63 \cdot 10^{-2}$	-0.209	0.196	-0.102	$-5.133 \cdot 10^{-2}$
1.5	0.5	0.5	o	2.105	$5.723 \cdot 10^{-2}$	-0.235	$9.543 \cdot 10^{-2}$	-0.274	0.168	$2.927 \cdot 10^{-2}$
1.5	0.55	0.55	e	2.374	$6.82 \cdot 10^{-3}$	$-7.678 \cdot 10^{-3}$	-0.407	0.706	-0.423	-0.136
1.5	0.55	0.55	o	2.195	$5.736 \cdot 10^{-2}$	-0.302	0.668	-1.392	0.805	0.186
1.5	0.6	0.6	e	2.463	$1.054 \cdot 10^{-2}$	$-5.172 \cdot 10^{-2}$	$-9.26 \cdot 10^{-2}$	$7.395 \cdot 10^{-2}$	$-5.224 \cdot 10^{-2}$	$-4.083 \cdot 10^{-2}$
1.5	0.6	0.6	o	2.284	$5.252 \cdot 10^{-2}$	-0.314	0.918	-1.896	1.097	0.259
1.5	0.65	0.65	e	2.463	$7.799 \cdot 10^{-3}$	$-3.08 \cdot 10^{-2}$	-0.239	0.46	-0.299	-0.107
1.5	0.65	0.65	o	2.374	$4.624 \cdot 10^{-2}$	-0.301	0.996	-2.062	1.196	0.284
1.5	0.7	0.7	e	2.553	$4.23 \cdot 10^{-3}$	$-9.297 \cdot 10^{-4}$	-0.446	0.971	-0.62	-0.192
1.5	0.7	0.7	o	2.463	$3.996 \cdot 10^{-2}$	-0.278	0.985	-2.052	1.192	0.284
1.7	0.45	0.45	e	2.195	$3.137 \cdot 10^{-3}$	$3.56 \cdot 10^{-2}$	-0.598	0.894	-0.491	-0.147
1.7	0.45	0.45	o	2.016	$3.95 \cdot 10^{-2}$	$-2.907 \cdot 10^{-2}$	-1.176	2.133	-1.185	-0.3
1.7	0.5	0.5	e	2.284	$5.413 \cdot 10^{-3}$	$8.166 \cdot 10^{-3}$	-0.454	0.703	-0.4	-0.126
1.7	0.5	0.5	o	2.105	$5.386 \cdot 10^{-2}$	-0.216	$3.071 \cdot 10^{-2}$	-0.158	0.104	$1.428 \cdot 10^{-2}$
1.7	0.55	0.55	e	2.374	$8.957 \cdot 10^{-3}$	$-3.346 \cdot 10^{-2}$	-0.175	0.168	$-9.088 \cdot 10^{-2}$	$-4.76 \cdot 10^{-2}$
1.7	0.55	0.55	o	2.195	$5.478 \cdot 10^{-2}$	-0.287	0.623	-1.315	0.764	0.177
1.7	0.6	0.6	e	2.463	$5.067 \cdot 10^{-3}$	$-1.994 \cdot 10^{-3}$	-0.407	0.763	-0.468	-0.149
1.7	0.6	0.6	o	2.284	$5.023 \cdot 10^{-2}$	-0.3	0.871	-1.811	1.05	0.248
1.7	0.65	0.65	e	2.463	$8.018 \cdot 10^{-3}$	$-3.693 \cdot 10^{-2}$	-0.152	0.249	-0.166	$-7.129 \cdot 10^{-2}$
1.7	0.65	0.65	o	2.374	$4.413 \cdot 10^{-2}$	-0.287	0.944	-1.963	1.14	0.27
1.7	0.7	0.7	e	2.553	$5.91 \cdot 10^{-3}$	$-2.143 \cdot 10^{-2}$	-0.255	0.525	-0.343	-0.119
1.7	0.7	0.7	o	2.463	$3.836 \cdot 10^{-2}$	-0.267	0.946	-1.976	1.149	0.273
1.9	0.45	0.45	e	2.195	$5.242 \cdot 10^{-3}$	$1.254 \cdot 10^{-2}$	-0.406	0.462	-0.228	$-7.785 \cdot 10^{-2}$
1.9	0.45	0.45	o	2.016	$3.266 \cdot 10^{-2}$	$1.646 \cdot 10^{-2}$	-1.394	2.553	-1.423	-0.358
1.9	0.5	0.5	e	2.284	$2.397 \cdot 10^{-3}$	$3.261 \cdot 10^{-2}$	-0.585	0.977	-0.562	-0.167
1.9	0.5	0.5	o	2.105	$5.125 \cdot 10^{-2}$	-0.2	$-2.993 \cdot 10^{-2}$	$-4.574 \cdot 10^{-2}$	$4.172 \cdot 10^{-2}$	$-8.16 \cdot 10^{-4}$
1.9	0.55	0.55	e	2.374	$4.329 \cdot 10^{-3}$	$7.913 \cdot 10^{-3}$	-0.433	0.732	-0.431	-0.136
1.9	0.55	0.55	o	2.195	$5.294 \cdot 10^{-2}$	-0.276	0.583	-1.24	0.722	0.167
1.9	0.6	0.6	e	2.463	$5.791 \cdot 10^{-3}$	$-1.295 \cdot 10^{-2}$	-0.288	0.478	-0.29	-0.101
1.9	0.6	0.6	o	2.284	$4.874 \cdot 10^{-2}$	-0.291	0.837	-1.745	1.013	0.239
1.9	0.65	0.65	e	2.463	$5.437 \cdot 10^{-3}$	$-1.299 \cdot 10^{-2}$	-0.299	0.572	-0.361	-0.122
1.9	0.65	0.65	o	2.374	$4.237 \cdot 10^{-2}$	-0.275	0.889	-1.854	1.077	0.255
1.9	0.7	0.7	e	2.553	$6.06 \cdot 10^{-3}$	$-2.572 \cdot 10^{-2}$	-0.189	0.358	-0.237	$-8.991 \cdot 10^{-2}$
1.9	0.7	0.7	o	2.463	$3.681 \cdot 10^{-2}$	-0.256	0.897	-1.879	1.093	0.259

Fully etched uncapped LNOI waveguide coefficients

w	τ	h	pol	λ_{max}	A	B	C	D	E	F
0.5	0.45	0.45	e	1.658	$5.511 \cdot 10^{-2}$	-0.162	-1.051	2.541	-1.636	-0.472
0.5	0.45	0.45	o	1.568	0.481	-2.678	10.39	-19.09	10.584	2.529
0.5	0.5	0.5	e	1.747	0.101	-0.587	1.662	-3.039	1.637	0.355
0.5	0.5	0.5	o	1.747	0.351	-2.084	8.414	-15.798	8.848	2.13
0.5	0.55	0.55	e	1.837	$9.619 \cdot 10^{-2}$	-0.613	2.099	-4.036	2.251	0.518
0.5	0.55	0.55	o	1.837	0.262	-1.647	6.866	-13.143	7.426	1.798
0.5	0.6	0.6	e	1.926	$8.895 \cdot 10^{-2}$	-0.611	2.346	-4.665	2.656	0.629
0.5	0.6	0.6	o	1.926	0.198	-1.306	5.575	-10.854	6.179	1.503
0.5	0.65	0.65	e	2.016	$3.054 \cdot 10^{-2}$	-0.132	-0.675	1.929	-1.321	-0.403
0.5	0.65	0.65	o	2.016	0.151	-1.048	4.556	-9.008	5.162	1.261
0.5	0.7	0.7	e	2.105	$4.618 \cdot 10^{-2}$	-0.308	0.711	-1.201	0.598	0.103
0.5	0.7	0.7	o	2.195	0.122	-0.883	3.934	-7.896	4.555	1.117
0.5	0.75	0.75	e	2.195	$4.12 \cdot 10^{-2}$	-0.291	0.749	-1.334	0.693	0.131
0.5	0.75	0.75	o	2.284	$9.67 \cdot 10^{-2}$	-0.728	3.279	-6.668	3.867	0.951
0.7	0.45	0.45	e	1.837	$9.166 \cdot 10^{-2}$	-0.605	2.442	-5.135	2.991	0.724
0.7	0.45	0.45	o	1.658	0.37	-2.088	8.039	-14.899	8.296	1.987
0.7	0.5	0.5	e	1.926	$4.563 \cdot 10^{-2}$	-0.259	0.361	-0.621	0.283	$2.543 \cdot 10^{-2}$
0.7	0.5	0.5	o	1.837	0.271	-1.644	6.605	-12.505	7.03	1.695
0.7	0.55	0.55	e	2.016	$4.015 \cdot 10^{-2}$	-0.251	0.475	-0.895	0.461	$7.555 \cdot 10^{-2}$
0.7	0.55	0.55	o	1.926	0.206	-1.327	5.536	-10.684	6.06	1.47
0.7	0.6	0.6	e	2.105	$3.285 \cdot 10^{-2}$	-0.218	0.403	-0.774	0.402	$6.477 \cdot 10^{-2}$
0.7	0.6	0.6	o	2.016	0.157	-1.068	4.576	-8.98	5.13	1.25
0.7	0.65	0.65	e	2.195	$3.08 \cdot 10^{-2}$	-0.202	0.257	-0.278	$5.17 \cdot 10^{-2}$	$-3.942 \cdot 10^{-2}$
0.7	0.65	0.65	o	2.195	0.123	-0.884	3.89	-7.755	4.461	1.092
0.7	0.7	0.7	e	2.284	$2.46 \cdot 10^{-2}$	-0.171	0.197	-0.228	$4.823 \cdot 10^{-2}$	$-3.254 \cdot 10^{-2}$
0.7	0.7	0.7	o	2.284	$9.672 \cdot 10^{-2}$	-0.725	3.238	-6.541	3.783	0.928
0.7	0.75	0.75	e	2.374	$2.019 \cdot 10^{-2}$	-0.145	0.126	-0.103	$-1.667 \cdot 10^{-2}$	$-4.595 \cdot 10^{-2}$
0.7	0.75	0.75	o	2.374	$7.696 \cdot 10^{-2}$	-0.601	2.718	-5.558	3.23	0.794
0.9	0.45	0.45	e	1.926	$3.307 \cdot 10^{-2}$	-0.18	0.198	-0.564	0.319	$4.862 \cdot 10^{-2}$
0.9	0.45	0.45	o	1.747	0.298	-1.674	6.25	-11.616	6.476	1.55
0.9	0.5	0.5	e	2.105	$3.37 \cdot 10^{-2}$	-0.199	0.279	-0.541	0.256	$2.101 \cdot 10^{-2}$
0.9	0.5	0.5	o	1.837	0.23	-1.403	5.591	-10.642	5.998	1.448
0.9	0.55	0.55	e	2.195	$2.525 \cdot 10^{-2}$	-0.156	0.147	-0.302	0.133	$-3.305 \cdot 10^{-3}$
0.9	0.55	0.55	o	2.016	0.173	-1.127	4.66	-9.038	5.136	1.246
0.9	0.6	0.6	e	2.284	$1.835 \cdot 10^{-2}$	-0.113	$-5.614 \cdot 10^{-2}$	0.152	-0.139	$-7.202 \cdot 10^{-2}$
0.9	0.6	0.6	o	2.105	0.133	-0.921	3.928	-7.746	4.434	1.081
0.9	0.65	0.65	e	2.284	$1.867 \cdot 10^{-2}$	-0.131	0.141	-0.271	0.118	$-3.874 \cdot 10^{-3}$
0.9	0.65	0.65	o	2.195	0.103	-0.753	3.285	-6.573	3.786	0.926
0.9	0.7	0.7	e	2.374	$1.776 \cdot 10^{-2}$	-0.13	0.154	-0.234	$7.848 \cdot 10^{-2}$	$-1.854 \cdot 10^{-2}$
0.9	0.7	0.7	o	2.374	$8.246 \cdot 10^{-2}$	-0.63	2.812	-5.706	3.305	0.81
0.9	0.75	0.75	e	2.463	$1.254 \cdot 10^{-2}$	$-9.081 \cdot 10^{-2}$	$-5.37 \cdot 10^{-2}$	0.218	-0.192	$-8.692 \cdot 10^{-2}$
0.9	0.75	0.75	o	2.463	$6.579 \cdot 10^{-2}$	-0.525	2.376	-4.876	2.837	0.697
1.1	0.45	0.45	e	2.016	$2.382 \cdot 10^{-2}$	-0.123	$2.554 \cdot 10^{-2}$	-0.267	0.158	$1.036 \cdot 10^{-2}$
1.1	0.45	0.45	o	1.747	0.263	-1.467	5.367	-9.997	5.58	1.335
1.1	0.5	0.5	e	2.195	$1.732 \cdot 10^{-2}$	$-8.877 \cdot 10^{-2}$	-0.14	0.148	$-9.649 \cdot 10^{-2}$	$-5.436 \cdot 10^{-2}$
1.1	0.5	0.5	o	1.926	0.196	-1.191	4.601	-8.762	4.938	1.19
1.1	0.55	0.55	e	2.284	$2.095 \cdot 10^{-2}$	-0.134	0.168	-0.41	0.213	$1.987 \cdot 10^{-2}$
1.1	0.55	0.55	o	2.016	0.153	-1.003	4.101	-7.974	4.536	1.1
1.1	0.6	0.6	e	2.374	$1.435 \cdot 10^{-2}$	$-8.948 \cdot 10^{-2}$	$-6.124 \cdot 10^{-2}$	$9.843 \cdot 10^{-2}$	$-9.002 \cdot 10^{-2}$	$-5.564 \cdot 10^{-2}$
1.1	0.6	0.6	o	2.105	0.118	-0.823	3.48	-6.882	3.944	0.961
1.1	0.65	0.65	e	2.463	$9.104 \cdot 10^{-3}$	$-5.048 \cdot 10^{-2}$	-0.285	0.622	-0.411	-0.139
1.1	0.65	0.65	o	2.284	$9.223 \cdot 10^{-2}$	-0.677	2.939	-5.898	3.401	0.831
1.1	0.7	0.7	e	2.463	$1.573 \cdot 10^{-2}$	-0.12	0.222	-0.44	0.217	$2.074 \cdot 10^{-2}$
1.1	0.7	0.7	o	2.374	$7.277 \cdot 10^{-2}$	-0.562	2.485	-5.054	2.929	0.717
1.1	0.75	0.75	e	2.553	$1.001 \cdot 10^{-2}$	$-7.281 \cdot 10^{-2}$	$-6.778 \cdot 10^{-2}$	0.212	-0.178	$-8.136 \cdot 10^{-2}$
1.1	0.75	0.75	o	2.463	$5.803 \cdot 10^{-2}$	-0.469	2.102	-4.321	2.514	0.616
1.3	0.45	0.45	e	2.105	$1.347 \cdot 10^{-2}$	$-4.902 \cdot 10^{-2}$	-0.295	0.329	-0.173	$-6.883 \cdot 10^{-2}$
1.3	0.45	0.45	o	1.747	0.237	-1.306	4.635	-8.632	4.816	1.151
1.3	0.5	0.5	e	2.195	$1.51 \cdot 10^{-2}$	$-7.706 \cdot 10^{-2}$	-0.113	$5.335 \cdot 10^{-2}$	$-3.19 \cdot 10^{-2}$	$-3.637 \cdot 10^{-2}$
1.3	0.5	0.5	o	1.926	0.179	-1.078	4.084	-7.781	4.385	1.055
1.3	0.55	0.55	e	2.284	$1.026 \cdot 10^{-2}$	$-4.713 \cdot 10^{-2}$	-0.279	0.474	-0.295	-0.105
1.3	0.55	0.55	o	2.016	0.141	-0.922	3.728	-7.261	4.133	1.002
1.3	0.6	0.6	e	2.374	$1.355 \cdot 10^{-2}$	$-8.701 \cdot 10^{-2}$	$1.019 \cdot 10^{-2}$	$-8.581 \cdot 10^{-2}$	$2.75 \cdot 10^{-2}$	$-2.413 \cdot 10^{-2}$
1.3	0.6	0.6	o	2.195	0.108	-0.748	3.121	-6.179	3.541	0.861
1.3	0.65	0.65	e	2.463	$8.564 \cdot 10^{-3}$	$-4.885 \cdot 10^{-2}$	-0.218	0.452	-0.303	-0.11
1.3	0.65	0.65	o	2.284	$8.454 \cdot 10^{-2}$	-0.623	2.679	-5.384	3.105	0.758
1.3	0.7	0.7	e	2.553	$3.94 \cdot 10^{-3}$	$-1.02 \cdot 10^{-2}$	-0.465	1.036	-0.664	-0.205
1.3	0.7	0.7	o	2.374	$6.678 \cdot 10^{-2}$	-0.518	2.276	-4.633	2.685	0.656
1.3	0.75	0.75	e	2.642	$9.23 \cdot 10^{-3}$	$-6.86 \cdot 10^{-2}$	$-1.758 \cdot 10^{-2}$	$6.709 \cdot 10^{-2}$	$-8.14 \cdot 10^{-2}$	$-5.41 \cdot 10^{-2}$
1.3	0.75	0.75	o	2.553	$5.335 \cdot 10^{-2}$	-0.434	1.935	-3.982	2.317	0.566
1.5	0.45	0.45	e	2.105	$1.299 \cdot 10^{-2}$	$-4.83 \cdot 10^{-2}$	-0.237	0.191	$-8.845 \cdot 10^{-2}$	$-4.702 \cdot 10^{-2}$
1.5	0.45	0.45	o	1.747	0.202	-1.059	3.375	-6.187	3.425	0.809
1.5	0.5	0.5	e	2.284	$7.672 \cdot 10^{-3}$	$-1.632 \cdot 10^{-2}$	-0.428	0.688	-0.399	-0.128
1.5	0.5	0.5	o	1.926	0.165	-0.983	3.622	-6.886	3.876	0.93
1.5	0.55	0.55	e	2.374	$9.707 \cdot 10^{-3}$	$-4.536 \cdot 10^{-2}$	-0.223	0.327	-0.199	$-7.864 \cdot 10^{-2}$
1.5	0.55	0.55	o	2.105	0.127	-0.817	3.183	-6.18	3.51	0.847

1.5	0.6	0.6	e	2.374	$7.936 \cdot 10^{-3}$	$-3.768 \cdot 10^{-2}$	-0.253	0.443	-0.278	$-9.92 \cdot 10^{-2}$
1.5	0.6	0.6	o	2.195	0.101	-0.702	2.903	-5.749	3.295	0.8
1.5	0.65	0.65	e	2.553	$9.157 \cdot 10^{-3}$	$-5.753 \cdot 10^{-2}$	$-9.153 \cdot 10^{-2}$	0.142	-0.107	$-5.735 \cdot 10^{-2}$
1.5	0.65	0.65	o	2.284	$7.95 \cdot 10^{-2}$	-0.586	2.502	-5.033	2.902	0.707
1.5	0.7	0.7	e	2.642	$5.96 \cdot 10^{-3}$	$-3.149 \cdot 10^{-2}$	-0.259	0.56	-0.37	-0.127
1.5	0.7	0.7	o	2.463	$6.25 \cdot 10^{-2}$	-0.485	2.115	-4.306	2.495	0.609
1.5	0.75	0.75	e	2.642	$6.603 \cdot 10^{-3}$	$-4.263 \cdot 10^{-2}$	-0.159	0.372	-0.264	-0.101
1.5	0.75	0.75	o	2.553	$5.007 \cdot 10^{-2}$	-0.408	1.811	-3.731	2.171	0.53
1.7	0.45	0.45	e	2.195	$6.82 \cdot 10^{-3}$	$3.164 \cdot 10^{-4}$	-0.479	0.666	-0.359	-0.113
1.7	0.45	0.45	o	1.389	0.477	-2.732	11.223	-20.736	11.528	2.763
1.7	0.5	0.5	e	2.284	$1.042 \cdot 10^{-2}$	$-4.303 \cdot 10^{-2}$	-0.204	0.188	$-9.581 \cdot 10^{-2}$	$-4.901 \cdot 10^{-2}$
1.7	0.5	0.5	o	1.837	0.173	-1.028	3.844	-7.296	4.104	0.985
1.7	0.55	0.55	e	2.374	$5.237 \cdot 10^{-3}$	$-4.556 \cdot 10^{-3}$	-0.46	0.833	-0.501	-0.156
1.7	0.55	0.55	o	2.105	0.119	-0.76	2.882	-5.576	3.16	0.76
1.7	0.6	0.6	e	2.463	$9.317 \cdot 10^{-3}$	$-5.319 \cdot 10^{-2}$	$-9.31 \cdot 10^{-2}$	$6.739 \cdot 10^{-2}$	$-4.418 \cdot 10^{-2}$	$-3.735 \cdot 10^{-2}$
1.7	0.6	0.6	o	2.195	$9.676 \cdot 10^{-2}$	-0.669	2.736	-5.415	3.101	0.752
1.7	0.65	0.65	e	2.553	$4.677 \cdot 10^{-3}$	$-1.317 \cdot 10^{-2}$	-0.374	0.764	-0.483	-0.155
1.7	0.65	0.65	o	2.284	$7.638 \cdot 10^{-2}$	-0.562	2.387	-4.8	2.767	0.674
1.7	0.7	0.7	e	2.642	$6.648 \cdot 10^{-3}$	$-3.958 \cdot 10^{-2}$	-0.156	0.307	-0.211	$-8.411 \cdot 10^{-2}$
1.7	0.7	0.7	o	2.463	$5.984 \cdot 10^{-2}$	-0.465	2.013	-4.099	2.375	0.578
1.7	0.75	0.75	e	2.732	$4.242 \cdot 10^{-3}$	$-1.889 \cdot 10^{-2}$	-0.296	0.665	-0.439	-0.145
1.7	0.75	0.75	o	2.553	$4.789 \cdot 10^{-2}$	-0.391	1.725	-3.553	2.066	0.503
1.9	0.45	0.45	e	2.195	$6.262 \cdot 10^{-3}$	$5.759 \cdot 10^{-3}$	-0.486	0.67	-0.359	-0.113
1.9	0.45	0.45	o	1.837	0.229	-1.31	4.877	-9.178	5.143	1.233
1.9	0.5	0.5	e	2.284	$6.162 \cdot 10^{-3}$	$-2.92 \cdot 10^{-3}$	-0.448	0.709	-0.407	-0.129
1.9	0.5	0.5	o	1.568	0.321	-1.97	8.453	-15.996	8.993	2.173
1.9	0.55	0.55	e	2.374	$7.218 \cdot 10^{-3}$	$-2.238 \cdot 10^{-2}$	-0.307	0.478	-0.281	$-9.728 \cdot 10^{-2}$
1.9	0.55	0.55	o	2.016	0.125	-0.793	3.057	-5.903	3.344	0.805
1.9	0.6	0.6	e	2.463	$6.062 \cdot 10^{-3}$	$-1.847 \cdot 10^{-2}$	-0.329	0.604	-0.373	-0.124
1.9	0.6	0.6	o	2.195	$9.117 \cdot 10^{-2}$	-0.625	2.494	-4.923	2.815	0.68
1.9	0.65	0.65	e	2.553	$7.228 \cdot 10^{-3}$	$-3.704 \cdot 10^{-2}$	-0.178	0.315	-0.207	$-8.192 \cdot 10^{-2}$
1.9	0.65	0.65	o	2.374	$6.851 \cdot 10^{-2}$	-0.499	2.033	-4.075	2.343	0.567
1.9	0.7	0.7	e	2.642	$5.349 \cdot 10^{-3}$	$-2.304 \cdot 10^{-2}$	-0.269	0.567	-0.371	-0.126
1.9	0.7	0.7	o	2.463	$5.414 \cdot 10^{-2}$	-0.419	1.762	-3.584	2.074	0.503
1.9	0.75	0.75	e	2.732	$6.326 \cdot 10^{-3}$	$-3.882 \cdot 10^{-2}$	-0.125	0.267	-0.192	$-7.972 \cdot 10^{-2}$
1.9	0.75	0.75	o	2.553	$4.272 \cdot 10^{-2}$	-0.349	1.49	-3.067	1.781	0.431

Partially etched capped LNOI waveguide coefficients

w	τ	pol	λ_{max}	A	B	C	D	E	F
0.5	0.65	e	2.105	$7.176 \cdot 10^{-3}$	$9.986 \cdot 10^{-2}$	-1.618	3.464	-2.105	-0.574
0.5	0.65	o	2.195	$7.748 \cdot 10^{-2}$	-0.44	1.334	-2.69	1.545	0.368
0.5	0.65	e	2.105	$1.505 \cdot 10^{-2}$	$4.029 \cdot 10^{-2}$	-1.346	2.971	-1.835	-0.51
0.5	0.65	o	2.195	$7.971 \cdot 10^{-2}$	-0.459	1.44	-2.899	1.664	0.397
0.5	0.65	e	2.105	$2.156 \cdot 10^{-2}$	$-1.477 \cdot 10^{-2}$	-1.063	2.429	-1.529	-0.435
0.5	0.65	o	2.195	$8.159 \cdot 10^{-2}$	-0.477	1.538	-3.096	1.778	0.425
0.5	0.65	e	2.105	$2.625 \cdot 10^{-2}$	$-5.93 \cdot 10^{-2}$	-0.811	1.93	-1.241	-0.364
0.5	0.65	o	2.195	$8.325 \cdot 10^{-2}$	-0.492	1.631	-3.284	1.887	0.453
0.5	0.65	e	2.105	$2.862 \cdot 10^{-2}$	$-8.602 \cdot 10^{-2}$	-0.648	1.599	-1.049	-0.316
0.5	0.65	o	2.195	$8.424 \cdot 10^{-2}$	-0.503	1.694	-3.41	1.96	0.471
0.7	0.65	e	2.284	$1.644 \cdot 10^{-2}$	$-3.211 \cdot 10^{-2}$	-0.617	1.373	-0.872	-0.261
0.7	0.65	o	2.284	$6.601 \cdot 10^{-2}$	-0.396	1.249	-2.52	1.447	0.343
0.7	0.65	e	2.284	$2.017 \cdot 10^{-2}$	$-6.549 \cdot 10^{-2}$	-0.441	1.031	-0.677	-0.213
0.7	0.65	o	2.284	$6.734 \cdot 10^{-2}$	-0.409	1.327	-2.68	1.541	0.367
0.7	0.65	e	2.284	$2.3 \cdot 10^{-2}$	$-9.383 \cdot 10^{-2}$	-0.277	0.701	-0.486	-0.165
0.7	0.65	o	2.284	$6.812 \cdot 10^{-2}$	-0.418	1.378	-2.782	1.6	0.382
0.7	0.65	e	2.284	$2.45 \cdot 10^{-2}$	-0.112	-0.164	0.469	-0.35	-0.131
0.7	0.65	o	2.284	$6.878 \cdot 10^{-2}$	-0.425	1.423	-2.875	1.654	0.395
0.7	0.65	e	2.284	$2.504 \cdot 10^{-2}$	-0.122	$-9.616 \cdot 10^{-2}$	0.325	-0.265	-0.11
0.7	0.65	o	2.284	$6.952 \cdot 10^{-2}$	-0.433	1.476	-2.985	1.719	0.412
0.9	0.65	e	2.374	$1.779 \cdot 10^{-2}$	$-7.845 \cdot 10^{-2}$	-0.156	0.348	-0.25	$-9.861 \cdot 10^{-2}$
0.9	0.65	o	2.374	$5.588 \cdot 10^{-2}$	-0.342	1.04	-2.102	1.205	0.284
0.9	0.65	e	2.374	$1.943 \cdot 10^{-2}$	$-9.567 \cdot 10^{-2}$	$-5.778 \cdot 10^{-2}$	0.149	-0.134	$-6.964 \cdot 10^{-2}$
0.9	0.65	o	2.374	$5.659 \cdot 10^{-2}$	-0.349	1.089	-2.204	1.266	0.299
0.9	0.65	e	2.374	$2.041 \cdot 10^{-2}$	-0.108	$1.855 \cdot 10^{-2}$	$-8.247 \cdot 10^{-3}$	$-4.183 \cdot 10^{-2}$	$-4.642 \cdot 10^{-2}$
0.9	0.65	o	2.374	$5.694 \cdot 10^{-2}$	-0.354	1.117	-2.262	1.299	0.307
0.9	0.65	e	2.374	$2.091 \cdot 10^{-2}$	-0.117	$7.662 \cdot 10^{-2}$	-0.132	$3.187 \cdot 10^{-2}$	$-2.76 \cdot 10^{-2}$
0.9	0.65	o	2.374	$5.742 \cdot 10^{-2}$	-0.359	1.153	-2.337	1.343	0.318
0.9	0.65	e	2.374	$2.068 \cdot 10^{-2}$	-0.118	$9.209 \cdot 10^{-2}$	-0.167	$5.255 \cdot 10^{-2}$	$-2.231 \cdot 10^{-2}$
0.9	0.65	o	2.374	$5.768 \cdot 10^{-2}$	-0.363	1.179	-2.393	1.377	0.327

1.1	0.65	e	2.463	$1.685 \cdot 10^{-2}$	$-9.105 \cdot 10^{-2}$	$4.191 \cdot 10^{-2}$	-0.113	$3.458 \cdot 10^{-2}$	$-2.388 \cdot 10^{-2}$
1.1	0.65	o	2.374	$5.192 \cdot 10^{-2}$	-0.326	1.034	-2.109	1.215	0.287
1.1	0.65	e	2.463	$1.766 \cdot 10^{-2}$	-0.101	0.102	-0.236	0.107	$-5.516 \cdot 10^{-3}$
1.1	0.65	o	2.463	$4.755 \cdot 10^{-2}$	-0.29	0.808	-1.63	0.93	0.214
1.1	0.65	e	2.463	$1.785 \cdot 10^{-2}$	-0.106	0.132	-0.299	0.144	$3.806 \cdot 10^{-3}$
1.1	0.65	o	2.463	$4.789 \cdot 10^{-2}$	-0.295	0.837	-1.691	0.967	0.224
1.1	0.65	e	2.463	$1.782 \cdot 10^{-2}$	-0.108	0.153	-0.345	0.172	$1.083 \cdot 10^{-2}$
1.1	0.65	o	2.463	$4.825 \cdot 10^{-2}$	-0.299	0.867	-1.756	1.005	0.234
1.1	0.65	e	2.463	$1.757 \cdot 10^{-2}$	-0.109	0.161	-0.364	0.184	$1.406 \cdot 10^{-2}$
1.1	0.65	o	2.463	$4.84 \cdot 10^{-2}$	-0.301	0.885	-1.795	1.029	0.24
1.3	0.65	e	2.463	$6.508 \cdot 10^{-3}$	$-4.182 \cdot 10^{-3}$	-0.484	1.018	-0.64	-0.196
1.3	0.65	o	2.463	$4.432 \cdot 10^{-2}$	-0.273	0.762	-1.55	0.887	0.205
1.3	0.65	e	2.463	$6.975 \cdot 10^{-3}$	$-1.083 \cdot 10^{-2}$	-0.441	0.924	-0.584	-0.182
1.3	0.65	o	2.463	$4.456 \cdot 10^{-2}$	-0.276	0.785	-1.6	0.917	0.212
1.3	0.65	e	2.463	$7.137 \cdot 10^{-3}$	$-1.468 \cdot 10^{-2}$	-0.414	0.867	-0.55	-0.173
1.3	0.65	o	2.463	$4.47 \cdot 10^{-2}$	-0.279	0.802	-1.636	0.939	0.218
1.3	0.65	e	2.463	$7.111 \cdot 10^{-3}$	$-1.676 \cdot 10^{-2}$	-0.396	0.826	-0.525	-0.167
1.3	0.65	o	2.463	$4.487 \cdot 10^{-2}$	-0.281	0.82	-1.676	0.963	0.224
1.3	0.65	e	2.463	$6.896 \cdot 10^{-3}$	$-1.674 \cdot 10^{-2}$	-0.392	0.815	-0.518	-0.165
1.3	0.65	o	2.463	$4.489 \cdot 10^{-2}$	-0.282	0.83	-1.697	0.975	0.227
1.5	0.65	e	2.463	$8.288 \cdot 10^{-3}$	$-2.873 \cdot 10^{-2}$	-0.26	0.506	-0.327	-0.114
1.5	0.65	o	2.463	$4.195 \cdot 10^{-2}$	-0.26	0.727	-1.49	0.855	0.197
1.5	0.65	e	2.463	$8.297 \cdot 10^{-3}$	$-3.06 \cdot 10^{-2}$	-0.248	0.481	-0.312	-0.111
1.5	0.65	o	2.463	$4.204 \cdot 10^{-2}$	-0.262	0.742	-1.522	0.874	0.202
1.5	0.65	e	2.553	$7.257 \cdot 10^{-3}$	$-2.325 \cdot 10^{-2}$	-0.293	0.579	-0.37	-0.125
1.5	0.65	o	2.463	$4.212 \cdot 10^{-2}$	-0.264	0.755	-1.551	0.891	0.206
1.5	0.65	e	2.553	$7.164 \cdot 10^{-3}$	$-2.409 \cdot 10^{-2}$	-0.285	0.559	-0.358	-0.122
1.5	0.65	o	2.463	$4.213 \cdot 10^{-2}$	-0.265	0.763	-1.569	0.902	0.209
1.5	0.65	e	2.553	$7.015 \cdot 10^{-3}$	$-2.412 \cdot 10^{-2}$	-0.282	0.55	-0.353	-0.121
1.5	0.65	o	2.463	$4.227 \cdot 10^{-2}$	-0.267	0.778	-1.602	0.922	0.214
1.7	0.65	e	2.553	$7.656 \cdot 10^{-3}$	$-2.912 \cdot 10^{-2}$	-0.207	0.367	-0.237	$-8.958 \cdot 10^{-2}$
1.7	0.65	o	2.463	$4.009 \cdot 10^{-2}$	-0.249	0.692	-1.426	0.819	0.188
1.7	0.65	e	2.553	$7.633 \cdot 10^{-3}$	$-3.027 \cdot 10^{-2}$	-0.199	0.352	-0.228	$-8.732 \cdot 10^{-2}$
1.7	0.65	o	2.463	$4.012 \cdot 10^{-2}$	-0.25	0.702	-1.448	0.833	0.192
1.7	0.65	e	2.553	$7.468 \cdot 10^{-3}$	$-3.014 \cdot 10^{-2}$	-0.199	0.351	-0.227	$-8.712 \cdot 10^{-2}$
1.7	0.65	o	2.463	$4.016 \cdot 10^{-2}$	-0.252	0.713	-1.473	0.848	0.196
1.7	0.65	e	2.553	$7.289 \cdot 10^{-3}$	$-2.974 \cdot 10^{-2}$	-0.2	0.352	-0.228	$-8.719 \cdot 10^{-2}$
1.7	0.65	o	2.463	$4.012 \cdot 10^{-2}$	-0.252	0.718	-1.484	0.855	0.198
1.7	0.65	e	2.553	$7.036 \cdot 10^{-3}$	$-2.838 \cdot 10^{-2}$	-0.207	0.367	-0.237	$-8.95 \cdot 10^{-2}$
1.7	0.65	o	2.463	$4.019 \cdot 10^{-2}$	-0.253	0.728	-1.505	0.867	0.201
1.9	0.65	e	2.553	$4.929 \cdot 10^{-3}$	$-4.442 \cdot 10^{-3}$	-0.361	0.708	-0.444	-0.143
1.9	0.65	o	2.463	$3.865 \cdot 10^{-2}$	-0.24	0.66	-1.366	0.785	0.18
1.9	0.65	e	2.553	$4.956 \cdot 10^{-3}$	$-5.886 \cdot 10^{-3}$	-0.35	0.685	-0.43	-0.14
1.9	0.65	o	2.463	$3.857 \cdot 10^{-2}$	-0.24	0.665	-1.377	0.793	0.182
1.9	0.65	e	2.553	$4.768 \cdot 10^{-3}$	$-5.297 \cdot 10^{-3}$	-0.353	0.689	-0.432	-0.14
1.9	0.65	o	2.463	$3.866 \cdot 10^{-2}$	-0.242	0.677	-1.403	0.808	0.186
1.9	0.65	e	2.553	$4.676 \cdot 10^{-3}$	$-5.51 \cdot 10^{-3}$	-0.349	0.68	-0.426	-0.139
1.9	0.65	o	2.463	$3.861 \cdot 10^{-2}$	-0.242	0.681	-1.413	0.815	0.188
1.9	0.65	e	2.553	$4.565 \cdot 10^{-3}$	$-5.244 \cdot 10^{-3}$	-0.349	0.681	-0.426	-0.139
1.9	0.65	o	2.463	$3.852 \cdot 10^{-2}$	-0.242	0.681	-1.414	0.815	0.188

Partially etched uncapped LNOI waveguide coefficients

w	τ	pol	λ_{max}	A	B	C	D	E	F
0.5	0.65	e	2.016	$2.137 \cdot 10^{-2}$	$1.849 \cdot 10^{-2}$	-1.588	3.759	-2.374	-0.664
0.5	0.65	o	2.016	0.154	-1.039	4.442	-8.742	4.999	1.219
0.5	0.65	e	2.016	$3.093 \cdot 10^{-2}$	$-6.531 \cdot 10^{-2}$	-1.17	2.98	-1.941	-0.56
0.5	0.65	o	2.016	0.153	-1.04	4.46	-8.786	5.027	1.226
0.5	0.65	e	2.016	$3.589 \cdot 10^{-2}$	-0.124	-0.825	2.292	-1.545	-0.462
0.5	0.65	o	2.016	0.153	-1.045	4.502	-8.881	5.084	1.241
0.5	0.65	e	2.016	$3.525 \cdot 10^{-2}$	-0.145	-0.66	1.936	-1.333	-0.408
0.5	0.65	o	2.016	0.152	-1.048	4.535	-8.954	5.128	1.252
0.5	0.65	e	2.016	$3.054 \cdot 10^{-2}$	-0.132	-0.675	1.929	-1.321	-0.403
0.5	0.65	o	2.016	0.151	-1.048	4.556	-9.008	5.162	1.261
0.7	0.65	e	2.195	$3.261 \cdot 10^{-2}$	-0.165	$-4.725 \cdot 10^{-2}$	0.384	-0.344	-0.14
0.7	0.65	o	2.105	0.124	-0.866	3.727	-7.387	4.237	1.034
0.7	0.65	e	2.195	$3.549 \cdot 10^{-2}$	-0.199	0.156	$-2.328 \cdot 10^{-2}$	-0.109	$-8.193 \cdot 10^{-2}$
0.7	0.65	o	2.105	0.123	-0.864	3.735	-7.412	4.254	1.039
0.7	0.65	e	2.195	$3.589 \cdot 10^{-2}$	-0.217	0.278	-0.283	$4.524 \cdot 10^{-2}$	$-4.29 \cdot 10^{-2}$
0.7	0.65	o	2.105	0.122	-0.866	3.757	-7.466	4.287	1.047
0.7	0.65	e	2.195	$3.391 \cdot 10^{-2}$	-0.215	0.298	-0.341	$8.324 \cdot 10^{-2}$	$-3.254 \cdot 10^{-2}$

0.7	0.65	o	2.195	0.124	-0.883	3.869	-7.703	4.428	1.083
0.7	0.65	e	2.195	$3.08 \cdot 10^{-2}$	-0.202	0.257	-0.278	$5.17 \cdot 10^{-2}$	$-3.942 \cdot 10^{-2}$
0.7	0.65	o	2.195	0.123	-0.884	3.89	-7.755	4.461	1.092
0.9	0.65	e	2.284	$2.236 \cdot 10^{-2}$	-0.129	$6.294 \cdot 10^{-2}$	$-7.39 \cdot 10^{-2}$	$-6.814 \cdot 10^{-3}$	$-3.709 \cdot 10^{-2}$
0.9	0.65	o	2.195	0.106	-0.759	3.276	-6.525	3.75	0.915
0.9	0.65	e	2.284	$2.292 \cdot 10^{-2}$	-0.142	0.152	-0.264	0.106	$-8.323 \cdot 10^{-3}$
0.9	0.65	o	2.195	0.105	-0.757	3.277	-6.537	3.76	0.918
0.9	0.65	e	2.284	$2.221 \cdot 10^{-2}$	-0.145	0.186	-0.34	0.153	$3.788 \cdot 10^{-3}$
0.9	0.65	o	2.195	0.105	-0.756	3.284	-6.558	3.773	0.922
0.9	0.65	e	2.284	$2.051 \cdot 10^{-2}$	-0.139	0.17	-0.318	0.142	$1.609 \cdot 10^{-3}$
0.9	0.65	o	2.195	0.104	-0.755	3.286	-6.567	3.78	0.924
0.9	0.65	e	2.284	$1.867 \cdot 10^{-2}$	-0.131	0.141	-0.271	0.118	$-3.874 \cdot 10^{-3}$
0.9	0.65	o	2.195	0.103	-0.753	3.285	-6.573	3.786	0.926
1.1	0.65	e	2.374	$1.113 \cdot 10^{-2}$	$-4.577 \cdot 10^{-2}$	-0.359	0.802	-0.524	-0.169
1.1	0.65	o	2.284	$9.461 \cdot 10^{-2}$	-0.683	2.929	-5.848	3.364	0.82
1.1	0.65	e	2.374	$1.095 \cdot 10^{-2}$	$-5.004 \cdot 10^{-2}$	-0.326	0.731	-0.481	-0.158
1.1	0.65	o	2.284	$9.389 \cdot 10^{-2}$	-0.681	2.932	-5.863	3.374	0.823
1.1	0.65	e	2.374	$1.045 \cdot 10^{-2}$	$-5.191 \cdot 10^{-2}$	-0.303	0.674	-0.446	-0.148
1.1	0.65	o	2.284	$9.321 \cdot 10^{-2}$	-0.679	2.931	-5.87	3.381	0.825
1.1	0.65	e	2.374	$9.344 \cdot 10^{-3}$	$-4.792 \cdot 10^{-2}$	-0.315	0.692	-0.454	-0.15
1.1	0.65	o	2.284	$9.287 \cdot 10^{-2}$	-0.68	2.944	-5.902	3.401	0.831
1.1	0.65	e	2.463	$9.104 \cdot 10^{-3}$	$-5.048 \cdot 10^{-2}$	-0.285	0.622	-0.411	-0.139
1.1	0.65	o	2.284	$9.223 \cdot 10^{-2}$	-0.677	2.939	-5.898	3.401	0.831
1.3	0.65	e	2.463	$1.105 \cdot 10^{-2}$	$-5.542 \cdot 10^{-2}$	-0.207	0.446	-0.304	-0.111
1.3	0.65	o	2.284	$8.753 \cdot 10^{-2}$	-0.635	2.714	-5.428	3.124	0.761
1.3	0.65	e	2.463	$1.077 \cdot 10^{-2}$	$-5.728 \cdot 10^{-2}$	-0.189	0.406	-0.279	-0.105
1.3	0.65	o	2.284	$8.645 \cdot 10^{-2}$	-0.63	2.696	-5.402	3.11	0.758
1.3	0.65	e	2.463	$1.015 \cdot 10^{-2}$	$-5.584 \cdot 10^{-2}$	-0.192	0.408	-0.28	-0.105
1.3	0.65	o	2.284	$8.581 \cdot 10^{-2}$	-0.628	2.694	-5.404	3.114	0.759
1.3	0.65	e	2.463	$9.394 \cdot 10^{-3}$	$-5.302 \cdot 10^{-2}$	-0.2	0.419	-0.285	-0.106
1.3	0.65	o	2.284	$8.51 \cdot 10^{-2}$	-0.625	2.685	-5.39	3.107	0.758
1.3	0.65	e	2.463	$8.564 \cdot 10^{-3}$	$-4.885 \cdot 10^{-2}$	-0.218	0.452	-0.303	-0.11
1.3	0.65	o	2.284	$8.454 \cdot 10^{-2}$	-0.623	2.679	-5.384	3.105	0.758
1.5	0.65	e	2.463	$1.249 \cdot 10^{-2}$	$-7.644 \cdot 10^{-2}$	$1.022 \cdot 10^{-2}$	$-6.436 \cdot 10^{-2}$	$1.298 \cdot 10^{-2}$	$-2.709 \cdot 10^{-2}$
1.5	0.65	o	2.284	$8.316 \cdot 10^{-2}$	-0.605	2.576	-5.156	2.968	0.722
1.5	0.65	e	2.463	$1.207 \cdot 10^{-2}$	$-7.558 \cdot 10^{-2}$	$7.336 \cdot 10^{-3}$	$-5.882 \cdot 10^{-2}$	$9.741 \cdot 10^{-3}$	$-2.792 \cdot 10^{-2}$
1.5	0.65	o	2.284	$8.184 \cdot 10^{-2}$	-0.598	2.547	-5.107	2.941	0.716
1.5	0.65	e	2.553	$1.032 \cdot 10^{-2}$	$-6.301 \cdot 10^{-2}$	$-6.843 \cdot 10^{-2}$	0.1	$-8.422 \cdot 10^{-2}$	$-5.184 \cdot 10^{-2}$
1.5	0.65	o	2.284	$8.094 \cdot 10^{-2}$	-0.593	2.53	-5.078	2.926	0.713
1.5	0.65	e	2.553	$9.706 \cdot 10^{-3}$	$-6.022 \cdot 10^{-2}$	$-8.021 \cdot 10^{-2}$	0.121	$-9.605 \cdot 10^{-2}$	$-5.468 \cdot 10^{-2}$
1.5	0.65	o	2.284	$8.037 \cdot 10^{-2}$	-0.591	2.526	-5.077	2.927	0.713
1.5	0.65	e	2.553	$9.157 \cdot 10^{-3}$	$-5.753 \cdot 10^{-2}$	$-9.153 \cdot 10^{-2}$	0.142	-0.107	$-5.735 \cdot 10^{-2}$
1.5	0.65	o	2.284	$7.95 \cdot 10^{-2}$	-0.586	2.502	-5.033	2.902	0.707
1.7	0.65	e	2.553	$5.947 \cdot 10^{-3}$	$-1.66 \cdot 10^{-2}$	-0.369	0.761	-0.484	-0.155
1.7	0.65	o	2.284	$8.113 \cdot 10^{-2}$	-0.59	2.518	-5.045	2.904	0.707
1.7	0.65	e	2.553	$5.698 \cdot 10^{-3}$	$-1.662 \cdot 10^{-2}$	-0.366	0.754	-0.479	-0.154
1.7	0.65	o	2.284	$7.927 \cdot 10^{-2}$	-0.579	2.461	-4.936	2.842	0.692
1.7	0.65	e	2.553	$5.369 \cdot 10^{-3}$	$-1.583 \cdot 10^{-2}$	-0.366	0.753	-0.478	-0.154
1.7	0.65	o	2.284	$7.805 \cdot 10^{-2}$	-0.572	2.429	-4.876	2.809	0.684
1.7	0.65	e	2.553	$5.035 \cdot 10^{-3}$	$-1.478 \cdot 10^{-2}$	-0.368	0.753	-0.477	-0.153
1.7	0.65	o	2.284	$7.728 \cdot 10^{-2}$	-0.568	2.414	-4.853	2.798	0.681
1.7	0.65	e	2.553	$4.677 \cdot 10^{-3}$	$-1.317 \cdot 10^{-2}$	-0.374	0.764	-0.483	-0.155
1.7	0.65	o	2.284	$7.638 \cdot 10^{-2}$	-0.562	2.387	-4.8	2.767	0.674
1.9	0.65	e	2.463	$1.056 \cdot 10^{-2}$	$-5.894 \cdot 10^{-2}$	$-5.53 \cdot 10^{-2}$	$6.477 \cdot 10^{-2}$	$-6.084 \cdot 10^{-2}$	$-4.507 \cdot 10^{-2}$
1.9	0.65	o	2.284	$8.169 \cdot 10^{-2}$	-0.595	2.56	-5.131	2.954	0.719
1.9	0.65	e	2.553	$8.951 \cdot 10^{-3}$	$-4.707 \cdot 10^{-2}$	-0.128	0.217	-0.151	$-6.815 \cdot 10^{-2}$
1.9	0.65	o	2.284	$7.682 \cdot 10^{-2}$	-0.56	2.372	-4.758	2.74	0.666
1.9	0.65	e	2.553	$8.415 \cdot 10^{-3}$	$-4.448 \cdot 10^{-2}$	-0.139	0.237	-0.162	$-7.06 \cdot 10^{-2}$
1.9	0.65	o	2.374	$7.082 \cdot 10^{-2}$	-0.514	2.103	-4.206	2.417	0.585
1.9	0.65	e	2.553	$7.809 \cdot 10^{-3}$	$-4.09 \cdot 10^{-2}$	-0.157	0.272	-0.182	$-7.551 \cdot 10^{-2}$
1.9	0.65	o	2.374	$6.941 \cdot 10^{-2}$	-0.505	2.059	-4.121	2.369	0.573
1.9	0.65	e	2.553	$7.228 \cdot 10^{-3}$	$-3.704 \cdot 10^{-2}$	-0.178	0.315	-0.207	$-8.192 \cdot 10^{-2}$
1.9	0.65	o	2.374	$6.851 \cdot 10^{-2}$	-0.499	2.033	-4.075	2.343	0.567

Acknowledgement

At the end for this four-and-a-half-year journey, I need to express my wholehearted gratitude to all the people that accompanied me through this endeavour. First and foremost, I want to thank my supervisor Christine. Her constant joy and excitement in doing physics, pushing the limits of knowledge and questioning even our basic assumptions have been a constant driver to improve the quality of my research. Moreover, I am impressed by her infallibility in choosing the right people to be part of her group. The international yet warm and familiar atmosphere experience in her group is the most important legacy I will carry with me in the future years.

A special thanks is required for my two office mates, Michael and Vahid. Thanks for enduring my continuous stream of questions and my chatty Italian style. I know it was a bit too much sometimes. And thanks Michael for teaching me how to write papers. Thanks for your patience. And for introducing me to StarCraft 2.

The boardgame nerd gang met here was the greatest unexpected surprise and gift I could have hoped for. Marcello, Jano, Michael, Tanya, Angelina, I greatly enjoyed your friendship and your diverse passions, and you made my days in Paderborn much more bearable. Such an amazing group of friends will be hard to come by again.

Another big special thanks to my friends at the Bib Wohnheim, in particular Michael, Demir and Nina. I really miss our tea chats in the middle of the night and our endless discussions on the more disparate topics.

I would like to thank all my other colleagues. I really enjoyed sharing this scientific journey with you. I'd like to thank Christof, Laura and Raimund, who taught me the secrets for the production of KTP waveguides. Thanks to Helge, who mentored me along the first few conferences and during my lab experience. Debugging your code won't be forgotten.

Thanks to Kai for giving me some insights into the Chinese culture. I will miss watching you serving the tea with precise and gentle movements and being called "Shushu" by Lobu.

Thanks to Sonja, Johannes, Benni and Kai for the great joy that their children have brought to our group: it warms my heart seeing courageous couples deciding to gift the world with new lives, despite the difficult times we are facing.

Thanks to the rest of the IQO group, the current members - Thomas, Syam, Renee, Lennard, Sebastian, Nidhin, Viktor, Harald, Felix, Rita, Petra - and the past ones - Regina, Fabian, Evan, Linda, John -, to the Azubis and to the MQO group.

I want to thank my Italian friends Davide, Valeria, Alessandro, Adele and Mirko for helping getting through my PhD. You always believed in me more than I did. I missed and will miss you.

Finally, I feel endless gratitude to my family. To my parents, because they always

were there when I was in need, because they supported every decision and because they pushed me into this journey. And to my siblings: Daniele, who always drives me to be better than him, to Chiara, for her kindness and her art, and Gabriele, whose serendipity will always amaze me.

Bibliography

- [1] D. Marcuse. *Theory of dielectric optical waveguides*. Academic Press, 1991.
- [2] T. Tamir, R. Alferness, W. K. Burns, et al. *Guided-Wave Optoelectronics*. 1st ed. Springer-Verlag Berlin Heidelberg, 1988.
- [3] T. Suhara and M. Fujimura. *Waveguide Nonlinear-Optic Devices*. 1st ed. Springer-Verlag Berlin Heidelberg, 2003.
- [4] D. Khalil. "Extension of the radiation spectrum method for the reflection calculation at the end of a strongly guiding optical waveguide". *Optical and Quantum Electronics* **35**, 801–809 (2003).
- [5] E. A. J. Marcatili. "Dielectric Rectangular Waveguide and Directional Coupler for Integrated Optics". *Bell System Technical Journal* **48**, 2071–2102 (1969).
- [6] W. J. Westerveld, S. M. Leinders, K. W. A. V. Dongen, and H. P. Urbach. "Extension of Marcatili's Analytical Approach for Rectangular Silicon Optical Waveguides". *Journal of Lightwave Technology* **30**, 2388–2401 (2012).
- [7] C. Grossmann, H.-G. Roos, and M. Stynes. *Numerical Treatment of Partial Differential Equations*. Springer Berlin Heidelberg, 2007.
- [8] P. Kumar. "Quantum frequency conversion". *Optics Letters* **15**, 1476–1478 (1990).
- [9] M. H. Chou, K. R. Parameswaran, M. M. Fejer, and I. Brener. "Multiple-channel wavelength conversion by use of engineered quasi-phase-matching structures in LiNbO₃ waveguides." *Optics letters* **24**, 1157–1159 (1999).
- [10] G. Cerullo and S. De Silvestri. "Ultrafast optical parametric amplifiers". *Review of Scientific Instruments* **74**, 1–18 (2003).
- [11] M. Pysher, R. Bloomer, O. Pfister, et al. "Broadband amplitude squeezing in a periodically poled KTiOPO₄ waveguide". *Optics Letters* **34**, 256–258 (2008).
- [12] K. Thyagarajan, J. Lugani, S. Ghosh, et al. "Generation of polarization-entangled photons using type-II doubly periodically poled lithium niobate waveguides". *Physical Review A - Atomic, Molecular, and Optical Physics* **80**, 1–8 (2009).
- [13] M. Stefszky, R. Ricken, C. Eigner, et al. "Waveguide Cavity Resonator as a Source of Optical Squeezing". *Physical Review Applied* **7**, 1–5 (2017).
- [14] M. A. Albota and F. N. C. Wong. "Efficient single-photon counting at 1550 μm by means of frequency upconversion". *Optics Letters* **29**, 1449–1451 (2004).
- [15] R. V. Roussev, C. Langrock, J. R. Kurz, and M. M. Fejer. "Periodically poled lithium niobate waveguide sum-frequency generator for efficient single-photon detection at communication wavelengths". *Optics letters* **29**, 1518–1520 (2004).

Bibliography

- [16] A. P. Vandevender and P. G. Kwiat. “High efficiency single photon detection via frequency up-conversion”. *Journal of Modern Optics* **51**, 1433–1445 (2004).
- [17] J. S. Pelc, L. Yu, K. De Greve, et al. “Downconversion quantum interface for a single quantum dot spin and 1550-nm single-photon channel”. *Optics Express* **20**, 27510–27519 (2012).
- [18] H. Rütz, K. H. Luo, H. Suche, and C. Silberhorn. “Quantum Frequency Conversion between Infrared and Ultraviolet”. *Physical Review Applied* **7**, 1–7 (2017).
- [19] N. Maring, P. Farrera, K. Kutluer, et al. “Photonic quantum state transfer between a cold atomic gas and a crystal”. *Nature* **551**, 485–488 (2017).
- [20] A. Orioux and E. Diamanti. “Recent advances on integrated quantum communications”. *Journal of Optics* **18**, 083002 (2016).
- [21] N. Montaut, L. Sansoni, E. Meyer-Scott, et al. “High-Efficiency Plug-and-Play Source of Heralded Single Photons”. *Phys. Rev. Applied* **8**, 24021 (2017).
- [22] L. K. Shalm, E. Meyer-Scott, B. G. Christensen, et al. “Strong Loophole-Free Test of Local Realism”. *Phys. Rev. Lett.* **115**, 250402 (2015).
- [23] G. Harder, V. Ansari, B. Brecht, et al. “An optimized photon pair source for quantum circuits”. *Optics Express* **21**, 13975–13985 (2013).
- [24] N. C. Menicucci, P. Van Loock, M. Gu, et al. “Universal quantum computation with continuous-variable cluster states”. *Physical Review Letters* **97**, 13–16 (2006).
- [25] R. W. Boyd. *Nonlinear Optics*. 3rd. Orlando, FL, USA: Academic Press, Inc., 2008.
- [26] J. M. Manley and H. E. Rowe. “General Energy Relations in Nonlinear Reactances”. *Proceedings of the IRE* **47**, 2115–2116 (1959).
- [27] A. Christ, B. Brecht, W. Mauerer, and C. Silberhorn. “Theory of quantum frequency conversion and type-II parametric down-conversion in the high-gain regime”. *New Journal of Physics* **15**, 053038 (2013).
- [28] B. Brecht. “Engineering ultrafast quantum frequency conversion”. PhD thesis. Paderborn University, 2013.
- [29] G. Harder. “Optimized Down-Conversion Source and State-Characterization Tools for Quantum Optics”. PhD thesis. Paderborn University, 2016.
- [30] C. K. Law, I. A. Walmsley, and J. H. Eberly. “Continuous frequency entanglement: Effective finite hilbert space and entropy control”. *Physical Review Letters* **84**, 5304–5307 (2000).
- [31] A. Eckstein, B. Brecht, and C. Silberhorn. “A quantum pulse gate based on spectrally engineered sum frequency generation”. *Optics Express* **19**, 13770–13778 (2011).
- [32] V. Ansari, E. Roccia, M. Santandrea, et al. “Heralded generation of high-purity ultrashort single photons in arbitrary temporal shapes”. **26**, 2764–2774 (2017).
- [33] W. H. Zachariasen. *Skr. Norske Vid.-Ada. Oslo, Mat. Naturv.* (1928).

- [34] B. T. Matthias and J. P. Remeika. "Ferroelectricity in the Ilmenite Structure". *Phys. Rev.* **76**, 1886–1887 (1949).
- [35] T. Volk and M. Wöhrke. *Lithium Niobate - Defects, Photorefraction and Ferroelectric Switching*. Springer, 2008.
- [36] D. N. Nikogosyan. *Nonlinear optical crystals - A complete survey*. Springer, 2005.
- [37] D. Jundt. "Temperature-dependent Sellmeier equation for the index of refraction, $n(e)$, in congruent lithium niobate." *Optics Letters* **22**, 1553–1555 (1997).
- [38] G. J. Edwards and M. Lawrence. "A temperature-dependent dispersion equation for congruently grown lithium niobate". *Optical and Quantum Electronics* **16**, 373–375 (1984).
- [39] R. Regener and W. Sohler. "Efficient second-harmonic generation in Ti:LiNbO₃ channel waveguide resonators". *Journal of the Optical Society of America B* **5**, 267–277 (1988).
- [40] J. Amin, V. Pruneri, J. Webjörn, et al. "Blue light generation in a periodically poled Ti:LiNbO₃ channel waveguide". *Optics Communications* **135**, 41–44 (1997).
- [41] H. Kanbara, H. Itoh, M. Asobe, and K. Noguchi. "All-Optical Switching Based on Cascading of Second-Order Nonlinearities in a Periodically Poled Titanium-Diffused Lithium Niobate Waveguide". *IEEE Photonics Technology Letters* **11**, 328–330 (1999).
- [42] K. H. Luo, H. Herrmann, S. Krapick, et al. "Direct generation of genuine single-longitudinal-mode narrowband photon pairs". *New Journal of Physics* **17**, 073039 (2015).
- [43] L. Sansoni, K. H. Luo, C. Eigner, et al. "A two-channel, spectrally degenerate polarization entangled source on chip". *npj Quantum Information* **3**, 1–5 (2017).
- [44] M. Stefszky, V. Ulvila, Z. Abdallah, C. Silberhorn, and M. Vainio. "Towards optical-frequency-comb generation in continuous-wave-pumped titanium-indiffused lithium-niobate waveguide resonators". *Physical Review A* **98**, 1–9 (2018).
- [45] R. Kruse, L. Sansoni, S. Brauner, et al. "Dual-path source engineering in integrated quantum optics". *Physical Review A - Atomic, Molecular, and Optical Physics* **92**, 1–6 (2015).
- [46] P. R. Sharapova, K. H. Luo, H. Herrmann, et al. "Toolbox for the design of LiNbO₃-based passive and active integrated quantum circuits". *New Journal of Physics* **19**, 123009 (2017).
- [47] K. H. Luo, S. Brauner, C. Eigner, et al. "Nonlinear integrated quantum electro-optic circuits". *Science Advances* **5**, 1–8 (2018).
- [48] E. Strake, G. P. Bava, and I. Montrosset. "Guided Modes of Ti:LiNbO₃ Channel Waveguides: A Novel Quasi-Analytical Technique in Comparison with the Scalar Finite-Element Method". *Journal of Lightwave Technology* **6**, 1126–1135 (1988).
- [49] M. Zhang, C. Wang, R. Cheng, A. Shams-Ansari, and M. Lončar. "Monolithic ultra-high-Q lithium niobate microring resonator". *Optica* **4**, 1536–1537 (2017).

Bibliography

- [50] C. Wang, M. Zhang, B. Stern, M. Lipson, and M. Lončar. “Nanophotonic Lithium Niobate Electro-optic Modulators”. *Optics Express* **26**, 1547–1555 (2017).
- [51] C. Wang, M. Zhang, R. Zhu, H. Hu, and M. Lončar. “Monolithic photonic circuits for Kerr frequency comb generation, filtering and modulation”. *Nature Communications*, 1–6 (2018).
- [52] B. Desiatov, A. Shams-Ansari, M. Zhang, C. Wang, and M. Lončar. “Ultra-low-loss integrated visible photonics using thin-film lithium niobate”. *Optica* **6**, 380–384 (2019).
- [53] L. Ouvrard and M. Troost. “Recherches sur les phosphates doubles de titane, d’étain et de cuivre”. *Compt Rend* **111**, 177–179 (1890).
- [54] F. C. Zumsteg, J. D. Bierlein, and T. E. Gier. “ $K_xRb_{1-x}TiOPO_4$: A new nonlinear optical material”. *Journal of Applied Physics* **47**, 4980–4985 (1976).
- [55] A. Zukauskas, G. Strömqvist, V. Pasiskevicius, et al. “Fabrication of submicrometer quasi-phase-matched devices in KTP and RKTP”. *Optical Materials Express* **1**, 1319–1325 (2011).
- [56] O. Driesner. “Vergrabene Lichtwellenleiter in Kalium Titanyl Phosphat”. Master Thesis. Paderborn University, 2014.
- [57] G. Lindgren, A. Zukauskas, V. Pasiskevicius, F. Laurell, and C. Canalias. “Studies of sub-millisecond domain dynamics in periodically poled Rb-doped $KTiOPO_4$, using online in situ second harmonic generation”. *Optics Express* **23**, 20332–20339 (2015).
- [58] K. Kato and E. Takaoka. “Sellmeier and thermo-optic dispersion formulas for KTP”. *Applied optics* **41**, 5040–5044 (2002).
- [59] B. Boulanger, J. P. Fève, G. Marnier, et al. “Relative sign and absolute magnitude of $d^{(2)}$ nonlinear coefficients of KTP from second-harmonic-generation measurements”. *JOSA B* **11**, 750–757 (1994).
- [60] L. K. Cheng, L. T. Cheng, J. Galperin, P. A. Morris Hotsenpiller, and J. D. Bierlein. “Crystal growth and characterization of $KTiOPO_4$ isomorphs from the self-fluxes”. *Journal of crystal growth* **137**, 107–115 (1994).
- [61] J. D. Bierlein, A. Ferretti, L. Brixner, and W. Hsu. “Fabrication and characterization of optical waveguides in $KTiOPO_4$ ”. *Applied physics letters* **50**, 1216–1218 (1987).
- [62] J.-J. Yin, F. Lu, X.-B. Ming, Z.-H. Qin, and Y.-J. Ma. “Theoretical modeling and experiment of refractive index change in He^+ ion-implanted KTP waveguide.” *Applied optics* **51**, 2400–2406 (2012).
- [63] S. Campbell, R. R. Thomson, D. P. Hand, et al. “Frequency doubling in femto-second-written periodically-poled potassium titanyl phosphate waveguides”. *Conference on Lasers and Electro-Optics, 2007, CLEO 2007* **15**, 17146–17150 (2007).
- [64] F. Laurell, T. Calmano, S. Müller, et al. “Laser-written waveguides in KTP for broadband Type II second harmonic generation”. *Optics Express* **20**, 22308 (2012).

- [65] S. Müller, T. Calmano, P. W. Metz, et al. "Highly efficient continuous wave blue second-harmonic generation in fs-laser written periodically poled Rb:KTiOPO₄ waveguides". *Optics Letters* **39**, 1274–1277 (2014).
- [66] M. Volk, C. E. Rüter, M. Santandrea, et al. "Fabrication of low-loss Rb-exchanged ridge waveguides in z-cut KTiOPO₄". *Optical Materials Express* **8**, 2768–2770 (2018).
- [67] C. Eigner, M. Santandrea, L. Padberg, et al. "Periodically poled ridge waveguides in KTP for second harmonic generation in the UV regime". *Optics Express* **26**, 28827–28833 (2018).
- [68] L. Padberg. "Analysis and optimisation of rubidium in-diffused waveguides in KTP". PhD thesis. Paderborn University, 2017.
- [69] P. T. Callahan, K. Shafak, P. R. Battle, T. D. Roberts, and F. X. Kärtner. "Fiber-coupled balanced optical cross-correlator using PPKTP waveguides". *Optics Express* **22**, 1423–1431 (2014).
- [70] R. Regener and W. Sohler. "Loss in low finesse Ti:LiNbO₃ optical waveguide resonators". *Applied Physics B Photophysics and Laser Chemistry* **36**, 143–147 (1985).
- [71] A. De Rossi, V. Ortiz, M. Calligaro, et al. "Measuring propagation loss in a multimode semiconductor waveguide". *Journal of Applied Physics* **97**, 073105 (2005).
- [72] M. Yamada, N. Nada, M. Saitoh, and K. Watanabe. "First-order quasi-phase matched LiNbO₃ waveguide periodically poled by applying an external field for efficient blue second-harmonic generation". *Applied Physics Letters* **62**, 435–436 (1993).
- [73] S. Kim, V. Gopalan, K. Kitamura, and Y. Furukawa. "Domain reversal and non-stoichiometry in lithium tantalate". *Journal of Applied Physics* **90**, 2949–2963 (2001).
- [74] C. Canalias, J. Hirohashi, V. Pasiskevicius, and F. Laurell. "Polarization-switching characteristics of flux-grown KTiOPO₄ and RbTiOPO₄ at room temperature". *Journal of Applied Physics* **97**, (2005).
- [75] C. Kurz, J. Huwer, M. Schug, P. Müller, and J. Eschner. "A high-rate source for single photons in a pure quantum state". *New Journal of Physics* **15**, 055005 (2013).
- [76] C. Kurz, M. Schug, P. Eich, et al. "Experimental protocol for high-fidelity heralded photon-to-atom quantum state transfer". *Nature Communications* **5**, 5527 (2014).
- [77] C. Kurz, P. Eich, M. Schug, P. Müller, and J. Eschner. "Programmable atom-photon quantum interface". **93**, 1–5 (2016).
- [78] M. Karlsson. "Four-wave mixing in fibers with randomly varying zero-dispersion wavelength". *Journal of the Optical Society of America B* **15**, 2269–2275 (1998).
- [79] P. W. M. Mackwitz. "Nonlinear analysis of periodically poled waveguides in KTP : A fundamental study". PhD thesis. Paderborn University, 2017.

Bibliography

- [80] H. Rütz, K. H. Luo, H. Suche, and C. Silberhorn. “Towards a quantum interface between telecommunication and UV wavelengths: design and classical performance”. *Applied Physics B: Lasers and Optics* **122**, 1–8 (2016).
- [81] Synopsys. *RSoft*.
- [82] M. Avenhaus, A. Eckstein, P. J. Mosley, and C. Silberhorn. “Fiber-assisted single-photon spectrograph”. *Optics Letters* **34**, 2873–2875 (2009).
- [83] S. Helmfrid and G. Arvidsson. “Influence of randomly varying domain lengths and nonuniform effective index on second-harmonic generation in quasi-phase matching waveguides”. *Journal of Opt. Soc. Am. B* **8**, 797–804 (1991).
- [84] E. J. Lim, S. Matsumoto, and M. M. Fejer. “Noncritical phase matching for guided-wave frequency conversion”. *Applied Physics Letters* **57**, 2294–2296 (1990).
- [85] M. L. Bortz, S. J. Field, M. M. Fejer, et al. “Noncritical Quasi-Phase-Matched Second Harmonic Generation in an Annealed Proton-Exchanged LiNbO₃ Waveguide”. *IEEE Transactions on Quantum Electronics* **30**, 2953–2960 (1994).
- [86] M. Allgaier, V. Ansari, L. Sansoni, et al. “Highly efficient frequency conversion with bandwidth compression of quantum light”. *Nature Communications* **8**, 1–6 (2017).
- [87] T. Ito and S. Okazaki. “Pushing the limits of lithography”. *Nature* **406**, 1027–1031 (2000).
- [88] S. Helmfrid, G. Arvidsson, and J. Webjörn. “Influence of various imperfections on the conversion efficiency of second-harmonic generation in quasi-phase-matching lithium niobate waveguides”. *Journal of Opt. Soc. Am. B* **10**, 222–229 (1992).
- [89] D. Chang, C. Langrock, Y.-W. Lin, et al. “Complex-transfer-function analysis of optical-frequency converters”. *Optics Letters* **39**, 5106–5109 (2014).
- [90] J. S. Pelc, C. Langrock, Q. Zhang, and M. M. Fejer. “Influence of domain disorder on parametric noise in quasi-phase-matched quantum frequency converters.” *Optics letters* **35**, 2804–2806 (2010).
- [91] J. S. Pelc, C. R. Phillips, D. Chang, C. Langrock, and M. M. Fejer. “Efficiency pedestal in quasi-phase-matching devices with random duty-cycle errors.” *Optics letters* **36**, 864–866 (2011).
- [92] C. R. Phillips, J. S. Pelc, and M. M. Fejer. “Parametric processes in quasi-phase matching gratings with random duty cycle errors”. *Journal of the Optical Society of America B* **30**, 982–993 (2013).
- [93] M. Santandrea. *PyNumericalPhasematching*. 2019.
- [94] M. Farahmand and M. de Sterke. “Parametric amplification in presence of dispersion fluctuations.” *Optics Express* **12**, 136–142 (2004).
- [95] W. P. Bowen, N. Treps, R. Schnabel, and P. K. Lam. “Experimental Demonstration of Continuous Variable Polarization Entanglement”. *Physical Review Letters* **89**, 1–4 (2002).

- [96] M. Yukawa, R. Ukai, P. V. Loock, and A. Furusawa. “Experimental generation of four-mode continuous-variable cluster states”. *Physical Review A* **78**, 012301 (2008).
- [97] J. Aasi, J. Abadie, B. P. Abbott, et al. “Enhanced sensitivity of the LIGO gravitational wave detector by using squeezed states of light”. *Nature Photonics* **7**, 613–619 (2013).
- [98] D. K. Serkland, M. M. Fejer, R. L. Byer, and Y. Yamamoto. “Squeezing in a quasi-phase-matched LiNbO₃ waveguide.” *Optics letters* **20**, 1649–1651 (1995).
- [99] R. Nouroozi. “All Optical Wavelength Conversion and Parametric Amplification in Ti:PPLN Channel Waveguides for Telecommunication Applications”. PhD thesis. Paderborn University, 2010.
- [100] L. Oslslager, J. Cussey, A. T. Nguyen, et al. “Frequency-bin entangled photons”. *Physical Review A - Atomic, Molecular, and Optical Physics* **82**, 1–7 (2010).
- [101] T. Zhong, H. Zhou, R. D. Horansky, et al. “Photon-efficient quantum key distribution using time-energy entanglement with high-dimensional encoding”. *New Journal of Physics* **17**, 022002 (2015).
- [102] R. J. A. Francis-Jones and P. J. Mosley. “Characterisation of longitudinal variation in photonic crystal fibre”. *Optics Express* **24**, 24836–24845 (2016).
- [103] Y. L. Lee, Y. C. Noh, C. Jung, et al. “Reshaping of a second-harmonic curve in periodically poled Ti:LiNbO₃ channel waveguide by a local-temperature-control technique”. *Applied Physics Letters* **86**, 011104 (2005).
- [104] R. Nouroozi. “Effect of Waveguide Inhomogeneity in a $\chi^{(2)}$ -Based Pulsed Optical Parametric Amplifier”. *Journal of Lightwave Technology* **35**, 1693–1699 (2017).
- [105] M. Santandrea, M. Stefszky, V. Ansari, and C. Silberhorn. “Fabrication limits of waveguides in nonlinear crystals and their impact on quantum optics applications”. *New Journal of Physics* **21**, (2019).
- [106] T. Harlé, M. Barbier, M. Cordier, et al. “Constraints on photonic crystal fibers homogeneity for photon pair generation”. In: *Quantum Information and Measurement*. Optical Society of America, 2017.
- [107] F. R. Nash, G. D. Boyd, M. I. Sargent, and P. M. Bridenbaugh. “Effect of Optical Inhomogeneities on Phase Matching in Nonlinear Crystals”. *Journal of Applied Physics* **41**, 2564 (1970).
- [108] K. Saitoh and M. Koshiba. “Empirical relations for simple design of photonic crystal fibers”. *Optics Express* **13**, 267–274 (2005).
- [109] V. Berger. “Second-harmonic generation in monolithic cavities”. *J. Opt. Soc. Am. B* **14**, 1351–1360 (1997).
- [110] M. Fujimura, T. Suhara, and H. Nishihara. “Theoretical Analysis of Resonant Waveguide Optical Second Harmonic Generation”. *Journal of Lightwave Technology* **14**, 1899–1906 (1996).

Bibliography

- [111] C. Wang, X. Xiong, N. Andrade, et al. "Second harmonic generation in nanostructured thin-film lithium niobate waveguides". *Optics Express* **25**, 6963–6973 (2017).
- [112] C. Wang, C. Langrock, A. Marandi, et al. "Ultra-high-efficiency wavelength conversion in nanophotonic periodically poled lithium niobate waveguides". *Optica* **5**, 1438 (2018).
- [113] M. Zhang, B. Buscaino, C. Wang, et al. "Broadband electro-optic frequency comb generation in a lithium niobate microring resonator". *Nature* **568**, 373–377 (2019).
- [114] Lumerical Inc. <https://www.lumerical.com/products/>.
- [115] H. Hu, R. Ricken, and W. Sohler. "Lithium niobate photonic wires". *Optics Express* **17**, 24261–24268 (2009).
- [116] F. K. Reinhart, I. Hayashi, and M. B. Panish. "Mode reflectivity and waveguide properties of double-heterostructure injection lasers". *Journal of Applied Physics* **42**, 4466–4479 (1971).
- [117] T. Ikegami. "Reflectivity of Mode at Facet and Oscillation Mode in Double-Heterostructure Injection Lasers". *IEEE Journal of Quantum Electronics* **8**, 470–476 (1972).
- [118] H. H. El-Riffaey and D. Khalil. "Rigorous modal analysis of multi-mode interference (MMI) structures by radiation spectrum method with multiple reflection". *Optics Communications* **144**, 306–314 (1997).
- [119] I. Krasnokutska, J.-L. J. Tambasco, X. Li, and A. Peruzzo. "Ultra-low loss photonic circuits in lithium niobate on insulator". *Optics Express* **26**, 897–904 (2018).